

Investigations in Flatland

Scanning Tunnelling Microscopy Measurements of Noble Metal Surface States and Magnetic Atoms on Magnesium Oxide

by

Andrew James Macdonald

B.Sc. (Hon. Mathematical Physics Co-op), The University of Waterloo, 2011

A THESIS SUBMITTED IN PARTIAL FULFILMENT OF
THE REQUIREMENTS FOR THE DEGREE OF

DOCTOR OF PHILOSOPHY

in

THE FACULTY OF GRADUATE AND POSTDOCTORAL STUDIES

(Physics)

THE UNIVERSITY OF BRITISH COLUMBIA

(Vancouver)

September 2017

© Andrew James Macdonald, 2017

Abstract

At the atomic scale, surfaces exhibit a rich variety of physical phenomena that can be probed using a scanning tunnelling microscope (STM). The STM measures the quantum tunnelling of electrons between a metallic tip and conducting sample and can be used to characterize the nanoscale surface. This thesis presents STM measurements taken at low-temperature in ultra-high vacuum, which are used to characterize two different nanoscale environments: the two-dimensional surface states of Ag(111) and Cu(111) and the magnetic moments of iron and cobalt atoms deposited on a thin-film of magnesium oxide.

Fourier-transform scanning tunnelling spectroscopy (FT-STs) analysis of quasiparticle interference, created by impurity scattering on the surfaces of the noble metals Ag(111) and Cu(111), is used to compare the most common modes of acquiring FT-STs data and shows, through both experiment and simulations, that artifact features can arise that depend on how the STM tip height is stabilized throughout the course of the measurement. Such artifact features are similar to those arising from physical processes in the sample and are susceptible to misinterpretation in the analysis of FT-STs in a wide range of important materials. A prescription for characterizing and avoiding these artifacts is proposed, which details how to check for artifacts using measurement acquisition modes that do not depend on tip height as a function of lateral position and careful selection of the tunnelling energy.

In a separate set of experiments a spin resonance technique is coupled to an STM to probe the spin states of individual iron atoms on a magnesium oxide bilayer. The magnetic interaction between the iron atoms and surrounding spin centres shows an inverse-cubic distance dependence at distances greater than one nanometre. This distance-dependence demonstrates that the spins are coupled via a magnetic dipole-dipole interaction. By characterizing this interaction and combining it with atomic manipulation techniques a new form of nanoscale magnetometry is invented. This nanoscale magnetometer can be combined with trilayeration to probe the spin structure of individual atoms and nanoscale structures. The information gained characterizing these new forms of magnetic sensing sets the stage for the study of complex magnetic systems like molecular magnets.

Lay Summary

This thesis gives an account of two different forays into the nanoscale flatland of atomic surfaces using the scanning tunnelling microscope (STM). The STM operates by measuring a current between a metallic tip and a conducting surface. The first study focuses on measurement artifacts that arise when probing the electronic states of the surfaces of silver and copper. A theoretical framework is developed that demonstrates that these artifacts are a product of how the STM measurement is performed, and provides insight into how to identify and avoid these artifacts in measurements of more complex materials. The second set of experiments explores the magnetism of single iron atoms deposited on an insulating thin film. The iron atoms magnetic interaction is fully characterized using spin resonant STM measurements. This characterization allows for a new type of nanoscale magnetic sensor that can be used to locate nearby magnetic atoms and determine their magnetic moment.

Preface

The study of the set-point effect in measurements of the Ag(111) surface state presented in Chapter 4 has been published in *IOP Nanotechnology*, **27**(41):17, September 2016. The experimental work was performed at the University of British Columbia's Laboratory for Atomic Imaging Research under the supervision of Prof. S. A. Burke and Prof. Doug Bonn. Sample preparation and STM data acquisition was led by A. J. Macdonald working with Y.-S. Tremblay-Johnston, S. Grothe, and Dr. S. Chi. Theoretical modelling of the modulation in the density of states was done by Prof. Steve Johnston, with modifications made by A. J. Macdonald. FT-STS analysis code was developed in Python by A. J. Macdonald and Y.-S. Tremblay-Johnston. The set-point model of the tunnelling current and differential tunnelling conductance was developed in MATLAB by A. J. Macdonald. Prof. S. A. Burke oversaw all aspects of the data acquisition and analysis and wrote the resulting paper with A. J. Macdonald and Y.-S. Tremblay-Johnston. Technical support was provided by Pinder Dosanjh.

The characterization of the atomic-scale dipole-dipole interaction of iron atoms on magnesium oxide in Chapter 6 was performed at the IBM Almaden Research Centre and the results have been published in *Nature Nanotechnology*, 2017 **12**, 420-424. The project was done under the supervision of Dr. A. Heinrich and experimental runs were led by Dr. T. Choi, with guidance provided by C. Lutz and Dr. W. Paul. Dr. T. Choi, Dr. W. Paul, A. J. Macdonald, S. Rolf-Pissarczyk, Dr. F. D. Natterer, Dr. K. Yang, and P. Willke ran the experimental measurements, shifts, analyzed the initial results, spin-polarized tips, and used atomic manipulation to design and measure nanoscale structures. A. J. Macdonald, S. Rolf-Pissarczyk, W. Paul and Taeyoung Choi collected the bulk of the measurements used in the dipole-dipole characterization curves as a function of frequency and performed sample preparation of the Ag(100) single crystal, growth of the MgO thin-film, and deposition of the magnetic species. Dr. T. Choi wrote the resulting manuscript with comments, edits, and revisions provided by all authors. Technical support was provided by Bruce Meloir.

Table of Contents

Abstract	ii
Lay Summary	iii
Preface	iv
Table of Contents	v
List of Tables	viii
List of Figures	ix
List of Acronyms	xxi
List of Symbols	xxii
Acknowledgements	xxiii
Dedication	xxv
I Introduction to Scanning Tunnelling Microscopy	1
1 Welcome to Flatland	2
1.1 Flatland: The Nanoscale Surface	2
1.1.1 Measuring Electrons at the Nanoscale Surface	4
1.2 Surface Science at the Atomic Scale	5
1.2.1 Quantum Tunnelling	5
1.2.2 Early History	6
1.2.3 The Scanning Tunnelling Microscope	7
1.2.4 Theory of the STM Tunnelling Junction	9
1.3 Outlook	16
2 Experimental Methods	19
2.1 The Laboratory for Atomic Imaging Research	19
2.1.1 The CreaTec LT-STM	20
2.2 The IBM-Almaden Nanoscience Laboratory	23
2.2.1 The IBM 1-K STM	23

2.3	Comparison Between the CreaTec and the 1-K STM	25
2.4	Data Acquisition Modes of the STM	26
2.4.1	Topography	26
2.4.2	Spectroscopic Imaging using a Lock-In Amplifier	27
2.4.3	Scanning Tunnelling Spectroscopy (STS)	30
2.4.4	Spectroscopic Imaging via Spectroscopic Grid	31
2.5	Conclusions	33
 II Quasiparticle Interference in Noble Metal Surfaces		34
3	Quasiparticle Interference and Fourier-Transform Scanning Tunnelling Spectroscopy	35
3.1	Introduction: Quasiparticle Interference as Measured by Scanning Tunnelling Microscopy	35
3.1.1	Derivation of Friedel Oscillations in the Electronic Density of States	37
3.2	Fourier-Transform Scanning Tunnelling Spectroscopy Measurements of Quasiparticle Interference	43
3.2.1	History of FT-STs Measurements	43
3.3	FT-STs Measurements of the Noble Metals Surface States	43
3.3.1	Acquiring and Analyzing FT-STs Data	46
3.4	Outlook	50
4	Acquisition-Dependent Artifacts in FT-STs of the Ag(111) Surface State	52
4.1	Topography and Electronic Character of Ag(111)	53
4.1.1	The Ag(111) Surface State	53
4.1.2	Sample Preparation and Measurement Protocol	54
4.2	Experimentally Observed Set-Point Effects in Different Acquisition Modes	56
4.2.1	Spectroscopic Grids as a Function of Set-Point Parameters	56
4.2.2	Spectroscopic Grids and Constant-Current dI/dV maps	59
4.2.3	Constant-Height dI/dV Maps	62
4.2.4	Comparison Between all Acquisition Modes	63
4.2.5	Experimental Conclusions	65
4.3	Modelling the Set-point Effect	69
4.3.1	Sample Density of States via T-matrix	69
4.3.2	Analytic Set-Point Theory	71
4.3.3	Set-Point Simulations	73
4.4	Conclusions	80
5	Characterization of the Cu(111) Surface with Multiple FT-STs Acquisition Modes	81
5.1	Characterizing the Set-Point Effect in Cu(111)	81
5.1.1	The Cu(111) Surface State	81

5.1.2	Measured Set-Point Effects in Cu(111)	83
5.2	Discussion and Outlook	86
III Magnetic Sensing and Control of Single Atoms on MgO		89
6	Electron Spin Resonance Scanning Tunnelling Microcopy	90
6.1	Electron Spin Resonance in Bulk Materials	90
6.2	Electron Spin Resonance and Scanning Tunnelling Microscopy	91
6.2.1	Energy Resolution, STS, and ESR-STM	91
6.2.2	Previous Work to Pair ESR with STM	92
6.2.3	ESR-STM at IBM	92
6.3	Outlook	99
7	Single Atom Magnetic Sensing on the Surface of MgO	102
7.1	Characterization of an Atomic-Scale Magnetic Dipole-Dipole Sensor	102
7.1.1	Sample Preparation and Measurement Protocol	103
7.1.2	Magnetic Dipole-Dipole Sensing using ESR-STM	105
7.1.3	Single-Atom Magnetometry from ESR Dipole Sensing	109
7.2	Engineering a Nano-Scale Magnetometer Array	113
7.2.1	Nano-scale Magnetic Trilateration	116
7.3	Conclusions	119
IV Future Direction and Open Questions		120
8	Conclusions	121
8.1	Summary of Results	121
8.2	The Future of the Set-Point Model	123
8.3	Proposed Experiments with Magnetic Dipole-Dipole Sensing	125
8.4	Leaving Flatland	126
Bibliography		128
A	Upgrades and Operation for the UBC CreaTec LT-STM	150
A.1	A Brief History of the CreaTec LT-STM	150
A.2	Components of the CreaTec	150
B	Real Space Simulation of Multiple Scatterers	156
B.1	Using Bessel Functions to Simulate QPI Data	156
C	A Scheme for Pulsed ESR-STM	158
C.1	Development of a Pulsed ESR-STM Technique	158
C.1.1	Introduction to Pulsed ESR	159
C.1.2	A Scheme for Tip-Oscillating Pulsed (TOP) ESR-STM	161
C.1.3	Benchmarking the TOP ESR-STM Technique	162

C.2 Conclusion 165

List of Tables

2.1	A comparison of the technical specifications of the CreaTec at the LAIR and the 1-K STM at the Nanoscience Laboratory. . . .	25
A.1	History of the CreaTec highlighting major upgrades.	150

List of Figures

- 1.1 **Complex structure from base units and well-described interactions.** From left to right: the works of Shakespeare stem from the alphabet and the rules of grammar; the superconducting Meissner effect is a result of the interaction of electrons and nuclei within a superconductor; *Canis lupus familiaris*, the modern dog, arises from specific arrangements of the four base proteins in DNA, according to the rules of genetics. Image credit for DNA in Reference [17] and for Shakespeare in Reference [18]. 3
- 1.2 **Nanoscale Flatland** (a) Ripples in the electronic density of Cu(111) caused by impurity scattering. (b) Iron atoms sitting atop the oxygen site of a magnesium oxide bilayer. 4
- 1.3 **Scaling from the size of everyday objects to the nanoscale.** A competition level chessboard is roughly 50 cm across and the individual pieces can be easily manipulated by human fingers. An individual hydrogen atom has an atomic radius ten billion times smaller. To manipulate the hydrogen atom with any dexterity requires scientific tools capable of operating on this length scale. Image credit for chessboard in Reference [28]. 5
- 1.4 **A visual interpretation of quantum tunnelling.** A tiger, trapped behind a classically impenetrable barrier at the top is able to use quantum tunnelling to penetrate the barrier and give chase to a bystander on the other side. Inspired by Reference [34]. 6
- 1.5 **Essential components of an STM.** 1) The tip-sample junction, 2) a current amplifier, 3) piezoelectric motors, 4) a feedback control system, and 5) a DC applied bias. The tip-sample junction is shown magnified through a telescopic camera and then in an artistic interpretation at the nanoscale, with electrons crossing the vacuum gap. The DC bias in this case is applied to the sample but could instead be applied to the tip. 8
- 1.6 **Atomic resolution on the surface of graphite.** The tunnelling current measured on highly oriented pyrolytic graphite. The brightest intensity corresponds to the centre of the hexagons formed by rings of six carbon atoms. Imaging conditions: $I_s = 15$ pA, $V_b = 600$ mV, and $T = 4.5$ K. 11

-
- 1.7 **Measuring $\rho_s(E)$ with STS.** (a) In the low-temperature limit, electrons from a metallic tip held at a bias of $E_F + eV_b$ tunnel into a sample which has the onset of a state at $\epsilon(0)$. (b) The sample can be characterized by measurements of I_t and dI_t/dV_b . The particular bias $E_F + eV_b$ leads to the data point denoted by the black circles. Sweeping the bias and measuring gives the two curves in red. The tunnelling current shows the onset of the sample state as a kink while the differential tunnelling conductance exhibits a step that reflects the step in $\rho_s(E)$ 14
- 2.1 **The CreaTec LT-STM in c-pod.** (a) The vacuum chamber consists of the (1) manipulator arm, (2) preparation chamber, (3) cryostat, and (4) pumping system. (b) The STM/AFM head. The visible components are the (5) tunnelling current cold finger, (6) damping springs, (7) walking disc, and (8) sample holder mounted in the measurement position. 20
- 2.2 **The CreaTec Baseline Noise Characterization.** (a) Amplitude spectral density of the CreaTec tunnelling junction measured in a 1 kHz range with 977 mHz resolution. The curves labelled FEMTO DLPCA-200 and FEMTO LCA-4K-1C are the noise baselines of the tunnelling current pre-amplifiers when their inputs are grounded. The out-of-tunnelling curve is the noise baseline of the FEMTO LCA-4K-1C amplifier when its input is connected to the STM tip but the tip is not close enough to the sample to produce a measurable tunnelling current. The tunnelling curve shows the noise spectrum when tunnelling is occurring with a 100 mV bias and 100 pA tunnelling current. (b) Accelerometer measurements of the linear spectral density of the Createc inertial block. Spikes in the linear spectral density are indicative of mechanical resonances within c-pod. For more details on the vibration and acoustic noise level in the LAIR see References [123, 124]. 22
- 2.3 **The 1-K STM system at the Nanoscience Laboratory.** (a) (1) The vertical manipulator arm for sample transfer (2) Fe and Co evaporators (3) rotary feedthrough flange and sample preparation chamber (4) ^3He pumping system. (b) Internal schematic of the 1-K STM cooling stages and magnet alignment. Certain details, such as heat exchangers, have been omitted for clarity. 24
- 2.4 **Topography of the Ag(111) surface.** (a) A 282×282 nm area of the surface of the noble metal Ag(111). A plane subtraction has been performed to flatten the image. (b) An apparent height profile following the black line shown in (a) shows a double step edge, which can be used to vertically calibrate the STM against the atomic lattice. Imaging conditions: $V_b = -40$ mV, $I_s = 540$ pA. 27

2.5	Constant-height and constant-current dI/dV maps. (a) Measurement schematic, including AC modulation on the bias and lock-in amplifier acquisition of the dI/dV signal. In constant-current mode the tip adjusts the tip-sample gap via the feedback as it rasters over step edges and adsorbates while in constant-height mode the tip height stays constant. (b) Constant-current dI/dV maps acquired at various different energies on the Ag(111) surface show ripples of intensity off of surface impurities. (c) Constant-height dI/dV maps on the Ag(111) surface also show ripples off of impurities but with a lower signal-to-noise ratio.	28
2.6	Acquisition of the dI_t/dV_b by modulating the applied bias. The signal measured by the lock-in amplifier is proportional to the change in the tunnelling current ΔI_t caused by the modulation of the applied bias with strength and frequency given by V_{AC}	30
2.7	STS of Ag(111) (a) STS point spectra averaged from a 100 nm^2 clean area of the Ag(111) surface. (b) The corresponding differential tunnelling conductance by way of the numerical derivative.	31
2.8	Acquisition of a spectroscopic grid on Ag(111) At every pixel of the grid the feedback stabilizes the tunnelling junction at some apparent height, which yields a topography for the grid. Once stabilized, the feedback is disengaged and the bias is swept over a specified range, allowing acquisition of $I(V)$ curves. Once $I(V)$ curves have been acquired at every pixel the analysis proceeds by Gaussian smoothing each curve and taking the numerical derivative. This gives a dI/dV curve at every pixel allowing for reconstruction in real space of the differential tunnelling conductance at each bias.	32
3.1	Quasiparticle interference in Cu(111). (a) Constant current image of QPI from impurities and step edges taken at the Nanoscience Laboratory. Imaging conditions: $T = 4 \text{ K}$, $V_b = 100 \text{ mV}$, $I_s = 1000 \text{ pA}$, and $50 \times 50 \text{ nm}^2$. Adapted with permission from Macmillan Publishers Ltd: Nature [154], copyright (1993). (b) Differential tunnelling conductance of Cu(111) acquired from a constant current dI/dV map taken using the CreaTec in 2017. Imaging conditions: $T = 4.5 \text{ K}$, $V_b = -100 \text{ mV}$, $I_s = 900 \text{ pA}$, and $80 \times 80 \text{ nm}^2$	36
3.2	The T-matrix as a sum of Feynman diagrams.	40
3.3	Quasiparticle interference in real-space, momentum-space, and scattering space. (a) In the absence of an impurity the density of states of a two-dimensional electron gas is flat with a parabolic dispersion relation $\epsilon(\mathbf{k})$. No signal in scattering space is observed. (b) In the presence of an impurity the sample density of states acquires a dependence on the back scattering vector $ \mathbf{q} = 2 \mathbf{k} $	42

-
- 3.4 **Fourier transform analysis of quasiparticle interference.**
 (a) (i) A constant current STM image of QPI in Be(0001). Imaging conditions: $T = 150$ K, $V_b = 4$ mV, $I_s = 1.5$ nA, and 4×4 nm². (ii) The associated $|S(\mathbf{q}, E)|$ intensity exhibits a ring of intensity associated with scattering across the Fermi surface and lattice Bragg peaks from the atomic lattice. Adapted from Reference [85]. Reprinted with permission from AAAS. (b) (i) Differential tunnelling conductance image of LiFeAs. (ii) The corresponding Fourier transform shows the complexity of the FT-STs signal in a multi-band system. Imaging conditions: $T = 4.5$ K, $V_b = 10$ mV, and 26×26 nm. Adapted figure with permission from S. Chi, S. Johnston, G. Levy *et al.*, Physical Review B, 89, 1–10, 2014 [97]. Copyright 2014 by American Physical Society. 44
- 3.5 **Extracting scattering information from dI/dV by analyzing QPI.** (a) Differential tunnelling conductance of Ag(111) at the Fermi energy, $V_b = 0$ mV. (b) The absolute value of the Fourier transform of the differential tunnelling conductance, ie. the FT-STs scattering intensity $|S(\mathbf{q}, E)|$. The bright ring denotes the preferred scattering vector for quasiparticles in the surface. (c) A radial projection of the scattering intensity $|S(q_r, E)|$. The primary feature at $q_r = 2k_F$ corresponds to the scattering vector of the Ag(111) surface state at the Fermi energy. 47
- 3.6 **Scattering dispersion $\epsilon(q_r)$ from a spectroscopic grid.** (a) $|S(q_r, E)|$ line cuts for a spectroscopic grid on Ag(111). The primary feature, corresponding to scattering of a surface state, changes position or disperses as a function of energy. This figure only shows three percent of the data obtained in the grid measurement shown in (b). To represent all the $|S(q_r, E)|$ data taken in the grid the scattering intensity can be plotted as function of energy and q_r , where the maximum in intensity corresponds to the peaks seen in (a). 48
- 3.7 **Filtering processes for FT-STs data.** (a) No filtering is applied to the real-space differential tunnelling conductance image. Step edges and carbon monoxide scattering centres are both visible on the surface. The $|S(\mathbf{q}, E)|$ intensity exhibits a ring associated with the carbon monoxide QPI and a near vertical line of intensity associated with the step edge. (b) Real-space filtering averages out the step edges, filtered region denoted by dashed white lines. The $|S(\mathbf{q}, E)|$ intensity associated with the step edge is reduced. (c) Angular filtering is performed before taking the radial projection. (d) Comparison of the radially projected scattering intensity $|S(q_r, E)|$ between the three methods. 51

-
- 4.1 **Lattice structure of the Ag(111) surface.** (a) STM topographic image of the Ag(111) surface showing multiple step edges. Imaging conditions: $V_b = -40$ mV, $I_s = 540$ pA, and apparent height 0 – 2.3 nm. Inset shows atomic resolution on the Ag(111) surface. Imaging conditions: $V_b = 5$ mV, $I_s = 90$ nA, and apparent height 0 – 16 pm. (b) LEED measurement of the Ag(111) surface (Energy = 152 V, Current = 0.08 mA) after sputtering and annealing cycles. (c) Model which illustrates the Ag(111) lattice parameter and face-centred cubic lattice. 53
- 4.2 **Characterization of the Ag(111) surface state band.** (a) The \mathbf{k} -space dispersion extracted from dI/dV tunnelling spectroscopy (solid points). A parabolic fit to these data is plotted along the solid line. The dashed curve is the dispersion as measured by photoelectron spectroscopy. The inset is a dI/dV spectrum showing the surface state onset. Reprinted figure with permission from L. Jiutao, W.-D Schneider, R. Berndt, Physical Review B, 56, 7656–7659, 1997 [81]. Copyright 1997 by American Physical Society. (b) ARPES data of the surface state dispersion in \mathbf{k} -space shows the parabolic band. Reprinted figure with permission from F. Reinert, G. Nicolay, S. Schmidt, D. Ehm, and S. Hüfner, Physical Review B, 63, 1–7, 2001 [167]. Copyright 2001 by the American Physical Society. 55
- 4.3 **The three different energy regions in which the stabilization bias V_s can be set when measuring Ag(111).** 57
- 4.4 **Ag(111) spectroscopic grids with different set-point parameters.** Top panels are the differential tunnelling conductance evaluated at the Fermi energy $V_b = 0$. The bottom panels are the corresponding FT-STs scattering intensity $|S(\mathbf{q}, E)|$. Vertically aligned features of high intensity in the bottom panels are caused by the step edges present in the top panels. (a) $V_b = (-100, 120)$ mV, 239×239 nm² with 380×380 pixels. (b) $V_b = (-40, 40)$ mV 280×280 nm² with 400×400 pixels. (c) $V_b = (-100, 100)$ mV, 240×240 nm² with 350×350 pixels. 58
- 4.5 **Scattering dispersion calculated from three spectroscopic grids with different set-point conditions.** Horizontal and vertical lines indicate $E = E_F = 0$ meV and $q_r = 2k_F$ respectively. (a) No secondary features observed. (b) Broad non-dispersing feature above E_F and below $2k_F$. (c) Broad non-dispersing feature below E_F and above $2k_F$. (d) Radial projection of the FT-STs signal at E_F for each grid. Imaging conditions match Figure 4.4. 60

-
- 4.6 **Energy dispersion from spectroscopic grids and constant-current dI/dV maps.** Horizontal and vertical lines indicate $E = -40$ meV and $q_r = 2k_F$ respectively and the parabola represents a free electron model. (a) Spectroscopic grid with imaging conditions: 60×60 nm², 230×230 pixels. (b) Dispersion constructed from constant-current dI/dV maps with imaging conditions: 60×60 nm², 512×512 pixels. (c) The scattering intensity at -40 meV for both grid and map measurements scaled so that the surface state feature has the same intensity. 62
- 4.7 **Constant-height dI/dV maps and spectroscopic grids.** (a) Constant-height dI/dV map radial projections of $|S(\mathbf{q}, E)|$ show only the surface state feature. Imaging conditions: 65×65 nm², 512×512 pixels. (b) Constant-current dI/dV maps show two features away from E_F . The imaging conditions for (b) are the same as in Figure 4.6. 64
- 4.8 **The effect of stabilization bias on the observed FT-STs pattern.** (a) $|S(q_r, E = 50 \text{ meV})|$ comparing two grids with different stabilization biases, a constant-current dI/dV map, and a constant-height dI/dV map. (b-e) the corresponding FT-STs pattern at $E = 50$ meV from (b) a spectroscopic grid with $V_s = 50$ mV, $I_s = 100$ pA, (c) a spectroscopic grid with $V_s = -50$ mV, $I_s = 100$ pA, (d) constant-current map at $V_s = 50$ mV, $I_s = 100$ pA, and (e) a constant-height map at $V_s = 50$ mV, and initial current $I_s = 100$ pA. For the constant-height data a restricted \mathbf{q} -space angular filter was used to reduce the influence of a step edge running across the top of the image. 66
- 4.9 **Comparison of all features $|S(\mathbf{q}_r, E)|$ in different acquisition modes.** Vertical and horizontal lines indicate E_F and $q_F = 2k_F$ respectively. Only the constant-current maps show a strongly dispersing set-point peak. All three modes map out the surface state intensity, agreeing well with a free electron model. 67
- 4.10 **Full-width at half-maximum of the fits for all features in $|S(\mathbf{q}_r, E)|$ in different acquisition modes.** (a) FWHM values resulting from fits of the surface state peaks in FT-STs for all three measurement modes. (b) FWHM values resulting from fits of the set-point peaks in FT-STs for constant-current dI/dV maps and spectroscopic grids. 68
- 4.11 **Optimizing the scattering phase δ .** (a) Theoretical $|S(q_r, E)|$ intensity for a strong scattering impurity (b) Theoretical $|S(q_r, E)|$ intensity for a weak scattering impurity. (c) Comparison of the theoretical $|S(q_r, E_F)|$ with experimental data from a spectroscopic grid. (d) Residuals of the theoretical $|S(q_r, E_F)|$ with the experimental data, the mix of two phases does the best job minimizing the residuals around the surface state peak. 70

-
- 4.12 **Simulation of a grid with stabilization bias $V_s = -100$ mV.** (a) Simulated $|\delta\rho|$ in scattering-space. (b) The calculated $T(z_s)$ of this $|\delta\rho|$ with $V_s = -100$ meV stabilization bias. (c) The product of $|\delta\rho|$ with $T(z_s)$ gives the first term in Equation 4.11 (d) Experimental grid data with stabilization bias $V_s = -100$ mV. 75
- 4.13 **Simulation of a grid with stabilization bias $V_s = 100$ mV.** (a) Simulated $|\delta\rho|$ in scattering-space. (b) The calculated $T(z_s)$ of this $|\delta\rho|$ with $V_s = 100$ meV stabilization bias, (c) The product of $|\delta\rho|$ with $T(z_s)$ with $V_s = -100$ meV stabilization bias. (d) Experimental grid data shown with stabilization bias $V_s = 100$ mV. 76
- 4.14 **Simulation of constant-current dI/dV maps.** (a) Simulated $|\delta\rho|$ in scattering-space. (b) The calculated $T(z_s)$ of this $|\delta\rho|$ for a stabilization bias that matches the bias being probed $V_s = V_b$. (c) The product of $|\delta\rho|$ with $T(z_s)$. (d) Experimental FT-STs from constant-current dI/dV maps. 77
- 4.15 **$|S(q_r, E)|$ comparison between simulated constant-height maps, spectroscopic grids, and constant-current maps.** (a) Simulated constant-height dI/dV maps at $I_s = 100$ pA show only the surface state feature. (b) Simulated constant-current dI/dV maps at $I_s = 100$ pA show a dispersing secondary feature. (c) Simulated spectroscopic grid data with $V_s = 100$ mV, $I_s = 100$ pA shows a non-dispersing secondary feature. 79
- 5.1 **Spectroscopic grid measurement of Cu(111)** (a) The differential tunnelling conductance exhibits two step edges and a number of tip changes, corresponding to the higher degree of noise in the top half of the image. The inset at top right shows oscillations around individual point defects and a step edge. (b) FT-STs shows the expected intra-band scattering intensity. (c) The scattering dispersion of the entire surface state band. Vertical line denotes $q_F = 2k_F = 0.42 \text{ \AA}^{-1}$ and horizontal line shows $E = -250$ mV for reference to (a) and (b). Imaging conditions: $V_s = -520$ meV, $I_s = 150$ pA, 325×325 pixels. 82
- 5.2 **Set-point effects in grids on Cu(111).** (a) A spectroscopic grid measurement exhibits a secondary non-dispersing feature just above the Fermi scattering vector $q_F = 2k_F$. Imaging conditions: $V_s = 30$ meV, $I_s = 150$ pA, 124×124 nm, 176×176 pixels. (b) A spectroscopic grid with stabilization bias below the band onset shows no secondary features. Imaging conditions: $V_s = -520$ meV, $I_s = 150$ pA, 225×225 nm, 325×325 pixels. . . 84
- 5.3 **Constant height and constant current dI/dV maps of Cu(111).** (a) $|S(q_r, E)|$ extracted from constant height dI/dV maps over areas ranging from 80 – 140 nm in length at $I_s = 900$ pA. (b) $|S(q_r, E)|$ extracted from constant current dI/dV maps over areas ranging from 80 – 140 nm in length. $I_s = 900$ pA. . . 85

-
- 5.4 **Comparison of Cu(111) dispersing features with Sessi *et al.* [113]** Vertical and horizontal lines indicate E_F and $q_F = 2k_F$ respectively. (a) Peak maxima extracted from constant current and constant height maps both show the surface state dispersion in good agreement with a free electron model from Equation 4.1. The constant-current dI/dV maps show the set-point feature while constant-height dI/dV maps exhibit a previously unobserved feature. (b) Constant-current dI/dV maps by Sessi map out the surface state dispersion. The theoretical dispersion of an acoustic surface plasmon agrees well with secondary features below E_F but deviates above. 87
- 6.1 **Logarithmic Energy Scale** Above the energy scale a select number of energies important in condensed matter are listed while below the energy scale the limit of STS resolution is shown at various tip-sample temperatures. References: Hyperfine energy of hydrogen (H) water [222], superconducting (SC) gap energies [223], work function of silver [81], and quantum limit of STS energy resolution [221]. 92
- 6.2 **STS spectra of a single Fe atom with and without a spin-polarized tip.** STS spectra of the same Fe atom on MgO with a spin-polarized tip and a normal tip which averages over all available spin channels. Spectra were acquired using a lock-in amplifier to extract the differential tunnelling conductance. Set-point parameters: $V_s = 10$ mV, $I_s = 50$ pA for the normal tip and $V_s = 10$ mV, $I_s = 100$ pA for the spin-polarized tip. 94
- 6.3 **ESR-STM measurement scheme.** (a) A magnetic atom sitting on an insulating thin film on a bulk conducting crystal has is sent into resonance by application of an microwave bias excitation along the DC bias line. A spin-polarized tip is used to read-out the change in tunnelling current. (b) The microwave pulse train for this method, dubbed continuous wave ESR. (c) The microwave frequency is swept until a resonance peak in the tunnel current signal is detected via the lock-in amplifier. 95
- 6.4 **STS spectra of Fe on MgO** The jump in differential tunnelling conductance at $V_b = 14$ meV corresponds to the transition for the ground state to the first excited state. Topographic height of Fe atom in inset is $h = 0.17$ nm. (b) The five lowest lying states of an Fe atom on MgO [86]. 98
- 6.5 **Single Fe atom ESR resonance.** (a) Thermal population of the low-energy quantum states of an Fe atom on MgO in a magnetic field. (b) Resonant population in continuous wave mode (c) ESR-STM spectra showing resonance at various magnetic field strengths. 100

-
- 6.6 **ESR-STM spectra of the same Fe atom with two oppositely spin-polarized tips.** The ESR peak (dip) is caused by a lower (higher) tunnelling magnetoresistance at resonance. The frequency splitting between the observed features is independent of tip, though the absolute frequency at which each resonance is observed is tip dependent. The rich structure of the ESR spectra is caused by the proximity of nearby magnetic atoms on the surface, which will be discussed in detail in Chapter 7. The above spectra were taken in a magnetic field of $B = 4.8$ T and at a temperature of $T = 1.2$ K. 101
- 7.1 **ESR-STM for magnetic dipole detection.** (a) Schematic for sensing the dipole-dipole interaction between two iron atoms. (b) Constant-current STM image of four Fe atoms (0.17 nm apparent height) on the surface. Imaging conditions are $V_{DC} = 0.1$ V, $I = 10$ pA, $B_z = 0.18$ T, $B_x = 5.7$ T and $T = 1.2$ K. 105
- 7.2 **Magnetic dipole-dipole interaction detected via ESR.** (a) ESR spectrum (black curve) of an Fe atom when another Fe atom (target) is positioned 2.46 nm away ($B_z = 0.17$ T, $T = 1.2$ K, $V_{DC} = 5$ mV, $I_{DC} = 1$ pA, $V_{RF} = 10$ mV_{pp}). A fit to two Lorentzian functions (red curve) yields the frequency splitting (Δf). The difference in amplitude between the two observed features can be attributed to the ratio in thermal occupation probability of the $|0\rangle$ and $|1\rangle$ states. (b) Topography of the sensor Fe atom (outlined in black) and the Fe target. (c) The underlying MgO lattice provides a metric to measure the distance between the two Fe atoms. 106
- 7.3 **ESR spectra of multi-atom structures.** (a) ESR spectrum taken on the middle atom (Fe) in (c) shows four ESR peaks. (b) ESR spectrum taken on the left atom (Fe) in (c) also exhibits four ESR peaks. (c) STM image of the three atom arrangement, with two Fe atoms and one Co atom. The binding-site assignment model (lower panel) shows distances between atoms in units of the atomic lattice spacing (0.2877 nm for $T < 20$ K). Imaging condition are 10 mV, 10 pA, $B_z = 0.2$ T, and $T = 1.2$ K. 107
- 7.4 **Log-log plot of $\Delta f \propto r^\alpha$.** The measured splitting as a function of the distance r of atom pairs of Fe-Fe (red squares), Fe-Co (blue circles), and Fe-‘tall’ Fe (green diamonds). Data from the shaded region below 1 nm are excluded from the fits. Error bars in the r and Δf axes represent uncertainty in the determination of the interatomic distance and the measured Δf error due to frequency drift. Distances are obtained using the Ag lattice constant measured at low temperature by x-ray diffraction [186, 260]. 108

-
- 7.5 **Distance-dependent ESR splitting (Δf) for atoms separated by less than 1.0 nm** (a) Δf vs distance r for close atoms, zoomed in from Figure 7.4 on the Fe-Fe curve. (b) STM images of two close Fe atoms before and after placing a third (“remote”) Fe atom in the vicinity. The imaging conditions are 10 mV, 10 pA, $B_z = 0.17$ T, and $T = 1.2$ K. (c) ESR splitting before and after adding the remote atom. 109
- 7.6 **Magnetic dipole-dipole interaction detected via ESR** A schematic of the dipole-dipole interaction. The resonant frequency of the isolated sensor atom (f_0) is split into two frequencies (f_\uparrow and f_\downarrow) corresponding to the two spin states of the target atom. $\Delta f = f_\downarrow - f_\uparrow$ is the measured splitting. 111
- 7.7 **Construction of the dipole sensing array.** (a) Five Fe atoms were gathered and arranged to form an array of four sensors and one target in the array centre. (b) The tip atom, another Fe, is placed outside the array for safekeeping. (c) The target Fe atom is picked up from the centre of the sensor array. (d) The target is placed at a lower symmetry position, corresponding to (-3,1) oxygen lattice sites from the array centre. (e) The entire structure is imaged in order to find the tip atom again. (f) The tip is spin-polarized by picking up the Fe tip atom. 114
- 7.8 **Measuring a target atom at a low symmetry site with a nano-sensor array.** Five Fe atom structure with four equally spaced corner atoms and a middle Fe (sensor atom) which is positioned at (-3, 1) lattice sites from the centre of the square (oxygen binding sites indicated by white open circles). For clarity, the 1.2 K spectra is offset by -60 fA. Imaging conditions are $V_{DC} = 10$ mV, $I = 10$ pA, and $B_z = 0.17$ T. 115
- 7.9 **Measuring a target atom at a low symmetry site with a nano-sensor array.** (b) The Fe sensor atom is placed in the exact centre of the square at a distance of 2.034 nm from the four target atoms. This creates a four-fold symmetry which leads to degeneracy of the excited spin states. Imaging conditions are $V_{DC} = 10$ mV, $I = 10$ pA, and $B_z = 0.17$ T. 116
- 7.10 **Magnetic imaging by using trilateration.** (a) Measured ESR spectra ($T = 0.6$ K) from each sensor atom (black) and the predicted unbroadened spectrum (red) due to all atoms excluding the target. (b) ESR spectra of (a) after deconvolving the effect of the other sensor atoms. The results show ESR spectra (peaks are indicated by black arrows) due solely to dipolar interaction of the target atom and the sensor atom under the tip. (c) Predicted location of the target by trilateration. (d) Agreement of the target location between STM topography and nanoGPS. 118
- 8.1 **Artistic depiction of nanoscale Flatland as a chessboard with electronic pieces.** 127

-
- A.1 **The CreaTec LT-STM in c-pod.** (a) The vacuum chamber consists of (1) the manipulator arm, (2) the preparation chamber, (3) the cryostat, and (4) the pumping system. (b) The STM/AFM head being installed outside of vacuum. The visible components are (5) tunnelling current cold finger, (6) damping springs, (7) walking disc, and (8) a sample holder mounted in the measurement position. (c) The manipulator is used to move samples within the vacuum space. It consists of (9) sample bias and annealing contacts and (10) sample clamping mechanism. (d) The sample holder (11) with a graphite sample mounted, coin shown for scale. 151
- A.2 **The CreaTec STM head.** (a) The upgraded UBC STM head used for the bulk of the measurements in Part II. The wiring is designed to be slack to avoid coupling vibration into the tip-sample junction and is extremely fine in order to prevent heat leaks from room temperature to the STM head. (B) A model of the original CreaTec head when mounted inside the heat shields. 153
- A.3 **Operation of a beetle/Besocke style STM head.** (a) The voltage profile applied to the quadrants of a piezo tube to make it move. The voltage is slowly ramped from a constant value up to a maximum before being quickly inverted. This produces a sawtooth waveform that moves the walking plate. (b) A basic model of a beetle-style STM head such as the one used in the CreaTec STM. (c) Forces generated from the piezo tubes on the walking plate for X and Y motion. (d) Torque on the walking plate from the piezo tubes in Z motion. When all three piezo tubes produce clockwise forces a net torque is produced that moves the walking plate and STM tip towards the sample. Counterclockwise forces produce a net torque that moves the walking plate and STM tip away from the sample. 154
- B.1 **Spectroscopic grid simulated in real-space by Bessel functions.** (a) Experimental measurement of the differential tunnelling conductance at E_F from a spectroscopic grid with measurement conditions: $V_s = -100$ mV, $I_s = 100$ pA, $V_b = (-100, 120)$ mV, 239×239 nm² with 380×380 pixels. (b) Simulation of the experimental data using Equation B.2 and identifying the pixels corresponding to the centre of each CO. (c) FT-STs scattering intensity of both experiment and simulation projected onto the q_r axis. The simulation results deviate from the experiment at low- q_r , possibly indicating the need to add a degree of noise to the simulation data. 157

-
- C.1 **Continuous wave versus pulsed ESR-STM** (a) Continuous wave ESR-STM uses (i) a chopped microwave frequency sweep to (ii) randomly walk the spin state along the Bloch sphere, resulting in (iii) an increase in the tunnel current. (b) Pulsed ESR-STM uses a (i) series of resonant pulses to (ii) coherently manipulate the spin state around the Bloch sphere, resulting in (iii) observation of Rabi oscillations in the tunnelling current signal. 160
- C.2 **Tip Oscillating Scheme** (a) A single set of TOP ESR-STM signals over one period of the tip oscillation. The V_μ pulse is triggered at the maximum tip sample separation and V_{DC} is used for initialization of the spin and read-out using a positive polarity DC bias pump. (b) Many tip shaking cycles occur during one cycle of the lock-in measurement. The lock-in measurement compares the average tunnelling current during sequences with and without the spin-manipulation microwave pulses. 163
- C.3 **Characterization of the tip modulation amplitude.** (a) $I_t(z)$ spectroscopy can be used to fit for the κ factor at a particular point, giving a relation between the tunnelling current and the relative tip-sample gap. (b) The tunnelling current is measured as a function of tip modulation amplitude. 164
- C.4 **Tip response as a function of modulation frequency.** A relatively stable area, away from mechanical resonances, is found at 17241 Hz and so this frequency is chosen for TOP ESR-STM. The inset is a STM topograph of an Fe atom taken while the STM tip is being modulated with a peak-to-peak height of 2 Å. Imaging conditions are $I_s = 25$ pA, $V_b = 100$ mV, and 30×30 Å. 166

List of Acronyms

2DEG	Two-dimensional Electron Gas
AFM	Atomic Force Microscopy
ARC	Almaden Research Centre
ARPES	Angle-resolved Photoemission Spectroscopy
ASP	Acoustic Surface Plasmon
ESR-STM	Electron Spin Resonance Scanning Tunnelling Microscopy
FT-STs	Fourier-transform Scanning Tunnelling Spectroscopy
FWHM	Full-width half-maximum
IBM	International Business Machines
LAIR	Laboratory for Atomic Imaging Research
LEED	Low-energy Electron Diffraction
QPI	Quasiparticle Interference
STM	Scanning Tunnelling Microscope
STS	Scanning Tunnelling Spectroscopy
UBC	University of British Columbia
XMCD	X-ray Magnetic Circular Dichroism

List of Symbols

$S(\mathbf{q}, E)$	FT-STs scattering intensity
$S(q_r, E)$	FT-STs scattering intensity projected onto the \mathbf{q} radial axis
ρ_s	Sample local density of states
$\delta\rho_s$	Impurity induced modulation in the local density of states
ρ_t	Tip local density of states
I_t [A]	Tunnelling current
V_b [V]	Applied bias (DC)
I_s [A]	Set-point current
V_s [V]	Stabilization bias
dI_t/dV_b or dI/dV [S]	Differential tunnelling conductance
E_{dd}	Magnetic dipole-dipole energy
M_{ts}	Bardeen's tunnelling matrix element
$f_{t,s}$	Thermal factor
$T(z, E, V_b)$	Tunnelling transmission probability or transmission function
z	Tip-sample gap
h	Apparent height
G	Green's function
T_1	Energy relaxation time
T_2	Quantum phase coherence time
m^*	Effective electron mass
e	Free electron charge
E_F	Fermi energy
\mathbf{q}	Scattering-space vector
\mathbf{k}	Momentum-space vector
k_F	Fermi wave vector
q_F	Fermi scattering vector
k_B	Boltzmann constant
\hbar	Dirac constant

Acknowledgements

First and foremost, I want to acknowledge my supervisors Professor Sarah Burke and Professor Doug Bonn, who have provided mentorship, guidance, and instruction from the beginning of my time at the LAIR. I want to thank them for going the extra mile to provide me with opportunities to perform interesting work, the chance to learn from failing, and the support necessary to work with researchers internationally. They have shaped who I am as a researcher today and I am very grateful for that.

This thesis couldn't have been completed without the support of the people at the UBC LAIR, the UBC Superconductivity Group, and the IBM Nanoscience Laboratory. At the LAIR I want to acknowledge the role of the CreaTec team: Dr. Stephanie Grothe, Dr. Shun Chi, Gelareh Farahi, and Yann-Sebastien Tremblay-Johnston. I want to thank Katherine Cochrane for being my desk mate for these past six years, for the long weekend fills, and of course for the gummy bears. I also want to thank Dr. Agustin Schiffrin, Martina Capsoni, Tanya Roussy, Rob Delaney, Damien Quentin, and Ben MacLeod for making the LAIR a rich scientific environment to work in. In the Superconductivity Group, I want to acknowledge the support of Pinder Dosanjh, without whom the CreaTec would still be lying in pieces on a table somewhere. Thank you to James Day for the mentorship, the conversations over coffee, and for the constant inspiration. Walter Hardy for always having time to discuss the details of a scientific problem with me, particularly if it involved a grounding problem — I hope I was able to return the favour. Thank you to Ellen Schelew and Nathan Evetts for entertaining my ideas about topics completely outside of my field.

For the extraordinary experience I had visiting the IBM Almaden Research Centre I want to thank Andreas Heinrich, who was my host, running coach, and scientific role model. I want to thank William Paul, and his family Sara, Juliet, and Teddy, for welcoming a fellow Canadian to the Bay area and putting me up when my car was stolen. I learned more about electronics from Will in a week than I did in my entire undergraduate education. I want to thank Taeyoung Choi, and his family Lei, Alex, and Julian, for their hospitality. Taeyoung led the charge on the dipole coupling work and I learned a great deal about managing a scientific project working alongside him. Christopher Lutz is the most inspirational scientist I have had the honour of working alongside; I try my best to think about problems the way he does. Thank you to Susanne Baumann, Fabian Natterer, Steffen Rolf-Pissarczyk, Kai Yang, and Philip Willke for trading ideas on the white board and discussing scientific data. Bruce Meloir was an excellent colleague to discuss design problems and trade stories with. The

IBM lunch crowd for the excellent lunchtime conversations.

The Natural Sciences and Engineering Research Council of Canada CREATE QuEST program, PGS D program, and UBC Four-Year Fellowship provided the financial support necessary for me to undertake the research presented herein. My supervisory committee of Prof. Rob Kiefl, Prof. Scott Oser, and Prof. Marcel Franz provided insightful comments and direction throughout the thesis work.

My friends and scientific colleagues who helped me grow outside the laboratory. Particularly Adam Shaw, Stephanie Grothe, Natasha Holmes, Luke Govia, Brad Ramshaw, Tim Cox, Amanda Parker, Samara Pillay, Dorothea von Bruch, and Mohammad Samani for being good friends and putting every problem in context.

Lastly, I want to thank my family, my parents, grandparents, and brothers, for encouraging me to be a scientist and to take this as far as I could go. And of course I want to thank my wife Tegan, who was not only there to see me through the worst and best parts of this degree, but is the only person who has read and edited and re-read every section of this thesis more diligently than I thought possible.

Dedication

To Mom and Dad, for teaching me persistence.

To my wife Tegan, who makes me a better scientist and a better person.

To Stephanie, who helps me keep in mind what is important.

And to the four-legged creatures that keep my sense of wonder close at hand.

Part I

Introduction to Scanning Tunnelling Microscopy

Chapter 1

Welcome to Flatland

Facts are not science - as the dictionary is not literature.

Martin H. Fischer - 1944 [1]

Quantum tunnelling, a classically forbidden process, can be harnessed by instruments like the scanning tunnelling microscope (STM) to characterize and engineer atomic-scale surface properties. In this chapter, the central concepts of the nanoscale surface, quantum tunnelling, and the STM are introduced, and the basic components, operation, and theory of an STM are discussed. This chapter lays the groundwork for making STM measurements in two regimes that the STM cannot normally access: momentum-space electronic properties and micro-electronvolt electronic transitions. Measurements of these two regimes are performed on two different nanoscale surfaces: the (111)-terminated noble metals and magnesium oxide thin films.

1.1 Flatland: The Nanoscale Surface

In 1884 Edwin A. Abbott published the short novel Flatland: A Romance of Many Dimensions [2]. The story's main character, A. Square, lives in a two-dimensional space known as Flatland and dreams of Lineland, a one-dimensional equivalent to Flatland, and Spaceland, a three-dimensional space similar to our own. Though Abbott was not a scientist, Flatland as a theoretical concept has proven extremely useful to physicists. In relativity the warping of our four-dimensional space-time by matter and energy can be visualized as a thought experiment by the stretching of a two-dimensional elastic sheet in the presence of heavy objects [3]. In condensed matter physics there exist materials with protected two-dimensional states on the edges of three-dimensional bulk materials [4, 5]. What is more, in nanotechnology research there is a direct physical analogy to Abbott's Flatland: the nanoscale surface.

The surface of a material is the simplest type of two-dimensional interface in condensed matter physics; it delineates the bulk of a material from vacuum. Inside the bulk, the electromagnetic field created by the atomic nuclei interacts with the electrons to determine the material's properties. The physics of this bulk region is described with great success by single-electron band theory [6] and Landau Fermi-liquid theory [7] in many classes of materials. Outside the bulk, particles maintain their free-space atomic properties like spin, mass, and charge

as measured in particle physics experiments. The surface is a global defect [8] where the worlds of the bulk and the vacuum collide. The surface breaks the translational and inversion symmetry of the bulk crystal, and combined with the interplay between bulk and vacuum electronic states can lead to electronic states of matter that cannot be realized in either alone [4, 5, 9]. It is possible for the physical properties and excitations at the surface to be radically different from those of the bulk or the vacuum [10–15].

Condensed matter physicists and surface scientists already know that the base chemical unit that creates the surface is atoms, composed of electrons and nuclei, interacting in a way described extremely well by quantum electrodynamics [16]. However, knowing the constituents and interactions of the surface is not enough to predict all of the weird and wonderful behaviour that emerges. States of matter like superconductivity, ferromagnetism, or ferroelectricity stem from the complex interaction of $\sim 10^{23}$ of these base units in a macroscopic piece of matter. This is an example of simple, well-understood rules and constituents giving rise to macroscopically complex behaviour: like literature from letters and grammar, Meissner diamagnetism from electrons and quantum electrodynamics, or life from base proteins and genetics (Figure 1.1).



Figure 1.1: **Complex structure from base units and well-described interactions.** From left to right: the works of Shakespeare stem from the alphabet and the rules of grammar; the superconducting Meissner effect is a result of the interaction of electrons and nuclei within a superconductor; *Canis lupus familiaris*, the modern dog, arises from specific arrangements of the four base proteins in DNA, according to the rules of genetics. Image credit for DNA in Reference [17] and for Shakespeare in Reference [18].

Nanoscale engineering of the atomic surface makes it possible for physicists to design surfaces that give insight into fundamental physics and provide prototypes for new technological platforms. Atomic-scale control has allowed surface

scientists to measure new fundamental excitations that have only been predicted to exist in particle physics [19] and to test the predictions of quantum electrodynamics for elements far heavier than have ever been synthesized in accelerator facilities [20]. Current theoretical proposals rely on atomic manipulation techniques to implement new quantum computing architectures [9] and to better the efficiency of existing technologies, like organic solar cells [21].

1.1.1 Measuring Electrons at the Nanoscale Surface

Over one hundred years after the publication of Abbott's work, this thesis characterizes the behaviour of A. N. Electron in two different Nanoscale Flatland environments using the scanning tunnelling microscope (STM): the (111)-terminated noble metals and magnetic atoms atop a magnesium oxide thin-film (Figure 1.2). The (111)-terminated surfaces of the noble metals offer the opportunity to probe the physics of a two-dimensional electron gas (2DEG), a conducting medium strictly localized on the metallic surface. Scattering of this 2DEG off of localized impurities on the surface creates a striking pattern in the electronic density known as quasiparticle interference, which will be probed extensively in Part II. On the other end of the conductivity spectrum, monolayer and bilayer insulators serve as a two-dimensional test bed for studying magnetic interactions in the limit of discrete electronic energy levels. By growing thin films of magnesium oxide (MgO) on a silver crystal, an experimental Flatland is engineered where it is possible to probe the magnetic dipolar interaction between individual iron atoms. Fully characterizing this interaction allows for the invention of a new form of nanoscale magnetometry in Part III. Before moving onto the details of these experiments, the remainder of Part I introduces the experimental technique of STM, its history, and its limitations.

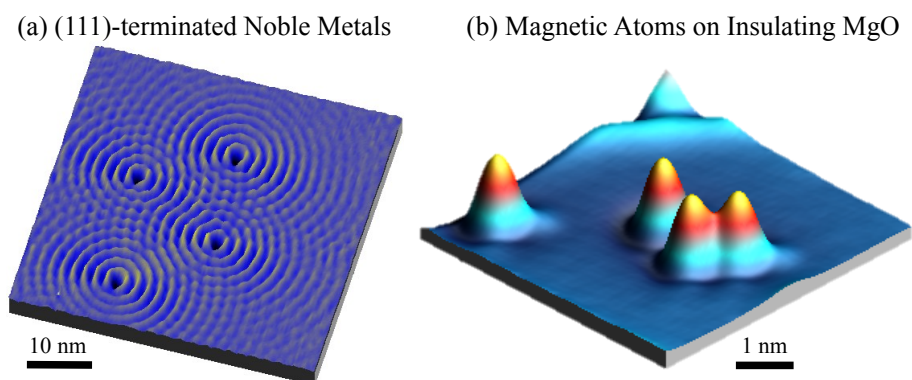


Figure 1.2: **Nanoscale Flatland** (a) Ripples in the electronic density of Cu(111) caused by impurity scattering. (b) Iron atoms sitting atop the oxygen site of a magnesium oxide bilayer.

1.2 Surface Science at the Atomic Scale

In order to customize nanoscale surfaces to explore new science and create novel materials, scientists must be able to manipulate and measure individual surface atoms. If successful, this amounts to a game of atomic-scale chess where the pieces and the board can be tailored to the scientists' individual needs. The caveat is that scientific tools are required that can measure and manipulate individual atoms and molecules. The chief difficulty to overcome in this regard is that an atom of hydrogen is roughly a factor of ten billion smaller than the length of a chessboard, as illustrated in Figure 1.3. This change in scale represents a significant technical hurdle. Over the last forty years, a number of tools capable of measuring the atomic scale properties of solids have been developed. Techniques such as transmission electron microscopy [22, 23], atomic force microscopy [24, 25], and scanning tunnelling microscopy [26, 27] are all capable of measuring atomic scale properties of a material's surface. These techniques rely on the quantum properties of matter for their basic operation. Central to this thesis work is the scanning tunnelling microscope, which takes advantage of the wave-particle duality of the electron to perform quantum tunnelling.

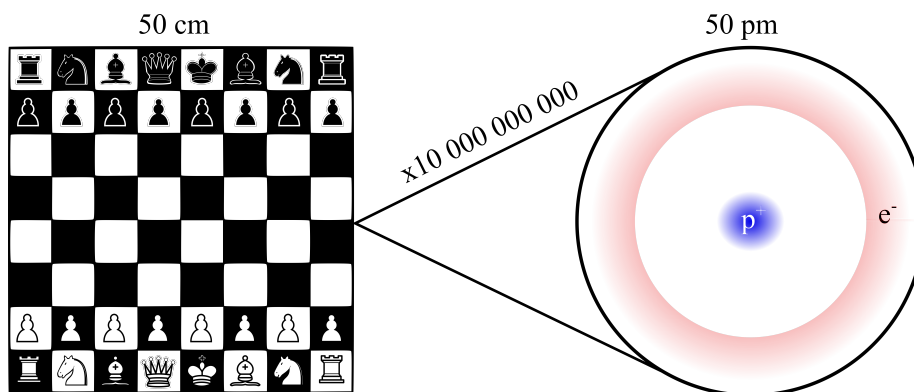


Figure 1.3: **Scaling from the size of everyday objects to the nanoscale.**

A competition level chessboard is roughly 50 cm across and the individual pieces can be easily manipulated by human fingers. An individual hydrogen atom has an atomic radius ten billion times smaller. To manipulate the hydrogen atom with any dexterity requires scientific tools capable of operating on this length scale. Image credit for chessboard in Reference [28].

1.2.1 Quantum Tunnelling

Quantum tunnelling describes the process by which a quantum object can pass through a potential barrier that would be impenetrable to a classical object. The

quantum tunnelling of light and matter is a direct result of the wave character of quantum objects [29]. Figure 1.4 illustrates the essence of tunnelling by visualizing a tiger tunnelling through a classically impenetrable barrier, much to the chagrin of the character on the other side. In the mathematical language of quantum mechanics, tunnelling describes the process by which a plane wave incident on a barrier has a finite probability of travelling through the barrier even if the barrier's energy is greater than the wave's own. Inside the barrier, a classically forbidden region, the plane wave exponentially decays in magnitude. Without quantum tunnelling nuclear fusion could not occur in the heart of stars [30], alpha decay of radioactive nuclei would not be possible [31–33], and the field of surface science would be missing one of its central tools [26]. No less than five Noble prizes have been awarded for work on quantum tunnelling in semiconductors, superconductors, and the invention of new devices like the scanning tunnelling microscope [29].

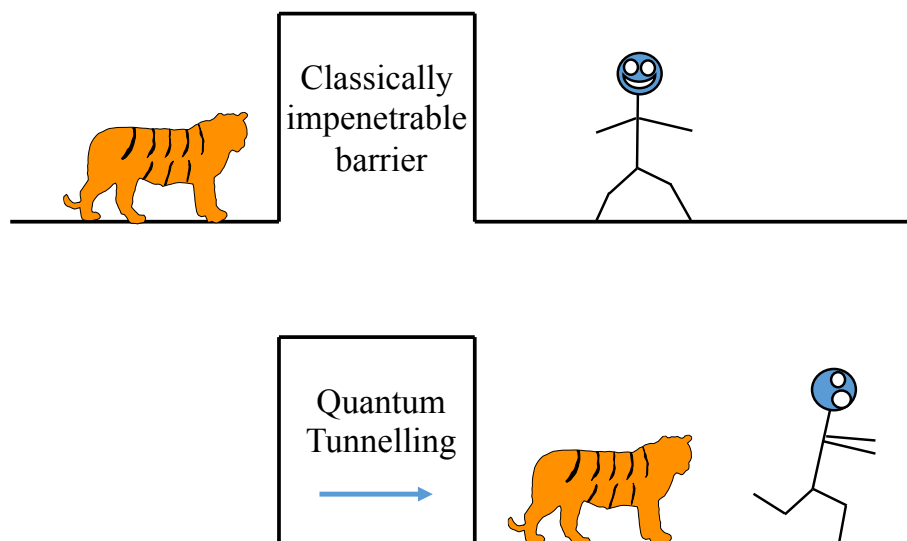


Figure 1.4: **A visual interpretation of quantum tunnelling.** A tiger, trapped behind a classically impenetrable barrier at the top is able to use quantum tunnelling to penetrate the barrier and give chase to a bystander on the other side. Inspired by Reference [34].

1.2.2 Early History

The first theoretical work to employ the concept of quantum tunnelling was performed in the late 1920's with the then newly minted theory of quantum

mechanics. Frederich Hund calculated the quantum mechanical barrier penetration – what is now called quantum tunnelling – in the context of molecular spectroscopy [35, 36]. His work was followed up by Fowler and Nordheim’s explanation of field emission [37, 38], Oppenheimer’s work analyzing the tunnelling in the continuous portion of the hydrogen atom spectrum [39, 40], and Gamow, Gurney, and Condon’s work that showed that tunnelling inside the nucleus was responsible for alpha decay [31–33]. In solid state physics, early applications of the theory of tunnelling in the 1930’s led to Zener’s theory of interband tunnelling in solids [41] and the first tunnelling device, the field-emission microscope invented by Müller [42, 43].

Over the next thirty years the theory of quantum tunnelling was put on firmer theoretical footing by theorists [44, 45] while experimentalists used the tunnelling properties of matter to design tunnelling junctions and study superconductivity [46, 47]. Building upon previous tunnelling devices in 1972 Young, Ward, and Scire designed the topographiner [48], in many ways the STM’s direct predecessor. Then, in 1982, Binnig and Rohrer at IBM Zurich invented the scanning tunnelling microscope [26, 49]. In 1983, they published the first images of the surface of Si(7×7), solving a longstanding mystery about its surface character [50]. By 1986 they had won the Nobel Prize for their invention and a decade later there were thousands of papers per year being published in the new field of STM studies [27].

1.2.3 The Scanning Tunnelling Microscope

The STM measures a convolution of integrated electronic density of states and apparent atomic height by taking ‘topographs’ of a surface. Through careful experimentation and analysis, STM experiments have opened new vistas in surface science, such as untangling surface reconstructions [50, 51], observing new forms of charge order [52], and cataloguing step-by-step molecular reactions on surfaces [53]. STMs can be built to operate in liquid, in air, in ultra-high vacuum, and from room temperature to milliKelvin temperatures. Regardless of the construction details every STM has a number of essential components, shown in Figure 1.5 and enumerated below:

1. **Tip:** A sharp metallic tip, held in close proximity to a sample of interest.
2. **Motors:** A motor system that can drive the tip in three-dimensions with sub-nanometer control over a millimetre range, typically accomplished by the use of piezoelectric devices.
3. **Current Amplifier:** A means of detecting a tunnelling current across the tip-sample junction, typically involving a high-gain current amplifier or electrometer.
4. **Feedback Control:** An electronic feedback system that can control the tip-sample distance as the tip is rastered across the surface.
5. **DC Bias:** A direct current (DC) bias applied between tip and sample.

Researchers can use an STM to do more than just image a nanoscale surface. The tip of the STM can be used to perform feats of nano-engineering: manipulating individual atoms into specific patterns to probe electronic states [54–56], store information [57], and even develop the world’s smallest stop action movie [58]. The STM can also be used for spectroscopic characterization, via scanning tunnelling spectroscopy (STS), that delves into the electronic energy levels of molecules [21, 59] and electronic dispersion of solids [60], providing complementary information to other modern spectroscopic techniques like angle-resolved photoemission (ARPES) [61], but with a far more localized real-space probe. STMs have been combined with magnetic fields, low temperature, and laser pulses to probe all manner of physics from solar cells [21, 62] to superconductors [63] to magnetism [64].

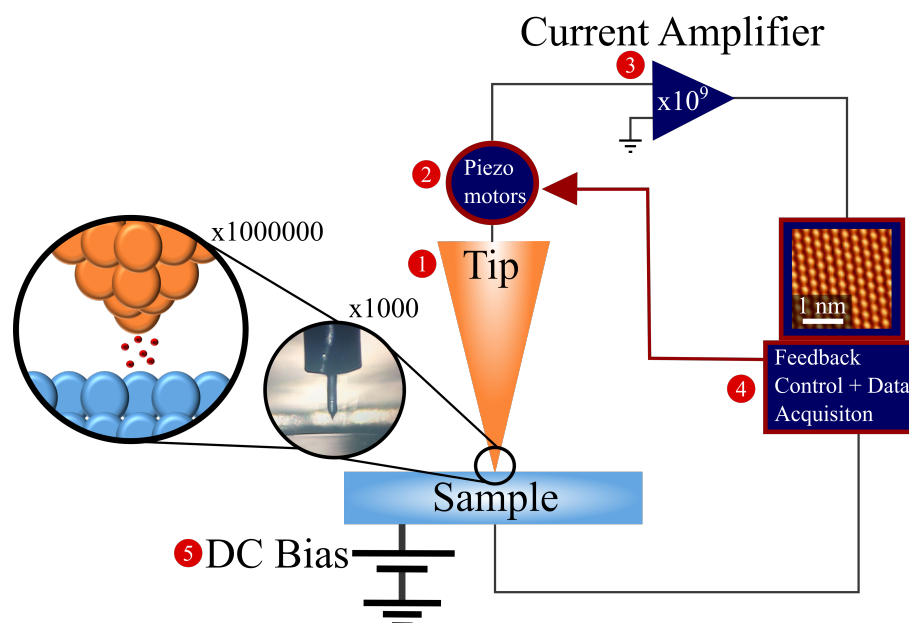


Figure 1.5: **Essential components of an STM.** 1) The tip-sample junction, 2) a current amplifier, 3) piezoelectric motors, 4) a feedback control system, and 5) a DC applied bias. The tip-sample junction is shown magnified through a telescopic camera and then in an artistic interpretation at the nanoscale, with electrons crossing the vacuum gap. The DC bias in this case is applied to the sample but could instead be applied to the tip.

1.2.4 Theory of the STM Tunnelling Junction

The Tunnelling Current

At its core, the STM relies on bringing the tip and conducting sample close enough together ($\approx 10 \text{ \AA}$) that there is significant overlap between their electronic wave functions [49]. At this distance the tunnelling probability becomes non-trivial. Combined with a DC bias, applied to either tip or sample while the other remains grounded, electrons will preferentially travel from one to the other, thus creating a measurable tunnelling current. The magnitude of the tunnelling current depends on the tip-sample gap, the relative density of electronic states of tip and sample, and the magnitude of the applied bias. Relating the tunnelling current to the physical quantity of interest, be it the local electronic density of states of a sample (ρ_s) or sample work function (ϕ), requires a theoretical framework.

Tersoff and Haman [65, 66] developed the first model of the STM tunnelling current shortly after the invention of the STM. Based on Bardeen's transfer Hamiltonian method [44], the Tersoff-Haman model is remarkably useful, in spite of a number of approximations explicitly built into the theory. In many cases, the Tersoff-Haman model accurately describes the observed physics and because of its straightforward relation between the tunnelling current and the sample local density of states it has proved popular in the interpretation of STM data.

In the Tersoff-Haman model the relation between the tunnelling current I_t and the local density of states of tip ρ_t and sample ρ_s is derived in the context of the interaction of two weakly bound metallic electrodes. Applying first-order perturbation theory [65–67] the tunnelling current is given by

$$I_t = \frac{4\pi e}{\hbar} \int_{-\infty}^{\infty} \rho_s(\mathbf{r}, E) \rho_t(E - eV_b) |M_{ts}|^2 f_{ts}(E, V_b) dE, \quad (1.1)$$

where e is the electron charge, \hbar is the reduced Planck constant, \mathbf{r} denotes lateral position of the tip over the sample, ρ_s is the sample local density of states, ρ_t is the tip density of states, V_b is the applied bias on the sample with reference to a grounded tip (as in Figure 1.5), E is the electron energy, and $M_{t,s}$ is Bardeen's matrix element describing tunnelling between the states of the tip and those of the sample [68, 69]. The thermal factor,

$$f_{ts} = \frac{1}{1 + e^{(E - eV_b - \mu_t)/k_B T}} - \frac{1}{1 + e^{(E - \mu_s)/k_B T}}, \quad (1.2)$$

is a function of the Fermi-Dirac distribution of the tip and sample and is responsible for temperature-related energy broadening. Here T is the temperature of the tip and the sample, k_B is Boltzmann's constant, and μ_s and μ_t are the chemical potential of the sample and tip respectively.

Equation 1.1 shows that the tunnelling current is a measure of the integrated

density of states of the sample, convoluted with effects from the tip density of states, the tunnelling barrier, and finite temperature. In practice, a great deal of effort is made to ensure that the tip density of states is independent of energy, i.e. flat, over the energy range being measured so that it can be safely ignored when analyzing the STM data. Furthermore, STM research focused on electronic states as a function of energy will typically be cryogenically cooled to reduce thermal energy broadening.

Under the approximations of a spherical tip with a flat density of states, a square tunnelling barrier treated semi-classically, and low temperature, Equation 1.1 can be simplified to

$$I_t \propto e^{-\kappa z} \int_0^{eV_b} \rho_s(x, y, E) dE \quad (1.3)$$

where κ is a constant related to the work function of the tip and the sample and z is the distance between the sample surface and the last atom on the tip. This equation makes explicit the tunnelling current's exponential dependence on the tip-sample gap and shows that the tunnelling current is a function of the integrated local density of states of the sample. The exponential dependence of the tunnelling current on the tip-sample gap is responsible for the STM's atomic level resolution; it makes the tunnelling current exponentially sensitive to any change in the tip-sample gap created by moving the tip over defects, step edges, or individual atoms.

An image of the tunnelling current measured on highly oriented pyrolytic graphite is shown in Figure 1.6. The ordered structure illustrates the atomic corrugation associated with the ordering of the underlying carbon lattice. It is important to note that the tunnelling current is a measure of electronic density of states, and not a direct measure of the position of atomic nuclei¹. Nevertheless, the hexagonal structure of the graphite lattice can be observed in the image.

An assumption of the Tersoff-Hamam model is that the tip has an ideal, spherically-symmetric wave function and that both the tip and sample are metallic. A considerable amount of theoretical work has been done to derive more generalized forms that do not require as many assumptions: Appelbaum *et al.* examined how many-body effects change the tunnelling current [73] while Chen examined different non-spherical orbital characters for the tip [70, 71]. Feuchtwang developed what is perhaps the most comprehensive theory of the tunnel junction independent of the transfer-matrix Hamiltonian relied upon by Tersoff and Hamam [74–78]. The Tersoff-Hamam model will be used to interpret data in this thesis due to its ability to correctly describe the observed experimental data and its relative ease of use.

¹A more complete understanding of the STM's atomic resolution on graphite requires abandoning some of the assumptions of the Tersoff-Hamam model and treating the tip wave function with more care [70–72].

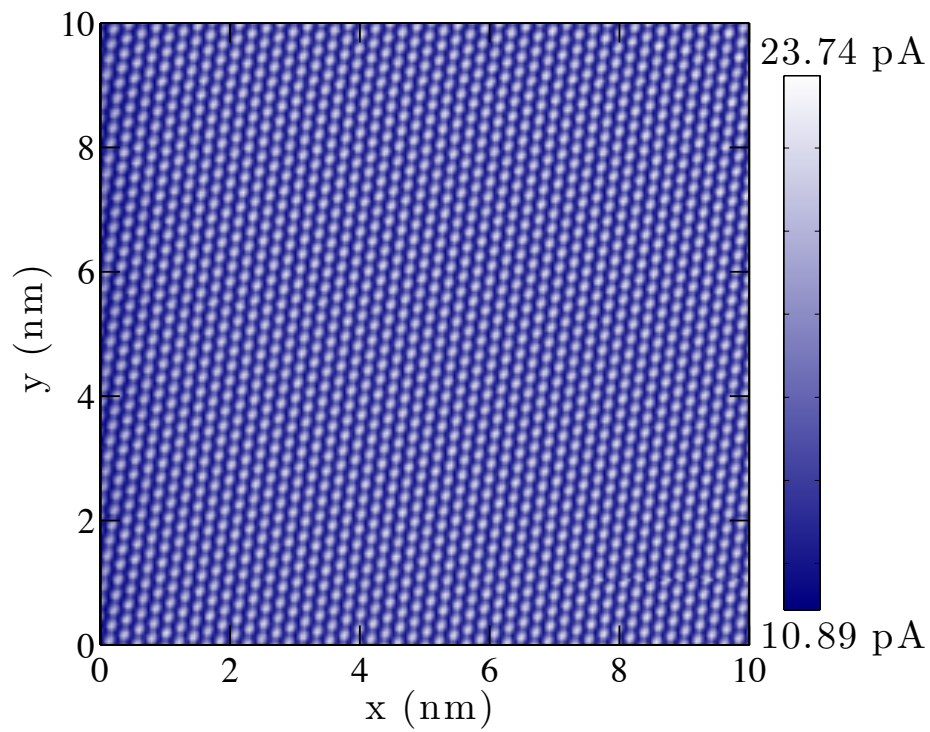


Figure 1.6: **Atomic resolution on the surface of graphite.** The tunnelling current measured on highly oriented pyrolytic graphite. The brightest intensity corresponds to the centre of the hexagons formed by rings of six carbon atoms. Imaging conditions: $I_s = 15$ pA, $V_b = 600$ mV, and $T = 4.5$ K.

The Tunnelling Transmission Probability

The Bardeen matrix element M_{ts} can be expressed in terms of a tunnelling transmission probability $T(z, E, V_b)$, ie. $|M_{ts}|^2 = T(z, E, V_b)$ [69, 73]. Under the approximation that the tunnelling barrier is trapezoidal it can be treated semi-classically in the Wentzel-Kramers-Brillouin (WKB) approximation to yield [27]

$$T(z, V_b, E) = \exp\left(-\left[2\sqrt{\frac{2m}{\hbar^2}\left(\phi + \frac{eV_b}{2} - E\right) + k_{\parallel}^2}\right]z\right) = e^{-\kappa z}, \quad (1.4)$$

where ϕ is the effective amplitude of the tunnelling barrier, m is the free electron mass, and k_{\parallel} is the component of tunnelling electron momentum parallel to the tunnelling junction interface [69]. The exponential decay of the tunnelling electron wave function inside the tunnel barrier has an inverse length scale given by the factor $\kappa \approx 1 - 2 \text{ \AA}^{-1}$ [49, 70, 72]. The magnitude of κ means that a one Angstrom change in the tip-sample separation produces roughly a $e^{-(1 \text{ \AA}^{-1})(1 \text{ \AA})} = 1/e$ change in the tunnelling current signal. As a consequence, the tunnelling current is dominated by the current flowing through the atom on the tip closest to the sample surface². It is this Angstrom-scale sensitivity of the tunnelling current to changes in the tip-sample separation z that gives the STM a vertical sensitivity on the order of 0.1 \AA. The lateral sensitivity of the STM is strongly dependent on the orbital character of the last tip atom, as shown by Chen [70–72]. Ideal, metallic single atom tips achieve a lateral resolution of 1 \AA [72] or better, allowing the STM to measure atomic sized surface corrugations.

Results reported in Part II and Part III of this thesis were taken using low-temperature STMs with a maximum measurement temperature of $T = 4.8$ K. At these temperatures the thermal energy $E = k_B T = 0.41$ meV or smaller. Features of interest in the tunnelling current signal are larger than 1 meV and so it is reasonable to collapse the Fermi-Dirac temperature distributions inside the function f_{ts} in Equation 1.3 into step functions so that $f_{ts} = 1$. Suppressing the constant pre-factors, assuming small positive³ bias ($V_b < 1$ V) applied to the tip, and substituting the tunnelling transmission probability into Equation 1.1 the tunnelling current becomes

$$I_t(\mathbf{r}, z, V_b) = \int_{E_F}^{E_F + eV_b} \rho_s(\mathbf{r}, E) \rho_t(E - eV_b) T(z, E, V_b) dE. \quad (1.5)$$

The integral runs from the Fermi energy of the sample E_F , to the energy of the Fermi energy plus the energy of the applied bias $E_F + eV_b$. It is common notation to use a change of variables in the integral so that the bounds run from 0 to eV_b [79, 80]. Equation 1.5 is useful for interpreting STM data gathered by rastering the tip over a sample and measuring the change in the tunnelling cur-

²Leading to the STM practitioners idiom: “The last atom wins.”

³For negative bias the integral runs from $-eV_b$ to zero.

rent. Changes in the measured tunnelling current are a result of either changes in the integrated tip local density of states, the integrated sample density of states, or the tip-sample distance. In practice, a great deal of effort is put into ensuring that the tip is metallic with a local density of states that is constant as a function of energy $\rho_t(E) = \rho_t$. This ensures that the tip's density of states becomes merely a factor of proportionality.

The Differential Tunnelling Conductance

Equation 1.5 illustrates that the tunnelling current is sensitive to the integrated sample local density of states $\int_0^{eV_b} \rho_s(\mathbf{r}, E) dE$. It is often desirable to probe the sample local density of states $\rho_s(\mathbf{r}, E)$ directly, as important physics often occurs at a single energy, e.g. the energy onset of a surface state. A more direct measure of the sample local density of states is the differential tunnelling conductance dI_t/dV_b . The differential tunnelling conductance measures the local density of states at a single energy corresponding to the applied bias energy eV_b , acquisition modes that measure it are classified as scanning tunnelling spectroscopy (STS).

The differential tunnelling conductance can be derived by taking the derivative of the tunnelling current with respect to the applied bias [69]. Taking the derivative of Equation 1.5 yields

$$\begin{aligned} \frac{dI_t}{dV_b} &= \rho_s(\mathbf{r}, eV_b)\rho_t(0)T(z, eV_b, V_b) \\ &+ \int_0^{eV} \rho_s(\mathbf{r}, E) \frac{d\rho_t(E - eV_b)}{dV_b} T(z, E, V_b) dE \\ &+ \int_0^{eV} \rho_s(\mathbf{r}, E)\rho_t(E - eV_b) \frac{dT(z, E, V_b)}{dV_b} dE. \end{aligned} \quad (1.6)$$

The second and third terms in Equation 1.6 are often, though not always, negligible in comparison to the first term [81, 82]. These latter terms can also be reformulated so that they are expressed in terms of the tunnelling current [79, 80]. If the second and third terms can be neglected and the tip density of states is constant as a function of energy, then the differential tunnelling conductance is

$$\frac{dI_t}{dV_b} \propto \rho_s(\mathbf{r}, eV_b)T(z, eV_b, V_b), \quad (1.7)$$

an approximation that is so useful that it is commonly taken as the starting point for analysis of STS data [83].

Figure 1.7 illustrates the relation between the sample local density of states, the tunnelling current, and the differential tunnelling conductance for a simple model. The sample local density of states exhibits a sharp step, similar to that exhibited by noble metal surfaces at their surface state onset. This is measured

as a kink in the tunnelling current, which otherwise has a constant slope. The constant slope follows from Ohm's Law for the tunnelling current between two metals, each with flat density of states. The differential tunnelling conductance exhibits a step at the energy of the onset $\epsilon(0)$, allowing an experimentalist to measure its energy via STS.

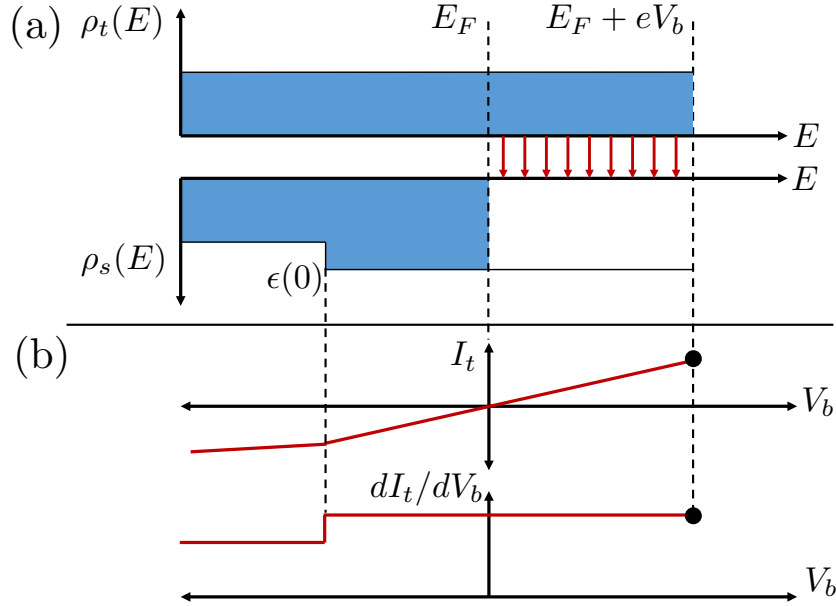


Figure 1.7: **Measuring $\rho_s(E)$ with STS.** (a) In the low-temperature limit, electrons from a metallic tip held at a bias of $E_F + eV_b$ tunnel into a sample which has the onset of a state at $\epsilon(0)$. (b) The sample can be characterized by measurements of I_t and dI_t/dV_b . The particular bias $E_F + eV_b$ leads to the data point denoted by the black circles. Sweeping the bias and measuring gives the two curves in red. The tunnelling current shows the onset of the sample state as a kink while the differential tunnelling conductance exhibits a step that reflects the step in $\rho_s(E)$.

Equation 1.7 establishes a proportionality between the differential tunnelling conductance and the density of states of the sample multiplied by the tunnelling transmission probability. In order to remove the dependence on the tunnelling transmission probability in STS data there are number of normalization schemes used by experimentalists and theorists [79, 80, 84]. These schemes are necessary, as without them features in the STS spectra do not necessarily correspond to those in the local density of states of the sample. Separating features of the sample local density of states from those of the tunnelling transmission probability, particularly in the previously unexplored context of Fourier analysis

of the dI_t/dV_b signal, will be the main focus of Part II.

Thermally-Limited Energy Resolution

The temperature of the tip-sample junction plays a crucial role in the stability of the STM tip, adatom mobility on the surface, and the energy resolution of any STS measurement. To achieve the most stable measurement conditions possible the experimental data presented in this thesis was acquired at temperatures of $T = 4.8$ K or lower. Such low temperatures rob the surface atoms of kinetic energy and ensure that the Flatland under study remains effectively frozen when probed by the STM.

When considering the effect of temperature on STS measurements it is illustrative to briefly examine the effect of finite temperature on the differential tunnelling conductance within the Tersoff-Hamann model. The effect of finite temperature on the energy resolution can be observed by returning to Equation 1.1. Writing the bias dependence into the sample local density of states instead of the tip local density of states this takes the form

$$I_t(\mathbf{r}, z, V_b) = \frac{4\pi e}{\hbar} \int_{-\infty}^{\infty} \rho_s(\mathbf{r}, E + eV_b) \rho_t(E) |M_{ts}|^2 f_{ts}(E, V_b) dE. \quad (1.8)$$

Assuming ρ_t and M_{ts} are independent of the electronic energy, which holds true for energies on the order of a few hundred millielectronvolts, Equation 1.8 can be rewritten as follows

$$I_t = A \int_{-\infty}^{\infty} \rho_s(\mathbf{r}, E + eV_b) f_{ts}(E, V_b) dE, \quad (1.9)$$

where A is a constant that contains all of the factors independent of the electronic energy and applied bias.

When performing FT-STs, the differential tunnelling conductance, dI_t/dV_b , is the measured quantity, which will be affected by the presence of the function $f_{ts}(E, V_b)$ at finite temperature. Taking the derivative of Equation 1.9 with respect to the applied bias while suppressing functional dependencies not explicitly related to the bias or energy yields

$$\frac{dI_t}{dV_b} \propto \int_{-\infty}^{\infty} \left[\frac{d\rho_s(E + eV_b)}{dV_b} f_{ts}(E, V_b) + \frac{df_{ts}(E, V_b)}{dV_b} \rho_s(E + eV_b) \right] dE. \quad (1.10)$$

Taking these derivatives and introducing the change of variable $\eta = E + eV_b$, the differential tunnelling conductance can be written

$$\frac{dI_t}{dV_b} \propto \int_{-\infty}^{\infty} \rho_s(\eta) \left(-\frac{d}{d\eta} \frac{1}{1 + e^{(\eta - eV_b)/k_B T}} \right) d\eta. \quad (1.11)$$

This expressions shows that the sample density of states is multiplied by a function that is the derivative of the Fermi-Dirac distribution. In the limit of zero temperature, this function collapses to a delta function $\delta(\eta - eV_b)$, and evaluating the integral produces the expected result shown in Equation 1.7 (where here the tunnelling transmission probability has been suppressed). At finite temperature, however, the dI_t/dV_b signal is a convolution of the sample local density of states and the derivative of the Fermi-Dirac distribution. This latter contribution is a peaked function with a full-width at half maximum equal to $3.5k_B T$, which proves a good way to quantify the thermally limited energy resolution of an STS measurement at temperature T . For the remainder of this thesis, the Fermi-Dirac factors will be suppressed when discussing the tunnelling current, however quoted measurements of the energy resolution in a particular measurement will be calculated as $3.5k_B T$.

1.3 Outlook

Part I: Flatland and the Scanning Tunnelling Microscope

The STM is a probe of electronic density with nanoscale resolution and the ability to engineer devices atom-by-atom. The scientific results presented in this thesis have all been obtained using low-temperature, ultra-high vacuum scanning tunnelling microscopes. The operation and characterization of these instruments, the CreaTec LT-STM at the UBC Laboratory for Atomic Imaging Research and the 1-K STM at the IBM Nanoscience Laboratory will be discussed in detail in Chapter 2 before delving into specific science cases in Parts II and III.

One of the biggest strengths of the STM technique is its versatility, which will be demonstrated in this thesis by examining two markedly different nanoscale Flatlands in Part II and Part III. The physical properties of these two radically different nanoscale environments will be exploited to obtain information which cannot be accessed in traditional STM data: the momentum-space energy dispersion of the electronic states and the electromagnetic interactions between magnetic atoms at an energy scale below the energy resolution of thermally-limited scanning probe techniques. In Part II this constitutes revisiting the basics of an STM analysis technique invented twenty years ago [85]: Fourier-transform scanning tunnelling spectroscopy (FT-STs) of quasiparticle interference. In Part III new interaction regimes will be measured using a technique that is still in its infancy: electron spin resonance scanning tunnelling microscopy (ESR-STM) [86].

Part II: Quasiparticle Interference and Momentum Space-Properties

Part II is dedicated to the study of the momentum-space properties of the two-dimensional free electron gases at the (111)-terminated surfaces of the noble metals silver and copper. Chapter 3 describes how the FT-STs technique can be

used to obtain detailed information about the momentum-space electronic properties via measurement of scattering events on the surface. This momentum-space information complements the real-space local density of states information collected by conventional STM measurements. The FT-STs technique has been used extensively in the last two decades to study complex materials like superconducting cuprates [87–93], superconducting iron arsenides [94–98], heavy fermion compounds [99–101], topological insulators/materials [102–109], and graphene [110–112]. Despite its extensive use, no systematic comparison of artifact features across different STM acquisition modes used in FT-STs has ever been performed.

Chapter 4 presents the first rigorous comparison between acquisition modes using FT-STs measurements of the Ag(111) surface state. Measurements from multiple different STM acquisition modes are presented and analyzed for features related to the set-point parameters, which are used to stabilize the tip-sample distance. These set-point features are then simulated using a model based on the Tersoff-Hamann theory backed up by T-matrix simulations of the sample local density of states. The conclusions drawn from this work give a comprehensive catalogue of set-point related artifacts caused by modulation of the tunnelling junction and offer possible solutions to minimize such effects.

Chapter 5 demonstrates that the conclusions drawn from the Ag(111) set-point model are applicable for FT-STs measurements of the Cu(111) surface. Multiple acquisition modes are used to confirm the presence of set-point related artifacts in the FT-STs analysis. Correctly identifying set-point artifacts and choosing the appropriate acquisition mode is particularly important in measurements of the Cu(111) surface state, as it is revealed that a set-point artifact related to the most commonly used measurement mode for FT-STs acquisition obscures a secondary feature that may be caused by many-body interactions in the sample surface [113].

Part III: Characterizing the Magnetic Dipolar Interaction of Single Atoms with ESR-STM

Part III employs a newly characterized STM measurement mode, ESR-STM [86], to study the magnetic dipolar interaction between iron and cobalt atoms on a magnesium oxide bilayer. Chapter 6 details the utility of spin-resonance techniques, showing how ESR-STM is capable of measuring magnetic interactions with an energy resolution that exceeds the limits imposed on traditional STS, while maintaining the nanoscale resolution of the STM. A discussion of spin-polarized STM and previous attempts at measurements of ESR-STM signals illustrate the technical elements needed to perform this technique.

Chapter 7 presents a study using the atomic manipulation properties of the STM to characterize the dipolar interaction between individual iron and cobalt atoms on the MgO surface. Fitting the frequency splitting observed in ESR-STM spectra to the dipole-dipole curve derived from theory allows for extraction of the magnetic moments of atoms on the surface close to an iron atom under the STM tip. The correspondence with theory and the insensitiv-

ity of the signal to changes in the tip, temperature, or magnetic field allows for the commissioning of a new form of magnetometry capable of sensing the nanoscale magnetic environment in a four nanometre radius around each iron atom. A magnetic sensor array of iron atoms is constructed and used to perform nanoscale trilateration (dubbed nanoGPS) by combining this sensing technique with the nano-engineering capabilities of the STM. A proof of principle of the capabilities of nanoGPS is demonstrated, showing that the position and magnetic moment of a nearby target iron atom can be extracted solely based off the ESR-STM signal of three iron atoms in the sensor array.

Part IV: Future Directions and Open Questions

Part IV summarizes the main results presented in Part II and Part III. Future experiments in the noble metals employing the knowledge of set-point artifacts gained in Part II are proposed, with some thought given to the expected technical challenges and results from each experiment. The technique of nanoscale magnetic sensing developed in Chapter 7 can potentially be used to measure a variety of physical systems, like nuclear spins or molecular magnets. A few candidate systems for these experiments are suggested.

Appendix A details the technical details and upgrades of the CreaTec STM throughout the course of the thesis. Appendix B shows the results of real-space simulations of impurity scattering in Ag(111). Appendix C details a measurement scheme for performing pulsed ESR-STM. Pulsed ESR-STM, unlike the continuous wave mode used in Chapter 7, could allow for coherent manipulation of the atomic spin, with potential applications in quantum computing. By oscillating the STM tip in-phase with microwave bias pulses, the first measurements using this technique are characterized.

Chapter 2

Experimental Methods

...quantum phenomena do not occur in a Hilbert space, they occur in a laboratory.

Asher Peres - 1995 [114]

Modern STMs used to probe complex materials and many-body physics are designed with specifications that exceed the five essential components listed in Chapter 1. STM laboratories have been constructed that employ low-vibration construction methods for tunnel junction stability, cryogenic cooling to increase energy resolution, and ultra-high vacuum to preserve surface integrity for days to weeks [115–122]. Two such laboratories are the Laboratory for Atomic Imaging Research at the University of British Columbia and the Nanoscience Laboratory at the IBM Almaden Research Center. This chapter delves into the details of these two laboratories and the specific instruments used for the work presented in Part II and III of this thesis. A comparison is made between the construction, modes of operation, and relative strengths and weaknesses of the STMs at each laboratory. This is done in conjunction with further development of the theoretical framework necessary to interpret STM data acquired in different measurement modes.

2.1 The Laboratory for Atomic Imaging Research

The Laboratory for Atomic Imaging Research (LAIR) at the University of British Columbia (UBC) is a low-vibration facility that houses three distinct low-temperature, ultra-high vacuum (UHV) STMs. Each STM floats on pneumatic isolators during measurement. The individual STMs are contained inside acoustically-isolated pods, which are separate from each other and the building foundation. The construction of the LAIR, thoroughly documented by MacLeod in references [123, 124], allows for the STM tunnelling junction stability that is necessary to probe quantum materials and develop new STM measurement techniques.

The three separate instruments at the LAIR are the Omicron LT-STM/AFM, the CreaTec LT-STM, and a custom-built STM that includes a dilution refrigerator to access milliKelvin temperatures, a vector magnet for studies of surface

magnetism, and a molecular beam epitaxy system for in-situ growth of thin films. The oldest of the STMs, the CreaTec LT-STM, was used to acquire the data presented in Part II. The operation and technical specifications of the CreaTec are introduced below while a more detailed discussion of its components and upgrades can be found in Appendix A.

2.1.1 The CreaTec LT-STM

The Createc LT-STM at the LAIR, referred to as the CreaTec henceforth, is based on the design of Sven Söphel and Gerard Meyer [125]. Shown in Figure 2.1 (a), it is one of the first commercialized versions of this system sold. An in-depth description of its previous measurement configurations can be found in References [126–128]. Since 2012, the CreaTec has been operated within a low-vibration pod, called c-pod, in the LAIR. Between 2012 and 2017 the CreaTec received several major upgrades, which are detailed in Appendix A. The most recent upgrade was a complete retrofit of the STM head to allow for atomic force microscopy capability.

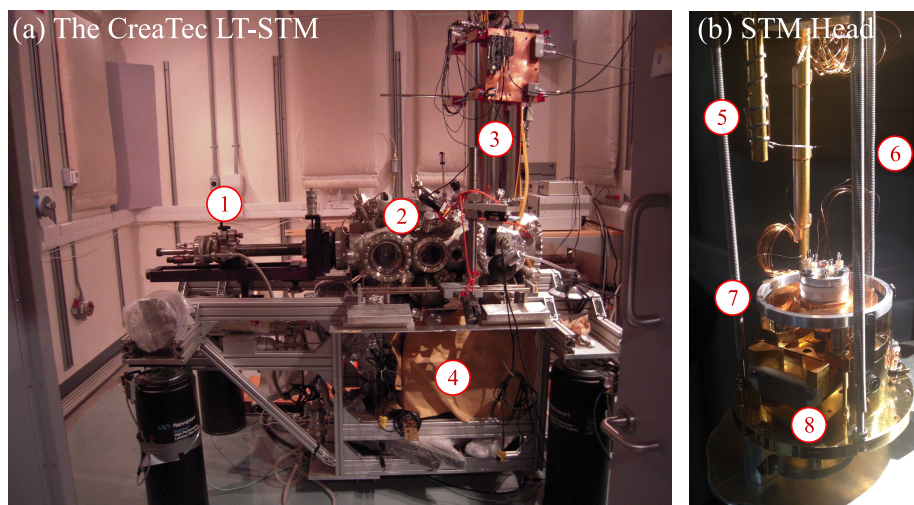


Figure 2.1: **The CreaTec LT-STM in c-pod.** (a) The vacuum chamber consists of the (1) manipulator arm, (2) preparation chamber, (3) cryostat, and (4) pumping system. (b) The STM/AFM head. The visible components are the (5) tunnelling current cold finger, (6) damping springs, (7) walking disc, and (8) sample holder mounted in the measurement position.

The CreaTec STM head, shown in Figure 2.1 (b), is a beetle-style¹ design

¹The term beetle-style STM originates from the loose resemblance of the STM head to an insect in this design [129, 130].

[129, 131] that hangs off the bottom of a liquid helium cryogenic bath. The bath is coupled directly to the STM head via a series of damping springs and a custom-built thermal braid [128], giving a base temperature of $T = 4.5$ K during measurement. This beetle-style STM head design allows for coarse, millimetre-scale positioning of the STM tip over the sample followed by fine nanometre scale control when scanning the surface. The STM head is encased in a series of two heat shields, one coupled to the liquid helium bath and the other coupled to a liquid nitrogen shroud. The heat shields and the STM head are mounted within an ultra-high vacuum chamber that has a base pressure of 10^{-10} mbar. Ultra-high vacuum is a necessary condition for measurement of pristine atomic surfaces over timescales exceeding hours. The vacuum chamber housing the STM head is coupled to an ultra-high vacuum sample preparation chamber that can be used to prepare samples through sputtering with argon ions, annealing, or cleaving. Specific sample preparation procedures for noble metal samples are detailed in Chapter 4 and Chapter 5.

In order to acquire the long-duration, high-resolution spectroscopy data presented in this thesis, considerable work was performed to optimize the electrical, vibration, and acoustic noise in the CreaTec’s experimental set-up. The results of this optimization are shown in Figure 2.2, which characterizes the tunnelling current, amplifier electrical noise, and ambient vibration noise of the CreaTec under ideal measurement conditions. The CreaTec is equipped with two different high-gain current amplifiers, both produced by FEMTO Messtechnik GmbH, each with slightly different noise characteristics and bandwidths (see Appendix A for details). The in-tunnelling curves and out-of-tunnelling curves shown in Figure 2.2 were acquired using the higher bandwidth LCA-4K-1G amplifier, which was used for the measurements presented in Part II.

As detailed in Chapter 1 the energy resolution of spectroscopic measurements made with the CreaTec is set by the tip and sample temperature, and their associated Fermi-Dirac thermal distributions. The STM tip-sample junction sits at a temperature of $T = 4.5 - 4.8$ K during measurement and has a thermally limited energy resolution of $1.3 - 1.5$ meV. The maximum uninterrupted measurement period possible on the CreaTec is 72 hours, at which point the cryogenics used to cool the STM head must be replenished. The CreaTec tunnelling junction demonstrates a high level mechanical stability – under 2 pm peak-to-peak noise in the tip height when stabilized by the STM feedback circuit – and good isolation of the tip-sample junction from the environment. Combining these strengths with ultra-high vacuum conditions it is possible to maintain the tip’s position over the same area on the surface while refilling cryogenics, allowing for repeated measurements of the same area of the sample over the course of weeks. The ability to return to the same spot on the sample and the high degree of mechanical stability allows researchers using the CreaTec to probe the spatial and energy landscape of a surface at a level that can measure subtle many-body interactions [132].

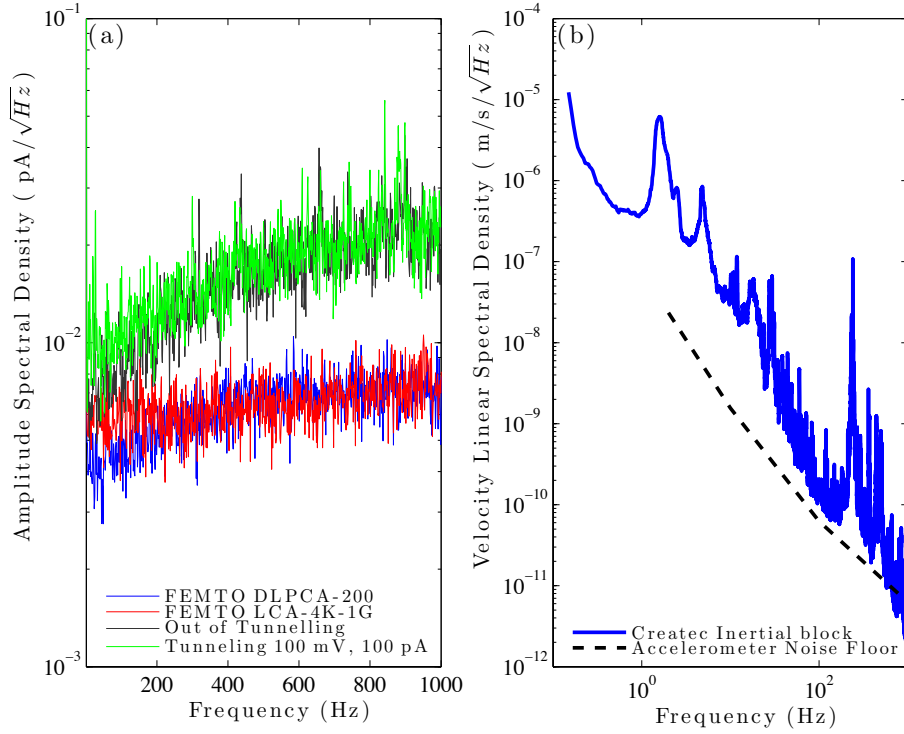


Figure 2.2: **The CreaTec Baseline Noise Characterization.** (a) Amplitude spectral density of the CreaTec tunnelling junction measured in a 1 kHz range with 977 mHz resolution. The curves labelled FEMTO DLPCA-200 and FEMTO LCA-4K-1G are the noise baselines of the tunnelling current pre-amplifiers when their inputs are grounded. The out-of-tunnelling curve is the noise baseline of the FEMTO LCA-4K-1C amplifier when its input is connected to the STM tip but the tip is not close enough to the sample to produce a measurable tunnelling current. The tunnelling curve shows the noise spectrum when tunnelling is occurring with a 100 mV bias and 100 pA tunnelling current. (b) Accelerometer measurements of the linear spectral density of the CreaTec inertial block. Spikes in the linear spectral density are indicative of mechanical resonances within c-pod. For more details on the vibration and acoustic noise level in the LAIR see References [123, 124].

2.2 The IBM-Almaden Nanoscience Laboratory

The Nanoscience Laboratory at the IBM Almaden Research Centre (ARC) has played a significant role in the history and development of STM [133–135]. In 1990, only eight years after the invention of the STM by Binnig and Rohrer, Donald Eigler and his team successfully commissioned the first STM operational at liquid helium temperatures [136] and used this STM to demonstrate the first use of atomic manipulation by spelling the letters IBM using xenon atoms on the surface of Ni(110) [136]. Researchers at the Nanoscience Laboratory have been world experts at lateral and vertical atomic manipulation for the past 27 years, manipulating individual atoms to form quantum corrals [55], quantum mirages [56], atomic scale magnetic bytes [137], and an atomically small movie set [58]. These experiments have served not only to increase understanding of nanoscale physical processes but have also been the STM works best suited to capture public imagination².

As of 2014, the Nanoscience Laboratory includes three STM systems in acoustically isolated and electromagnetically shielded rooms. The STM used to acquire the data presented in Part III is an ultra-high vacuum STM capable of reaching temperatures below 1 K by the use of a ³He refrigerator. This STM, henceforth referred to as the 1-K STM, was designed by Andreas Heinrich [138] to perform studies of single-atom magnetism, and was built with a 7 T superconducting magnet centred on the STM tunnelling junction.

2.2.1 The IBM 1-K STM

The 1-K STM has been used to perform a number of landmark studies in the field of single atom magnetism on surfaces [86, 137–145]. In the design of the 1-K STM, the STM head is thermally coupled but vibrationally isolated from a ³He reservoir, both of which are surrounded by a 4.2 K set of heat shields cooled by a ⁴He reservoir. The ³He is continuously circulated through a Joule-Thomson stage, keeping the STM head at a temperature of $T = 1.2$ K and eliminating the need for a pumped ⁴He supply [146]. By pumping on the ³He reservoir the STM head can be cooled further to a temperature of 600 mK for up to ten hours [138]. Magnetic fields of up to 7 T can be applied in the direction parallel to the surface inside the STM head, as illustrated in Figure 2.3. High-frequency cabling built into the bias line allows for electrical pump-probe measurements [143] and electron spin resonance experiments at microwave frequencies [86].

The 1-K STM uses a vertically oriented manipulator arm to transfer samples from the preparation chamber down into the STM head and inside the ³He fridge. The nominal pressure in the preparation chamber is 10^{-9} mbar. Mounted to the preparation chamber are a series of electron beam evaporators that can be used to deposit metallic atoms on a sample while it is mounted

²At last count the STM choreographed stop motion animation “A Boy and his Atom” has over six million views on YouTube [58].

in the STM head. In the data presented in Chapter 6, these evaporators were used to deposit the magnetic atoms iron and cobalt onto the surface of the sample. The preparation chamber has also been equipped with the tools necessary for oxide thin film growth and characterization. Single crystals samples can be cleaned through the use of an argon ion sputtering gun and electron-beam sample heater. Growth of thin film oxides on single crystals can be measured in real-time by an Auger spectrometer mounted on the preparation chamber. These features allow the 1-K STM to measure and study the properties of single magnetic atoms on oxide thin films.

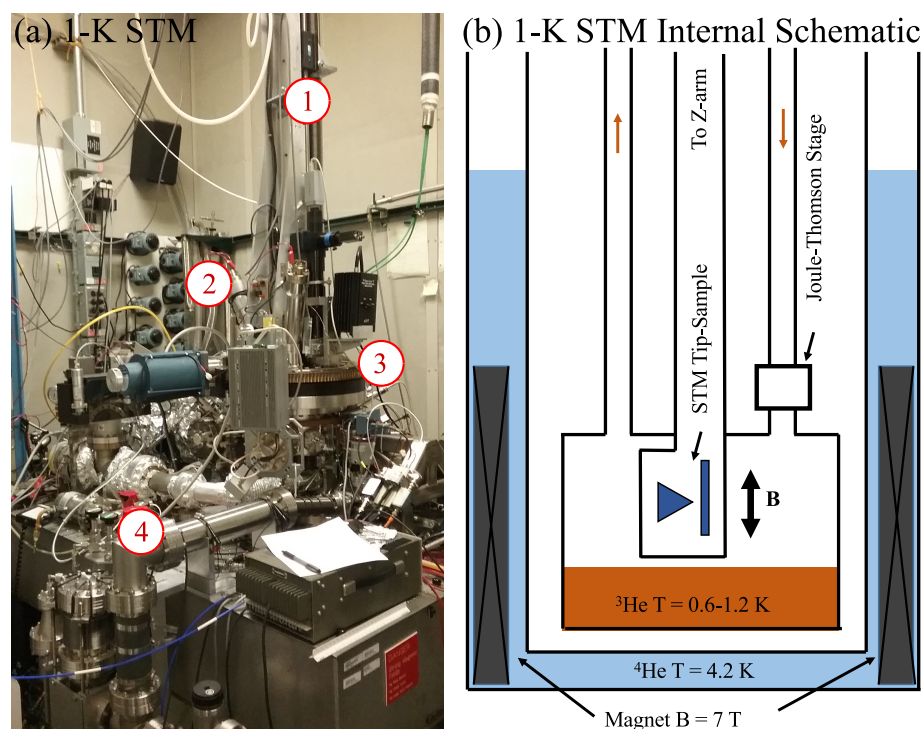


Figure 2.3: **The 1-K STM system at the Nanoscience Laboratory.** (a) (1) The vertical manipulator arm for sample transfer (2) Fe and Co evaporators (3) rotary feedthrough flange and sample preparation chamber (4) ^3He pumping system. (b) Internal schematic of the 1-K STM cooling stages and magnet alignment. Certain details, such as heat exchangers, have been omitted for clarity.

2.3 Comparison Between the CreaTec and the 1-K STM

The CreaTec LT-STM at the LAIR and the 1-K STM at the Nanoscience Laboratory are optimized to perform different types of nanoscale science. The CreaTec has a standard set of features for a commercial 4 K instrument, and has the advantage of being optimized specifically to perform scanning tunnelling spectroscopy measurements of energy levels in different materials [97, 132, 147, 148]. In comparison to the 1-K STM, the CreaTec offers a higher throughput for preparing and transferring samples between the preparation and STM chamber, ideal for experiments that require many cycles of preparation of metal samples. The CreaTec data acquisition system, the Nanonis RC4/SC4 detailed in Appendix A, allows for interfacing with LabVIEW scripts, which is particularly useful for automating measurements that require a series of bias energies over the same location. The CreaTec was used to gather the spectroscopic data examined in Part II.

The 1 K-STM was used to gather the data presented in Part III. The 1-K STM is one of the few systems in the world equipped with all the necessary features needed to perform electron spin resonance scanning tunnelling microscopy experiments: a magnetic field, oxide growth capability, a bias line that can transmit high-frequency signals, a base temperature below 1 K, and software specifically designed for atomic manipulation. The 1-K STM head's construction differs substantially from the CreaTec in terms of material design, as the 7 T magnet system precludes the use of magnetic materials. The data acquisition system, originally written in MS DOS by D. Eigler, has recently been upgraded to interface with MATLAB. MATLAB scripts were used to execute the timing of voltage pulses needed for ESR experiments. A direct comparison between the two STM's features is shown in Table 2.1.

Table 2.1: A comparison of the technical specifications of the CreaTec at the LAIR and the 1-K STM at the Nanoscience Laboratory.

Parameter	CreaTec	1-K STM
Feedback	Digital	Analog
Bias	Sample	Tip
Cryogen Hold Time	72 hrs	120 hrs
Energy Resolution	1.3 meV	0.2 meV
In-situ Deposition	Yes	Yes
Sample Preparation	Yes	Yes
Oxide Growth	No	Yes
High-Frequency Cabling	No	Yes
Magnetic Field	No	Yes

2.4 Data Acquisition Modes of the STM

Different STM acquisition modes are used to gather information about the tunnelling current, surface height, and differential tunnelling conductance. Measurement with an STM can be performed in a variety of ways: at a single spatial location on the sample while varying the bias (e.g. STS point spectroscopy, ESR-STM), moving the tip across the sample (e.g. topography, spectroscopic maps), or a combination of both (e.g. spectroscopic grids). These different acquisition modes, introduced and described below, depend on when and how the STM feedback circuit is used to change the height of the tip during the measurement, a factor that will be crucial in Part II.

2.4.1 Topography

The first acquisition mode invented for the STM was the topographic scan [26]. In this measurement mode, the STM feedback circuit attempts to keep the tunnelling current constant at a user-defined set-point tunnelling current and bias voltage by varying the tip height as the tip is moved over the sample. Data in this measurement mode is acquired in the form of an image, which is collected by rastering the tip along a slow scan and a fast scan axis. The resulting image is composed of individual pixels, with the number of pixels per nanometre set by the experimentalist using the control software.

Topographic measurements are used to record the apparent height of features on the sample. Apparent height, h , refers to the amount that the STM feedback circuit moves the tip in order to keep the tunnelling current constant from one pixel to the next. The feedback circuit operates by comparing a user specified set-point tunnelling current, I_s , with the measured tunnelling current at a given location or pixel I_i . The difference $\Delta I = I_i - I_s$ is converted to a change in tip height by inverting Equation 1.3 to solve for the change in the tip-sample gap necessary to make the measured current equal to the set-point current. The feedback circuit uses a proportional/integral controller to calculate the voltage signal necessary to make the measured current closer to the set point current and applies that voltage to the tip piezo actuator. By recording this output signal as the tip moves from pixel to pixel an apparent height measurement is made. It is important to note that topography mode measures changes in the height of the tip and not the tip-sample gap directly.

The amount the tip moves is based on a convolution of electronic density and the physical height of features on the sample surface, thus care must be taken when interpreting the apparent height. Adsorbed atoms or molecules, which sit on top of the surface, can appear as depressions due to a lower electronic density than the surrounding surface eg. carbon monoxide on Ag(111) or Cu(111). Despite this complication, the topographic mode is extremely useful for imaging surface structure, allowing glimpses into surface reconstructions [50], probing the arrangement of deposited molecules or atoms on a surface [149], and measuring the height of atomic steps. Figure 2.4 shows a measurement of the topography of an Ag(111) surface with five distinct step edges visible in the image. By

taking measurements of the topography that show single atomic step edges and atomically resolved surface corrugations, the topography mode can be used to calibrate the STM piezoelectric motors against x-ray diffraction measurements of the interatomic spacing. Topographic data can therefore provide a means to measure the size and distance between nanoscale features.

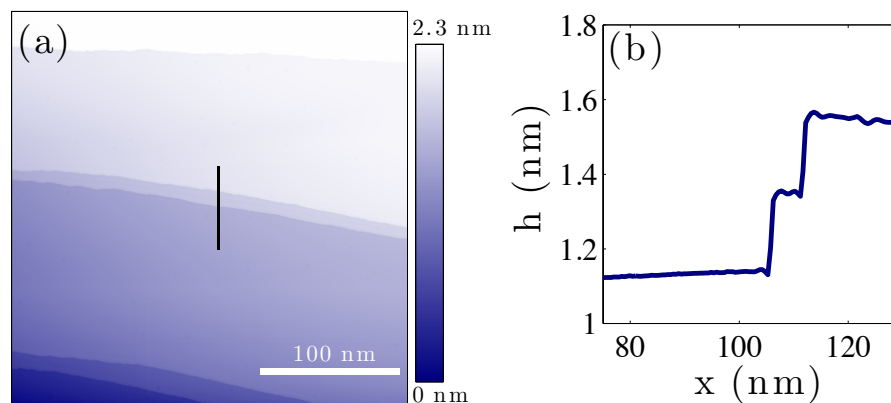


Figure 2.4: **Topography of the Ag(111) surface.** (a) A 282×282 nm area of the surface of the noble metal Ag(111). A plane subtraction has been performed to flatten the image. (b) An apparent height profile following the black line shown in (a) shows a double step edge, which can be used to vertically calibrate the STM against the atomic lattice. Imaging conditions: $V_b = -40$ mV, $I_s = 540$ pA.

2.4.2 Spectroscopic Imaging using a Lock-In Amplifier

A lock-in amplifier can be used to extract information about the differential tunnelling conductance of a sample while the regular data acquisition system simultaneously acquires information about the tunnelling current and apparent height. This acquisition mode, dubbed spectroscopic-imaging STM, is useful for extracting information about the spatial properties of the sample local density of states. The lock-in measurement of the differential tunnelling conductance in spectroscopic-imaging STM requires adding a small AC bias modulation to the DC applied bias. The experimental set-up is illustrated in Figure 2.5 (a).

In spectroscopic imaging maps, the tip is rastered across a surface gathering information pixel-by-pixel just like in topography mode. However, unlike topography mode, spectroscopic imaging can be performed either with the STM feedback circuit engaged or disengaged. In Figure 2.5 (a) the path of the tip with the feedback engaged is noticeably different from the path of the tip with the feedback disengaged. Throughout this thesis, when the STM feedback circuit is engaged the measured quantity will be referred to as a constant-current dI/dV

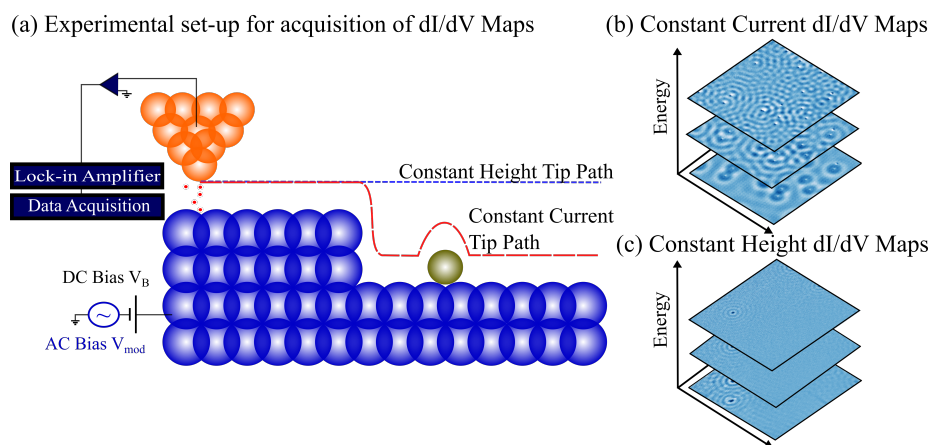


Figure 2.5: **Constant-height and constant-current dI/dV maps.** (a) Measurement schematic, including AC modulation on the bias and lock-in amplifier acquisition of the dI/dV signal. In constant-current mode the tip adjusts the tip-sample gap via the feedback as it rasters over step edges and adsorbates while in constant-height mode the tip height stays constant. (b) Constant-current dI/dV maps acquired at various different energies on the Ag(111) surface show ripples of intensity off of surface impurities. (c) Constant-height dI/dV maps on the Ag(111) surface also show ripples off of impurities but with a lower signal-to-noise ratio.

map. The data in this mode is recorded as a two-dimensional image which contains information about the tunnelling current, apparent height, and differential tunnelling conductance. When the STM feedback circuit is disengaged the measurement will be called a constant-height dI/dV map. Like a constant-current dI/dV map, it contains information about the tunnelling current and differential tunnelling conductance; however, it does not provide information about the apparent height since the feedback is not adjusting the tip height based on surface features. In Figure 2.5 (a) and (b) the differential tunnelling conductance of the Ag(111) as a function of tip position is plotted at different energies, corresponding to different applied biases.

Constant-height dI/dV maps are considerably more difficult to acquire and analyze than constant-current dI/dV maps. The lack of feedback means that the tunnel junction must maintain its stability without any correction for changes in the surface height³. As such, there is no way for the feedback to stop the tip from contacting the sample if there is a sudden change in surface height. If the STM tip crashes in this way, the remaining data is lost and both tip and sample may be damaged. Despite this risk, constant-height dI/dV maps are a useful method of ensuring that features seen in constant-current dI/dV maps are reproducible independent of the acquisition mode.

The differential tunnelling conductance in constant-current and constant-height dI/dV maps is extracted by using a lock-in amplifier. A lock-in amplifier offers phase-sensitive detection at a specified frequency. The lock-in measurement of the differential tunnelling conductance requires adding a small AC bias modulation, $V_{AC} = V_0 e^{i(\omega t + \phi)}$ to the DC bias, $V_b = V_{DC}$. In Figure 2.6 the modulation of the bias around the DC value causes the tunnelling current signal to sample the tunnelling current in a small regime around the applied bias, giving a ΔI_t signal as a function of V_b . The lock-in amplifier is used to compare the frequency of this tunnelling current signal to a reference signal, extracting the contribution related to the differential tunnelling conductance as derived below.

By ensuring that $V_0 \ll V_{DC}$, it is valid to perform a Taylor expansion of the tunnel current around the DC bias as follows

$$I_t = I_t^{DC} + \left. \frac{dI_t}{dV_b} \right|_{V_{DC}} V_0 e^{i(\omega t + \Phi)} + O((V_{AC})^2). \quad (2.1)$$

Inside the lock-in amplifier a band-pass filter is applied to the tunnelling current signal centred around the bias excitation frequency ω . The signal is then mixed to zero and a low-pass filter is applied so that the final signal extracted by the lock-in amplifier is proportional to the differential tunnelling conductance at the applied DC bias, the second term in Equation 2.1. The constant of proportionality is given by the magnitude of the AC bias, V_0 ,

³The tunnelling current, measured concurrently, can be used to assess the degree of tip-sample stability throughout the measurement.

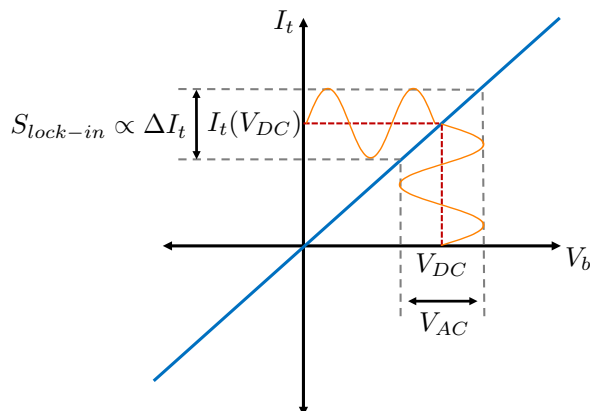


Figure 2.6: **Acquisition of the dI_t/dV_b by modulating the applied bias.** The signal measured by the lock-in amplifier is proportional to the change in the tunnelling current ΔI_t caused by the modulation of the applied bias with strength and frequency given by V_{AC} .

$$S_{lock-in} = \left. \frac{dI_t}{dV_b} \right|_{V_{DC}} V_0. \quad (2.2)$$

High-quality lock-in map acquisition requires measuring at each pixel of the map for several times the lock-in amplifier time constant, meaning that a high resolution map takes longer to acquire than a topography scan. The data presented in Part II required 6 – 9 hours for a single map with 512×512 pixels.

2.4.3 Scanning Tunnelling Spectroscopy (STS)

Scanning tunnelling spectroscopy is used to obtain the differential tunnelling conductance as a function of applied bias with the STM tip stabilized over a single spatial location. The acquisition of the differential tunnelling conductance can be performed either by measuring $I_t(V_b)$ as the bias is swept over a range, then taking the numerical derivative, or by simultaneously acquiring the tunnelling current and differential tunnelling conductance using a lock-in amplifier. In either case, the measurement process consists of using the STM feedback circuit to stabilize the tip at the set-point parameters and then disengaging the feedback. The bias is then swept over a user specified range while the tunnelling current and/or the lock-in signal are measured. STS is useful for resolving the energy structure of a sample in a localized area, with point spectra conveying information about the density of states of individual molecules [21], superconducting gaps [148], and magnetic transitions in single atoms [138, 139].

In Figure 2.7 the STS spectra obtained from an Ag(111) surface exhibit fea-

tures corresponding to the onset of a surface state. The surface state signature, which can be seen as a kink in the tunnelling current at a bias around $V_b = -65$ mV, appears as a sharp increase in the differential tunnelling conductance. The increase in the differential tunnelling conductance is reflective of the increase in the sample density of states as described by Equation 1.7. Note that the bias is swept from a negative to a positive regime. The bias voltage is referenced to the Fermi energy of the sample. At positive bias electrons tunnel from filled states of the tip to empty states of the sample. At negative bias electrons tunnel from filled states of the sample to empty states of the tip. Due to the structure of the tunnelling transmission probability, this means that with a negative bias the tunnelling current is more sensitive to the electronic structure of the tip, an effect which must be carefully experimentally controlled for when attempting to extract only the sample density of states.

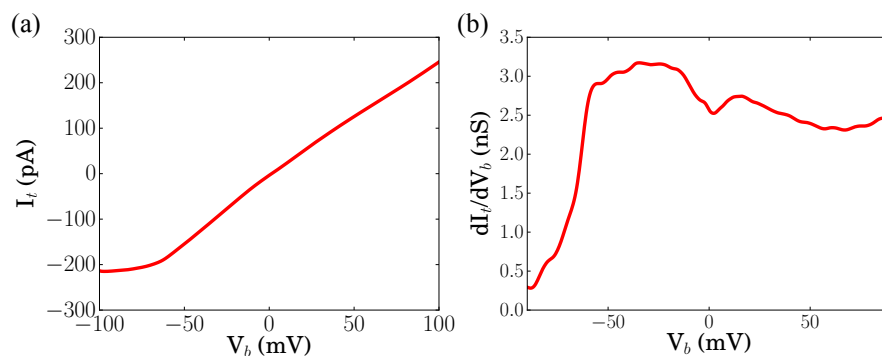


Figure 2.7: **STS of Ag(111)** (a) STS point spectra averaged from a 100 nm^2 clean area of the Ag(111) surface. (b) The corresponding differential tunnelling conductance by way of the numerical derivative.

2.4.4 Spectroscopic Imaging via Spectroscopic Grid

Spectroscopic grid acquisition combines the spatial measurements of topography with the bias measurements of STS. Acquiring a spectroscopic grid involves measuring the STS spectra at each pixel of an image. In the case of the CreaTec, the most efficient way to gather STS spectra at each pixel is to measure $I_t(V_b)$ at each pixel of an image and then take the derivative of each of these spectra numerically. The resulting data set contains spatial and energy information equivalent to n spectroscopic maps (where n is the number of points in the bias sweep). Spectroscopic grid acquisition allows for an order of magnitude more energies to be gathered per unit time than spectroscopic imaging with a lock-in amplifier, because in grid acquisition the time per pixel is limited only by how fast the bias can be changed (the slew rate) and the bandwidth of the tunnel current amplifier. However, the numerical derivative of the tunnelling

current can often be quite noisy. For this reason, high-resolution grid measurements are only possible in an STM that has been optimized for low electronic, acoustic, and vibrational noise and even then numerical smoothing of the $I_t(V)$ is required. The methodology for acquiring a spectroscopic grid and extracting the differential tunnelling conductance at each pixel is shown in Figure 2.8.

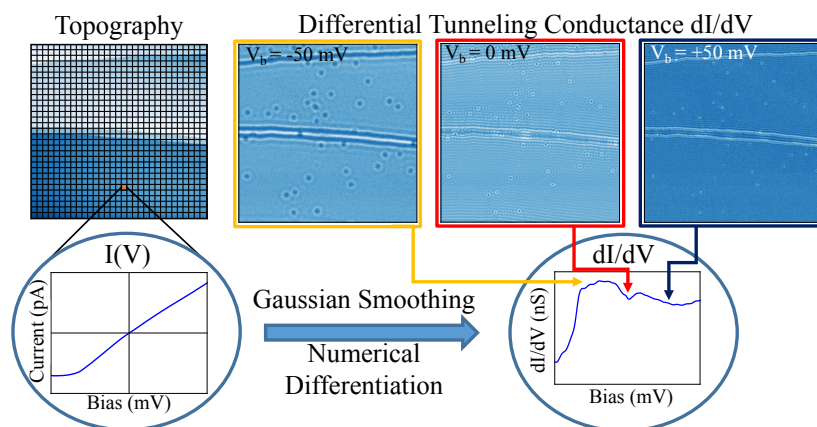


Figure 2.8: **Acquisition of a spectroscopic grid on Ag(111)** At every pixel of the grid the feedback stabilizes the tunnelling junction at some apparent height, which yields a topography for the grid. Once stabilized, the feedback is disengaged and the bias is swept over a specified range, allowing acquisition of $I(V)$ curves. Once $I(V)$ curves have been acquired at every pixel the analysis proceeds by Gaussian smoothing each curve and taking the numerical derivative. This gives a dI/dV curve at every pixel allowing for reconstruction in real space of the differential tunnelling conductance at each bias.

Grid measurements offer a powerful way to probe the local density of states as a function of energy and spatial location. A single, sufficiently large, grid measurement can take several days and involve the acquisition of over one million individual point spectra. A good grid measurement yields data on the surface topography and a slice of the differential tunnelling conductance at each energy in the bias sweep. Acquiring such a grid is a high stakes endeavour; if the STM tip interacts with the surface or changes electronically during the course of the measurement the grid will typically be rendered unsalvageable for analysis.

Tip interaction with the sample occurs frequently enough that crafting a tip capable of producing reproducible atomic-resolved images and STS point spectra without changing its state is a major component of performing STM experiments. Experimental results presented in this thesis were acquired with tips that underwent some level of nanoscale shaping through voltage pulses and controlled contact with a metallic surface. In order to control for selec-

tion bias introduced by only analyzing data acquired with the minority of tips, ie. those that were stable throughout days of measurement, every result was reproduced using at least one other macroscopically different tip and multiple different preparations of the sample.

2.5 Conclusions

This chapter introduced the STMs at the LAIR and Nanoscience Laboratory and the data acquisition techniques used in this thesis. This knowledge will be applied in the examination of the physics of two different surface systems. Spectroscopic measurements of the noble metal surface states using constant current dI/dV maps, constant height dI/dV maps, and spectroscopic grids taken with the CreaTec are presented in Part II. By taking the Fourier-transform of the resulting data a comparison will be made between the expected electronic behaviour in scattering-space and artifacts features that are dependent upon the acquisition mode. The development of electron spin resonance techniques using the 1-K STM is described in Part III and relies on characterization of the surface using topography mode and STS.

Part II

Quasiparticle Interference in Noble Metal Surfaces

Chapter 3

Quasiparticle Interference and Fourier-Transform Scanning Tunnelling Spectroscopy

A good idea has a way of becoming simpler and solving problems other than that for which it was intended.

Robert Tarjan [150]

Fourier-transform scanning tunnelling spectroscopy (FT-STs) is used to study a wide range of complex materials in condensed matter physics by analyzing the signatures of quasiparticle interference in a material's electronic density. Quasiparticle interference, originally derived in the context of Friedel oscillations, is a physical phenomenon that can be used to provide access to the momentum-space properties of the electrons in a material. FT-STs provides a means to extract information about these properties in scattering-space, provided there exists some initial knowledge of the material's band structure and the proper filtering techniques are applied. The history of FT-STs measurements illustrate its importance in the field of quantum materials: revealing the underlying physics of superconductors, heavy fermion materials, and topological materials.

3.1 Introduction: Quasiparticle Interference as Measured by Scanning Tunnelling Microscopy

When an impurity is placed inside a Fermi liquid, like an atom deposited on a metallic surface, the Fermi liquid rearranges to screen the electromagnetic potential created by the presence of the impurity [6]. Friedel was the first

to theoretically calculate the resulting fluctuations surrounding the impurity¹, which lead to standing waves in the electronic density [152]. These so-called Friedel oscillations, which are known as quasiparticle interference (QPI) when they occur at energies other than the Fermi energy² [153], can be observed in real-space using an STM. This effect was first reported simultaneously by two different groups in 1993 [154, 155]. In Figure 3.1 the very first real-space image of QPI on Cu(111), taken at the Nanoscience Laboratory in 1993, is shown next to an image of QPI on Cu(111) taken at the LAIR in 2017. In both images carbon monoxide molecules adsorbed on the surface create spherical waves in the measured signal, while in Figure 3.1 (a) step edges produce plane wave oscillations. Observation of QPI is a compelling demonstration of the ability of the STM to image quantum phenomena in real-space [156].

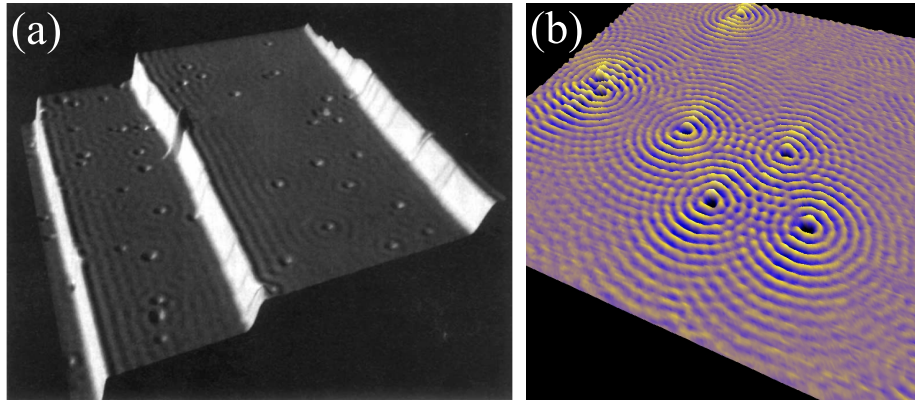


Figure 3.1: **Quasiparticle interference in Cu(111).** (a) Constant current image of QPI from impurities and step edges taken at the Nanoscience Laboratory. Imaging conditions: $T = 4$ K, $V_b = 100$ mV, $I_s = 1000$ pA, and 50×50 nm². Adapted with permission from Macmillan Publishers Ltd: Nature [154], copyright (1993). (b) Differential tunnelling conductance of Cu(111) acquired from a constant current dI/dV map taken using the CreaTec in 2017. Imaging conditions: $T = 4.5$ K, $V_b = -100$ mV, $I_s = 900$ pA, and 80×80 nm².

¹The theoretical developments leading to the discovery of Friedel oscillations throughout the 1950s are quite interesting. For a synopsis by Friedel's student Émile Daniel see reference [151].

²Friedel's original derivation was not specific to the Fermi level [152]; however, this definition of Friedel oscillations and QPI has been adopted in the intervening decades [153].

3.1.1 Derivation of Friedel Oscillations in the Electronic Density of States

Friedel oscillations play an important role in the physical properties of metallic solids, and have been extensively studied in the last sixty years [156, 157]. Over the course of these six decades the mathematical language used to describe the observed phenomenon has varied, often in a way that provides new perspectives but also makes it difficult to understand the entire body of literature in context [157]. This section briefly reviews Friedel oscillations: first in the context of using Friedel's original method of applying the scattering theory of quantum mechanics to understand impurity screening in a gas of electrons and second using a Green's function treatment of scattering from a localized impurity.

Screening and Phase Shifts

In classical electromagnetism, screening of a charged impurity embedded in a charged fluid occurs when the fluid rearranges itself to screen the impurity. This rearrangement of the fluid can be quantified as a change in the charge distribution $\delta\rho(r)$ and it falls off exponentially with distance from the impurity centre, $\delta\rho(r) \propto e^{-\alpha r}/r$. This screening distribution can be observed experimentally in fluids of electrolytes [158].

In a metal, the charged fluid is, to a good approximation, a gas of electrons and screening of a charged impurity must be calculated in the context of quantum mechanics. The first attempt to calculate the fluctuations in the charge distribution $e\delta\rho(r)$, or correspondingly the modulation of the density of states $\delta\rho(r)$, was performed by Thomas [159] and Fermi [160]. This theory makes the important approximation that the screened potential of the impurity $\delta V(r)$ and the screening charge $\delta\rho(r)$ are locally proportional, as they are in electrolytes. A result of this approximation is that the decay is again exponential: $\delta\rho(r) \propto e^{-\kappa r}/r$. The Thomas-Fermi screening model is useful because it shows that the characteristic screening length for electrons is smaller than or of order of the electron-electron distance in many materials. This explains why simple theories that neglect electron-electron correlations, like the Hartree-Fock treatment [6, 161], still accurately predict the properties of many materials. However, the Thomas-Fermi screening model does not predict oscillatory behaviour in the electronic density, as the assumption that $\delta\rho(r)$ is locally proportional to $\delta V(r)$ is only true for long-wavelength charge variations [162].

Friedel's approach abandoned the assumption of local proportionality between the screened potential and the charge distribution. He instead applied scattering theory, by that point a well-developed component of quantum mechanics, to scattering of electrons within a metal [152]. A simplified version of the original derivation, following reference [157], is given below.

In the absence of any impurities and suppressing the effect of the periodic lattice an electron wave function in a metal can be described by a plane wave characterized by momentum \mathbf{k}_i

$$\Psi_{\mathbf{k}_i}(\mathbf{r}) = e^{i\mathbf{k}_i \cdot \mathbf{r}}, \quad (3.1)$$

which satisfies the time-independent Schrödinger equation

$$H_{\mathbf{k}}|\Psi_{\mathbf{k}}\rangle = \epsilon(\mathbf{k})|\Psi_{\mathbf{k}}\rangle. \quad (3.2)$$

The energy eigenstates are described by the free-electron dispersion

$$\epsilon(\mathbf{k}) = \hbar^2|\mathbf{k}|^2/2m^* \quad (3.3)$$

where m^* denotes the quasiparticle effective mass and \hbar is the Dirac constant. The wave functions $|\Psi_{\mathbf{k}}\rangle$ have accompanying density of states

$$\rho(\mathbf{r}, \epsilon) = \sum_{\mathbf{k}} |\Psi_{\mathbf{k}}(\mathbf{r})|^2 \delta(\epsilon - \epsilon_{\mathbf{k}}). \quad (3.4)$$

Adding a spherically-symmetric charged impurity at the origin changes the solution to the Schrödinger equation. The wave functions that satisfy the Schrödinger equation in the presence of a radially symmetric potential can be written in terms of Bessel functions of the first $j_l(kr)$ and second $n_l(kr)$ kind and the Legendre polynomials $P_l(\cos(\theta))$

$$\Psi_k(r) = \sum_l (a_l j_l(kr) + b_l n_l(kr)) P_l(\cos(\theta)), \quad (3.5)$$

where the sum is over angular momentum denoted by l . The coefficients a_l, b_l can be re-parameterized in terms of an amplitude A_l and a phase δ_l

$$a_l = A_l \cos(\delta_l) \quad (3.6)$$

$$b_l = -A_l \sin(\delta_l). \quad (3.7)$$

This parametrization is useful because the angular momentum-dependent phase shift can be interpreted as a measure of how far the solution at the origin of the impurity is displaced from the free particle solution, for which $\delta_l = 0 \forall l$.

Making the assumption of radially symmetric s -wave scattering, all the amplitudes for $l > 0$ become zero so that only the zeroth order scattering phase shift δ_0 is relevant to the solution. The scattered wave function then simplifies to

$$\Psi_{\mathbf{k}_f}(\mathbf{r}) = \alpha e^{i\delta_0} \frac{e^{i\mathbf{k}_f \cdot \mathbf{r}}}{k_f r} \propto j_0(k_f r) \cos(\delta_0) - n_0(k_f r) \sin(\delta_0) \quad (3.8)$$

where α is an amplitude related to the scattering cross-section. The initial plane wave, in the absence of the impurity, can also be expressed in terms of Bessel functions. Taking the difference between the amplitude of the initial wave and scattered wave the density fluctuations caused by the presence of the impurity are given by

$$\delta\rho(r, k) = |\Psi_{\mathbf{k}_f}(\mathbf{r})|^2 - |\Psi_{\mathbf{k}_i}(\mathbf{r})|^2 \quad (3.9)$$

$$\delta\rho(r, k) \propto |j_0(k_f r) \cos(\delta_0) - n_0(k_f r) \sin(\delta_0)|^2 - |j_0(k_i r)|^2 \quad (3.10)$$

Employing the identities $j_0(x) = \sin(x)/x$, $n_0(x) = -\cos(x)/x$ and assuming that the energy dispersion $\epsilon(k)$ depends only on the magnitude of $|k|$ then

$$\delta\rho(r, k) \propto \frac{\cos(2k(\epsilon)r + \delta_0)}{r^2}. \quad (3.11)$$

This result, unlike the classical and Thomas-Fermi results, demonstrates that oscillations in the density of states are expected upon introduction of an impurity. The function $2k(\epsilon)$ is the inverse of the energy dispersion $\epsilon(k)$ and it is responsible for the wavelength of observed oscillations in experimental measurements using the STM. For the simple band structure and dispersion assumed here, one free-electron band with dispersion $\epsilon(\mathbf{k}) = \hbar^2|\mathbf{k}|^2/2m^*$, the $2k(\epsilon)$ function is heavily weighted towards the backscattering vector³ $2k(\epsilon) = |\mathbf{q}| = |\mathbf{k}_f| - |\mathbf{k}_i|$. For elastic scattering at the Fermi level this corresponds to the vector $q = 2k_F$. The damping function $1/r^2$ in three-dimensions, is dependent on the dimension of the electron gas, such that for a two-dimensional electron gas it has a $1/r$ dependence [157, 163, 164] and takes the following form at the Fermi energy

$$\delta\rho(r, E_F) \propto \frac{\cos(2k_F r + \delta_0)}{r}. \quad (3.12)$$

The surface states of Ag(111) and Cu(111) are very good approximation to a two-dimensional electron gas [8, 12, 81, 165–167] and Friedel oscillations on their surface are well described by Equation 3.12.

Quasiparticle interference and the T-matrix

Modern condensed matter theory treats the problem of Friedel oscillations, and the more general problem of QPI, using the formalism of Green's functions. This formalism comes from quantum electrodynamics and provides a more general way to derive Friedel oscillations in the presence of many-body interactions

³To understand why this vector is strongly preferred it is beneficial to look at Friedel oscillations in the context of linear response theory [157].

[168]. Rather than giving the full derivation here, the interested reader is instead directed towards reference [169]. This section will state the form of the electronic density changes caused by a localized impurity and explain it in the context of Green's functions and the T-matrix. This formalism will be used to simulate experimental results in Ag(111) in Chapter 4.

The T-matrix formalism attempts to solve the problem of how an initial wave function $|\psi_0\rangle$ is scattered by the presence of an impurity potential V into a new state $|\psi\rangle$. The scattered wave function can be solved for iteratively in the form of the Lippmann-Schwinger Equation

$$|\psi\rangle = |\psi_0\rangle + GV|\psi\rangle \tag{3.13}$$

where G is the Green's function of the initial wave function $|\psi_0\rangle$. The Green's function G is introduced as a function with the property

$$(E - H_0)G(E) = \delta(x - x') \tag{3.14}$$

where H_0 is the Hamiltonian for the time independent Schrödinger Equation in the absence of any impurity potential and E is the corresponding eigenenergy. The Green's function can be written in terms of the Hamiltonian as follows

$$G = \frac{1}{E - H_0 + i\eta}, \tag{3.15}$$

where η is a small number that is set to zero before calculating any physically measurable property. The Green's function is useful because it contains the full information necessary to solve the Schrödinger equation in the absence of the impurity scattering centre and acts as the propagator for particles from x to x' (or k to k' in momentum-space).

Returning to the Lippmann-Schwinger Equation of Equation 3.13, the scattered wave function can be substituted into itself iteratively to give the Born series, which is represented visually in Figure 3.2. The T-matrix is introduced as a succinct form of the Born series that takes the initial wave function to the scattered wave function. For more details about the derivation and role of the T-matrix in condensed matter physics see Callaway [170, 171].

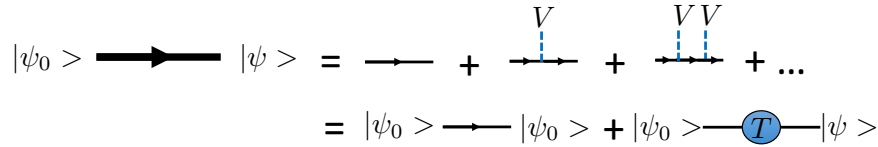


Figure 3.2: The T-matrix as a sum of Feynman diagrams.

Using the T-matrix the scattered state can be expressed in terms of the initial state and the Green's function

$$|\psi\rangle = |\psi_0\rangle + GT|\psi_0\rangle. \quad (3.16)$$

This equation allows for the solution of the wave function in the presence of an impurity scatterer. It is a more general form than Friedel's original derivation, better able to simulate QPI with fewer necessary assumptions. The fluctuations in the local density of states can be formulated in terms of the T-matrix and Green's functions and take the form

$$\delta\rho(\mathbf{q}, E) = -\frac{i}{2\pi} \sum_{\mathbf{k}} \text{Im}[G(\mathbf{k}, E)TG(\mathbf{k} + \mathbf{q}, E)]. \quad (3.17)$$

This expression will be used in the modelling section of Chapter 4 to simulate the QPI in Ag(111) introduced by the presence of carbon monoxide molecules on its surface [132].

QPI in a 2D Electron Gas

Figure 3.3 illustrates how the presence of QPI allows access to the band dispersion of a two-dimensional electron gas in scattering-space using an STM. Measurements of the differential tunnelling conductance using an STM provide information about the sample local density of states through the relation between dI_t/dV_b and ρ_s derived in Chapter 1. In the absence of a scattering impurity, the situation is as shown in Figure 3.3 (a), and an STM measurement of the differential tunnelling conductance cannot provide information about the momentum-space electronic properties or electronic dispersion $\epsilon(\mathbf{k})$.

Figure 3.3 (b) illustrates how the sample local density of states exhibits QPI in the presence of an impurity. Images of the differential tunnelling conductance that measure this QPI signature in the density of states contain information about the electronic dispersion relation because the oscillations in ρ_s are proportional to $\cos(2|k|r + \delta)/r$, and so depend on a scattering vector $\mathbf{q} = 2|\mathbf{k}|$ that connects two pieces of the allowed momentum states (at the Fermi energy this is called the Fermi surface). Measurement of the wave vector of the QPI pattern observed in the differential tunnelling conductance corresponds to a measurement of this scattering vector. When the scattering vector \mathbf{q} is extracted at different energies the dispersion in scattering space $\epsilon(\mathbf{q})$ can be constructed as shown in Figure 3.3 (b) (iii). The scattering-space dispersion can then be related back to the dispersion in momentum-space, providing information on important electronic properties that can't be measured in the absence of QPI. The scattering-space intensity $|S(\mathbf{q}, E)|$ is calculated by taking the Fourier transform of the differential tunnelling conductance, an analysis technique known as Fourier transform scanning tunnelling microscopy (FT-STs).

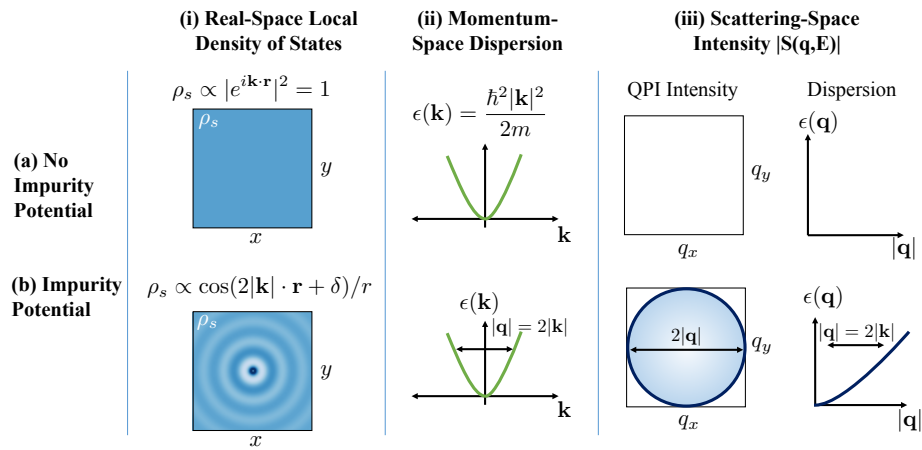


Figure 3.3: **Quasiparticle interference in real-space, momentum-space, and scattering space.** (a) In the absence of an impurity the density of states of a two-dimensional electron gas is flat with a parabolic dispersion relation $\epsilon(\mathbf{k})$. No signal in scattering space is observed. (b) In the presence of an impurity the sample density of states acquires a dependence on the back scattering vector $|\mathbf{q}| = 2|\mathbf{k}|$.

3.2 Fourier-Transform Scanning Tunnelling Spectroscopy Measurements of Quasiparticle Interference

3.2.1 History of FT-STs Measurements

Four years after the observation of the first QPI, independently by Crommie [54] and Hasegawa [155], it was realized that the Fourier-transform of images that exhibited QPI could be used to infer information about the momentum-space properties of the underlying material being imaged. The first Fourier-transform STM/STS measurements were performed on metal surfaces [85, 172–178]. In these early publications, there was some contention about how directly the FT-STs intensity corresponded to the material’s momentum-space properties [176]. Despite difficulties in exactly relating the observed FT-STs scattering intensity with the quasiparticle momentum, the authors of these early works predicted that FT-STs would prove a powerful technique in the study of the momentum-space properties of quantum materials. This prediction wound up being extremely accurate, as over the next two decades FT-STs was used to study superconducting cuprates [87–93], superconducting iron arsenides [94–98], heavy fermion compounds [99–101], topological insulators/materials [102–109], and graphene [110–112]. With the stability of modern STM instrumentation, large FT-STs data sets can be acquired yielding resolution in energy and momentum-space rivalling that of state-of-the-art ARPES [132] and allowing new insight into physical processes like electron-boson coupling [128, 132, 179].

Figure 3.4 shows FT-STs measurements, both the very first measurement reported by Sprunger *et al.* on the surface of Be(0001), and a more recent example from the LAIR of the surface of the superconductor LiFeAs. The STM constant current image of Be(0001) in Figure 3.4 (a) exhibits strong QPI. The absolute value of this image is shown in Figure 3.4 (b). It shows a ring of intensity that is associated with scattering of quasiparticles across the Fermi surface and Bragg peaks that correspond to the atomic lattice. QPI from a more complicated material is shown in Figure 3.4 (c); where a differential tunnelling conductance image of the iron pnictide superconductor LiFeAs exhibits QPI caused by different lattice defects. The FT-STs signal corresponding to this image, shown in Figure 3.4 (d), gives a much richer pattern, as well as showing the Bragg peaks associated with the atomic lattice. The more complicated FT-STs pattern can be attributed to a more complicated quasiparticle band structure in momentum-space, involving scattering between multiple bands [97].

3.3 FT-STs Measurements of the Noble Metals Surface States

Noble metal (111)-terminated surfaces have been a subject of intense study using FT-STs [113, 180, 181]. They were the first surfaces upon which QPI

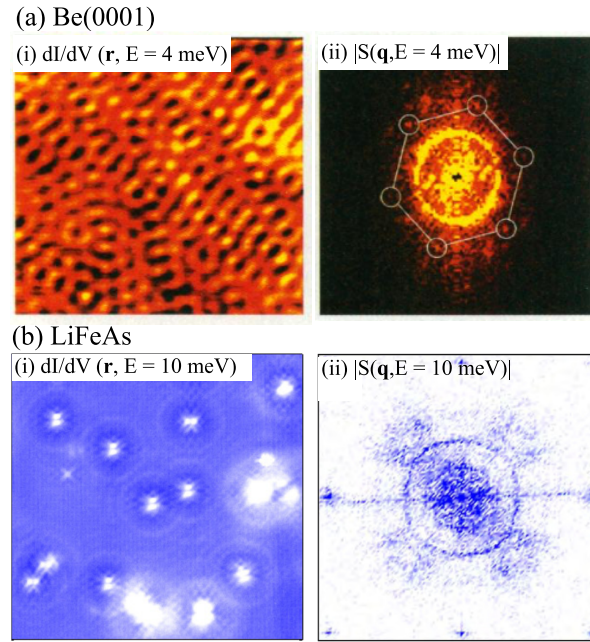


Figure 3.4: **Fourier transform analysis of quasiparticle interference.** (a) (i) A constant current STM image of QPI in Be(0001). Imaging conditions: $T = 150$ K, $V_b = 4$ mV, $I_s = 1.5$ nA, and 4×4 nm². (ii) The associated $|S(\mathbf{q}, E)|$ intensity exhibits a ring of intensity associated with scattering across the Fermi surface and lattice Bragg peaks from the atomic lattice. Adapted from Reference [85]. Reprinted with permission from AAAS. (b) (i) Differential tunnelling conductance image of LiFeAs. (ii) The corresponding Fourier transform shows the complexity of the FT-STs signal in a multi-band system. Imaging conditions: $T = 4.5$ K, $V_b = 10$ mV, and 26×26 nm. Adapted figure with permission from S. Chi, S. Johnston, G. Levy *et al.*, Physical Review B, 89, 1–10, 2014 [97]. Copyright 2014 by American Physical Society.

was measured [54, 155] and exhibit large QPI signatures because their surface termination supports the existence of a surface state that functions as a two-dimensional electron gas (2DEG). Following from Equation 3.12, QPI in a 2DEG is described by

$$\delta\rho(r, \epsilon) \propto \frac{\cos(2k(\epsilon)r + \delta_0)}{r}. \quad (3.18)$$

The lower order damping compared to materials with three-dimensional electronic character means that the oscillations are more long-lived on these surfaces and easier to measure with an STM.

Surface states are ubiquitous among the noble metals. They arise because at the surface of a crystal the discrete translational symmetry of the crystal lattice is broken, and Bloch's theorem no longer holds. Bloch electronic wave functions are therefore no longer valid solutions to the Schrödinger Equation. Instead, there exist valid solutions that are localized within several atomic radii of the surface, decaying exponentially into the bulk and into the vacuum. Such states were first characterized by Shockley in 1939 [182] and appear in many different terminations of face-centred cubic noble metals, such as (100), (111), and (110).

In (111) terminated noble metals the broken translational symmetry at the surface gives rise to *sp* derived electronic wave functions that are localized near the crystal surface [183], and form a parabolic band with onset below the Fermi energy [12, 165, 167]. This surface state, which is the source of the QPI in the (111)-terminated noble metals, has a band structure that agrees very well with the single-band free electron model at energies near the Fermi energy. This single, parabolic band supports only one intra-band back scattering vector that can be related to the momentum-space structure by a single factor of $\frac{1}{2}$ at a given energy. This band structure provides an easy way to infer momentum-space properties from FT-STs, unlike materials such as the cuprate superconductors, where there are eight primary scattering vectors at any given energy [88, 89, 91]. In the (111) noble metals, QPI measured by FT-STs is reflective of the surface properties rather than the bulk, as the surface state band across which quasiparticles scatter is caused by, and localized to, the surface. The combination of large QPI oscillations combined with a simple band structure made the noble metals some of the first materials characterized using FT-STs [180].

Despite their simple band structure, secondary scattering features that are not compatible with the expected intra-band scattering vector have a long history in FT-STs measurements of the noble metals [113, 132, 173, 176, 180, 181]. Petersen *et al.* first reported a secondary scattering feature in FT-STs in Au(111) and Cu(111) and ascribed this to scattering across a neck in the bulk Fermi surface [180]. Schouteden *et al.* performed further measurements of these secondary features and attributed their behaviour above the Fermi energy (E_F) to inelastic electron relaxation [181]. Sessi *et al.* demonstrated that the secondary features are not compatible with the positions of the bulk bands in

Au(111), Cu(111), or Ag(111). They instead attributed the secondary features to an acoustic surface plasmon dispersion [113]. Data presented in Chapter 4 and Chapter 5 will provide another possible explanation for the presence of secondary scattering features in the FT-STs scattering intensity: measurement artifacts caused by modulation of the STM tunnelling barrier during data acquisition.

3.3.1 Acquiring and Analyzing FT-STs Data

A low-temperature, ultra-high-vacuum STM is a probe of real-space electronic properties at surfaces with sub-nanometre resolution of electronic density; however, in most cases it is not possible to access the momentum-space electronic properties of a sample using an STM. An exception occurs when quasiparticles within the sample scatter from defects, adsorbates, or step edges on a surface. By taking the absolute value of the Fourier transform of images of the differential tunnelling conductance that exhibit QPI a large amount of information relating to the material's band structure can be extracted.

Fourier-transform scanning tunnelling spectroscopy (FT-STs) can be performed using differential tunnelling conductance data acquired either from dI/dV maps using a lock-in amplifier or from spectroscopic grids. In either case, the analysis proceeds by taking the Fourier transform of an image of the differential tunnelling conductance of the sample, as shown in Figure 3.5 (a) and (b). The extracted scattering intensity $S(\mathbf{q}, E)$, is dependent on the modulation in the sample density of states caused by the presence of impurities

$$S(\mathbf{q}, E) \equiv FT\left(\frac{dI_t}{dV_b}(\mathbf{r}, E)\right) \propto \delta\rho_s(\mathbf{q}, E). \quad (3.19)$$

The scattering intensity is a complex quantity, to represent the real and imaginary parts it is common practice to plot $|S(\mathbf{q}, E)|$. At a single energy in scattering-space $|S(\mathbf{q}, E)|$ shows the backscattering vectors between allowed \mathbf{k} vectors at that energy. If $|S(\mathbf{q}, E)|$ is spherically symmetric, a further analysis step can be taken: the data can be projected onto a single radial vector in scattering space q_r , as shown in Figure 3.5 (c). Radial projection is performed by calculating the Euclidean distance of each pixel in the scattering intensity image from $\mathbf{q} = (0, 0)$ and then summing the intensity contribution from each pixel for each discrete distance, normalized by the number of pixels. Radial projection allows for an increase in the signal-to-noise background and for one-dimensional fitting of observed features in the FT-STs line cut.

For a single constant-current or constant-height dI/dV map Figure 3.5 encapsulates the full scope of FT-STs analysis. For a spectroscopic grid, however, the steps shown in Figure 3.5 can be repeated for every energy in the grid's bias range. The scattering intensity can therefore be constructed at each energy in the grid, along with a radial projection for each of these energies, as shown in Figure 3.6 (a). Grid measurements can probe hundreds of bias energies and so

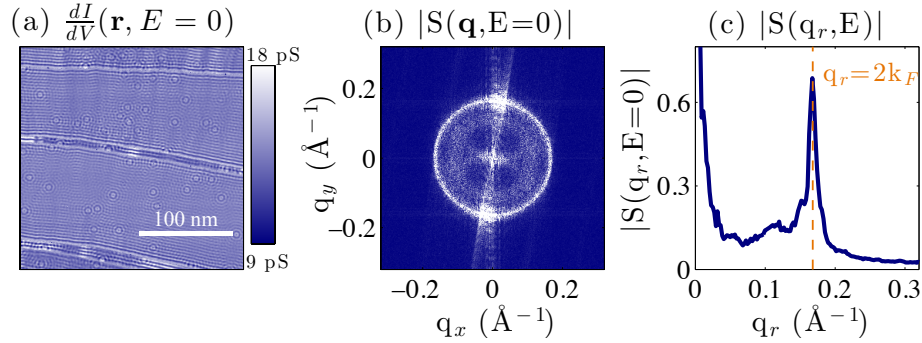


Figure 3.5: **Extracting scattering information from dI/dV by analyzing QPI.** (a) Differential tunnelling conductance of Ag(111) at the Fermi energy, $V_b = 0$ mV. (b) The absolute value of the Fourier transform of the differential tunnelling conductance, ie. the FT-STS scattering intensity $|S(\mathbf{q}, E)|$. The bright ring denotes the preferred scattering vector for quasiparticles in the surface. (c) A radial projection of the scattering intensity $|S(q_r, E)|$. The primary feature at $q_r = 2k_F$ corresponds to the scattering vector of the Ag(111) surface state at the Fermi energy.

a succinct way to represent all of the projected FT-STS line cuts is to construct an image of the scattering dispersion $\epsilon(q_r)$ as function of energy, as shown in Figure 3.6 (b). Plots such as Figure 3.6 (b) are extremely useful, as they exhibit the full scattering-space and energy resolution obtained by the grid, which in some cases match the resolution of state-of-the-art ARPES [132]. Dispersion plots can also be constructed from map data, it just requires taking many maps over the same area, typically a task that is too experimentally challenging to achieve with the same energy resolution as a grid measurement over the same area.

The resolution of FT-STS data in scattering space is set by the real-space size of the differential tunnelling conductance image. If an image has a real space size of $L \times L$ in nanometres then its resolution in scattering space Δq in inverse Angstroms is given by

$$\Delta q = \frac{2\pi}{10L} \quad (3.20)$$

The size of the Fourier-transformed image in scattering space Q is given by the scattering-space resolution multiplied by the number of pixels P in length L in the real-space image

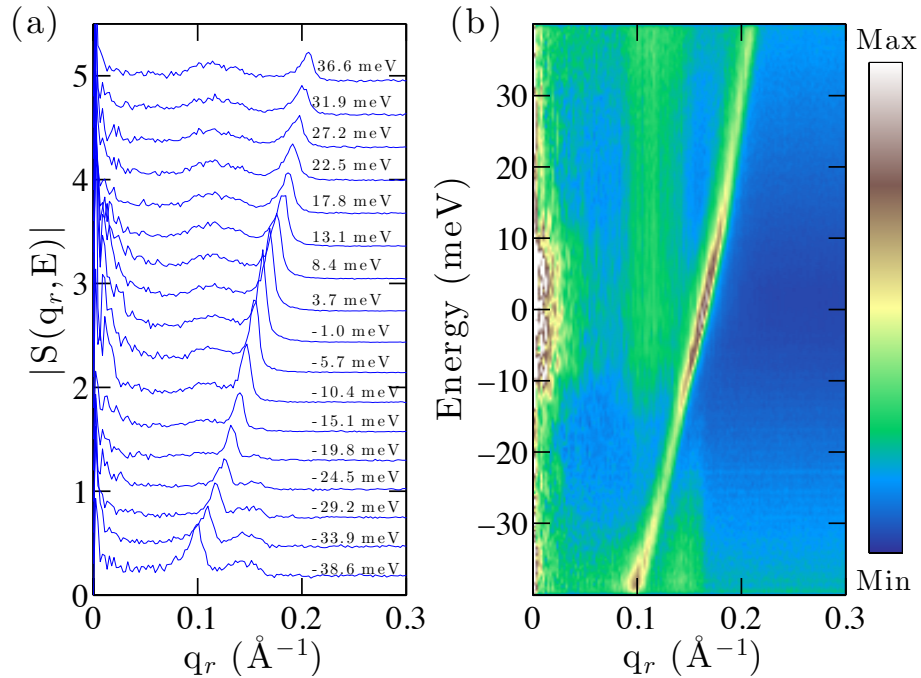


Figure 3.6: **Scattering dispersion $\epsilon(q_r)$ from a spectroscopic grid.** (a) $|S(q_r, E)|$ line cuts for a spectroscopic grid on Ag(111). The primary feature, corresponding to scattering of a surface state, changes position or disperses as a function of energy. This figure only shows three percent of the data obtained in the grid measurement shown in (b). To represent all the $|S(q_r, E)|$ data taken in the grid the scattering intensity can be plotted as function of energy and q_r , where the maximum in intensity corresponds to the peaks seen in (a).

$$Q = (\Delta q)P. \quad (3.21)$$

Equations 3.20 and 3.21 imply that the best FT-STs data, with the largest and highest-resolution view of scattering space, can be obtained by collecting the largest possible real-space image of the differential tunnelling conductance with the maximum number of pixels experimentally attainable with the experimental apparatus. The desire to maximize Q while simultaneously minimizing Δq leads to data acquisition over the largest areas of the sample accessible with the STM. For the Createc, such areas are on the order of 200 – 300 nm in linear dimension. Despite sample preparation cycles using sputtering and annealing it is often the case that there will be multiple scattering impurities in images of the surface. The most common type of scattering centres on the noble metal surfaces discussed in Chapter 4 and Chapter 5 are step edge dislocations in the crystal structure and carbon monoxide (CO) adsorbates. Carbon monoxide adsorbs onto the noble metal surfaces from the ultra-high vacuum environment, where it is present at a higher partial pressure than other gases due to its presence in the steel used in the chamber walls. In practice, the Createc is optimized to take a single, high-resolution spectroscopic grid every 72 hours. In this time, it can gather real-space tunnelling conductance information over hundreds of nanometers and with pixel densities high enough to obtain a scattering-space resolution $\Delta q = 0.0026 \text{ \AA}^{-1}$.

The energy resolution for spectroscopic grids is often comparable to the thermal limit imposed by the Fermi-Dirac distributions of tip and sample ($\Delta E = 1.5 \text{ meV}$ for $T = 4.2 \text{ K}$) while for maps it depends on the number of maps acquired and their spacing in bias. In practice this often means that the energy resolution of a scattering dispersion constructed from maps is an order of magnitude worse than the thermally-limited energy resolution.

Filtering in FT-STs analysis

Regardless of which acquisition mode is used to gather the differential tunnelling conductance data, FT-STs analysis often requires the application of filters, in both real-space and scattering-space. Filtering helps to suppress signals unrelated to the QPI that saturate the Fourier-transform signal. These filtering techniques are introduced in Figure 3.7 and are used heavily in the analysis of the data presented in Chapter 4.

Both steps edges and carbon monoxide produce QPI in the noble metal surface states. Step edges act like a line of one-dimensional scatterers and produce a scattering intensity with a preferred direction. Carbon monoxide acts as a radially symmetric scattering centre, which produces a radially isotropic pattern in scattering-space. When performing a radial projection of $|S(\mathbf{q}, E)|$ to produce $|S(q_r, E)|$, isolating the signal from the carbon monoxide scattering centres is preferred, since they do not produce a signal with a preferred direction. Focusing on the carbon monoxide scattering centres allows for more

direct, quantitative comparisons between images taken of different portions of the sample surface, since features in $|S(\mathbf{q},E)|$ are more easily separated from the topographic details of the real-space image.

Filtering of the step edge signals on the surface of Ag(111) is shown in Figure 3.7. Figure 3.7 (a) shows the differential tunnelling conductance and scattering intensity with no filters. The most intense signal in $|S(\mathbf{q},E)|$ is caused by the series of step edges in the real-space image. To isolate the ring of intensity caused by the carbon monoxide scattering centres, visible in the real-space image, the first step is to set the differential tunnelling conductance over the step edges to the average value of the differential tunnelling conductance in the image. This is performed over each step edge area, denoted by the white dashed lines in Figure 3.7 (b). The scattering intensity shows a corresponding drop in the asymmetric intensity associated with the step edges, though the pattern is still not isotropic.

Before taking the radial projection, a further step of angular filtering in scattering-space is performed. Angular filtering takes the radial projection focusing over an area of the $|S(\mathbf{q},E)|$ devoid of step edge induced signal. In Figure 3.7 (c) the filtered area is denoted by the white arrow between the dashed lines.

A comparison of $|S(q_r),E|$ for the case of no filters, real-space filter, and real-space and scattering-space filter is shown in Figure 3.7 (d). The recovered signal with both sets of filter can be attributed more readily to a single type of scattering centre, rather than a mix of step edges and point scattering centres. This makes the theoretical modelling of the scattering centres as radially isotropic in Chapter 4 apt and allows for better comparison between experiment and theory.

3.4 Outlook

FT-STs analysis of QPI is a powerful technique for extracting momentum-space information about quasiparticles imaged with atomic-scale resolution in real-space. As has been demonstrated in this chapter, the complexity of the momentum-space quasiparticle structure in real materials requires extreme care when interpreting FT-STs data. Interpretation of FT-STs can be further complicated by effects related to the acquisition mode used to measure the differential tunnelling conductance. Chapter 4 and Chapter 5 will examine how FT-STs data, even in measurements of a very simple band structure, are susceptible to the presence of secondary features in $|S(\mathbf{q},E)|$ related not to the quasiparticle dispersion, but to the measurement mode.

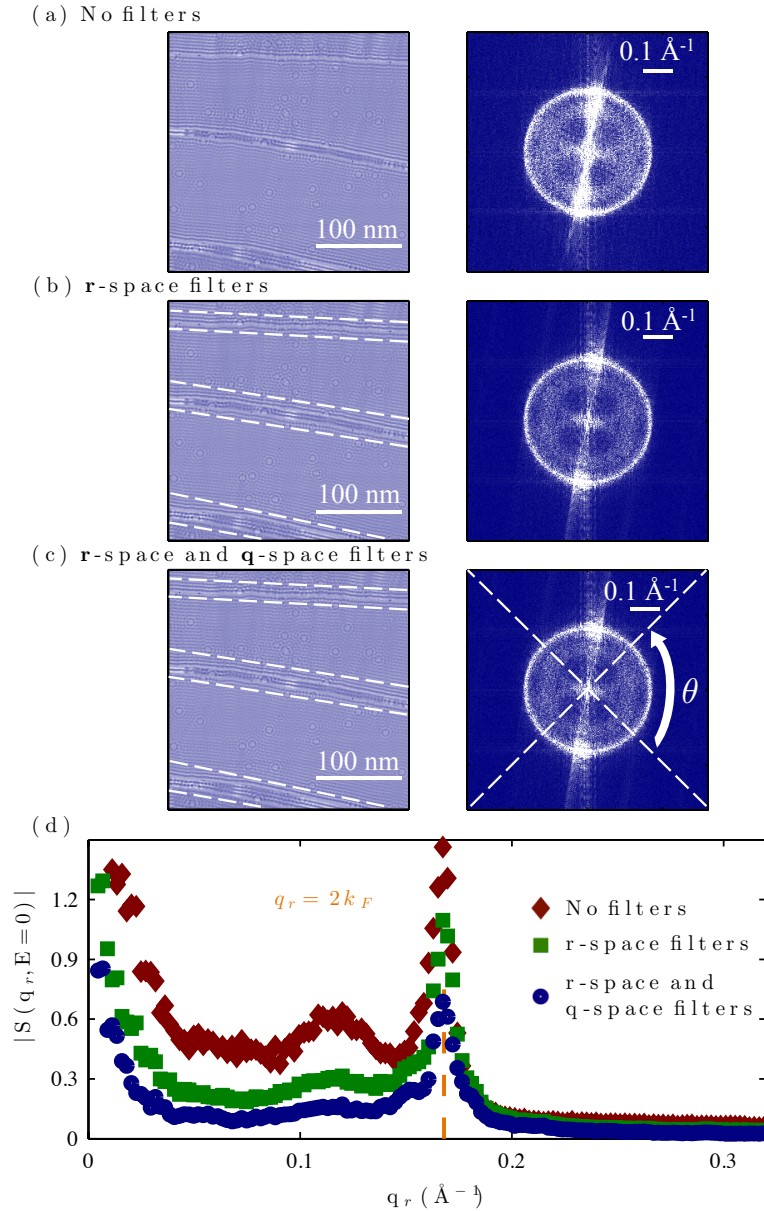


Figure 3.7: **Filtering processes for FT-STS data.** (a) No filtering is applied to the real-space differential tunnelling conductance image. Step edges and carbon monoxide scattering centres are both visible on the surface. The $|S(\mathbf{q}, E)|$ intensity exhibits a ring associated with the carbon monoxide QPI and a near vertical line of intensity associated with the step edge. (b) Real-space filtering averages out the step edges, filtered region denoted by dashed white lines. The $|S(\mathbf{q}, E)|$ intensity associated with the step edge is reduced. (c) Angular filtering is performed before taking the radial projection. (d) Comparison of the radially projected scattering intensity $|S(q_r, E)|$ between the three methods.

Chapter 4

Acquisition-Dependent Artifacts in FT-STs of the Ag(111) Surface State

What we see depends mainly on what we look for.

Jonathan Lubbock [184]

The following Chapter contains text and figures adapted from “Dispersing Artifacts in FT-STs: a comparison of set point effects across acquisition modes” IOP Nanotechnology, **27**(41):1-7 [185]. Figures are altered unless otherwise noted.

FT-STs is an important technique in the study of complex materials because it gives experimentalists the ability to map the electronic dispersion of both occupied and unoccupied bands, and locally correlate the electronic dispersion with the surface structure. There is a catch: some a priori knowledge of the underlying band structure is required to assign meaning to the features observed in FT-STs measurements. This chapter presents a comparison of the most common modes of acquiring FT-STs data on the well-characterized Ag(111) surface and demonstrates, through both experiment and simulations, that artifact features¹ can arise that depend on how the STM tip height is stabilized. The most dramatic effect occurs when a series of constant-current dI/dV maps at different energies are acquired; in this acquisition mode a feature that disperses in energy appears that is not observed in other measurement modes. Such artifact features are similar to those arising from real physical processes in the sample and are susceptible to misinterpretation.

¹Artifact vs artefact: The language in this thesis adheres to British written English instead of American, hence the use of tunnelling instead of tunneling. Artifact proves to be the one exception as the spelling ‘artefact’ only gained traction in British English around 1990.

4.1 Topography and Electronic Character of Ag(111)

4.1.1 The Ag(111) Surface State

Crystalline silver has a close-packed, face-centred-cubic crystal structure with a lattice constant of $a_0 = 0.409$ nm [186]. At a (111)-terminated surface, the atomic lattice is hexagonal with an atomic nearest-neighbour distance of $a_0\sqrt{2}/2 = 0.288$ nm. Figure 4.1 shows the surface structure: (a) imaged via an STM topograph, (b) measured by low-energy electron diffraction (LEED), and (c) drawn using a graphic model. The height of single step edges, predicted to be 2.4 Å, are used to calibrate the vertical scale of the STM piezoelectric motion. Atomically resolved images of the Ag(111) surface, as shown in the inset of Figure 4.1 (a), are used to calibrate the x and y motion of the STM piezos.

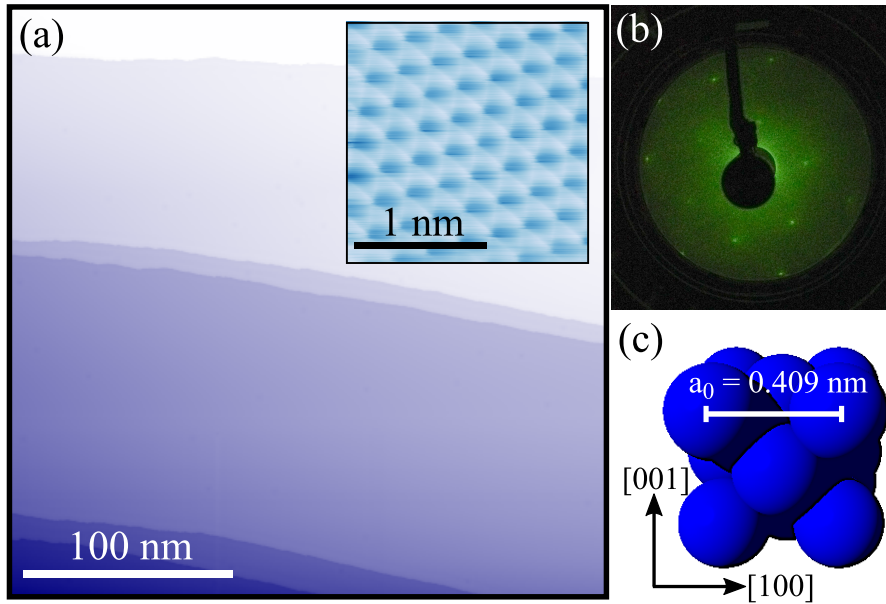


Figure 4.1: **Lattice structure of the Ag(111) surface.** (a) STM topographic image of the Ag(111) surface showing multiple step edges. Imaging conditions: $V_b = -40$ mV, $I_s = 540$ pA, and apparent height 0 – 2.3 nm. Inset shows atomic resolution on the Ag(111) surface. Imaging conditions: $V_b = 5$ mV, $I_s = 90$ nA, and apparent height 0 – 16 pm. (b) LEED measurement of the Ag(111) surface (Energy = 152 V, Current = 0.08 mA) after sputtering and annealing cycles. (c) Model which illustrates the Ag(111) lattice parameter and face-centred cubic lattice.

The (111) termination of a silver crystal surface supports a two-dimensional surface state, known as a Shockley state [182], that has been extensively studied experimentally and theoretically [8, 12, 60, 81, 128, 132, 165, 166, 187–194]. The Ag(111) surface state is an ideal candidate for the comparison of different FT-STIS acquisition modes as it is a well-characterized, theoretically understood material with a single band in momentum-space. The Shockley surface state arises from the breaking of crystalline symmetry between the bulk crystal states and the vacuum level [182]. This broken symmetry gives rise to *sp* derived electronic wave functions that are localized near the crystal surface [183], and form a parabolic band with onset below the Fermi energy [12, 165, 167]. Within the bias regime² probed in this chapter (–100 mV, 100 mV) the Ag(111) surface state band is well-described by a single free-electron band [81, 128, 132, 166, 167, 183, 188, 195] of the form

$$\epsilon(\mathbf{k}) = \frac{\hbar^2 \mathbf{k}_{\parallel}^2}{2m^*} - \mu, \quad (4.1)$$

where $\epsilon(\mathbf{k})$ is the band dispersion, \hbar is the reduced Planck constant, m^* is the effective electron mass, which for the Ag(111) surface state is approximately equal to 0.4 times the free electron mass, and $\mu = 65$ meV is the chemical potential of the band. The surface state band in the noble metals occupies a region of momentum-space devoid of bulk bands, known as the *L*-gap [167]. Within the surface state band the electric field of the surface state electrons is effectively screened by bulk electrons, reducing electron-electron interactions so that the free-electron model of Equation 4.1 works very well [193].

Figure 4.2 shows spectroscopic characterization of the Ag(111) surface state band using the STM and ARPES. The surface state band is centred at the Γ point in \mathbf{k} -space, corresponding to the point where $\mathbf{k}_{\parallel} = 0$ [183]. An advantage of the Γ point is that it is preferentially probed by STM tunnelling electrons. Modifications to the surface state band due to many-body effects such as electron-phonon coupling or plasmon formation have been probed by both ARPES [167, 195] and STM measurements [60, 113, 132, 187, 189, 191, 194] and do not compromise the conclusions drawn in this chapter.

4.1.2 Sample Preparation and Measurement Protocol

Measurements of the Ag(111) surface state were made at a temperature of $T = 4.5$ K using the CreaTec. The STM tip was made from electrochemically etched tungsten wire, which was further prepared *in situ* by sputtering and annealing to remove the oxide layer. Initial contact with the silver crystal resulted in a silver-terminated tip. The Ag(111) crystal was cleaned by three cycles of sputtering under 2.0×10^{-5} mbar argon atmosphere and annealed at 500°C to produce large, clean terraces with a low density of CO adsorbates that act as scattering centres. Spatial calibration was performed once prior to all measurements by

²The applied bias V_b in mV characterizes the electronic energy E being probed in meV.

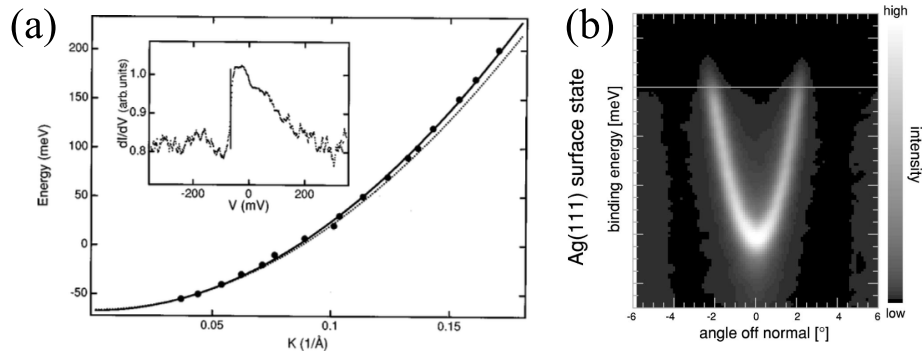


Figure 4.2: **Characterization of the Ag(111) surface state band.** (a) The \mathbf{k} -space dispersion extracted from dI/dV tunnelling spectroscopy (solid points). A parabolic fit to these data is plotted along the solid line. The dashed curve is the dispersion as measured by photoelectron spectroscopy. The inset is a dI/dV spectrum showing the surface state onset. Reprinted figure with permission from L. Jiutao, W.-D Schneider, R. Berndt, *Physical Review B*, 56, 7656–7659, 1997 [81]. Copyright 1997 by American Physical Society. (b) ARPES data of the surface state dispersion in \mathbf{k} -space shows the parabolic band. Reprinted figure with permission from F. Reinert, G. Nicolay, S. Schmidt, D. Ehm, and S. Hüfner, *Physical Review B*, 63, 1–7, 2001 [167]. Copyright 2001 by the American Physical Society.

obtaining atomic resolution of the Ag(111) surface, as seen in Figure 4.1 (a), to ensure accurate real and scattering-space measurements.

Spatially-resolved spectroscopic measurements of the differential tunnelling conductance were performed using three different acquisition modes: spectroscopic grids, constant-current dI/dV maps, and constant-height dI/dV maps. Spectroscopic grids were measured with varying size and spatial resolution (giving different pixel densities) and a thermally-limited energy resolution of 1.5 meV. Each tunnelling current spectrum $I_t(V)$ in the spectroscopic grids consisted of 512 data points in bias, which were Gaussian smoothed over 3 adjacent points in energy and averaged over 8–12 repeated measurements at each spatial location. Typical grid measurements took between 50 and 80 hours to complete. Constant-current and constant-height dI/dV maps were taken using a lock-in amplifier with a bias modulation frequency of 1.017 kHz and an amplitude of 5 mV. Spatial resolution in pixels for each map was set to 512×512 . As each map yields spectroscopic information at only one energy, a series of maps was acquired to investigate the scattering dispersion $\epsilon(\mathbf{q})$.

4.2 Experimentally Observed Set-Point Effects in Different Acquisition Modes

A “set-point effect” in scanning tunnelling microscopy describes a feature that is dependent on the stabilization bias V_s and set-point tunnelling current I_s , and not one characteristic of the surface under study. This section is dedicated to identifying set-point effects in FT-STs measurements of the Ag(111) surface state using spectroscopic grids, constant-current dI/dV maps, and constant-height dI/dV maps.

There are three separate bias or energy regions of the Ag(111) surface state band where set-point parameters can be probed. These regions are distinguished by where the set-point bias V_s is in relation to the band onset $\epsilon(0) = -65$ meV and the Fermi Energy $E_F = 0$ meV. The different energy regimes are illustrated in Figure 4.3. It is important to note that the stabilization bias only sets the energy at which the STM tip is stabilized by the feedback, and, depending on measurement mode it can be independent from the energy range probed by the measurement, which corresponds to the values of the tunnelling bias V_b . For example, a spectroscopic grid measurement could have a stabilization bias in Region I at $V_s = -100$ mV while probing an energy range in Region III, such as $V_b = 20 - 60$ mV.

4.2.1 Spectroscopic Grids as a Function of Set-Point Parameters

Spectroscopic grids measured with different set-point parameters exhibit different features in the FT-STs scattering intensity $|S(\mathbf{q}, E)|$. Figure 4.4 shows the differential tunnelling conductance and FT-STs scattering intensity evaluated

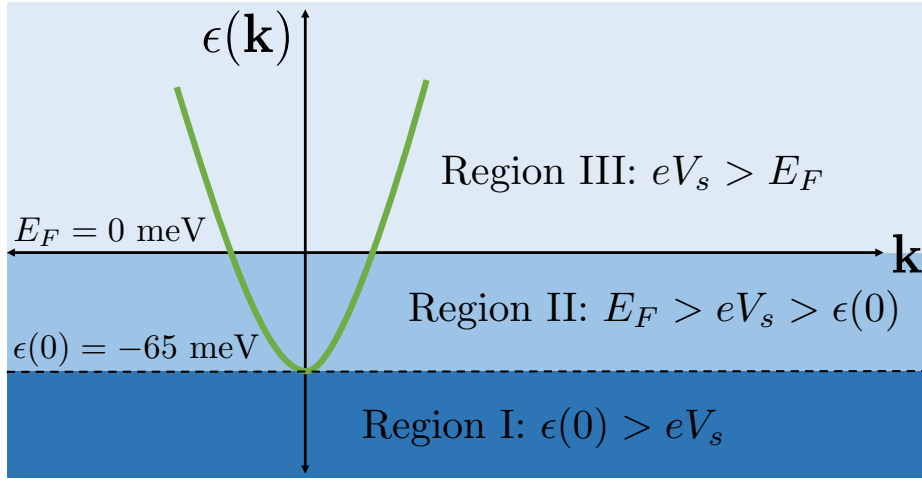


Figure 4.3: **The three different energy regions in which the stabilization bias V_s can be set when measuring Ag(111).**

at zero bias (the Fermi energy E_F) for three grids with different stabilization biases and set-point currents. The real-space images show different spatial regions with distributions of step edges and carbon monoxide molecules on the Ag(111) surface. These grids probe the three different energy regimes possible for the stabilization bias around the surface state band: Region I below the surface state onset $\epsilon(0) > eV_s$, Region II between the onset and Fermi energy $E_F > eV_s > \epsilon(0)$, and Region III above the Fermi energy $eV_s > E_F$. In all three cases step edges in the real-space images have been filtered using the prescription given in Figure 3.7.

All three grids in Figure 4.4 exhibit QPI; decaying plane waves can be observed near the step edges while the circular ripples surround the carbon monoxide molecules. FT-STIS analysis of the real-space images produces a scattering intensity that has a ring of intensity, of radius $q = 2k_F = 0.168 \pm 0.003 \text{ \AA}^{-1}$, corresponding to quasiparticles back-scattering across the surface state band at the Fermi energy E_F . High intensity features that run vertically through the FT-STIS data are caused by signal from the step edges that remains after the real-space filtering process. For the grid measurement with stabilization bias $V_s = -40 \text{ mV}$ in Region II, shown in Figure 4.4 (b), a second ring of intensity of smaller radius than $2k_F$ is present in the scattering intensity, indicated by the black arrow in the figure. Similarly, for the grid measurement with stabilization bias $V_b = 100 \text{ mV}$ in Region III, shown in Figure 4.4 (c), there is additional intensity beyond the $2k_F$ radius of the surface state scattering, again shown with a black arrow. Both the grids taken in Region II and Region III correspond to the grid measurements with stabilization bias above the band onset.

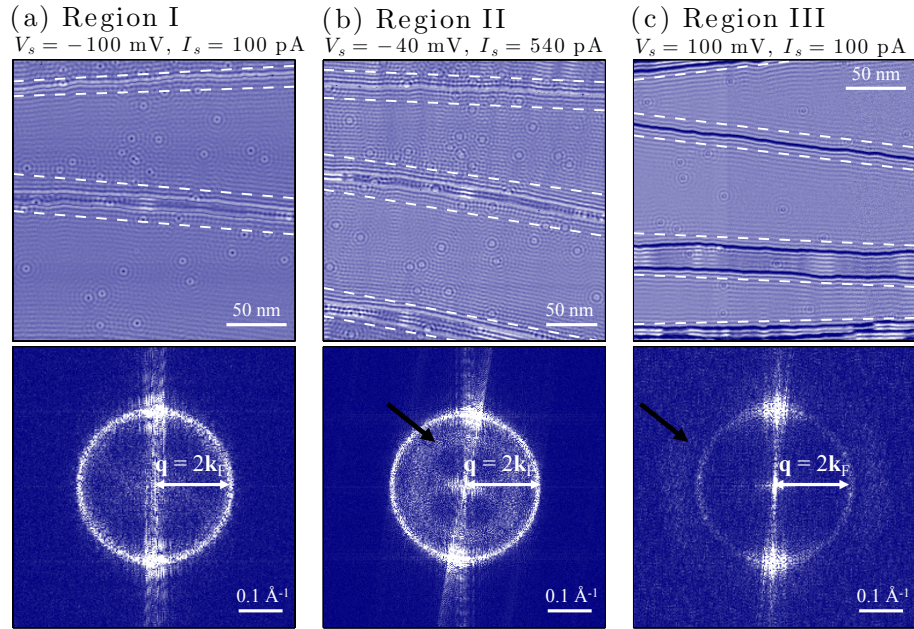


Figure 4.4: **Ag(111) spectroscopic grids with different set-point parameters.** Top panels are the differential tunnelling conductance evaluated at the Fermi energy $V_b = 0$. The bottom panels are the corresponding FT-STs scattering intensity $|S(\mathbf{q}, E)|$. Vertically aligned features of high intensity in the bottom panels are caused by the step edges present in the top panels. (a) $V_b = (-100, 120)$ mV, 239×239 nm² with 380×380 pixels. (b) $V_b = (-40, 40)$ mV 280×280 nm² with 400×400 pixels. (c) $V_b = (-100, 100)$ mV, 240×240 nm² with 350×350 pixels.

Analysis of spectroscopic grid scattering dispersion

In order to examine how the scattering intensity for different set-point parameters varies as a function of energy, Figure 4.5 shows the scattering dispersion for the same spectroscopic grids shown in Figure 4.4. $|S(q_r, E_F)|$ is plotted for each grid in Figure 4.5 (d), with a vertical offset to make the curves more easily distinguishable. In all cases, the primary feature is caused by the scattering intensity corresponding to the surface state band [132]. A high background at low $q_r \approx 0$ is visible in all three cases and is the product of broad low-frequency noise in the measurement of dI/dV causing sharp intensity in scattering-space as a byproduct of the Fourier-transform. Differences in the intensity of the surface state band scattering are related to the change in set-point current because higher tunnelling current produces larger QPI signals in the differential tunnelling conductance. Figure 4.5 (a) shows that there are no prominent features other than the surface state dispersion for the grid with stabilization bias below the onset of the band.

For the grid with stabilization bias in Region II, shown in Figure 4.5 (b), there is a broad vertical feature below $2k_F$ and above E_F centred at $q_r = 0.11 \pm 0.03 \text{ \AA}^{-1}$ and indicated by a black arrow in the figure. This feature diminishes in intensity as it nears the band intensity below E_F . A second broad feature appears on other side of the band at bias below $V_b = -20 \text{ mV}$, centred at $q_r = 0.15 \pm 0.02 \text{ \AA}^{-1}$. Neither of these features are present in scattering intensity of the Region I grid.

For the grid with stabilization bias in Region III, shown in Figure 4.5 (c), there is a broad feature at fixed $q_r = 0.22 \pm 0.03 \text{ \AA}^{-1}$ that appears (indicated by the black arrow) in addition to the surface state back scattering intensity. This additional feature can also be observed at E_F in Figure 4.5 (d), where it appear as a broad peak smaller in amplitude than the surface state feature. This peak in intensity is unique for the grid with stabilization bias in Region III and is visible even though this grid has the worst signal-to-noise ratio of the three data sets.

Subsequent grid measurements demonstrated that changes to the tunnelling current set-point I_s produced changes in signal intensity at all energies and values of q_r but did not cause the secondary scattering features observed in Figure 4.5 to change location. Therefore, for spectroscopic grid measurements, there is an additional feature in the scattering dispersion that depends on the bias used when the tip height is stabilized.

4.2.2 Spectroscopic Grids and Constant-Current dI/dV maps

In order to probe the nature of secondary features in the energy dispersion in more detail, the scattering dispersion was calculated based on measurements of the differential tunnelling conductance collected using the constant-current dI/dV map acquisition mode. Constant-current dI/dV maps were collected over two different $60 \times 60 \text{ nm}^2$ areas of the sample over a bias range $V_b = (-100, 180)$

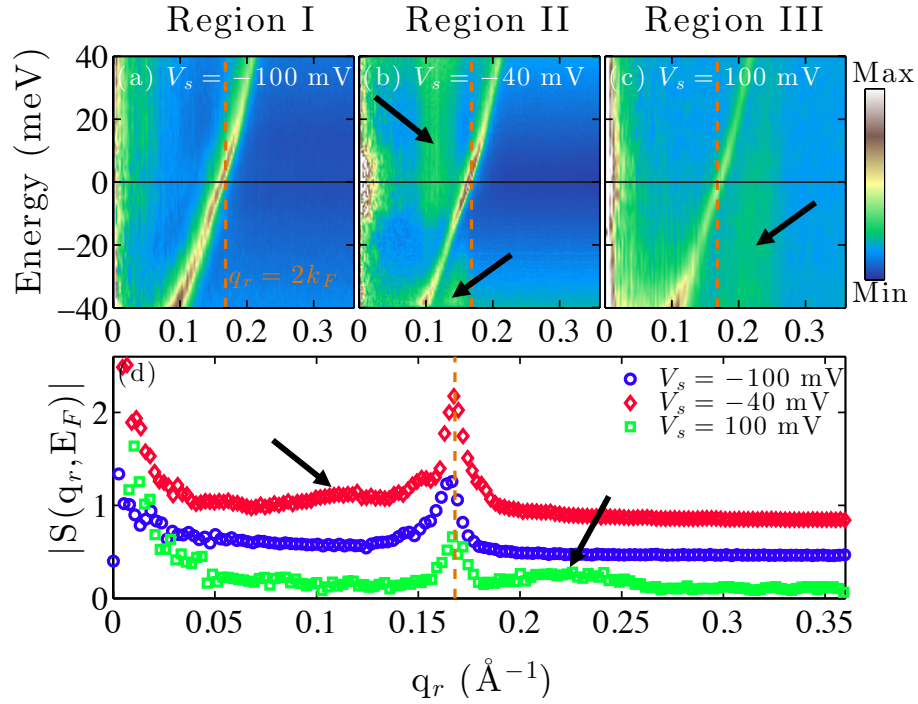


Figure 4.5: **Scattering dispersion calculated from three spectroscopic grids with different set-point conditions.** Horizontal and vertical lines indicate $E = E_F = 0$ meV and $q_r = 2k_F$ respectively. (a) No secondary features observed. (b) Broad non-dispersing feature above E_F and below $2k_F$. (c) Broad non-dispersing feature below E_F and above $2k_F$. (d) Radial projection of the FT-STIS signal at E_F for each grid. Imaging conditions match Figure 4.4.

mV. Neither of these areas included step edges, and so the observed QPI was driven primarily by the presence of carbon monoxide molecules scattering surface state electrons.

The FT-STIS data derived from the constant-current dI/dV maps were used to construct a scattering dispersion. A spectroscopic grid measurement with the same set-point current $I_s = 100$ pA and scattering-space resolution $\Delta q = 0.01$ \AA^{-1} was acquired for direct comparison between the two measurement modes. Figure 4.6 illustrates the scattering dispersion constructed from seventeen of the constant-current dI/dV maps and a grid with stabilization bias $V_s = 100$ mV (Region III). A comparison between these two measurement modes is particularly important, as they form the primary means of data acquisition in the FT-STIS literature, with constant-current dI/dV maps being more common [87–93, 96–98, 132, 196]. The constant-current dI/dV maps have lower energy resolution compared to grid measurements ($\Delta E_{maps} = 10.6$ meV vs $\Delta E_{grid} = 1.5$ meV) collected over the same time scale, due to the difference in the speed of data acquisition between the two measurement techniques mentioned in Chapter 2.

Both measurements show the expected parabolic dispersion of the surface state band, but differ in other features. The grid measurement shows significant intensity below the band onset at low- q_r . As determined previously in Grothe *et al.* [128, 132], the scattering intensity below the onset of the band is strongly dependent on the nature of the scattering impurities. The scattering intensity in this region varies in between measurements, regardless of acquisition mode, depending on whether the dominant scatterer is carbon monoxide, other impurities, or if there is significant intensity from step edge scattering that remains after filtering. This intensity below the band is therefore ignored to focus on features that vary only with the acquisition mode, ie. dispersive or non-dispersive FT-STIS features.

The grid measurement in Figure 4.6 (a) shows the same broad, vertical feature slightly above $\mathbf{q}_F = 2\mathbf{k}_F$, in agreement with Figure 4.5 (c). The appearance of the same feature during a different experimental run, including a different sample preparation and measured sample area, demonstrate the reproducibility of the observed features provided the set-point parameters remain the same. The measurements made by acquiring constant-current dI/dV maps at different energies, shown in Figure 4.6 (b), have an additional faint, and also broad feature appears that disperses, crossing $q_F = 2k_F$ at E_F . The constant-current dI/dV maps in Figure 4.6 (b) also show a strongly varying background intensity as a function of energy, strongest near the Fermi energy, that is not observed in the grid measurement. This varying background can be attributed to a change in signal intensity caused by variation in the tunnelling junction resistance. Though the set-point current was a constant $I_s = 100$ pA for all the acquired maps the stabilization bias V_s varied exactly with the bias being probed V_b .

Figure 4.6 (c) shows a comparison at a single bias $V_b = -40$ mV, where the primary surface state back-scattering feature occurs at the same q_r for both measurement modes but the secondary feature, indicated by the black arrows

for both measurement modes, does not. This clearly illustrates that acquiring the FT-STIS dispersion using different acquisition methods yields quantitatively different results.

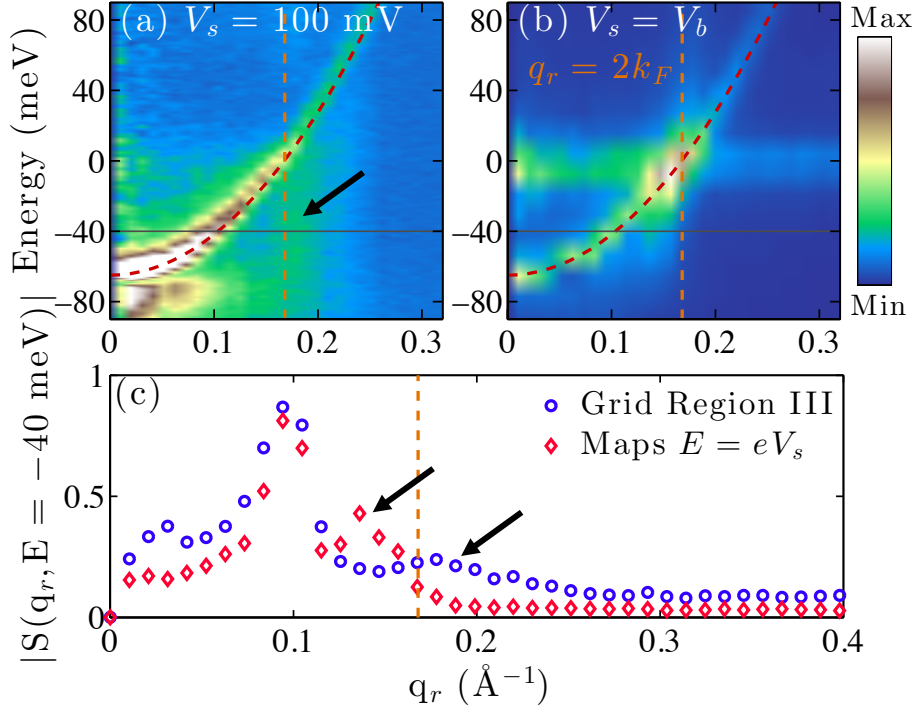


Figure 4.6: **Energy dispersion from spectroscopic grids and constant-current dI/dV maps.** Horizontal and vertical lines indicate $E = -40$ meV and $q_r = 2k_F$ respectively and the parabola represents a free electron model. (a) Spectroscopic grid with imaging conditions: 60×60 nm², 230×230 pixels. (b) Dispersion constructed from constant-current dI/dV maps with imaging conditions: 60×60 nm², 512×512 pixels. (c) The scattering intensity at -40 meV for both grid and map measurements scaled so that the surface state feature has the same intensity.

4.2.3 Constant-Height dI/dV Maps

Constant-height dI/dV maps, though experimentally more difficult to acquire, decouple the height of the tip set by the STM feedback from surface features that vary with lateral position. They are the acquisition mode least sensitive to effects caused by the values of the set-point parameters. A series of seven

constant-height maps was acquired over a bias range $V_b = (-90, 110)$ mV in order to compare the scattering intensity with constant-current dI/dV map results. The set-point current was $I_s = 150$ pA and the measured area was 65×65 nm² with no step edges observed. Reproducibility of the acquired FT-STs signal, independent of the detailed position of scattering centres, was checked by performing constant-height maps with identical acquisition parameters over two different areas at an acquisition bias of $V_b = 110$ mV. Like constant-current dI/dV maps, the stabilization bias in constant-height dI/dV maps is equivalent to the bias being measured V_b .

The energy resolution of the constant-height dI/dV map data is too low to effectively plot using a colour scale. Instead, a comparison of $|S(q_r, E)|$ between constant-height dI/dV maps and constant-current dI/dV maps at individual energies is plotted in Figure 4.7. In this figure, $|S(q_r, E)|$ curves at varying energies are plotted for both map acquisition modes, with offsets used to distinguish between curves and each curve scaled so that the surface state feature is the same strength. The constant-height dI/dV map data exhibits only one peak, corresponding to the expected scattering vector for the surface state band, at all values of V_b . The constant-current dI/dV maps exhibit secondary peaks shown by the black arrows, that below the Fermi energy are at larger q_r than the surface state peak but cross over above the Fermi energy to appear at lower q_r . The comparison between FT-STs intensity derived from constant-height dI/dV maps versus from constant-current dI/dV maps suggests that the secondary features are a result of the STM feedback changing the tip height during the measurement.

4.2.4 Comparison Between all Acquisition Modes

In order to make a more direct comparison between the different acquisition modes, FT-STs data were generated at the same energy, $E = 50$ meV, by the three different acquisition modes with four different set-point conditions: a grid with V_s corresponding to the same energy as the energy examined, $eV_s = E = 50$ meV, a grid with opposite polarity V_s from the energy examined, $eV_s = -E = -50$ meV, a constant-current dI/dV map where V_s always corresponds to the energy examined, $eV_s = E = 50$ mV, and a constant-height dI/dV map where the tip height is stabilized only at the first pixel of the image. The resulting $|S(q_r, E = 50 \text{ meV})|$ signals are shown in Figure 4.8. All four measurements exhibit a sharp peak at $q_r = 0.220 \pm 0.006 \text{ \AA}^{-1}$, corresponding to the intra-band scattering of the surface state at 50 meV. Away from this feature, the resulting signal varies significantly based on acquisition mode.

FT-STs of the grid with $V_s = 50$ mV produces a nearly identical signal to the FT-STs derived from the constant-current dI/dV map; this is expected if the additional feature is a set-point effect since the feedback is stabilized at each point with the same parameters for both measurements. Both exhibit a strong secondary feature just below the Fermi back-scattering vector $q = 2k_F$ (indicated by the black arrow) and otherwise are featureless, with the lowest levels of noise of the four measurements. The intensity $|S(\mathbf{q}, E = 50 \text{ meV})|$, plotted

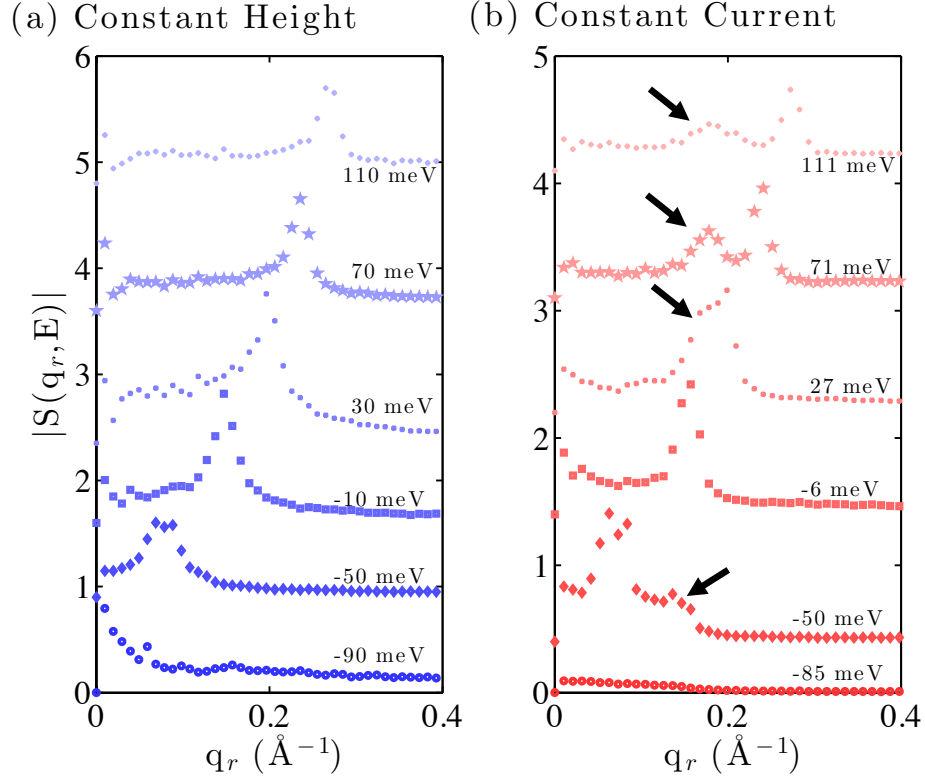


Figure 4.7: **Constant-height dI/dV maps compared with constant-current dI/dV maps and spectroscopic grids.** (a) Constant-height dI/dV map radial projections of $|S(\mathbf{q}, E)|$ show only the surface state feature. Imaging conditions: $65 \times 65 \text{ nm}^2$, 512×512 pixels. (b) Constant-current dI/dV maps show two features away from E_F . The imaging conditions for (b) are the same as in Figure 4.6.

in Figure 4.8 (b) and (d) for these two measurements, shows two concentric rings of intensity corresponding to the primary back scattering vector and the secondary feature.

For the grid acquired with $V_s = -50$ mV, while the surface state back scattering vector at $q_r = 0.22 \text{ \AA}^{-1}$ remains the same, there is now a much broader feature, shown by the red arrow, centred below $q_r = 2k_F$, and the feature seen with $V_s = +50$ mV is no longer observed. The constant-height dI/dV measurement has a larger low-frequency background with no clear secondary features. Each of the secondary features appear above the background level of the other line cuts, indicating that each are additional features tied only to the measurement mode and set-point parameters. The lack of any secondary features in the constant-height measurement, along with the dependence of the additional features on the bias used to stabilize the tip height at each position for grids and maps, provide further experimental evidence of the influence of the spatially varying tip height on the FT-STs measurement.

4.2.5 Experimental Conclusions

When the tip is stabilized at each pixel, a constant-current condition is met by the STM feedback circuit. That constant-current condition depends on the integrated density of states, convolved with the transmission function of the tunnelling junction. Since the density of states varies with both position and energy, the constant-current topography will contain spatial modulations due to the electronic structure that depend on the bias applied, modulating the physical tip-sample separation. As the dI/dV signal also depends on the tunnelling transmission probability, which depends on tip-sample separation, it is perhaps not surprising that extraneous features are observed in FT-STs that depend on the energy used to stabilize the tip height. This dependence of the FT-STs on the tip height explains the differences between grid and constant-current dI/dV map measurements: for a grid, only one stabilization bias is used for all energies probed, so a non-dispersing feature either above (positive V_s) or below (negative V_s) $2k_F$ is observed, but for constant-current dI/dV maps, the stabilization bias follows the energy being probed, generating a secondary feature that disperses.

The positions of the features observed in a grid measurement with $V = 100$ mV and a series of constant-current and constant-height dI/dV maps are shown in Figure 4.9 to summarize the potential set-point artifacts. Fits were performed by windowing the experimental line cuts around the peak feature, subtracting a linear background fit and then fitting the peak with either a Lorentzian, for the surface state peaks, or Gaussian functions, for the set-point dependent feature. Only one of every ten grid energies is plotted in Figure 4.9. For all three measurement modes the surface state peaks extracted from the data agree well with a free electron model of surface state scattering, reproducing the expected parabolic intra-band scattering dispersion. Fits to the STS grid data produce a vertical artifact feature, which appears at different scattering wave vectors above and below the Fermi level. The constant-current dI/dV maps generate a feature that disperses strongly below the Fermi level and then crosses the

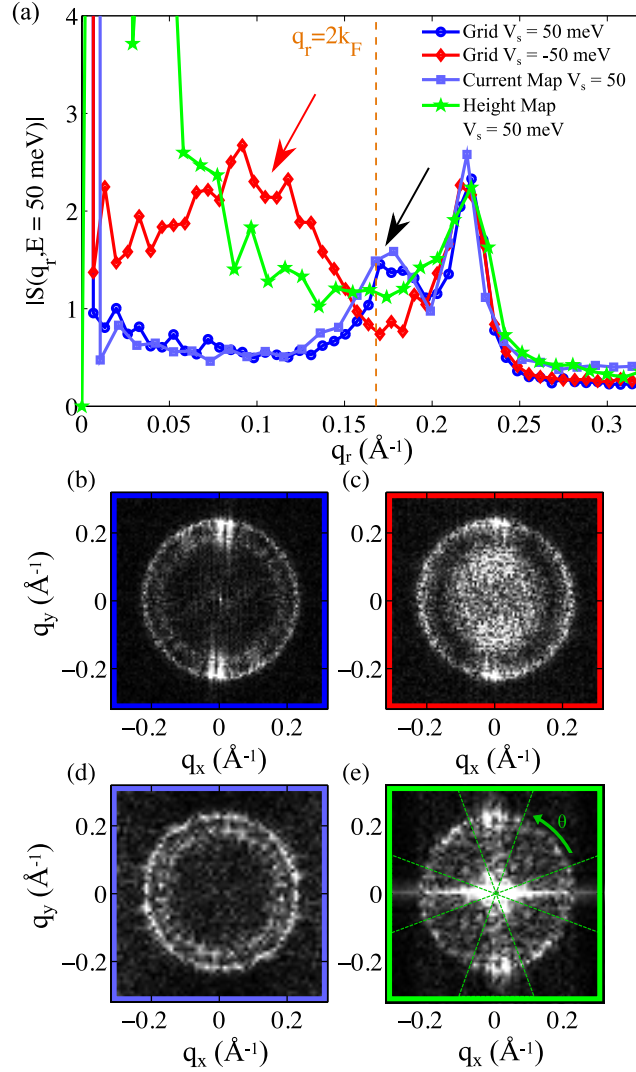


Figure 4.8: **The effect of stabilization bias on the observed FT-STIS pattern.** (a) $|S(q_r, E = 50 \text{ meV})|$ comparing two grids with different stabilization biases, a constant-current dI/dV map, and a constant-height dI/dV map. (b-e) the corresponding FT-STIS pattern at $E = 50 \text{ meV}$ from (b) a spectroscopic grid with $V_s = 50 \text{ mV}$, $I_s = 100 \text{ pA}$, (c) a spectroscopic grid with $V_s = -50 \text{ mV}$, $I_s = 100 \text{ pA}$, (d) constant-current map at $V_s = 50 \text{ mV}$, $I_s = 100 \text{ pA}$, and (e) a constant-height map at $V_s = 50 \text{ mV}$, and initial current $I_s = 100 \text{ pA}$. For the constant-height data a restricted \mathbf{q} -space angular filter was used to reduce the influence of a step edge running across the top of the image.

band dispersion at E_F . Above E_F this feature appears at roughly the same wave vector independent of the applied bias energy. The constant-height dI/dV maps showed no additional features beyond the surface state peak.

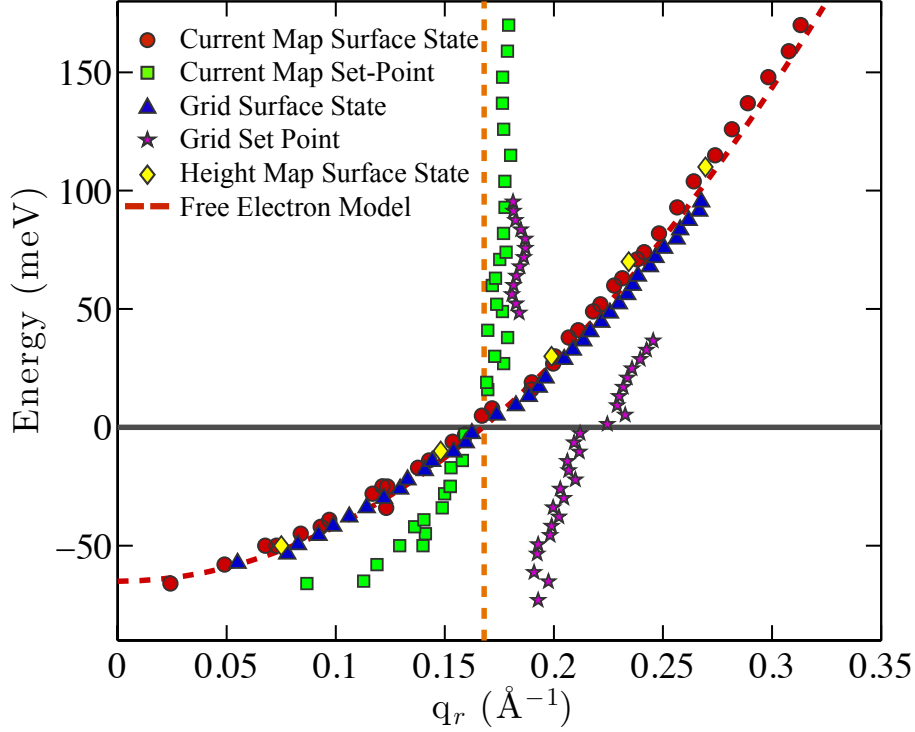


Figure 4.9: **Comparison of all features $|S(\mathbf{q}_r, \mathbf{E})|$ in different acquisition modes.** Vertical and horizontal lines indicate E_F and $q_F = 2k_F$ respectively. Only the constant-current maps show a strongly dispersing set-point peak. All three modes map out the surface state intensity, agreeing well with a free electron model.

The full-width half-maximum (FWHM) values resulting from the fits plotted in Figure 4.9 are plotted in Figure 4.10 as a function of the applied bias energy. The FWHM of the fits of the surface state peak, shown in (a), are smaller for all three measurement modes than for the set-point related features identified in (b) for constant-current dI/dV maps and the spectroscopic grid measurement. This trend is expected based on the line cuts plotted in Figures 4.5-4.8, as the surface state peak is always sharper and higher in amplitude than the set-point dependent feature, regardless of whether the mode of acquisition is constant-current dI/dV maps or spectroscopic grid.

As a function of energy the surface state peaks plotted in Figure 4.10 (a)

exhibit a similar FWHM, except near the band onset, where increases in the FWHM values correspond to broadening of the intra-band scattering peak. The FWHM of the set-point features plotted in Figure 4.10 (b) show that the set-point feature identified in grid measurements is broader below the onset of the band and the further away the energy is from the stabilization bias of $V_s = 100$ mV. For the constant-current dI/dV map fits the FWHM is largest near the band onset and then exhibits an increase as a function of increasing energy. This corresponds to a decreasing amplitude in the set-point peaks as the tunnelling energy is increased away from E_F , indicating a potential relationship between the number of energies in the sample being probed by the tunnelling current and the strength of the set-point peak in FT-STIS.

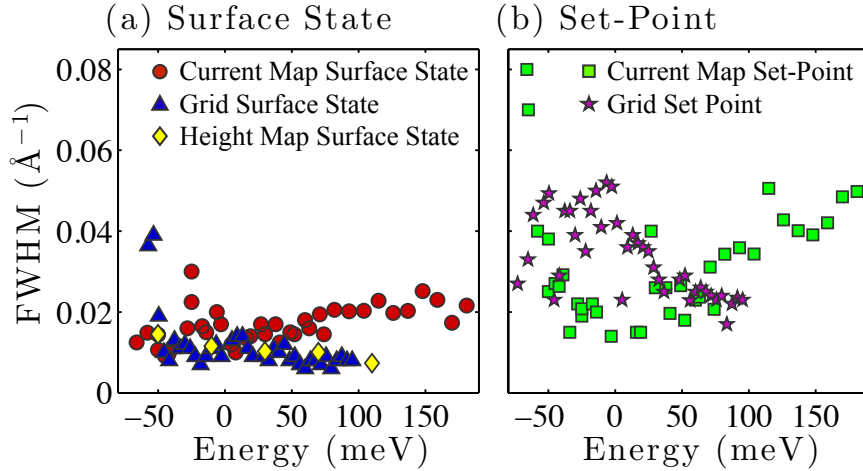


Figure 4.10: **Full-width at half-maximum of the fits for all features in $|S(\mathbf{q}_r, E)|$ in different acquisition modes.** (a) FWHM values resulting from fits of the surface state peaks in FT-STIS for all three measurement modes. (b) FWHM values resulting from fits of the set-point peaks in FT-STIS for constant-current dI/dV maps and spectroscopic grids.

The experimental data presented in Figures 4.4 through 4.10 demonstrates features in $|S(\mathbf{q}_r, E)|$ on Ag(111) that have a strong dependence on the acquisition mode used to acquire the differential tunnelling conductance. The next section will focus on theoretically modelling the tunnelling transmission probability, sample density of states, and acquisition modes in order to construct a model that can predict the observed features based on set-point parameters.

4.3 Modelling the Set-point Effect

4.3.1 Sample Density of States via T-matrix

An accurate model of the Ag(111) local density of states in the presence of impurities is necessary in order to model set-point effects in the various acquisition modes. Fortunately, a very detailed model of the Ag(111) surface state can be constructed with the help of scattering theory. Following Grothe *et al.* [132] the QPI scattering intensity from a single impurity, $|S(\mathbf{q}, E)| = |\delta\rho(\mathbf{q}, E)|$, can be obtained from the Fourier transform of the impurity-induced local density of states modulations

$$\delta\rho(\mathbf{q}, E) = -\frac{i}{2\pi} \sum_{\mathbf{k}} \text{Im}[G(\mathbf{k}, E)TG(\mathbf{k} + \mathbf{q}, E)]. \quad (4.2)$$

where $G(\mathbf{k}, E)$ is the bare Green's function and T is the T-matrix, which is taken to be

$$T = -V_0 \sin(\delta)e^{i\delta}, \quad (4.3)$$

where V_0 is the strength of the scattering potential produced by an impurity and δ is the scattering phase shift [132]. The scattering phase shift can be taken in two separate limits: $\delta \rightarrow \pi/2$ is the unitary limit of strong scattering while $\delta \rightarrow 0, \pi$ represents the Born or weak limit. For more details on the Green's function approach used here, including self-energy effects see Grothe *et al.* [128, 132].

A complicating factor in comparing the simulation results with experimental data is the presence of multiple types of scattering impurities in the experimental data, both step edges and carbon monoxide adsorbates, that have different scattering strengths. Bürgi [187] simulated step edges with a phase shift of $\delta \rightarrow 0$, corresponding to the Born limit, while Grothe [132] took the unitary limit of $\delta \rightarrow \pi/2$ when looking at carbon monoxide adsorbates and step edges, but used masking techniques to suppress the effects of the step edges. The QPI dispersion in scattering-space is strongly affected by the choice of δ .

Figure 4.11 shows how a total modulation in the density of states can be constructed by forming a linear combination of the Born and unitary scattering centres and optimizing the amplitudes in order to minimize the residuals between the theoretical QPI intensity and the experimental results from a spectroscopic grid. Rather than strictly unitary scattering at $\delta = \pi/2$, mixing Born and unitary character does the best job of capturing the peak shape, in agreement with Grothe [128]. The following ratio best replicates the experimental line shape at all energies

$$\delta\rho(\mathbf{q}, E)_{total} = 0.6\delta\rho(\mathbf{q}, E)_{\delta \rightarrow \pi/2} - 0.4\delta\rho(\mathbf{q}, E)_{\delta \rightarrow 0}. \quad (4.4)$$

As illustrated in Figure 4.11 (a) and (b) the expected scattering dispersion for a purely unitary scattering centre has pronounced differences compared with a purely Born scattering centre. For the purely unitary scattering centre, significant intensity is redistributed below the onset of the surface state band, similar to the intensity observed in the grid measurement of Figure 4.6 (a). This feature is completely absent for a purely Born scattering centre, which also has less intensity overall. Both scattering centres are capable of reproducing the surface state back-scattering associated with the Shockley surface state.

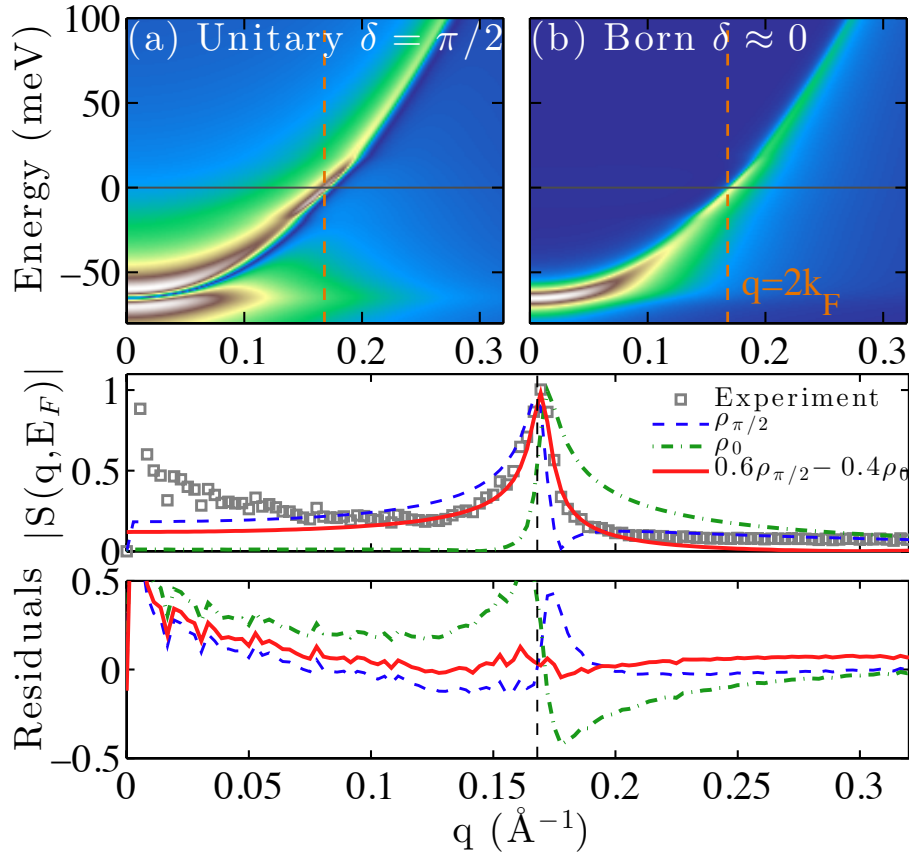


Figure 4.11: **Optimizing the scattering phase δ .** (a) Theoretical $|S(q_r, E)|$ intensity for a strong scattering impurity (b) Theoretical $|S(q_r, E)|$ intensity for a weak scattering impurity. (c) Comparison of theoretical $|S(q_r, E_F)|$ with experimental data from a spectroscopic grid. (d) Residuals of the theoretical $|S(q_r, E_F)|$ with the experimental data, the mix of two phases does the best job minimizing the residuals around the surface state peak.

After performing optimization of the scattering phase against experimental data sets, the calculated modulation in the local density of states $\delta\rho(\mathbf{q}, E)$ is used to seed calculations of the differential tunnelling conductance and expected $|S(\mathbf{q}, E)|$ intensity with different set-point parameters.

4.3.2 Analytic Set-Point Theory

T-matrix calculations provide a good approximation of the Ag(111) local density of states in the presence of a scatterer. However, a direct comparison between local density of states and the measured differential tunnelling conductance is not an appropriate comparison. Instead, the QPI pattern generated by an impurity must be interpreted in the context of a tunnelling measurement. This section calculates the tunnelling current, z -dependent tunnelling transmission probability, and other derived quantities with specific focus on isolating the set-point conditions V_s and I_s to allow for direct comparison with STM measurements.

As shown in Chapter 2, at low-temperature and positive applied bias, the tunnelling current $I_t = I(x, y, z, V_b)$ is

$$I_t(x, y, z, V_b) = \int_0^{eV_b} \rho(x, y, E) \rho_t(E - eV) T(z, E, V_b) dE. \quad (4.5)$$

When the set-point conditions are fulfilled by the feedback then $I_t = I_s(x, y, z_s, V_s)$ as follows

$$I_s(x, y, z_s, V_s) = \int_0^{eV_s} \rho(x, y, E) \rho_t(E - eV_s) T(z_s, V_s, E) dE, \quad (4.6)$$

where V_s is the stabilization bias and z_s is the tunnelling barrier gap that satisfies the set-point conditions. Following previous works [79, 80], the transmission tunnelling probability can be approximated using a trapezoidal tunnelling barrier and the WKB approximation to give

$$T(z_s, V_s, E) = \exp\left(-z_s \frac{2\sqrt{2m}}{\hbar} \sqrt{\phi + \frac{eV_s}{2} - E}\right), \quad (4.7)$$

where ϕ is the effective amplitude of the tunnelling barrier, E is the energy of the tunnelling electron, and m is the free electron mass. The effective tunnelling barrier can be calculated based on the average of the work function of the W tip ($\phi = 4.55$ eV) and the Ag sample ($\phi = 4.74$ eV) [81] to be $\phi = 4.65$ eV. In the low-bias approximation, Koslowski [197] let $T(z_s, V_s, E) \approx T(z_s)$. Inserting this into the right side of Equation 4.6 for I_s gives

$$I_s(x, y, z_s, V_s) = \int_0^{eV_s} \rho(x, y, E) \rho_t(E - eV_s) T(z_s) dE \quad (4.8)$$

or

$$I_s(x, y, z_s, V_s) = e^{\left(-z_s \frac{2\sqrt{2m\phi}}{\hbar}\right)} \int_0^{eV_s} \rho(x, y, E) \rho_t(E - eV_s) dE. \quad (4.9)$$

Equation 4.9 gives the condition necessary for the STM feedback to satisfy the set point current. Notably, it shows that this condition changes based on the lateral position of the tip over the sample because of potential lateral changes in magnitude of the local integrated density of states. If the sample local density of states is not featureless then the STM feedback will adjust the tip height as it scans, leading to different set point heights z_s at each pixel. Rearranging Equation 4.9 to solve for z_s gives

$$z_s(x, y, I_s, V_s) = -\frac{\hbar}{2\sqrt{2m\phi}} \ln \left(\frac{I_s}{\int_0^{eV_s} \rho(x, y, E) \rho_t(E - eV_s) dE} \right). \quad (4.10)$$

Equation 4.10 holds the key to understanding how the set-point parameters influence the FT-STs results differently for different acquisition modes. In grid acquisition $z_s = z(x, y, V_s, I_s)$ and is set by the feedback at each pixel based on the values of V_s and I_s . This makes the tip sensitive to lateral variations in the local density of states, but since V_s remains the same at every pixel this at most introduces a single spatial frequency corresponding to a non-dispersing feature in scattering-space. This feature appears at approximately the average of all scattering \mathbf{q} values between 0 and eV_s , as it is related to the integrated local density of states. This is not the case for constant-current dI/dV maps, where the stabilization bias is tied to the map energy E for each map. This means that $z_s = z(x, y, V_s = E/e, I_s)$ where V_s varies, changing the spatial features convolved into the differential tunnelling conductance measurement. Since z_s contains periodic spatial modulations at approximately the average of all q values between 0 and $V_s = E/e$, this leads to the presence of dispersing features in the FT-STs intensity. In contrast, constant-height dI/dV maps have no sensitivity to lateral variations of the local density of states. In a constant-height dI/dV map the tip height is set at one position, (x_s, y_s) , at the start of the map and then the feedback is disengaged, excluding the possibility of spatially dependent, feedback induced artifacts ie. $z_s = z(x_s, y_s, V_s = E/e, I_s)$.

Obtaining the contribution to the FT-STs intensity from set-point effects requires calculating the differential tunnelling conductance of the theoretically calculated tunnelling current while accounting for the effect of the set-point parameters. Taking the full derivative of the tunnelling current and assuming a constant tip density of states gives two terms with a z_s dependence [80]

$$\frac{dI_t(x, y, z_s, V_b)}{dV} \propto e\rho(eV_b)\rho_t(0)T(z_s) - \frac{\sqrt{2me}}{2\hbar\sqrt{\phi}}z_s I_t(z_s, V_b). \quad (4.11)$$

This expression puts particular emphasis on the role of the set point gap z_s . Previous works have studied the effect of z_s and $T(z_s)$ on the measured differential tunnelling conductance [69, 79, 81, 166, 197–199]. In all of these works it is made explicit that oscillations in dI/dV are not equivalent to oscillations in the sample local density of states ρ . The reason the two oscillations are not equivalent is that even though the tip is ostensibly ‘fixed’ at a tip–sample gap of z_s this height is a function of I_s and V_s which in turn are dependent on spatial variations in x and y of the local density of states and the tunnelling barrier. Analyzing term-by-term it is clear that in the first term of Equation 4.11 $\rho_s(eV)$ is weighted by $T(z_s)$, which varies exponentially with changes in z_s . The second term of Equation 4.11 contains a direct proportionality to z_s and I_t both of which can demonstrate oscillatory behaviour as a function of lateral position of the tip.

Comparison of the magnitude of the two terms of Equation 4.11 allows for identification of which term is the most relevant perturbation to the QPI signal of $\rho_s(eV)$. Taking the ratio of the first term to the second term indicates that the first term of Equation 4.11 is larger than the second term by approximately two orders of magnitude under typical experimental conditions. Therefore, the most suitable place to search for a modification to the QPI due to the stabilization bias effect is within the first term, focusing on any effects produced by the tunnelling transmission probability $T(z_s)$. This is in agreement with the approach taken by Li who concluded that for small applied bias integration over a small energy range led to oscillations in z_s [81]. Taken together with the QPI oscillations in ρ this leads to a ‘beating’ in the dI/dV signal. This phenomenon only occurs in the low bias regime $|V_b| < 1$ V. Burgi showed that this effect can be ignored when the bias is sufficiently high, as integration over a large number of frequencies results in a z_s that can be treated as constant as a function of spatial position [166]. This is not the case for the experimental measurements of Ag(111) presented here because the stabilization bias is too close to the Fermi energy.

Using these analytic results, the effect on the FT-STs pattern of the different measurement modes and their set-point artifacts can be simulated, expanding on previous work describing the effect of real-space oscillations of $T(z_s)$ in one-dimension [69, 80, 81, 197–199], in semi-conductors [82], and on molecules in two-dimensions [79].

4.3.3 Set-Point Simulations

The analytical framework built in the previous section allows each of the different STM acquisition modes to be simulated. Equation 4.2 was used to generate a modulation in the sample density of states due to a single impurity in scattering-space $\rho(\mathbf{q}, E)$ using T-matrix code written by S. Johnston. This modulation to

the local density of states was inverse Fourier-transformed into a modulation in the real-space density of states $\rho(\mathbf{r}, E)$ and used to calculate $z_s(x, y, I_s, V_s)$, $T(z_s)$, $I(x, y, z_s, V_s)$, and $dI_t(x, y, z_s, V_b)/dV$ under different set-point conditions from the analytic expressions derived in the previous section. $T(z_s)$ and $dI(x, y, z_s, V_s)/dV$ were then Fourier transformed back into scattering-space and compared with the original local density of states modulation, $\delta\rho(\mathbf{q}, E)$.

Grid with set-point in Region I

Figure 4.12 simulates the case of a spectroscopic grids measurement with stabilization bias below the band onset in Region I. Figure 4.12 (a) shows the modulated local density of states $|\delta\rho(\mathbf{q}, E)|$ with the scattering phase detailed in Section 4.3.1. The corresponding tunnelling transmission probability shown in Figure 4.12 (b) does not show any particularly sharp features but has a higher intensity before $q_r = 2k_F$. The simulated FT-STs intensity in Figure 4.12 (c) is qualitatively very similar to the local density of states, with the largest difference being a slight redistribution of intensity below the band onset. The simulated result agrees well with the experimental data in Figure 4.12 (d), both are free of spurious set-point features that could be confused as an additional scattering vector.

Grid with set-point in Region III

Figure 4.13 simulates a spectroscopic grid with stabilization bias above the Fermi energy, in Region III. The best experimental data for this set point had a predominantly unitary character, as a result the modulation in local density of states in Figure 4.13 (a) was calculated with a scattering phase equal to that of a unitary scatterer $\delta = \pi/2$. The tunnelling transmission probability in Figure 4.13 (b) shows the strongest intensity at just above $q_r = 2k_F$ and is constant as a function of energy. The simulated FT-STs intensity in Figure 4.13 (c) has significant intensity running vertically below the surface state band scattering just above $q_r = 2k_F$. This feature is not present in the modulated local density of states. The simulated result agrees well with the experimental data in Figure 4.13 (d): both exhibit high intensity below the band onset attributable to the unitary nature of the scattering centre(s). They also share a secondary feature, the vertical intensity at $q_r = 2k_F$ below the Fermi energy, that is not present below the band onset. The simulations suggest that this feature in the experimental data is caused by modulations in the transmission tunnelling probability $T(z_s)$ and not the sample local density of states.

Constant-current dI/dV maps

Figure 4.14 simulates the constant-current dI/dV map acquisition mode. The behaviour of the transmission tunnelling probability $T(z_s)$ is markedly different than for the case of the two grid measurements. It is strongly peaked along E_F and has a complicated dispersing structure away from E_F . Its lowest intensity feature runs along the scattering vector expected for the surface state

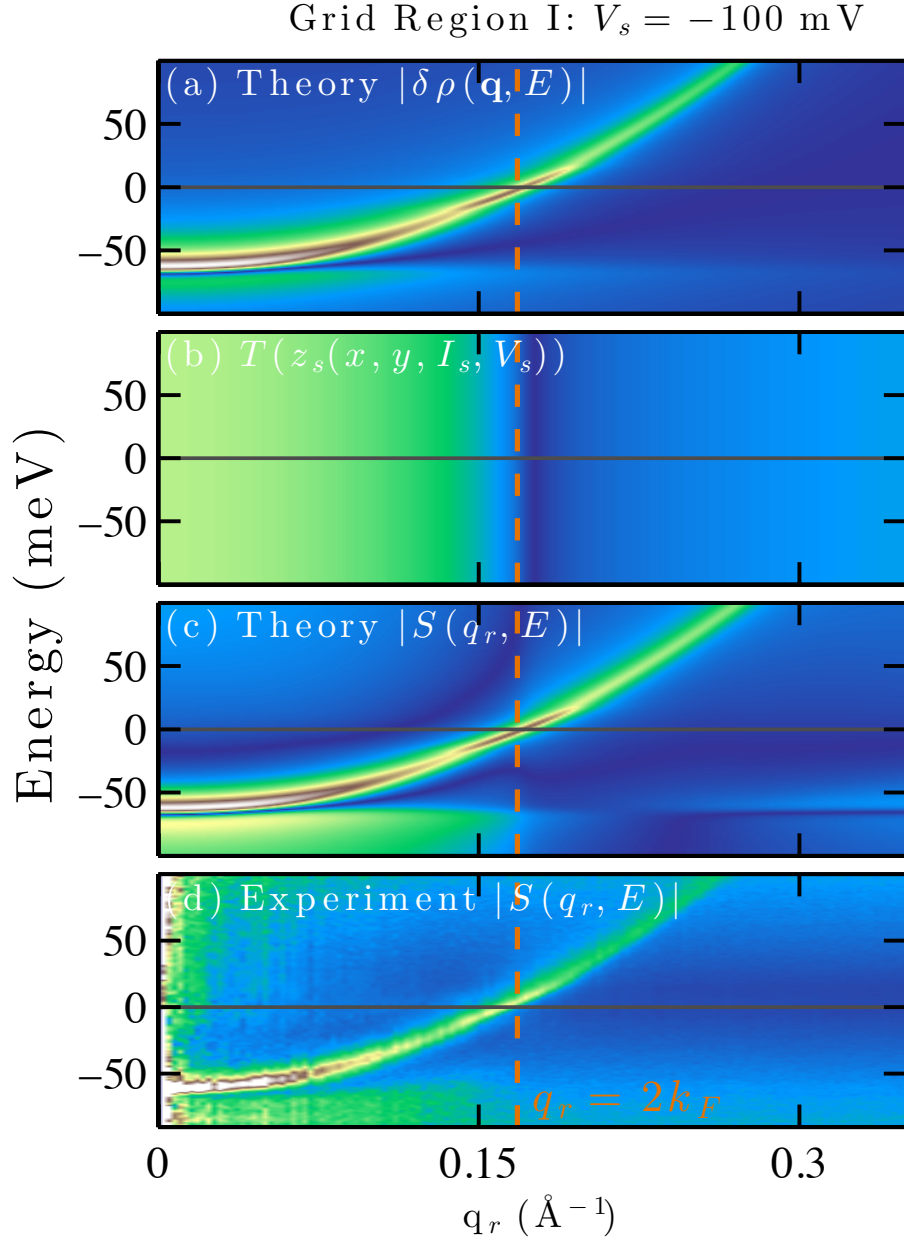


Figure 4.12: **Simulation of a grid with stabilization bias $V_s = -100$ mV.** (a) Simulated $|\delta\rho|$ in scattering-space. (b) The calculated $T(z_s)$ of this $|\delta\rho|$ with $V_s = -100$ meV stabilization bias. (c) The product of $|\delta\rho|$ with $T(z_s)$ gives the first term in Equation 4.11 (d) Experimental grid data with stabilization bias $V_s = -100$ mV.

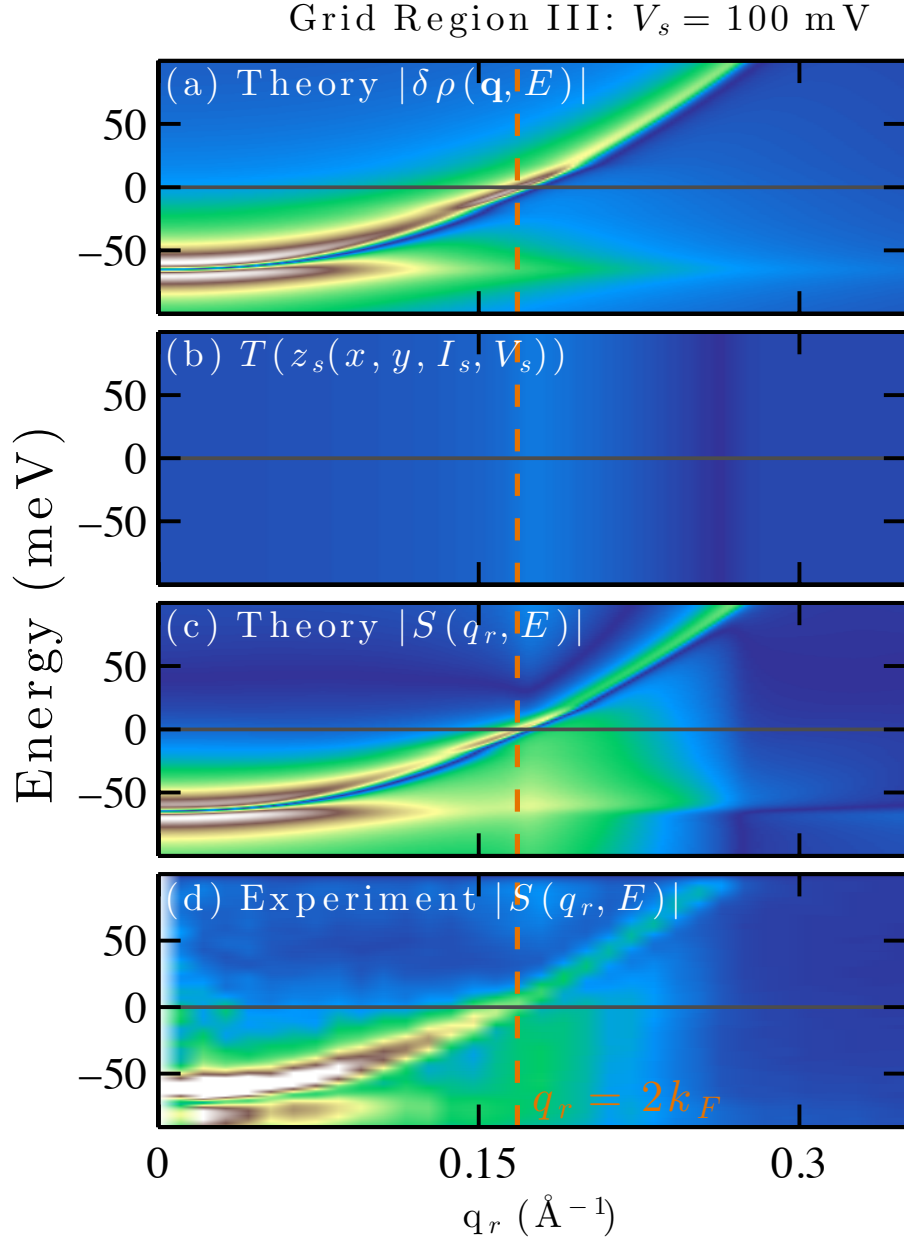


Figure 4.13: **Simulation of a grid with stabilization bias $V_s = 100$ mV.** (a) Simulated $|\delta\rho|$ in scattering-space. (b) The calculated $T(z_s)$ of this $|\delta\rho|$ with $V_s = 100$ meV stabilization bias, (c) The product of $|\delta\rho|$ with $T(z_s)$ with $V_s = -100$ meV stabilization bias. (d) Experimental grid data shown with stabilization bias $V_s = 100$ mV.

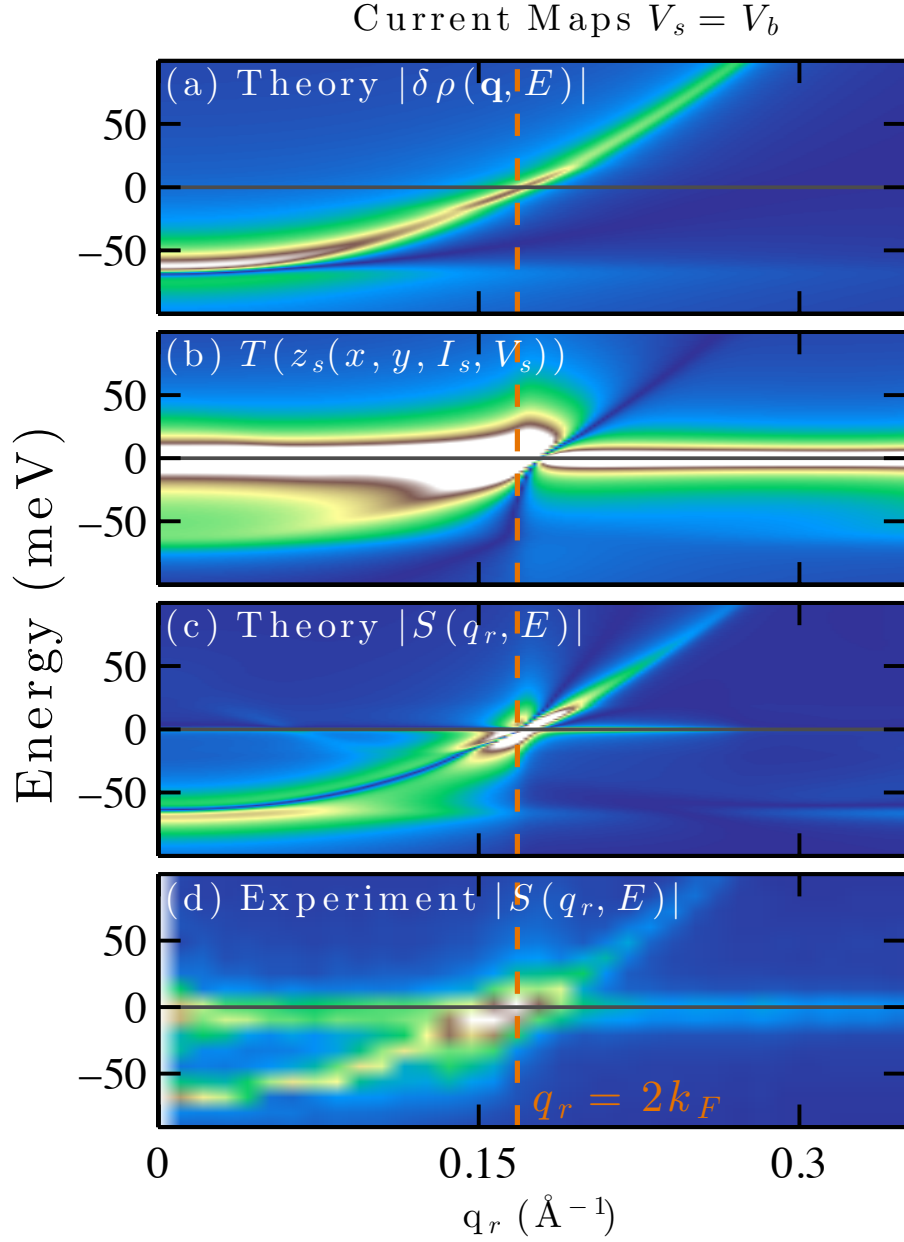


Figure 4.14: **Simulation of constant-current dI/dV maps.** (a) Simulated $|\delta\rho|$ in scattering-space. (b) The calculated $T(z_s)$ of this $|\delta\rho|$ for a stabilization bias that matches the bias being probed $V_s = V_b$. (c) The product of $|\delta\rho|$ with $T(z_s)$. (d) Experimental FT-STIS from constant-current dI/dV maps.

intraband scattering. The product of the modulated density of states $|\delta\rho|$ with this transmission function produces a scattering intensity that has a sharp peak in intensity at E_F , a strong back scattering intensity, and a set of secondary dispersing features that are different than the scattering intensity associated with the band. Though the energy resolution of the experimental data makes a direct comparison of features difficult, there is good qualitative agreement between the features observed in theory in Figure 4.14 (c) and the experimental constant-current dI/dV maps in Figure 4.14 (d).

Constant-height dI/dV maps

Constant-height dI/dV maps are the one acquisition mode that should remain unaffected by modulations in the tunnelling barrier probability caused by the STM feedback responding to the presence of QPI in the local density of states. Figure 4.15 shows the simulated $|S(q_r, E)|$ for three different acquisition modes: constant-height dI/dV maps, constant-current dI/dV maps, and a spectroscopic grid with stabilization bias above the band onset in Region III. This can be compared to the experimental data in Figure 4.7. As in the experimental constant-height dI/dV maps the only feature observed when the tip height is not adjusted by the feedback is that due to the intra-band scattering of quasiparticles across the surface state band. In both the constant-current dI/dV maps and spectroscopic grid simulations a secondary peak is clearly visible that crosses over with the surface state peak at E_F , as indicated by the black arrows. Qualitative agreement with the experimental data is again very good. Quantitative agreement with the experimental line cuts is not expected, as the T-matrix theory used to generate the theoretical local density of states takes only a single impurity scattering centre, while the experimental data features many different scattering centres, with potentially varying scattering phases³.

Figures 4.12-4.15 show that the secondary feature observed in certain FT-STs measurement modes can be reproduced by modelling the effect of the set-point parameters, particularly the stabilization bias V_s . The most striking feature due to this effect appears in FT-STs of constant-current dI/dV map data, where a secondary dispersing feature appears that crosses the surface state dispersion at E_F . The best measurement modes to avoid set-point artifacts, caused by modulations in $T(z_s)$, are spectroscopic grids with stabilization biases below the surface state onset and constant-height dI/dV maps. Given the experimental challenges associated with the acquisition of constant-height dI/dV maps it is likely that spectroscopic grids would be the preferred acquisition mode in most scenarios. For any subtle features observed in FT-STs data in which only constant-current dI/dV map acquisition is possible, it would be wise to attempt constant-height acquisition at at least a few energies, to rule out set-point related artifacts.

³For a simulation of multiple scattering centres in real-space see Appendix B.

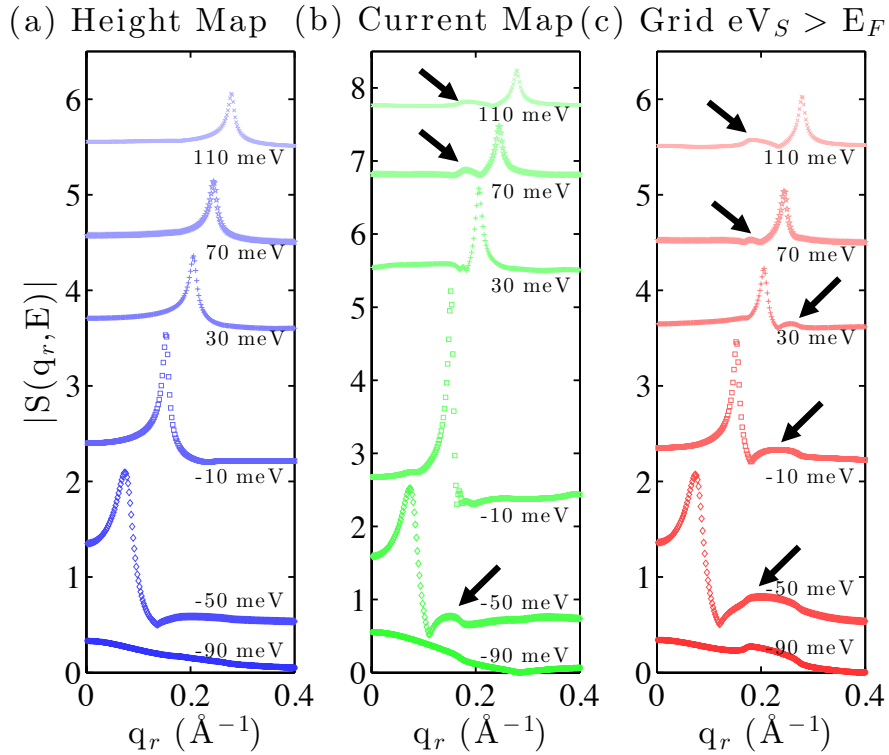


Figure 4.15: $|S(\mathbf{q}_r, E)|$ comparison between simulated constant-height maps, spectroscopic grids, and constant-current maps. (a) Simulated constant-height dI/dV maps at $I_s = 100$ pA show only the surface state feature. (b) Simulated constant-current dI/dV maps at $I_s = 100$ pA show a dispersing secondary feature. (c) Simulated spectroscopic grid data with $V_s = 100$ mV, $I_s = 100$ pA shows a non-dispersing secondary feature.

4.4 Conclusions

The comparison of the set-point simulations with the experimental data shows that the dominant factor yielding experimental artifacts in the FT-STIS arises from the contribution of the tunnelling transmission probability $T(z_s)$ to the differential tunnelling conductance. This is in agreement with the early work performed in real-space by Hörmandinger [198, 200], Ukraintsev [69], and Li [81], who realized that in attempting to extract the local density of states from the differential tunnelling conductance, the effect of the tunnelling transmission probability cannot be ignored. In the combined dI/dV simulation of the FT-STIS dispersion the main features introduced by modulations in $T(z_s)$ are as follows: for grids with a V_s above E_F there is a vertical, non-dispersing line above $2k_F$, for grids with a V_s below the onset of the band there is a weak very broad non-dispersing feature in $T(z_s)$ with little influence on the $S(q_r, E)$, and for the series of constant current dI/dV maps there is a dispersing feature which crosses $2k_F$ at E_F . The constant-current maps also show an overall increase in intensity near E_F arising from strong variations in $T(z_s)$.

In summary, artifact features in FT-STIS derived dispersions on Ag(111) can occur that depend on the momentum-space conditions used to stabilize the tip height; as demonstrated through a combination of measurements in different acquisition modes, and simulations of the expected FT-STIS patterns for these modes. Simulations show that this arises from spatial modulations in the transmission function due to variations in z_s at each (x, y) pixel that are dependent on the set-point conditions. This effect is most pronounced, and most concerning, for measurements acquired by taking dI/dV maps with a simultaneous constant-current feedback at each energy, which produces a relatively strong dispersing feature.

As mentioned at the outset of this chapter, dispersing features with similar \mathbf{q} -dependence have been observed on (111) noble metal surfaces using constant-current maps and attributed to a number of different sources [113, 180, 181]. Most recently, Sessi *et al.* [113] demonstrated that the secondary dispersion is not compatible with the position of the bulk bands in Au(111), Cu(111), or Ag(111) and instead attributed the secondary features to an acoustic surface plasmon dispersion [113]. Work presented in this chapter casts doubt on this conclusion, a feature following this same dispersion arises from an artifact of the constant-current measurement mode, which was the measurement mode used in the main results of Sessi's work. Since the set-point effect due to modulation of the tunnel barrier is not present in constant-height dI/dV maps a secondary dispersing feature is not predicted to appear in dispersions constructed from constant-height data. However, a secondary feature was observed by Sessi on Cu(111) at energies $E = \pm 250$ meV and reported in the supplementary material of their work [113]. To address this concern and to show the broader applicability of the results presented here to other (111) noble metals the next section will focus on FT-STIS acquired on Cu(111).

Chapter 5

Characterization of the Cu(111) Surface with Multiple FT-STs Acquisition Modes

An experiment is reproducible
until another laboratory tries to
repeat it.

Dr. Alexander Kohn [201]

Like Ag(111), Cu(111) possesses a Shockley surface state with a free electron-like dispersion. The Cu(111) surface state has been studied using the FT-STs technique and secondary features have been observed in constant-height dI/dV maps [113], features not observed in Ag(111). This chapter presents FT-STs data of the Cu(111) surface taken using spectroscopic grids, constant-current maps dI/dV maps, and constant-height dI/dV maps. A comparison between the acquisition modes allows for identification of the set-point effects and isolation of FT-STs features that cannot be attributed to the modulation of the tunnelling transmission probability.

5.1 Characterizing the Set-Point Effect in Cu(111)

5.1.1 The Cu(111) Surface State

A (111)-terminated copper surface supports the existence of a Shockley surface state, which has been thoroughly characterized by ARPES and STM [8, 12, 113, 165–167, 190, 193, 198, 202, 203]. Close to the Fermi energy, this surface state forms a parabolic band in \mathbf{k} -space well modelled by Equation 4.1, with a chemical potential $\mu = 420$ meV [190], but roughly the same effective electron mass as the band in Ag(111) [190]¹. Cu(111) shares the same crystal structure

¹Low temperature values measured for the effective mass range from $m^* = 0.38$ – 0.46 while the band onset has been measured anywhere from $\mu = 420$ – 440 meV [8, 167, 190, 198, 203].

as Ag(111) with a lattice constant of $a_0 = 0.361$ nm [186], giving an atomic spacing of on the (111) surface of $a_0\sqrt{2}/2 = 0.212$ nm.

The sample preparation and measurement details for data acquisition on Cu(111) followed the same protocols used for Ag(111). All measurements were performed using the CreaTec at a temperature of $T = 4.5$ K. The Cu(111) crystal was prepared via three cycles of sputtering and annealing. The annealing temperature was raised to 600°C due to the higher melting temperature of copper. This preparation procedure produced large, flat terraces with a low density of surface impurities. Impurities that were present were likely either CO molecules or sulphur atoms. Contact and sharpening of the STM tip on the Cu(111) surface likely resulted in a copper terminated tip.

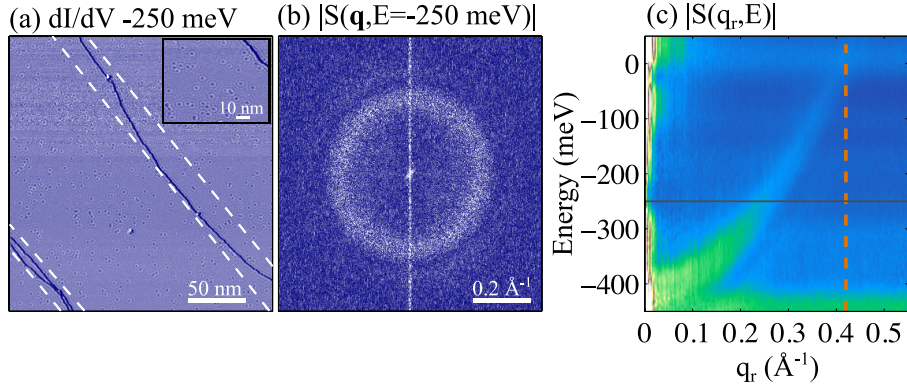


Figure 5.1: **Spectroscopic grid measurement of Cu(111)** (a) The differential tunnelling conductance exhibits two step edges and a number of tip changes, corresponding to the higher degree of noise in the top half of the image. The inset at top right shows oscillations around individual point defects and a step edge. (b) FT-STs shows the expected intra-band scattering intensity. (c) The scattering dispersion of the entire surface state band. Vertical line denotes $q_F = 2k_F = 0.42 \text{ \AA}^{-1}$ and horizontal line shows $E = -250$ mV for reference to (a) and (b). Imaging conditions: $V_s = -520$ meV, $I_s = 150$ pA, 325×325 pixels.

Stability issues between the STM tip and sample prevented the acquisition of spectroscopic grids without tip changes due to mechanical issues in the CreaTec STM head. This resulted in a higher degree of background noise in the grid measurements for Cu(111) than those presented for Ag(111). This higher noise level did not affect the ability to identify the surface state band from QPI, as shown in Figure 5.1. This figure shows data from a spectroscopic grid over a $250 \times 250 \text{ nm}^2$ area of the Cu(111) surface. The grid set-point voltage is $V_s = -520$ meV, below the onset of the surface state band. The differential tunnelling conductance at -250 mV in Figure 5.1 (a) shows two step edges and a multitude

of scattering centres sitting on large terraces. The FT-STs pattern exhibits a ring of intensity with a \mathbf{q} value that matches that expected from Equation 4.1. The vertical line of intensity in the centre of the FT-STs image results from the tip changes present in the image of the differential tunnelling conductance. STM tip changes in the image of the dI/dV data can be identified as spikes in intensity associated with the fast scan direction, causing an effect that resembles static noise. The Fourier transform of the noise associated with the tip changes is the vertical line observed in Figure 5.1 (b). The surface state dispersion from the onset, at approximately $\epsilon(0) = -420$ meV, to the Fermi energy is shown in Figure 5.1 (c) and fits the expected parabolic dispersion. No set-point artifact features are readily apparent, as expected for a grid measurement with stabilization bias below the band onset.

5.1.2 Measured Set-Point Effects in Cu(111)

As in Ag(111), spectroscopic grids were measured with different set-point parameters. Figure 5.2 shows a comparison between two spectroscopic grids, one with the stabilization bias above the Fermi energy $eV_s > E_F$ and one with the stabilization bias below the surface state onset $\epsilon(0) > eV_s$. The dispersing feature that appears in both data sets is the expected intra-band scattering intensity. A secondary feature is present at a constant \mathbf{q} just above $q_F = 2k_F$ for the grid with stabilization bias above E_F . This is analogous to the feature observed in Ag(111) in Figure 4.5 (c) and serves to confirm the set-point model's results in Cu(111) grids. As in Ag(111), the grid with $eV_s < \epsilon(0)$ shows no set-point related artifacts. The higher intensity at low- q_r in Figure 5.2 (b) compared to Figure 5.2 (a) is due to the presence of a number of step edges.

Constant-current dI/dV maps of the Cu(111) surface were measured to further demonstrate set-point artifacts in the measurement of surface state bands. Based on the model constructed for Ag(111) the constant-current dI/dV maps were predicted to show a dispersing set-point artifact below the E_F that becomes non-dispersing and approximately tracks the q_F value above E_F . This prediction was confirmed by the experimental data shown in Figure 5.3 (b). Two peaks are visible at every energy measured, one behaving as predicted by set-point theory and one following the expected surface state dispersion of Equation 4.1.

The final measurements of Cu(111) were performed using the constant-height dI/dV map acquisition mode. Based on the measured results in Ag(111) the expectation was that only the surface state peak would be visible. However, previous work by Sessi *et al.* [113] had measured a weak secondary feature in addition to the surface state band dispersion at $E = \pm 250$ meV.

At low tunnelling currents ($I_s \leq 300$ pA) the constant height measurements demonstrated only one peak, in agreement with the constant height dI/dV map results on Ag(111). However, Equation 4.11 contains a secondary term which is current dependent, which is present independent of the acquisition mode. Although it had been shown that this term did not contribute in a measurable way to Ag(111) measurements, it has had an impact on differential tunnelling

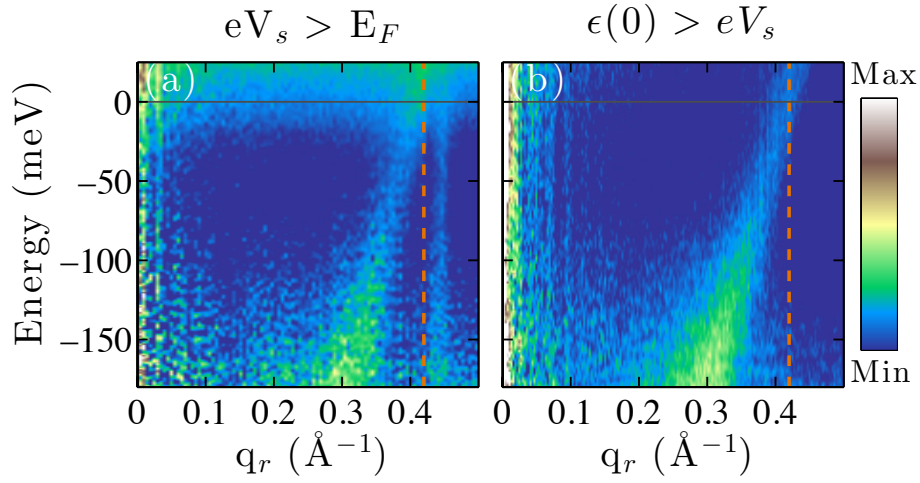


Figure 5.2: **Set-point effects in grids on Cu(111).** (a) A spectroscopic grid measurement exhibits a secondary non-dispersing feature just above the Fermi scattering vector $q_F = 2k_F$. Imaging conditions: $V_s = 30$ meV, $I_s = 150$ pA, 124×124 nm, 176×176 pixels. (b) A spectroscopic grid with stabilization bias below the band onset shows no secondary features. Imaging conditions: $V_s = -520$ meV, $I_s = 150$ pA, 225×225 nm, 325×325 pixels.

conductance measurements of two-dimensional electron gases in semi-conductors [82, 204]. As Sessi measured constant height dI/dV maps at higher current it was necessary to rule out this effect.

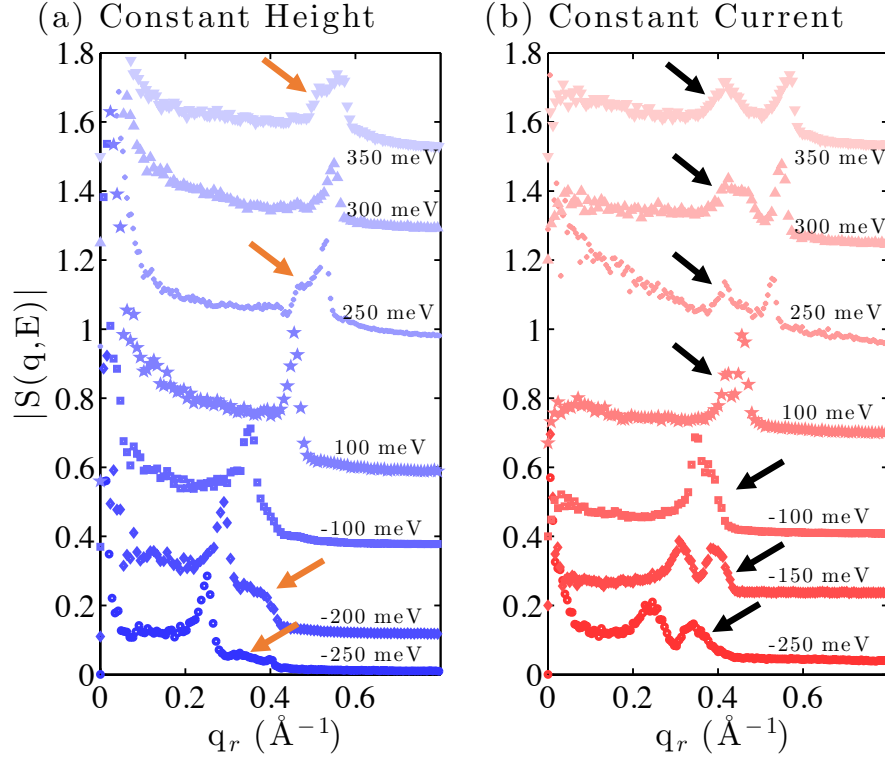


Figure 5.3: **Constant height and constant current dI/dV maps of Cu(111).** (a) $|S(q_r, E)|$ extracted from constant height dI/dV maps over areas ranging from 80 – 140 nm in length at $I_s = 900$ pA. (b) $|S(q_r, E)|$ extracted from constant current dI/dV maps over areas ranging from 80 – 140 nm in length. $I_s = 900$ pA.

At tunnelling currents centred around 1000 pA the constant-height dI/dV maps exhibited a secondary dispersing feature, indicated by the orange arrows in Figure 5.3 (a). This feature was weaker than the set-point peak seen in constant current dI/dV maps and exhibited roughly the same dispersion below E_F . However, above E_F this feature continued dispersing with the surface state band and did not remain at q_F like the set-point feature. This feature is visible in the constant height map data in Figure 5.3 in addition to the expected surface state peak. In order to acquire constant height dI/dV maps at such high currents the data acquisition was changed to re-engage the feedback momentarily at the end of every line of the tip fast scan axis. This ensured

tip stability throughout the measurement without allowing feedback induced modulations of $T(z_s)$.

5.2 Discussion and Outlook

Measurements of spectroscopic grids, constant current dI/dV maps, and low tunnelling current constant-height dI/dV maps confirmed the validity of the set-point model of FT-STs features on the noble metal surface states. As in Ag(111) grid measurements with stabilization bias above the band onset exhibited non-dispersing artifacts in the scattering intensity of the surface state. Data on Cu(111) from constant-current dI/dV maps demonstrated an artifact that disperses below E_F and remains roughly constant at q_F above E_F , just as in Ag(111).

Constant height dI/dV maps provided the first surprising result not observed in the analysis of the Ag(111) data. At high currents a new secondary dispersing feature was observed not seen in the other measurement modes. As the measurement of QPI by constant-height dI/dV maps is set-point independent this feature may be attributable to physics of the Cu(111) and not that of the tunnelling transmission probability. This feature may be the effect of the second term in Equation 4.11, though order of magnitude calculations in the set-point theory model indicate that this term would need an order of magnitude enhancement compared to the first term in order to be experimentally accessible.

Interestingly, this feature appears to follow the dispersion of an acoustic surface plasmon (ASP) as predicted theoretically by Sessi. Sessi's experimental measurements, acquired using constant current dI/dV map acquisition, show two features in Cu(111), the expected surface state peaks and a second peak, which they identify as a signature of the predicted ASP. However, comparing their measurements to constant-current dI/dV maps taken at the LAIR, as is done in Figure 5.4, the secondary feature in their data agrees better with the set-point feature in constant current dI/dV maps than the predicted ASP feature. In particular, above the Fermi energy both constant-current dI/dV secondary features become non-dispersing, while the ASP prediction continues to disperse with the surface state back-scattering intensity. This causes their theoretical prediction to deviate from their experimental data, and this may be because the surface state peak is masking any sign of the acoustic surface plasmon peak above E_F . By measuring in constant height mode, as shown in Figure 5.3 (a), the set-point feature is suppressed and it is possible to measure a secondary feature that continues dispersing above E_F . This secondary feature should also be visible in high-current grid measurement with stabilization bias below the band onset, but due to the transient nature of the STM tip stability on this surface such a grid could not be acquired. The constant-height secondary feature was also more difficult to observe than the previously observed set-point features, with not every FT-STs measurement demonstrating a peak, even at high tunnelling currents.

Figure 5.4 shows the extracted maxima of intensity for the surface state, set-point, and possible acoustic surface plasmon features observed experimentally on Cu(111), for both this work and Sessi *et al.* Figure 5.4 (b) also shows the theoretically predicted dispersion of the acoustic surface plasmon. This shows that the feature seen in constant height maps in Figure 5.4 (a) is a better candidate for the acoustic surface plasmon mode than the one seen by Sessi in constant current maps. More work, both theoretical and experimental, is needed to verify this. If it is truly a feature of the Cu(111) then it should also be a detectable feature in a high resolution grid with set-point below the band onset and if it is a universal feature of noble metal surface states then it should appear in Ag(111) constant height dI/dV maps at higher tunnelling currents.

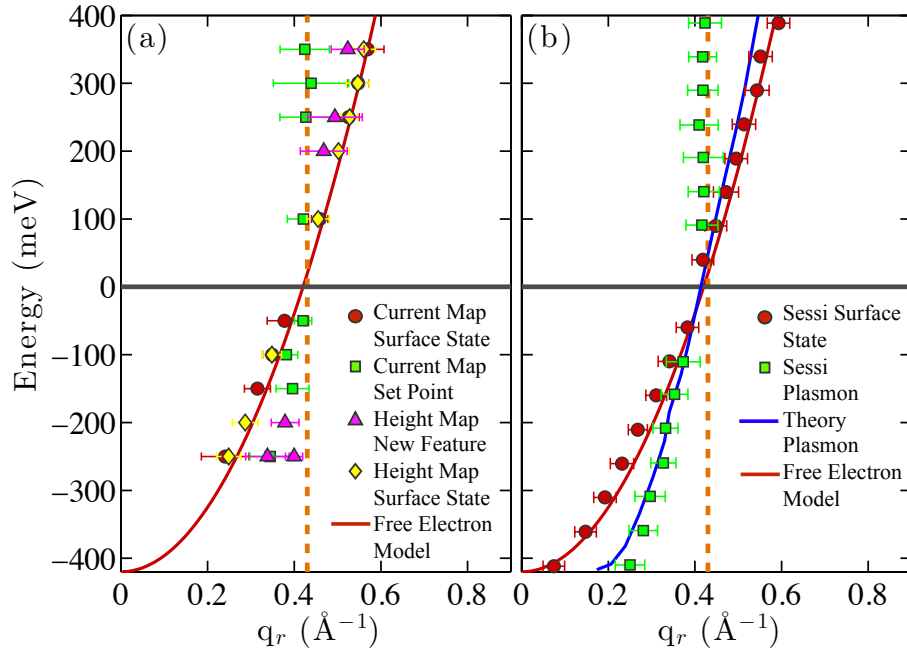


Figure 5.4: **Comparison of Cu(111) dispersing features with Sessi *et al.*** [113] Vertical and horizontal lines indicate E_F and $q_F = 2k_F$ respectively. (a) Peak maxima extracted from constant current and constant height maps both show the surface state dispersion in good agreement with a free electron model from Equation 4.1. The constant-current dI/dV maps show the set-point feature while constant-height dI/dV maps exhibit a previously unobserved feature. (b) Constant-current dI/dV maps by Sessi map out the surface state dispersion. The theoretical dispersion of an acoustic surface plasmon agrees well with secondary features below E_F but deviates above.

This chapter has provided a detailed look at the features observed in FT-STS data on the surfaces of Ag(111) and Cu(111). By developing a set-point theory of the data acquisition that linked the experimental set-point parameters with the modulation of the tunnelling barrier gap in each acquisition mode it was demonstrated that artifacts will be introduced that are roughly constant for grid measurements with stabilization bias' above the band onset and dispersing for constant current maps. This has implications for measurements of FT-STS in any system that exhibits QPI. As a general rule, if apparent height measurements exhibit QPI signatures then it should be expected that modulations in $T(z_s)$ will have a signature in the dI/dV . This can either be taken into account by acquiring data using multiple different acquisition modes or using an appropriate normalization scheme [82, 204, 205].

In grid measurements of the noble metals a choice of stabilization bias below the onset of the band showed a very weak influence with no distinct features, providing a way to avoid these effects without resorting to demanding constant height measurements, or a more elaborate program of returning the tip to the same location to reset the height for each measurement pixel, as has been done for AFM measurements [206]. These results urge caution in the field; features in QPI require careful consideration, and artifacts can arise depending on the measurement mode that may obscure or masquerade as physical processes in the sample.

Part III

Magnetic Sensing and Control of Single Atoms on MgO

Chapter 6

Electron Spin Resonance Scanning Tunnelling Microscopy

All of physics is either impossible or trivial. It is impossible until you understand it, and then it becomes trivial.

Ernest Rutherford

Spin resonance provides the high-energy resolution needed to examine biological and material structures by sensing weak magnetic interactions [207]. By pairing electron spin resonance techniques with scanning tunnelling microscopy, researchers at IBM have developed an experimental tool with the spatial resolution of the STM and energy resolution of ESR. The ESR-STM technique relies on the use of microwave bias pulses to resonantly excite the spin state of an iron atom sitting on the surface of magnesium oxide. The spin state of the iron atom is probed by a spin-polarized STM tip. In this chapter the basis of this technique will be explored in preparation for its use in Chapter 7.

6.1 Electron Spin Resonance in Bulk Materials

In spin resonance experiments, electromagnetic radiation is used to excite transitions between electronic states (ESR) or nuclear states (NMR). Traditional spin resonance experiments use electromagnetic radiation to interact resonantly with an ensemble of electron or nuclear spins via absorption and emission of photons. When performed on bulk materials ESR, experiments can reveal the electronic states of paramagnetic defects in solids [207, 208] and the presence of spin centres in biomolecules [209]. An ensemble of $10^7 - 10^{10}$ spins [207] is required to achieve sufficient signal detection in conventional, bulk ESR experiments. The need to measure such a large number of spins leads to line-width broadening of the ESR signal, as at the atomic level each spin is in a slightly different electromagnetic environment and so possesses a slightly different resonance frequency.

There has been considerable effort expended to develop experimental tools that can perform spin resonance on much smaller ensembles of spins, with the ultimate goal of single atom spin resonance. Single atom spin resonance is desirable for the local control it offers, and the potential for implementations of spin-based quantum computing architectures [210]. In certain systems magnetic resonance can be detected in single spin centres via force microscopy [211]. Couplings between itinerant and localized spins have been used to electrically detect magnetic resonance in small ensembles [212], spins in quantum dots [213], in single P atoms in Si [214, 215], and in individual magnetic molecules [216]. These works represent significant progress; however, none of these techniques have the atomic-scale control possible with the STM.

6.2 Electron Spin Resonance and Scanning Tunnelling Microscopy

6.2.1 Energy Resolution, STS, and ESR-STM

Scanning tunnelling spectroscopy measurements can reveal a great deal of information about the spectroscopic character of a surface, particularly when combined with analysis techniques like FT-STs as demonstrated in Part II. However, the thermally-limited energy resolution of the STS signal, derived in Chapter 2, can obscure features below a certain energy. In order to examine surfaces where better energy resolution can give important insight into the underlying physics, multiple ultra-low temperature STMs have been commissioned that achieve tip-sample temperatures below 100 mK [117, 217–220]. However, recent work by Ast in Reference [221] has revealed that there is a quantum mechanical limit to STS resolution that cannot be overcome by lowering the temperature of tip and sample.

Spin resonant techniques do not measure the same physical quantity, the sample density of states, that STS measures. However, because resonant processes are inherently out of thermal equilibrium, they potentially allow access to energies below the quantum limit of conventional STS. In the case of weak magnetic interactions, such as the dipole-dipole interactions between magnetic atoms nanometres apart, electron spin resonance offers a way to measure the relevant physics beyond the scope of conventional STM techniques.

Figure 6.1 shows a logarithmic energy scale in units of electronvolts. The energy scale of physical processes of interest are written above the line, highlighting quantities like metallic work functions, chemical bonding, superconducting gaps, and magnetic interactions. Below the energy scale in Figure 6.1 is the resolution of STS at various temperatures, which clearly demonstrates the need to cryogenically cool the STM in order to measure STS at the right energy scale. For the final interaction depicted the energy scale is beyond the quantum limit determined by Ast for STS [221]. Therefore, to probe this regime requires a new acquisition technique, motivating the development of ESR-STM as a way to measure a new energy regime, in addition to the possibility of resonant spin

control of a single atom.

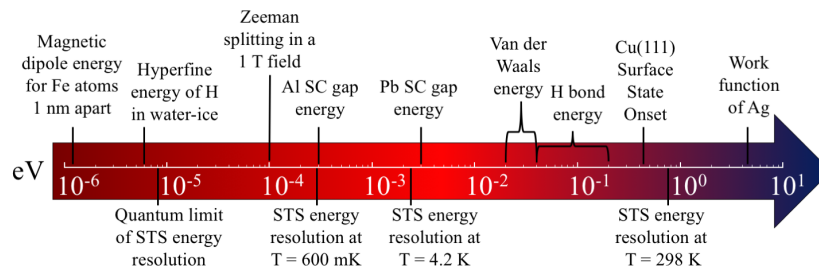


Figure 6.1: **Logarithmic Energy Scale** Above the energy scale a select number of energies important in condensed matter are listed while below the energy scale the limit of STS resolution is shown at various tip-sample temperatures. References: Hyperfine energy of hydrogen (H) water [222], superconducting (SC) gap energies [223], work function of silver [81], and quantum limit of STS energy resolution [221].

6.2.2 Previous Work to Pair ESR with STM

STM offers nanoscale spatial control and imaging while ESR provides high-energy resolution that is otherwise not possible with STM techniques. A number of research groups have attempted to realize electron spin resonance scanning tunnelling microscopy (ESR-STM), combining the strengths of these two techniques. The first attempts to pair ESR and STM measured the tunnelling current noise at the spin precession frequency in a room temperature experiment [224–226]. The frequency-dependent signal in this case was sporadic and was not widely adopted, though theoretical mechanisms for the observed effect have been proposed [227, 228]. A more recent experiment by Mullegger *et al.* applied a microwave electric field between 0.5–3.0 GHz to a magnetic molecule in a milliTesla magnetic field and attributed the frequency-dependent dI/dV feature to a spin resonance signal [229]. This work has yet to be reproduced and may potentially suffer from issues related to compensating the microwave power at the tip-sample junction, as discussed by Paul [230].

6.2.3 ESR-STM at IBM

Researchers at the Nanoscience Laboratory have developed their own ESR-STM technique [86]. This version of ESR-STM works at low temperature (≈ 1 K), in magnetic fields, on Fe atoms and has already been used in a number of experiments [86, 231, 232]. Of the ESR-STM techniques currently in the literature, this technique has been the most thoroughly documented [86, 230, 233] and offers the nanoscale manipulation and imaging properties of the STM combined with the energy resolution of ESR.

Spin-polarized STM

In order to understand the ESR-STM measurement scheme, it is necessary to introduce the basic theory of spin-polarized scanning tunnelling microscopy. When both the sample and tip possess a magnetic moment, the Tersoff-Hamann tunnelling current acquires a dependence on the spin orientation of the two [64, 234, 235]. The density of states for both the tip and the sample must then be expressed as a spin resolved quantity, $\rho_{t,s}^{\uparrow,\downarrow}$. By defining the quantities

$$n_t = \rho_t^{\uparrow} + \rho_t^{\downarrow}, \quad n_s = \rho_s^{\uparrow} + \rho_s^{\downarrow} \quad (6.1)$$

$$m_t = \rho_t^{\uparrow} - \rho_t^{\downarrow}, \quad m_s = \rho_s^{\uparrow} - \rho_s^{\downarrow} \quad (6.2)$$

it is possible to express the spin-polarized differential tunnelling conductance in the low bias limit as

$$dI/dV \propto (n_t n_s + m_t m_s \cos \theta) T(z, E, V) \quad (6.3)$$

where θ is the angle between the tip and sample magnetization [64, 235]. Equation 6.3 reduces to Equation 1.7 in the event that the tip or sample is non-magnetic. When tip and sample are both magnetized the maximum tunnelling current will be measured when the tip and sample magnetization are aligned ($\theta = 0$) and the minimum tunnelling current when they are anti-aligned ($\theta = \pi$). This means that the STM tip can be used to measure tunnelling magnetoresistance via the tunnelling current, making it an atomic-scale magnetic probe.

The degree of spin-polarization of the STM tip can be characterized by the behaviour of the differential tunnelling conductance when measuring inelastic magnetic transitions in STS. Figure 6.2 illustrates the difference between the STS spectra of a single Fe atom on the surface of a MgO bilayer taken with a normal (spin-averaging) STM tip versus a spin-polarized tip in a magnetic field. An inelastic transition is visible as steps at a bias of $V_B = \pm 14$ mV for the spectrum obtained with the normal tip. The spectrum taken with the spin-polarized tip also exhibits features at a bias of $V_B = \pm 14$ mV but these features are asymmetric as a function of the polarity of the bias and demonstrate peaks in addition to steps. As shown by Loth [144, 236], the asymmetry of the observed features in the spin-polarized STS spectrum is due to differences in the majority versus minority spin population in the tip. Furthermore, the shape of the peaks can be related to the spin-momentum transfer imparted to the Fe atom electrons by the spin-polarized tunnelling electrons.

Sensitivity to surface magnetic moments is of great experimental utility in the study of magnetic information storage [143, 237] and magnetic quasiparticles [238]. For the purposes of this work spin-polarized tips were characterized using the SP-STS spectra of either Fe or Co atoms. The spin-polarized tips were then used to detect the magnetic orientation of the electrons in ESR-STM experiments.

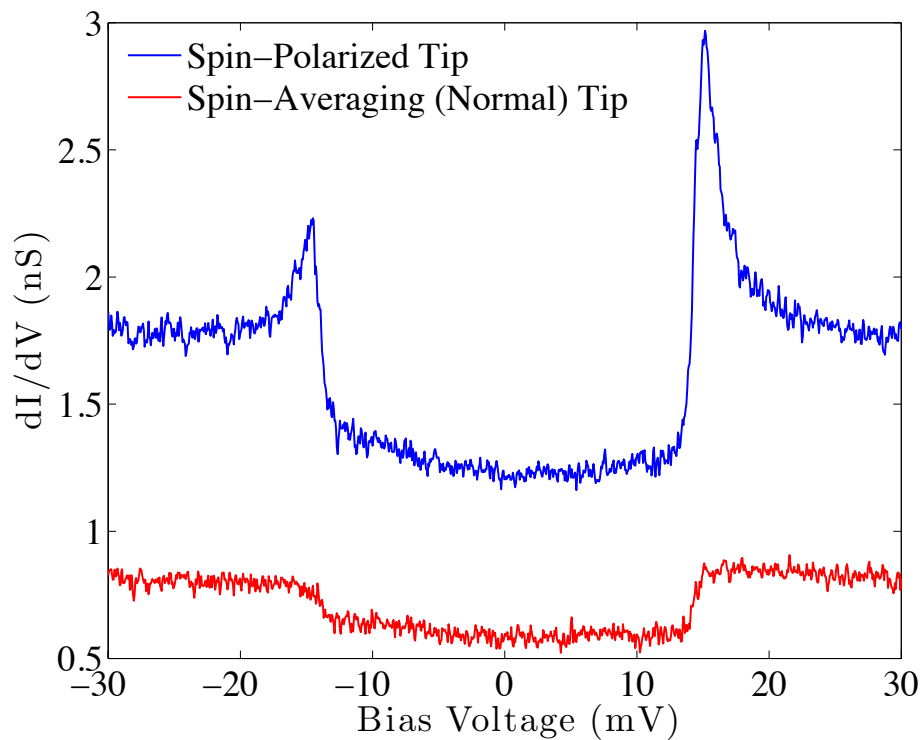


Figure 6.2: **STS spectra of a single Fe atom with and without a spin-polarized tip.** STS spectra of the same Fe atom on MgO with a spin-polarized tip and a normal tip which averages over all available spin channels. Spectra were acquired using a lock-in amplifier to extract the differential tunnelling conductance. Set-point parameters: $V_s = 10$ mV, $I_s = 50$ pA for the normal tip and $V_s = 10$ mV, $I_s = 100$ pA for the spin-polarized tip.

Experimental Set-up for ESR-STM

The experimental set-up for ESR-STM is illustrated in Figure 6.3. A spin-polarized tip is positioned over a magnetic atom on a surface in a magnetic field, as shown in Figure 6.3. The magnetic atom sits atop a thin-film insulator in order to preserve the atomic magnetic moment and spin relaxation lifetime from interactions with conduction electrons of the bulk sample. A microwave frequency electrical excitation is sent into the tunnelling junction via the tip. The frequency of this excitation is swept until it is equal to the energy difference between the two lowest lying electronic spin states. When this occurs, a resonance condition is achieved and the spin state becomes a coherent mixture of its two lowest lying states, changing the magnetization of the surface atom. This change in magnetization is detected via a change in the tunnelling magneto-resistance of the spin-polarized tunnel junction. By chopping the microwave excitation on and off, a scheme known as continuous wave ESR-STM as shown in Figure 6.3 (b), a lock-in amplifier can be used to take a difference measurement between the tunnelling current with and without microwave excitation. Measuring this lock-in signal as a function of microwave frequency produces the measured change in tunnelling current due to ESR observed in 6.3 (c).

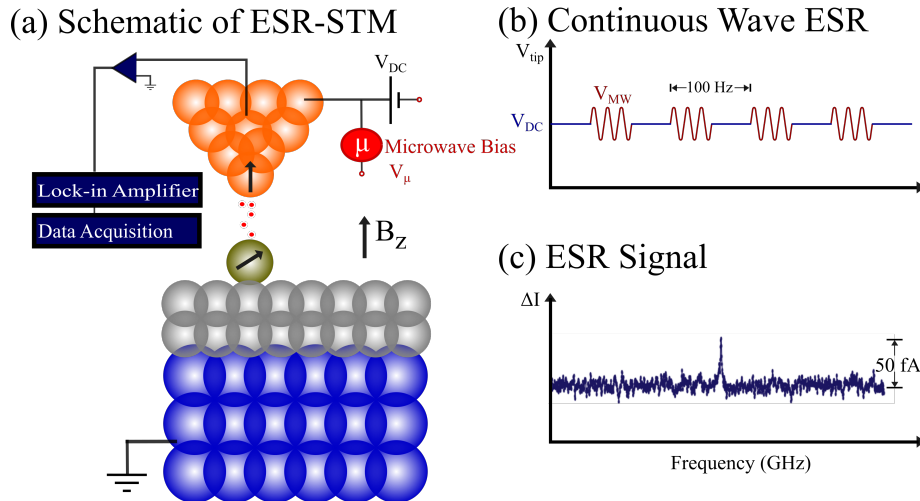


Figure 6.3: **ESR-STM measurement scheme.** (a) A magnetic atom sitting on an insulating thin film on a bulk conducting crystal has been sent into resonance by application of a microwave bias excitation along the DC bias line. A spin-polarized tip is used to read-out the change in tunnelling current. (b) The microwave pulse train for this method, dubbed continuous wave ESR. (c) The microwave frequency is swept until a resonance peak in the tunnel current signal is detected via the lock-in amplifier.

In the IBM experimental set-up for ESR-STM, Fe and Co atoms are deposited on a thin-film of MgO grown on a Ag(100) crystal substrate in a canted magnetic field (tilted 2° from parallel to the sample plane). Both the Fe and Co preferentially adsorb on the O site, and each shares four Mg atoms as nearest-neighbours, giving the binding site C_{4v} symmetry [239]. The ligand field of the neighbouring oxygens causes the Fe and Co atoms to exhibit a strong energetic preference for developing magnetization perpendicular to the surface, ie. in the direction of the easy-axis magnetic anisotropy [239]. An ESR-STM signal has only been observed when measuring Fe atoms on the MgO surface, and not Co atoms. This may be due to the threefold symmetry of the Co orbitals not being compatible with the fourfold symmetry of the MgO ligand field, and so the large time varying electric field caused by the microwave bias does not address the spin component of the Co electronic wave function in a way that could excite a resonance [86].

Spin-polarized tips are constructed by using vertical manipulation to pick up an Fe atom so that the tip is terminated by a single magnetic atom. The procedure for picking up single atoms consists of moving the tip close to the sample surface, corresponding to a tip-sample resistance of $\approx 1 \text{ M}\Omega$, increasing the bias voltage to 0.55 V, and then withdrawing the tip [86]. The same technique can be used to position single atoms and build structures on the surface by placing them from the tip onto specific atomic binding sites, as will be shown in Chapter 7. Characterization of the degree of spin polarization of the tip can be checked by using STS to measure inelastic magnetic transitions in individual Fe or Co atoms, as shown for an Fe atom in Figure 6.2.

The single atom on the tip apex has a sub-picosecond spin relaxation time due to its strong interaction with the conduction electrons of the tip, so it acts only as a spin filter and cannot be resonantly excited in the same way as atoms on the MgO surface. The lifetime of the atoms on the surface is considerably longer due to their decoupling from the conduction electrons of the Ag(100) crystal by the MgO thin film. This is crucial for the success of ESR-STM as a long energy relaxation time, T_1 , for excited magnetic states is necessary in order to observe spin resonance. Electrical pump-probe spectroscopy, in which a DC bias pulse called the pump is delivered to the tip-sample junction followed by a lower voltage probe pulse at increasing time intervals [143], is used to establish the magnitude of T_1 before attempting ESR-STM frequency sweeps. The T_1 time is one of three important parameters used to describe a resonantly driven magnetic moment, and optimizing T_1 is crucial for implementing quantum logic operations, as is discussed in the development of pulsed ESR in Appendix C and by Paul in Reference [233].

Once a spin-polarized tip has been crafted and a suitable Fe atom candidate on the surface has been found then the STM feedback circuit is used to stabilize the tip at low current and low DC voltage ($I_s = 1 \text{ pA}$, $V_s = 5 \text{ mV}$). The feedback is then disengaged and the microwave bias modulation scheme is applied through the tip, with $V_\mu = 5 - 10 \text{ mV}$ (peak-to-peak) producing a $10^6 - 10^7 \text{ V/m}$ time-varying electric field at the tip and sample [86]. Before any microwave bias is applied the microwave amplitude is calibrated to achieve constant power at all

frequencies in the sweep [230]. In order to keep the microwave power constant at the tip-sample junction at each frequency the source amplitude is varied by up to 40 dB, indicating that if such steps are not taken any measured signal will be dominated by variations in the microwave power at the junction as a function of frequency. The power-calibrated frequency is swept and the time-averaged tunnelling current is measured as the microwave bias is chopped at a 97 Hz audio frequency. A lock-in amplifier is then used to demodulate this signal and compare the tunnelling current when the microwave bias is applied and when it is not. Electron spin resonance of the Fe atom can be detected as a change¹ in the tunnelling current, as shown in Figure 6.5.

Theory of ESR-STM on single Fe atoms

The low-energy quantum states of Fe on MgO have been characterized using spin excitation spectroscopy [144, 236], x-ray absorption spectroscopy [239], and multiplet calculations [239–241]. These studies have shown that the spin and orbital angular momentum of the free Fe atom are largely preserved on the MgO surface and that it is a reasonable approximation to treat the Fe atom as if it is in a d^6 electronic configuration. Under this assumption the lowest Hund’s rule term dictates that Fe has an orbital moment $L = 2$ and spin $S = 2$ [86]. Detailed multiplet calculations of the multi-electron wave functions involved in the Fe-MgO system show that it is possible to accurately capture the essential physics needed to describe ESR-STM by using an effective spin Hamiltonian [240, 241]. By choosing the z-axis to align with the direction of the easy-axis anisotropy dictated by the MgO ligand field (out of the sample plane) the following Hamiltonian can be used to model the magnetic states and energies of Fe atom on MgO [86]

$$H_0 = DL_z^2 + F_0(L_+^4 + L_-^4) + \lambda \vec{L} \cdot \vec{S} + \mu_B(\vec{L} + \vec{S}) \cdot \vec{B}, \quad (6.4)$$

where $D = -433$ meV is the out-of-plane magnetic anisotropy, $F_0 = 2.19$ meV describes the strength of the ligand field from the MgO lattice, and $\lambda = -12.6$ meV is the spin-orbit coupling constant. The last term in the Hamiltonian represents the Zeeman coupling of the electron spins to the external magnetic field. The operator L_z addresses the z component of the orbital angular momentum, while L_+ , and L_- are the orbital angular momentum ladder operators.

Equation 6.4 has a manifold of five lowest lying eigenstates, which can be expressed as linear combinations of the z-axis orbital and spin quantum numbers $|m_L, m_S\rangle$. Transitions between the ground state and the excited states can be probed experimentally by STS measurements, as shown in Figure 6.4 (a). The step in the differential tunnelling conductance at $V_b = \pm 14$ mV step corresponds to an inelastic excitation of a spin-flip transition [138] as the tunnelling electron crosses the energy threshold needed to flip the Fe spin from the ground state

¹This change can be either an increase or a decrease depending on the majority spin population in the spin-polarized tip.

$|0\rangle$ to the excited state $|2\rangle$. This transition is illustrated with respect to the Fe atom low-energy spin states in Figure 6.4 (b).

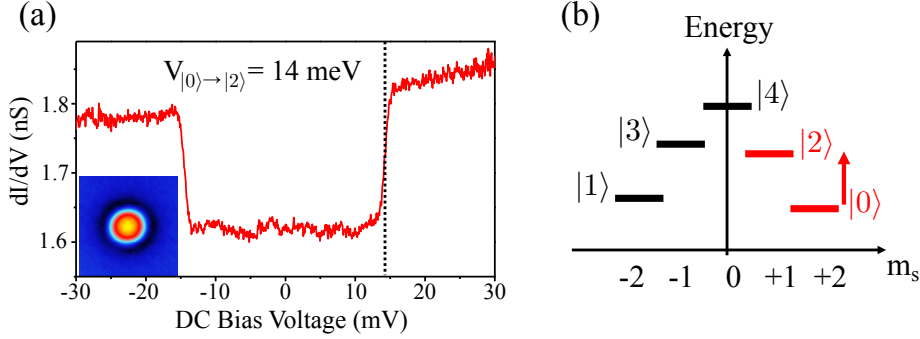


Figure 6.4: **STS spectra of Fe on MgO** The jump in differential tunnelling conductance at $V_b = 14$ meV corresponds to the transition for the ground state to the first excited state. Topographic height of Fe atom in inset is $h = 0.17$ nm. (b) The five lowest lying states of an Fe atom on MgO [86].

The two lowest lying states $|0\rangle$ and $|1\rangle$, are degenerate except for Zeeman splitting caused by the out-of-plane component of the external magnetic field, B_z . It is these states which are driven into resonance by application of the ESR-STM microwave bias. To leading order the $|0\rangle$ and $|1\rangle$ states can be expressed as

$$|0\rangle = 0.92 | +2, +2\rangle - 0.40 | -2, +2\rangle \quad (6.5)$$

$$|1\rangle = 0.92 | -2, -2\rangle - 0.40 | +2, -2\rangle. \quad (6.6)$$

Both states are polarized in their spin but mixed in their orbital angular momentum. They are separated by a large energy barrier, as illustrated in Figure 6.4 (b), decreasing the possibility for quantum tunnelling of the magnetization between the two states that would drastically shorten the lifetime of resonant spin states [240].

Spin resonance between the $|0\rangle$ and the $|1\rangle$ state is driven using a microwave bias voltage. Figure 6.5 (a) and (b) show the population equalization of the $|0\rangle$ and $|1\rangle$ states when resonance is achieved. At $T = 0.6$ K the occupation probability of the $|0\rangle$ state is 75% (Figure 6.5 (a)), as determined by a Boltzmann distribution [242]. Sufficient mixing between the $|m_L, m_S\rangle$ quantum numbers of the $|0\rangle$ and $|1\rangle$ states is accomplished by use of a large in-plane magnetic field B_x , while the out-of-plane component B_z sets the magnitude of the resonant frequency (100 μeV splitting gives a 25 GHz resonance) and spin polarizes the tip. Note that although the applied experimental field used is large, on the order

of several Tesla, it is still the weakest term in the spin Hamiltonian, justifying its treatment as a perturbation that mixes $|m_L, m_S\rangle$ states.

The microwave bias pulse introduces a time-dependent electric field that moves the Fe atom with respect to the MgO substrate. This modifies the ligand field parameters and so acts as a time-dependent perturbation that can be modelled by

$$H_1(t) = F_1(t)(L_+^4 + L_-^4) \quad (6.7)$$

where the strength of the parameter $F_1(t)$ is related to the magnitude of the driving microwave field. This term acts to drive coherent transitions between the $|0\rangle$ and the $|1\rangle$ states because it exhibits a non-vanishing coherent transition rate $\langle 0|H_1(t)|1\rangle$, particularly if a strong in-plane B_x field mixes the spin components of both states.

The microwave frequency is swept until it excites a resonant transition, which in a continuous wave mode of operation results in an equalization of the occupation probability of the $|0\rangle$ and $|1\rangle$ states (Figure 6.5 (b)). The change in occupation probability between a thermal and a resonant distribution changes the tunnelling magnetoresistance between the STM tip and Fe atom. Figure 6.5 (c) shows how this change can be measured in the spin-polarized tunnelling current as a function of the applied field. Whether the ESR-STM exhibits a peak or a dip at the resonance frequency depends upon the majority spin carrier of the spin-polarized tip, as illustrated in Figure 6.6. Individual spin-polarized tips will produce different local electromagnetic environments, causing the resonant frequency to shift even when measuring the same Fe atom. Among different Fe atoms the ESR-STM resonant frequency exhibits variations on the order of 5 GHz, even with the same tip. This can be attributed to different local environments creating different ligand fields, highlighting the need for an atomic-scale experimental approach. The ESR frequency also exhibits time-dependent drift on the order of minutes, which is likely caused by mechanical vibration of the tip-sample junction.

6.3 Outlook

The ESR-STM technique provides a powerful combination of atomic-scale resolution combined with high energy resolution of magnetic transitions. At first, it may appear to be limited in scope, as the experimental set-up works only for the use of single Fe atoms (so far). No observation of spin resonance has been observed on other magnetic species. In the next chapter it will be demonstrated that single Fe atom ESR is sensitive to the presence of magnetic moments in the nanoscale neighbourhood of the resonant atom. Using this sensitivity it is possible to use ESR-STM as a magnetic dipole-dipole sensor with a broad range of magnetic targets, greatly increasing the scope of future ESR-STM experiments.

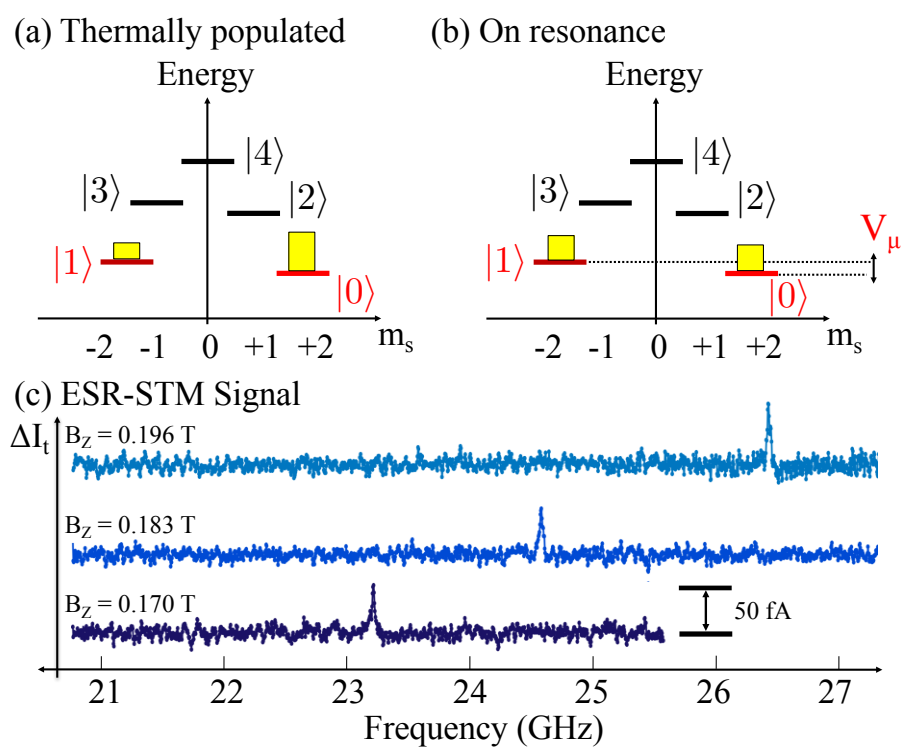


Figure 6.5: **Single Fe atom ESR resonance.** (a) Thermal population of the low-energy quantum states of an Fe atom on MgO in a magnetic field. (b) Resonant population in continuous wave mode (c) ESR-STM spectra showing resonance at various magnetic field strengths.

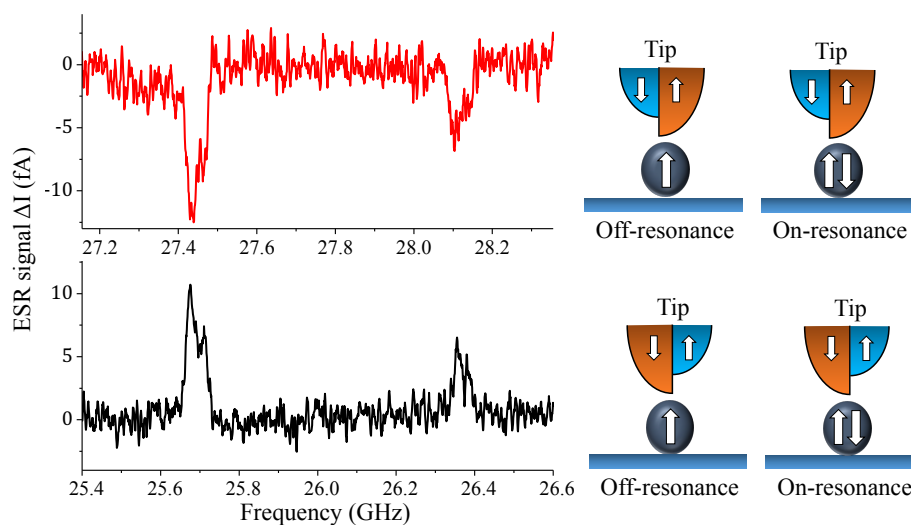


Figure 6.6: **ESR-STM spectra of the same Fe atom with two oppositely spin-polarized tips.** The ESR peak (dip) is caused by a lower (higher) tunnelling magnetoresistance at resonance. The frequency splitting between the observed features is independent of tip, though the absolute frequency at which each resonance is observed is tip dependent. The rich structure of the ESR spectra is caused by the proximity of nearby magnetic atoms on the surface, which will be discussed in detail in Chapter 7. The above spectra were taken in a magnetic field of $B = 4.8$ T and at a temperature of $T = 1.2$ K.

Chapter 7

Single Atom Magnetic Sensing on the Surface of MgO

But I am not afraid to consider the final question as to whether, ultimately — in the great future — we can arrange the atoms the way we want; the very atoms, all the way down!

Richard Feynman - 1959 [243]

The following Chapter contains text and figures adapted from “Atomic-scale sensing of the magnetic dipolar field from single atoms” *Nature Nanotechnology*, 12:420–424 [231]. Figures are altered unless otherwise noted.

Spin resonance provides the high-energy resolution needed to examine biological and material structures by sensing weak magnetic interactions [207]. By pairing electron spin resonance techniques with scanning tunnelling microscopy researchers at IBM have developed an experimental tool with the spatial resolution of the STM and energy resolution of ESR. In this chapter, this technique is used to develop a new form of nanoscale magnetometry, capable of determining the position and magnitude of nearby spin centres. This culminates in the demonstration of nanoscale trilateration, dubbed “nano-GPS”.

7.1 Characterization of an Atomic-Scale Magnetic Dipole-Dipole Sensor

Experimental strides in atomic-scale magnetometry have seen recent advances in the detection [211] and coherent control [213, 216, 244–246] of individual spin centres for sensitive local magnetometry [247–249]. However, sub-nanometre positioning and characterization of the spin centres remains a challenge [250, 251]. The ESR-STM technique offers a means to perform atomic-scale magnetometry and spin-spin sensing by using the resonance of a target Fe atom to sense the

dipolar magnetic field emanating from nearby spin centres. This dipolar sensor can determine the magnetic moment of individual nearby atoms with high accuracy and can be used to pinpoint their spatial location up to 4 nm away.

Detecting individual spins and their interactions has been pursued by means of atomic-scale spin centres such as optically trapped ions [246], nitrogen vacancy centres in diamond [247–249], spins in quantum dots [213], dopant atoms in semiconductors [245, 252], and single-molecule magnets in break junctions [216]. A resolution of 10 nm has been achieved for the controlled positioning and spin-resonant imaging of spin centres in solid-state materials [248, 250]. Atomic-scale control remains a challenging goal [251]. The STM excels at atomic scale positioning [54–56, 136], including of single atom magnets [137–139, 235, 237, 253–255], and so coupling this power to ESR-STM detection breaks new experimental ground and may ultimately allow for magnetic structural imaging of complex magnetic molecules, nanostructures, or spin-labelled biomolecules.

For magnetic atoms deposited onto metallic surfaces the dipole-dipole interaction is dominated by other interactions, such as Ruderman-Kittel-Kasuya-Yosida (RKKY) [253, 256] or superexchange [255, 257]. However, for magnetic atoms inside an insulator separated by nanometre distances the long-range dipole-dipole interaction dominates, and can lead to fascinating magnetic ground states [258] and excitations [259]. Fe and Co sitting atop the insulator MgO are expected to interact magnetically through the dipole-dipole interaction. This dipole-dipole coupling is too weak to measure using traditional scanning tunnelling spectroscopy techniques, even at low temperature. This coupling regime is accessible using the energy-resolution of ESR-STM.

7.1.1 Sample Preparation and Measurement Protocol

Measurements presented in this chapter were performed using the 1 K STM operating in ultra-high vacuum $P < 10^{-10}$ mbar. The majority of these measurements were performed with the tip and sample at the base temperature of $T = 0.6$ K but temperature dependence of the observed frequency splitting was also checked up to $T = 2.1$ K. A total magnetic field of $B = 4.8 - 6.6$ T was applied at an angle of 1.8° to the sample surface. This produced an out-of-plane magnetic field B_z ranging from $B = 0.15 - 0.21$ T.

Sample preparation began with repeated cycles of argon ion sputtering and annealing at $T = 450^\circ\text{C}$ of the Ag(100) crystal. MgO films were grown on top of the Ag(100) surface, which was heated to $T = 320^\circ\text{C}$ during growth, by thermally evaporating Mg from a Knudsen cell evaporator in an O_2 environment of $P_{O_2} \approx 10^{-6}$ mbar. The growth was monitored by Auger spectroscopy and characterized by STM/AFM measurements [86, 239, 240, 260] at 0.5 monolayer/minute. Experiments reported here were done with Fe and Co atoms deposited on bilayer MgO, where the MgO buffer layer is crucial to observing spin resonance [86] and also reduces scattering between conduction electrons of the Ag(100) and the deposited atoms, leading to longer spin relaxation times [233]. Fe and Co atoms were deposited using electron beam evaporators once

the sample had been transferred in the STM and cooled to 10 K. The coverage corresponded to a low dosage of Fe and Co atoms, roughly 1 atom/20 nm².

The STM tip was prepared from a mechanically cut Ir wire and prepared with field emission and controlled contact with the exposed Ag(100) surface *in-situ*. The tip was spin-polarized by using vertical atomic manipulation to transfer an Fe or Co atom from the MgO surface, following the prescription given in Chapter 6. The degree of tip spin-polarization was measured using STS on individual Fe and Co atoms [144] and magnetic pump-probe measurements [86, 143]. Systematic effects resulting from the tip magnetic field were accounted for by confirming results using more than 18 individually crafted microscopic tips, and performing repeated measurement of the same atom using different tips.

Calibration of the 1 K-STM piezo motion was accomplished using atomically-resolved images of the MgO surface. MgO has an epitaxial match with the Ag(100) surface [261], so the Ag(100) low-temperature lattice spacing of $a_0 = 0.4069$ [186] was used to calibrate distances between adatoms on the MgO surface [262]. The nearest-neighbour binding site distance using this calibration is $d_0 = a_0\sqrt{2} = 0.2877$ nm. Previous studies using STM and DFT had established the preferential binding site on top of the oxygen for both Fe and Co [86, 145, 239, 240].

ESR-STM was performed by sweeping microwave radiation at constant amplitude in the STM tunnelling junction [230] between 15 – 35 GHz. Standard set point parameters were $V_s = 5$ mV and $I_s = 1$ pA. The microwave bias amplitude was set at 10 mV peak-to-peak, which ensured that the instantaneous voltage between tip and sample was never more than 10 mV, so as to remain below the first inelastic spin excitation energy shown in Figure 6.4. Measurements were performed in continuous-wave mode using a lock-in amplifier to measure the time-averaged root-mean-square tunnelling current with a microwave bias chopping scheme at 95 Hz.

Electron spin resonance of individual Fe atoms on bilayer MgO/Ag(100) was driven by a microwave electric field at the tunnelling junction due to V_μ , as shown in Figure 7.1. The out-of-plane magnetic field B_z sets the resonance frequency. An in-plane magnetic field B_x mixes the spin states of Fe to increase the ESR signal [86]. A spin-polarized (SP) STM tip measures the spin resonance signal via changes in the tunnelling magnetoresistance.

Deposited Fe atoms were distinguished from Co by their STS signature, Fe atoms exhibit an inelastic transition at $V_b = 14$ mV [236] while Co atoms show an inelastic transition at $V_b = 58$ mV [145]. Vertical atom manipulation was used to position individual magnetic atoms at a prescribed distance in order to explore the ESR frequency splitting as a function of distance. In roughly 10% of cases positioning an Fe atom using this method resulted in an atom that had a measured apparent height taller than Fe atoms deposited by evaporation (0.23 nm versus 0.17 nm), with a different spectroscopic signature. This ‘tall’-Fe could be switched back to the as-deposited species by voltage pulses larger than 0.8 V or repeated vertical atom manipulation, and so was deduced to be a meta-stable charge state of Fe on MgO.

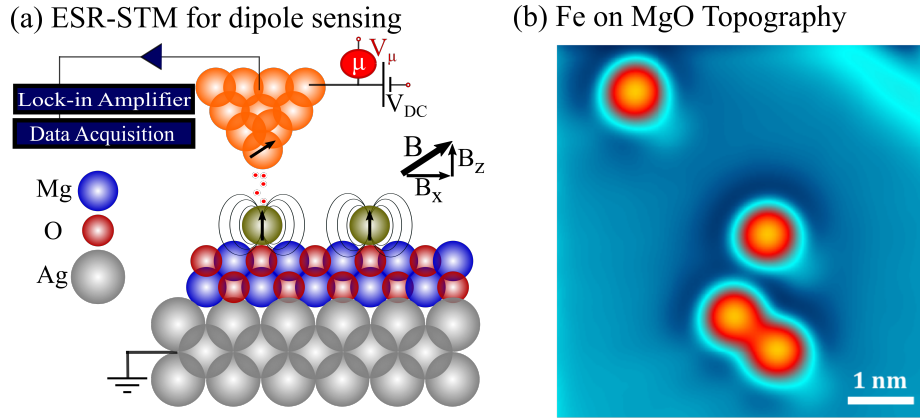


Figure 7.1: **ESR-STM for magnetic dipole detection.** (a) Schematic for sensing the dipole-dipole interaction between two iron atoms. (b) Constant-current STM image of four Fe atoms (0.17 nm apparent height) on the surface. Imaging conditions are $V_{DC} = 0.1$ V, $I = 10$ pA, $B_z = 0.18$ T, $B_x = 5.7$ T and $T = 1.2$ K.

7.1.2 Magnetic Dipole-Dipole Sensing using ESR-STM

Characterization of the dipole-dipole interaction between magnetic atoms on the MgO surface began with the ESR active species, the Fe adatoms. Atomic manipulation was used to precisely set the atomic spacing between Fe atoms in increments of the MgO lattice spacing and then ESR-STM spectra were measured at each spacing. This was performed by positioning the SP-STM tip over one Fe atom (the sensor) and detecting the signature of the nearby Fe atom (the target) using continuous wave ESR. Each ESR sweep in frequency showed a primary and a secondary feature, as shown in Figure 7.2 for two Fe atoms 2.46 nm apart. The observed spectral features corresponded to the spin up $|\uparrow\rangle$ and spin down $|\downarrow\rangle$ state of the target atom. The frequency splitting between these features gave the distance dependent magnetic interaction. The ESR peaks were fit with Lorentzian functions and the frequency difference between the peaks was recorded as a function of inter-atomic distance. This process was performed for more than 10 atomic pairs of Fe and the measured frequency splitting was reproducible regardless of microwave power, tip apex, temperature, or applied magnetic field.

The interaction between all ESR active Fe atoms was catalogued by constructing Fe-Fe pairs at different MgO lattice spaces and measuring the splitting in ESR frequency as a function of distance. Once this had been performed for over ten pairs of Fe atoms the dipole sensing technique was applied to different magnetic species by using an ESR active Fe atom as a sensor to detect a nearby magnetic target. In this case, the target atom was either Co or the charge state

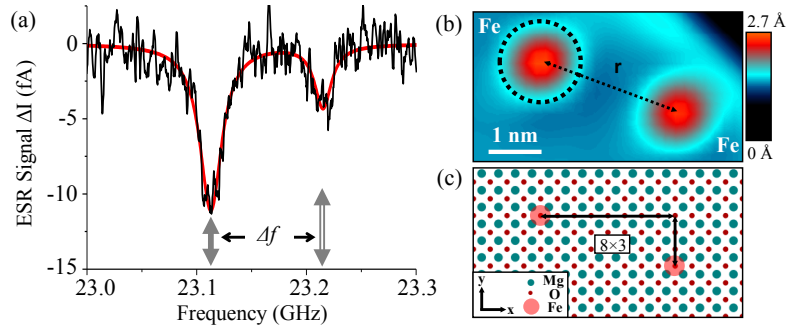


Figure 7.2: **Magnetic dipole-dipole interaction detected via ESR.** (a) ESR spectrum (black curve) of an Fe atom when another Fe atom (target) is positioned 2.46 nm away ($B_z = 0.17$ T, $T = 1.2$ K, $V_{DC} = 5$ mV, $I_{DC} = 1$ pA, $V_{RF} = 10$ mV_{pp}). A fit to two Lorentzian functions (red curve) yields the frequency splitting (Δf). The difference in amplitude between the two observed features can be attributed to the ratio in thermal occupation probability of the $|0\rangle$ and $|1\rangle$ states. (b) Topography of the sensor Fe atom (outlined in black) and the Fe target. (c) The underlying MgO lattice provides a metric to measure the distance between the two Fe atoms.

of Fe dubbed ‘tall’-Fe. Vertical atomic manipulation was used to move sensor Fe atoms at different spacings from these targets, so that the ESR frequency splitting could be measured. In many cases, more than one target atom would be present in the detection range of the Fe sensor. Figure 7.3 shows the ESR measurements and STM topographs of a three-atom nanostructure consisting of two Fe atoms and one Co atom. ESR-STM was performed on both of the Fe atoms in the structure, in both cases the ESR spectra exhibited four different spectral features. By tracking which frequency splittings remained constant using different sensor Fe atoms, spectral features could be correlated with the Fe-Fe interaction. The dotted vertical lines in Figure 7.3 connecting the spectra in (a) and (b) show the ESR frequency splitting that remained the same, indicating that this splitting is due to the magnetic interaction of the two Fe atoms. The other pairs of ESR splittings originate from magnetic interaction between each Fe atom and the Co atom, which changes due to the different inter-atomic separations involved.

The results of measuring the ESR frequency splittings as a function of inter-atomic distance for all magnetic targets on the MgO are shown in a log-log plot in Figure 7.4. The data is fit to a power law $\delta f \propto r^\alpha$ for each type of target atom: Fe, ‘tall’ Fe, and Co. The slope of the fit gives $\alpha = -3.01 \pm 0.04$ (Fe-Fe), -2.98 ± 0.04 (Fe-Co), and -2.94 ± 0.08 (Fe-tall Fe), in good agreement with the power law exponent expected for a magnetic dipole-dipole interaction ($\alpha = -3$) in each case. The intercept of the fits contains information about the

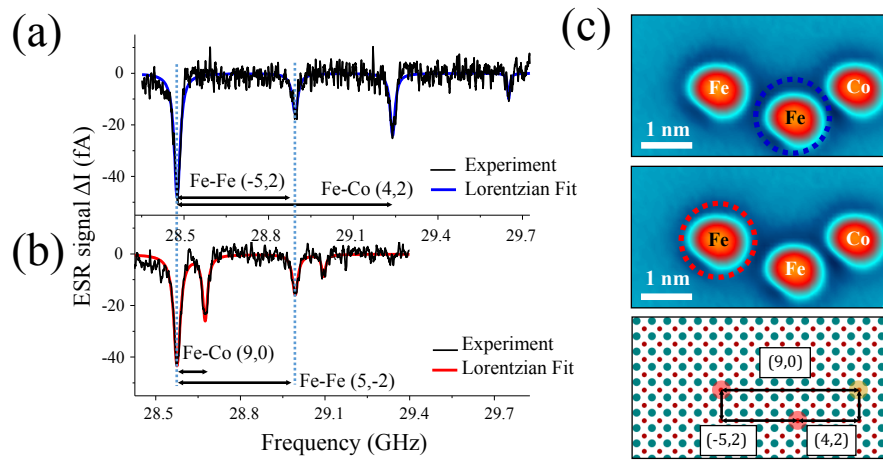


Figure 7.3: **ESR spectra of multi-atom structures.** (a) ESR spectrum taken on the middle atom (Fe) in (c) shows four ESR peaks. (b) ESR spectrum taken on the left atom (Fe) in (c) also exhibits four ESR peaks. (c) STM image of the three atom arrangement, with two Fe atoms and one Co atom. The binding-site assignment model (lower panel) shows distances between atoms in units of the atomic lattice spacing (0.2877 nm for $T < 20$ K). Imaging condition are 10 mV, 10 pA, $B_z = 0.2$ T, and $T = 1.2$ K.

magnetic moment of the sensor and target, information that can be extracted with the theory developed in the next section. For inter-atomic distances less than 1 nm significant deviation from the inverse cubic power law is observed. The short-range data ($r < 1$ nm, gray region in Figure 7.4) were not included in the power law fit.

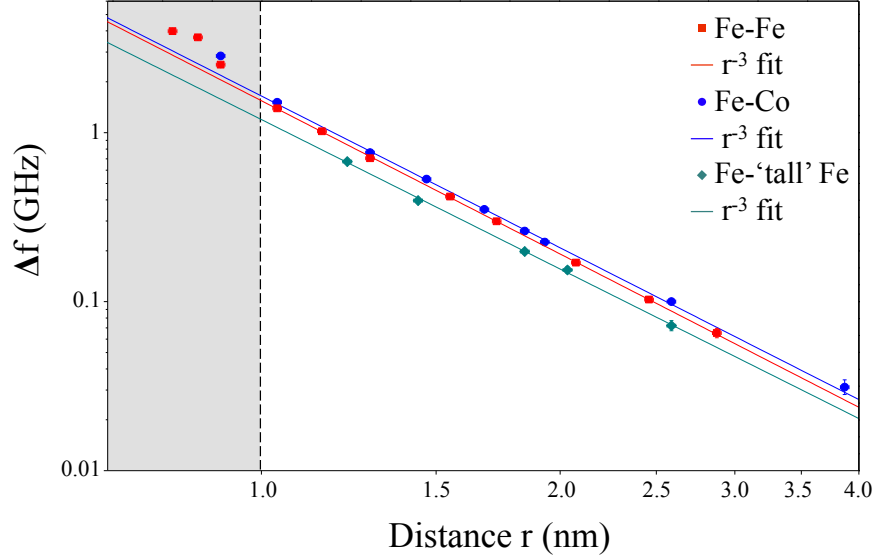


Figure 7.4: **Log-log plot of $\Delta f \propto r^\alpha$.** The measured splitting as a function of the distance r of atom pairs of Fe-Fe (red squares), Fe-Co (blue circles), and Fe-'tall' Fe (green diamonds). Data from the shaded region below 1 nm are excluded from the fits. Error bars in the r and Δf axes represent uncertainty in the determination of the interatomic distance and the measured Δf error due to frequency drift. Distances are obtained using the Ag lattice constant measured at low temperature by x-ray diffraction [186, 260].

Deviation from the power law behaviour at small atomic separations may indicate an additional interaction, such as exchange coupling, is becoming prominent or classical point-dipole approximation, which scales like r^{-3} , is no longer valid because at this distance the atomic size becomes comparable to the interatomic spacing. To investigate the discrepancy from the dipole interaction observed at short distances further experiments were performed for sensor and target atoms less than 1 nm apart. By using a sensor Fe atom situated in close proximity to a target Fe atom, but using it to probe targets at larger distances, it was possible to check whether the breakdown in the inverse cubic fit at small distance was caused by canting of the sensor magnetic moment. Figure 7.5 shows the ESR spectra and topography of a three Fe atom nanostructure. The

sensor Fe atom is indicated by a white dotted circle and is less than 1 nm away from one of the Fe targets. The ESR splitting measured on the Fe sensor due to the remote Fe target atom quantitatively follows the expected dipole-dipole ESR splitting from Figure 7.4, indicating that the magnetic moment of the sensor atom is not significantly changed due to the presence of the close Fe target. Thus, the deviation of Δf for close-spaced Fe-Fe pairs is not due to a change in magnetic moment but rather a change in the interaction between magnetic moments.

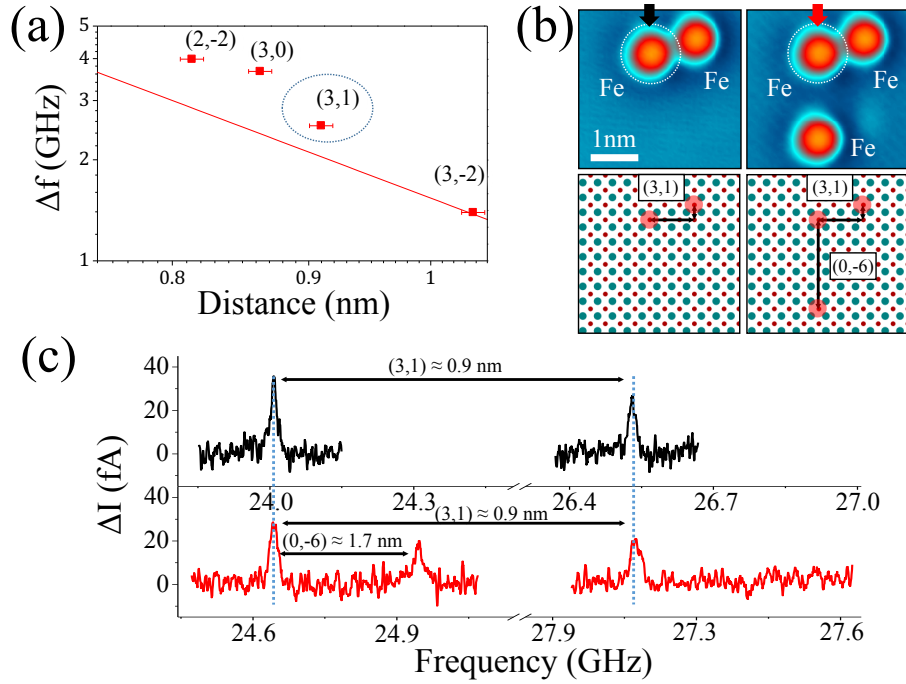


Figure 7.5: **Distance-dependent ESR splitting (Δf) for atoms separated by less than 1.0 nm** (a) Δf vs distance r for close atoms, zoomed in from Figure 7.4 on the Fe-Fe curve. (b) STM images of two close Fe atoms before and after placing a third (“remote”) Fe atom in the vicinity. The imaging conditions are 10 mV, 10 pA, $B_z = 0.17$ T, and $T = 1.2$ K. (c) ESR splitting before and after adding the remote atom.

7.1.3 Single-Atom Magnetometry from ESR Dipole Sensing

The magnetic dipole-dipole energy between two magnetic moments is given by

$$E_{dd} = \frac{\mu_0}{4\pi} \frac{1}{r^3} \left[\left(\vec{m}^{(1)} \cdot \vec{m}^{(2)} \right) - 3 \left(\vec{m}^{(1)} \cdot \hat{r} \right) \left(\vec{m}^{(2)} \cdot \hat{r} \right) \right] \quad (7.1)$$

where μ_0 is the vacuum permeability, r is the separation between the magnetic moments, and \hat{r} is a unit vector pointing in the direction linking the moments, and \vec{m}^i is the magnetic moment of atom i . The strong magnetic anisotropy for Fe on the O binding site means that the Fe atoms are fully polarized out-of-plane [86, 239]. This means that canting of the magnetic moment due to the in-plane field is minimal and so Equation 7.1 can be simplified to

$$E_{dd} = \frac{\mu_0}{4\pi} \frac{1}{r^3} \left(m_z^{(1)} m_z^{(2)} \right). \quad (7.2)$$

Equation 7.2 gives the magnetic dipole-dipole energy for two magnetic moments in the same plane with magnetic moments fully perpendicular to that plane. It shows that the expected dipole-dipole energy follows a power law with an inverse cubic dependency $E_{dd} \propto r^\alpha$ where $\alpha = 3$, in good agreement with the experimental fits. The sensor and target atom's magnetic moments can be represented in Dirac notation, ie. $|\uparrow_s\rangle$, $|\downarrow_s\rangle$, $|\uparrow_t\rangle$, $|\downarrow_t\rangle$, where the subscripts s and t denote sensor and target respectively. When on resonance the sensor is in a time-varying, coherent superposition of the up and down spin states: $\alpha|\uparrow_s\rangle + \beta|\downarrow_s\rangle$. In this state, the sensor's resonant frequency is affected by the spin state of the target, which has a thermally weighted probability of being either $|\uparrow_t\rangle$ or $|\downarrow_t\rangle$. This leads to four dipole-coupled microstates possible for the ESR to sample, as illustrated in Figure 7.6. As a result, the resonant frequency of the sensor in the absence of the target f_0 is split into two frequencies (f_\uparrow and f_\downarrow) corresponding to the two spin states of the target atom and giving a total change in frequency $\Delta f = f_\downarrow - f_\uparrow$ that is related to the magnetic dipole-dipole energy by

$$\Delta f = \frac{4E_{dd}}{h}. \quad (7.3)$$

where h is Planck's constant.

By relating the measured frequency splitting to the magnetic dipole-dipole energy it is possible to rearrange Equation 7.3 to solve for the magnetic moment of sensor and target. In the case where both target and sensor are Fe atoms this takes the form

$$m_z^{Fe} = \sqrt{\frac{h\pi}{\mu_0} r^3 \Delta f}. \quad (7.4)$$

Using this equation to fit Fe experimental data in Figure 7.4, with a fixed

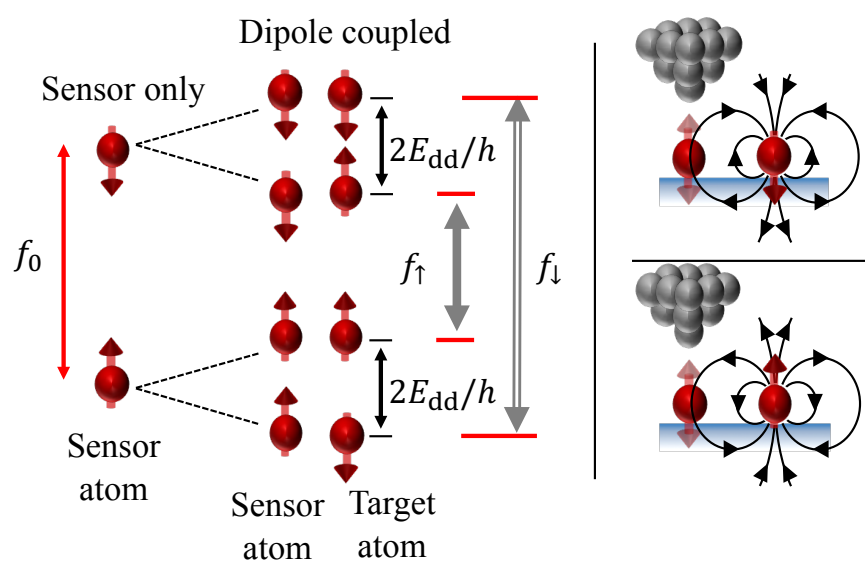


Figure 7.6: **Magnetic dipole-dipole interaction detected via ESR** A schematic of the dipole-dipole interaction. The resonant frequency of the isolated sensor atom (f_0) is split into two frequencies (f_{\uparrow} and f_{\downarrow}) corresponding to the two spin states of the target atom. $\Delta f = f_{\downarrow} - f_{\uparrow}$ is the measured splitting.

exponent of $\alpha = -3$, gives a magnetic moment of $m_z^{Fe} = 5.44 \pm 0.03\mu_B$. The uncertainty in the magnetic moment comes from a combination of uncertainty in the atomic lattice spacing $d = 0.2877 \pm 0.003$ (1%) nm, frequency drift which has an upper bound of 1% of the measured Δf , and the uncertainty in the fit parameters. The magnetic moment of Fe on MgO has also been determined by fitting multiplet simulations to X-ray magnetic circular dichroism (XMCD) spectra, giving $5.2\mu_B$ [239]. A comparison between the value of the moment extracted from fitting the dipole curve in ESR-STM and multiplet simulations of XMCD data is difficult, as no error bar is given for the XMCD fit. Furthermore, XMCD is an ensemble measurement technique which averages over $< 10^{10}$ atoms [145, 239], and potentially averages different charge states of Fe. The ESR-STM technique presented here has a unique advantage in this regard, as it can distinguish between measurements of Fe and ‘tall’ Fe.

With the magnetic moment of the sensor thus determined, ESR-STM provides a way to measure the magnetic moments of other atomic species with high precision. Knowledge of the Fe atom magnetic moment can be used, along with the frequency-splitting data as a function of atomic separation in Figure 7.4, to fit for the magnetic moment. For the data presented in Figure 7.4 the magnetic moments were determined to be $(5.88 \pm 0.06\mu_B)$ for Co and $(4.35 \pm 0.08\mu_B)$ for ‘tall’ Fe atoms using

$$m_z^{target} = \frac{h\pi}{\mu_0 m_z^{Fe}} r^3 \Delta f. \quad (7.5)$$

This nanoscale form of magnetometry can be used to characterize target atoms to within one MgO lattice site for sensor–target separations of up to 4 nm. The unique strengths of this form of magnetometry are its ability to measure the magnetic moments of atoms on different binding sites [232] or different charge states like Fe and ‘tall’ Fe, something not possible with an ensemble measurement technique. In order to calculate the magnetic moment of an unknown target a plot of distance dependent frequency splittings must be constructed between the target and an Fe sensor, as was done for Fe, Co, and ‘tall’ Fe in Figure 7.4.

The relative amplitude of the two observed ESR peaks also provides information about the thermal occupation probability of the target atom. For the case of an Fe target the $|\downarrow_t\rangle$ and $|\uparrow_t\rangle$ states correspond to the $|0\rangle$ and $|1\rangle$ states described in single-atom ESR. At the applied out-of-plane field $Bz = 0.15$ T used here these states are separated by a Zeeman energy of $95 \mu\text{eV}$ (23 GHz). The larger of the two ESR peaks corresponds to a measurement of the resonance frequency of the sensor when the target is in its ground state. This peak is the larger of the two as the target’s ground state is thermally populated with a higher thermal occupation probability. The smaller, secondary peak corresponds to a measurement of the resonance frequency of the sensor when the target is in its first excited state, which has a lower thermal probability of occupation. The ratio of the peak heights is given by the Boltzmann distribution $e^{-\Delta E/k_B T}$, and

can be used to quantitatively extract the electronic temperature. Sampling of both states is made possible by the relatively long spin relaxation time of the target atoms (for Fe pump-probe spectroscopy gives $100 \mu\text{s}$ [86, 230]), which is much faster than the data point averaging time for the ESR spectra (≈ 1 s). This means that the ESR spectra on the Fe sensor statistically samples the thermal population of the target Fe spin at each data point.

Development of a single atom magnetometer with such high spatial resolution offers a large step forward in the structural imaging of individual moments within magnetic molecules. Having already characterized a previously unmeasured magnetic species in ‘tall’ Fe the next section will illustrate how this nanoscale magnetometry technique could be used to spatially and magnetically characterize a completely unknown, complex target.

7.2 Engineering a Nano-Scale Magnetometer Array

Rather than using a single sensor Fe atom for dipole field detection, a sensor array of Fe atoms allows for multiple confirmations of the position and magnitude of target magnetic moments. Using vertical atom manipulation, as shown in Figure 7.7, a square sensor array was built using four Fe atoms. The sides of the square array were designed to be ten MgO lattice spacings apart so that the total size was $2.877 \times 2.877 \text{ nm}^2$. An additional Fe atom was chosen as the target, and positioned first at the very centre of the array and then at a position that was (-3,1) from the centre. This manipulation was achieved in conjunction with dropping off a sixth Fe atom that was used to spin-polarize the STM tip this atom is shown in Figure 7.7 (b) and (e).

Though the target atom in this case has already been fully characterized, this sensor array provides the opportunity to probe how the symmetry of a nano-engineered array is reflected in the degeneracy of the associated spin states. Using the corner atoms of the array as ESR dipole sensors, each ESR spectrum exhibits signals from the four Fe targets in range, reflecting the $2^4 = 16$ possible magnetic configurations of the target atoms. The ESR spectrum for the low symmetry configuration is shown in Figure 7.8 and the high symmetry configuration is shown in Figure 7.9. The dominant feature in both cases corresponds to the resonant frequency of the sensor when all target atoms are in their magnetic ground state, as this is the microstate most heavily favoured by the Boltzmann distribution. This spectral weight is redistributed to other states when the temperature is raised, as shown in the contrast between the ESR spectra at $T = 0.6 \text{ K}$ versus that at $T = 1.2 \text{ K}$. At both temperatures the expected spectral features with the lowest Boltzmann probability, those corresponding to three or more of the Fe atoms are in the $|1\rangle$ state, are either not visible or at the level of the current noise.

In the low-symmetry position of Figure 7.8 there are no degenerate ESR transitions. The various states and the associated orientation of the sensor and

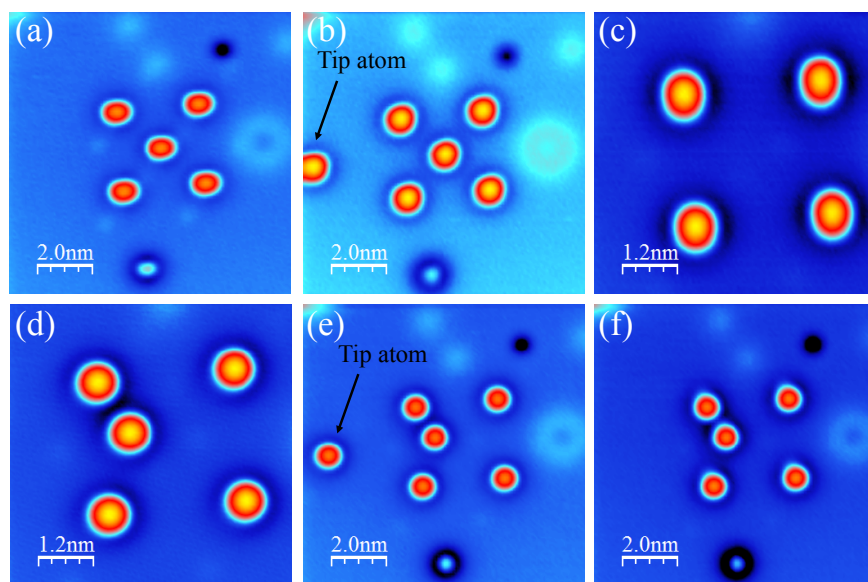


Figure 7.7: **Construction of the dipole sensing array.** (a) Five Fe atoms were gathered and arranged to form an array of four sensors and one target in the array centre. (b) The tip atom, another Fe, is placed outside the array for safekeeping. (c) The target Fe atom is picked up from the centre of the sensor array. (d) The target is placed at a lower symmetry position, corresponding to (-3,1) oxygen lattice sites from the array centre. (e) The entire structure is imaged in order to find the tip atom again. (f) The tip is spin-polarized by picking up the Fe tip atom.

target spins are illustrated through the use of circular symbols in the figure. A filled circle indicates that a spin on that atom is in its excited state at that frequency. The grey line indicates the ESR frequency of the Fe sensor with all corner (target) atoms in their magnetic ground state. Pink lines indicate ESR frequencies with one of the four target atoms in the excited state. Additional ESR lines arise (with less intensity) when two or more of the corner atoms are in the excited state. The ESR spectra were taken at two different sample temperatures: 0.6 K (upper spectra) and 1.2 K (lower) measured by a thermometer on the 1-K STM. The red and blue solid curves are modelled based on the dipole energy, the degeneracy of the states, and the thermal population of the states.

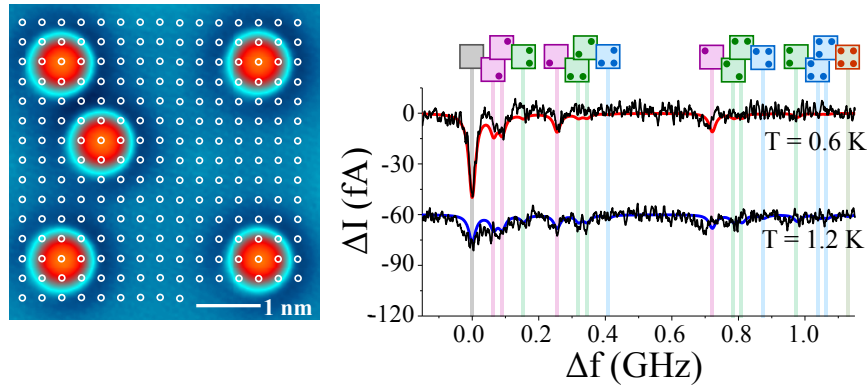


Figure 7.8: **Measuring a target atom at a low symmetry site with a nano-sensor array.** Five Fe atom structure with four equally spaced corner atoms and a middle Fe (sensor atom) which is positioned at $(-3, 1)$ lattice sites from the centre of the square (oxygen binding sites indicated by white open circles). For clarity, the 1.2 K spectra is offset by -60 fA. Imaging conditions are $V_{DC} = 10$ mV, $I = 10$ pA, and $B_z = 0.17$ T.

When atomic manipulation is used to manipulate the target from the low-symmetry position in Figure 7.8 to the high-symmetry position in Figure 7.9 the ESR spectrum exhibits changes that reflect the higher degree of symmetry in the magnetic states being probed. As the separation between the target and all four sensor atoms is now the same many of the weaker amplitude peaks observed in Figure 7.8 become degenerate, as highlighted by the coloured vertical lines. For example, the four pink lines are now degenerate at $\Delta f \approx 0.183$ Hz. The intensity of the ESR peaks in Figure 7.9 follows the degeneracy of the sensor atoms states¹, weighted by the Boltzmann distribution [242]. The Boltzmann distribution weighting is again evident when comparing the ESR spectra at $T = 0.6$ K versus at $T = 1.2$ K, where spectral weight is transferred to higher

¹The degeneracy can be calculated using Pascal's triangle (1:4:6:4:1).

energy states.

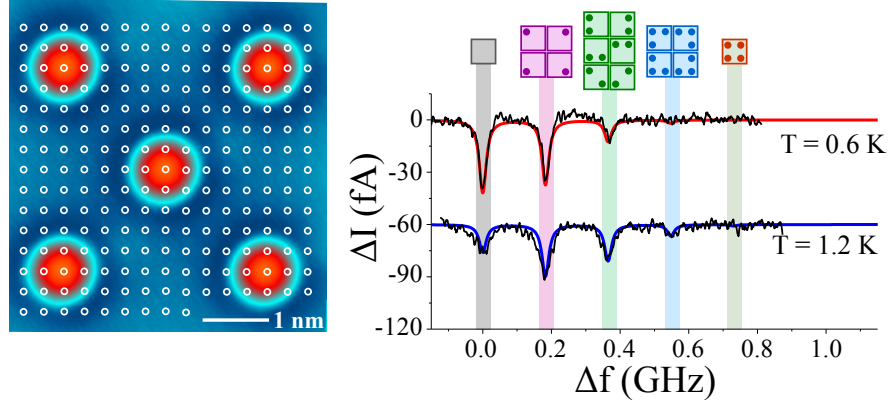


Figure 7.9: **Measuring a target atom at a low symmetry site with a nano-sensor array.** (b) The Fe sensor atom is placed in the exact centre of the square at a distance of 2.034 nm from the four target atoms. This creates a four-fold symmetry which leads to degeneracy of the excited spin states. Imaging conditions are $V_{DC} = 10$ mV, $I = 10$ pA, and $B_z = 0.17$ T.

The difference in the observed ESR spectra as a function of temperature allows the spin array to be used as a local thermometer, in addition to its function as a magnetometer. Since the relative amplitudes of the observed peaks are given by the Boltzmann ratio $e^{-\Delta E/k_B T}$ and the dipole-dipole energy can be measured from Equation 7.3 it is possible to extract temperatures of $T = 0.72 \pm 0.02$ K and $T = 1.43 \pm 0.13$ K for the measurements of Figure 7.9. These temperatures do not agree within statistical error with measurements of the temperature from a thermometer on the 1-K STM head, which reports $T = 0.6$ K and $T = 1.2$ K. There are a number of systematic issues that may cause such a disagreement, such as the ESR temperature measurement predominantly sampling the electronic temperature [221] while the head mounted thermometer is more sensitive to the phonon temperature. To use ESR thermometry in a quantitative way requires more exploration of systematics to develop a calibration.

7.2.1 Nano-scale Magnetic Trilateration

The nanoscale sensor array can be used to develop a new form of magnetic imaging based on trilateration of the ESR signal between the different corner sensors. Trilateration is the geometric technique used to calculate macroscopic positions on the surface of the Earth by the Global Positioning System (GPS) and so this technique is dubbed ‘nano-GPS’. This imaging technique allows for identification of the spatial location and magnitude of the magnetic moment

of the target independent of the topography mode of the STM. This is illustrated by extracting the position of the Fe target atom in the low symmetry configuration shown in Figure 7.8, as illustrated in Figure 7.10.

Measuring the ESR signal at three of the sensor atoms of the array gives three different frequency splittings Δf shown in Figure 7.10 (a). The goal of this experiment is to demonstrate that the sensor array can be used to characterize a target with an unknown magnetic moment. For this reason the target's magnetic moment is considered to be unknown, and is solved for numerically by finding the value for the moment for which all three ESR signals identify a unique point in space, rather than using Equation 7.4 to extract the known Fe magnetic moment. The problem consists of using the measured frequency splitting to simultaneously solve for three unknowns: the unknown target's x position, unknown target's y position, and the unknown target's magnetic moment.

Numbering the spin sensors as 1, 2, and 3, as shown in Figure 7.10, the measured ESR splittings from each sensor can be related to the three unknowns. For sensor 1 this takes the form

$$m_z^{target} = \frac{h\pi}{\mu_0 m_z^{Fe}} r_1^3 \Delta f_1 \quad (7.6)$$

where the distance between the sensor and the unknown target can be written

$$r_1 = \sqrt{(x_{Fe\text{sensor}} - x_{unknown})^2 + (y_{Fe\text{sensor}} - y_{unknown})^2}. \quad (7.7)$$

The deconvolved energy splittings extracted from the ESR signal three sets of parameters which can be used to solve the unknown coordinates and moment. The solution is illustrated by a single point of overlap for the three circles drawn around the sensor atoms in Figure 7.10 (c), which gives the position of the target atom, in agreement with the atom location measured by STM topography shown overlaid in Figure 7.10 (d).

A complication to the nano-GPS method is the presence of ESR peaks caused by the sensor atoms measuring each other. Fortunately, the Fe-Fe interaction between the sensors has been fully characterized in Figure 7.4. It is therefore possible to predict the position and magnitude of peaks caused by nearby sensor atoms and deconvolve the ESR signal to focus just on signals emanating from the target. The predicted ESR peaks due to the other sensors for Sensor 1 are shown Figure 7.10 (b) as a red curve. The peaks associated with the other sensors are subtracted off, with a magnitude determined by the expected ratio of the peak heights from the Boltzmann distribution. The spatial resolution derived from nano-GPS is better than 0.1 nm, as illustrated by the size of the black symbol in Figure 7.10 (d), and the magnetic moment resolution better than $0.1\mu_B$. Nano-GPS offers the ability to spatially pinpoint spin centres in complicated

bio-molecules², in which normal STM topography would not necessarily be able to clearly resolve individual atoms due to the delocalized nature of the electrons. Nano-GPS also offers chemical sensitivity, a weakness of traditional STM, via sensing of the target's magnetic moment.

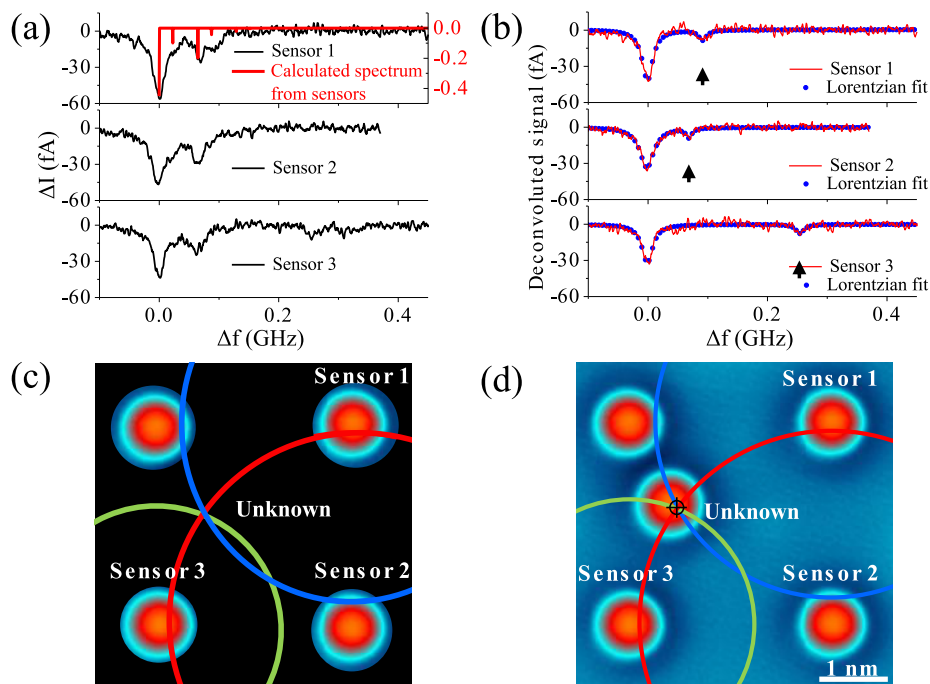


Figure 7.10: **Magnetic imaging by using trilateration.** (a) Measured ESR spectra ($T = 0.6$ K) from each sensor atom (black) and the predicted unbroadened spectrum (red) due to all atoms excluding the target. (b) ESR spectra of (a) after deconvolving the effect of the other sensor atoms. The results show ESR spectra (peaks are indicated by black arrows) due solely to dipolar interaction of the target atom and the sensor atom under the tip. (c) Predicted location of the target by trilateration. (d) Agreement of the target location between STM topography and nanoGPS.

²Subject to size constraints imposed by the 4 nm detection limit of the dipole sensing technique and practical limitations on the number of sensors atoms that would be required to trilaterate a large number of spin centres in the same nanoscale area.

7.3 Conclusions

By fully characterizing the magnetic dipole-dipole interaction a new form of atomic-scale magnetometry was developed that can identify the magnetic moment of unknown spin centres up to 4 nm away. Frequency splitting of the ESR-STM spectra into two peaks was investigated and it was determined that the presence of nearby magnetic moments caused changes in the local magnetic environment for the ESR-STM sensor atom that pushed the resonance frequency either up or down. The frequency splitting caused by specific magnetic species was shown to be robust against changes in STM tip, magnetic field, microwave power, and temperature.

Furthermore, when combined with the atomic manipulation techniques of the STM, nano-sensor arrays of Fe atoms could be engineered with controllable degrees of macroscopic symmetry. These arrays make it possible to perform trilateration on unknown spin centres to determine their position and moment. This provides a new route to atomic-scale structural imaging of nanostructures that can be assembled or placed on a surface, magnetic molecules or spin labelled biomolecules.

Part IV

Future Direction and Open Questions

Chapter 8

Conclusions

Distress not yourself if you cannot
at first understand the deeper
mysteries of Spaceland. By
degrees they will dawn upon you.

Edwin A. Abbott - 1884 [2]

8.1 Summary of Results

This thesis began by introducing the concept of the nanoscale surface and how it can be measured using the scanning tunnelling microscope. The importance of ultra-high-vacuum, low-temperature STMs to this thesis work was developed in Chapter 2, detailing the acquisition modes used for data collection, and the specific instruments: the Createc and 1-K STM.

In Part II, experimental results were presented demonstrating quasiparticle interference in the metals Ag(111) and Cu(111). The differential tunnelling conductance was acquired using multiple different acquisition modes and the effect of the tunnelling transmission probability was isolated and compared with simulation results based off of T-matrix scattering theory of the sample density of states and a Tersoff-Haman model of the tunnelling current. The simulation results agreed qualitatively with experimental measurements of the set-point artifacts in Ag(111) and Cu(111). The most dramatic set-point effect occurred when a series of constant-current dI/dV maps were acquired at different energies. An FT-STs feature appeared that dispersed in energy and was not observed in other measurement modes. This artifact is similar to features arising from real physical processes in the sample and is susceptible to misinterpretation and masking of other signals, as observed in the comparison of Cu(111) constant-height dI/dV maps to other acquisition modes.

Characterizing the set-point effect in FT-STs measurements has significant ramifications for future measurements of QPI in both the noble metals and in materials with more complex band structure. In the noble metals, the increasing scattering space resolution available with better instrumentation and more computational power means that researchers are examining noble metals QPI for subtle many-body effects [113, 132] not experimentally accessible when these metals were first characterized with FT-STs two decades ago. The signatures of these many-body effects, whether they are electron-phonon coupling or plas-

mon effects, are of the same order or smaller than the signal from the set-point effect, and so it is paramount that the set-point effect is taken into account when attempting future measurements. This thesis offers a prescription to rule out set-point effects in future noble metal FT-STs measurements: for spectroscopic grid measurements ensure the stabilization bias is set at a bias energy that does not show quasiparticle interference in the tunnelling current signal, such as below the onset of a surface state; and for constant-current dI/dV maps perform a number of checks using constant-height dI/dV maps using the same parameters in order to ensure that the features of interest are not caused by modulations of the tunnelling junction by the feedback.

For QPI in more complex materials, it is often not possible to follow the prescription of setting the stabilization bias below the onset of the band being probed; in many cases there are multiple bands being probed and these bands can be either hole or electron-like [88, 97, 111]. The greatest impact that this set-point work will have for studies in these materials is to serve as an important note of caution. Previously, features in the FT-STs intensity that did not change as a function of energy were attributed to the atomic lattice, noise, or static surface features while features that did change as a function of energy were considered to be caused by QPI and could be linked to the band structure. These results present a second possible source for dispersing features in the FT-STs intensity: set-point effects. A careful analysis of the expected set-point features will vary from material to material but a few general guidelines can be given: the appearance or disappearance of FT-STs features as a function of set-point conditions should be checked, at least two measurement acquisition modes should be used to verify any FT-STs intensity as each measurement mode exhibits slightly different set-point effects, and the FT-STs results should be compared with other techniques, such as ARPES, to verify that both techniques observe features that match the predicted band structure.

In Part III the dipole-dipole interaction of individual iron atoms on the surface of MgO was characterized over a length scale of 1.0 – 4.0 nm. In this regime, the distance-dependent frequency splitting of ESR-STM features was constant, independent of magnetic field, temperature, or STM tip. Fitting the iron ESR-STM frequency splitting as a function of the separation between Fe-Fe pairs showed that the splitting followed an inverse cubic distance dependence ($\delta f \propto r^\alpha$ with $\alpha = -3.01 \pm 0.04$). Relating the measured frequency splitting to the magnetic dipole-dipole energy this power law fitting allowed for the extraction of the Fe magnetic moment $m_z^{Fe} = 5.44 \pm 0.03 \mu_B$. With the Fe-Fe interaction fully characterized the Fe atoms on the surface could be used as sensors of nearby magnetic moments. A new form of nanoscale magnetometry was invented that allowed for the extraction of the magnetic moment of Co ($5.88 \pm 0.06 \mu_B$) and ‘tall’ Fe ($4.35 \pm 0.08 \mu_B$). To demonstrate the potential of this technique when combined with atomic manipulation, a four atom nano-sensor array was constructed to trilaterate the position and measure the magnetic moment of an Fe atom situated inside the array. This trilateration technique, nanoGPS, was used to locate a target magnetic moment with a precision of $\pm 0.1 \mu_B$ and in agreement with STM topograph measurements of the

atom's position with a spatial resolution better than one MgO lattice spacing.

Dipole sensing ESR-STM represents a new way to characterize the magnetic properties of single atoms on surfaces. The work presented in this thesis serves to characterize this emerging technique for the larger field of researchers working with atomic magnets on surfaces. Experiments using Fe atoms as remote magnetic sensors have the potential to probe aspects of magnetism previously inaccessible to experimentalists. For example, during the writing of this thesis Natterer and collaborators [232] demonstrated that the magnetic states of holmium atoms placed on MgO can be 'written' using voltage pulses with the STM tip and 'read' by measuring the tunnelling magnetoresistance. Dipole sensing ESR-STM on nearby Fe atoms was used to definitely show that the Ho atom behaviour had a magnetic origin and determine its magnetic moment on the MgO surface ($10.1 \pm 0.1\mu_B$).

The ESR experimental scheme presented herein also offers a template for researchers to invent other experimental set-ups that may work for electron spin resonance STM. For example, other commonly used insulating substrates, such as NaCl [21] or Cu₂N [137], have lattice sites that share the fourfold symmetry of the oxygen binding site in MgO, and could potentially be used to produce electron spin resonance in deposited iron atoms. Dipole-sensing ESR-STM on an iron atom on a Cu₂N thin film would be a particularly interesting experiment, as such measurements could prove complementary to the pump-probe magnetic sensing technique recently detailed in Reference [263]. There is also the possibility for significant collaboration with experts of other techniques, like X-ray magnetic circular dichroism (XMCD). Just as with FT-STS and ARPES, ESR-STM and XMCD are complementary techniques that together form a more complete picture of the system under study than possible with either alone.

8.2 The Future of the Set-Point Model

A number of experiments can also be suggested based on the results of Part II. These are elaborated below, along with comments on potential difficulties that may need to be overcome.

High-resolution spectroscopic grid measurements of the Cu(111) surface state

The spectroscopic grid data presented in this thesis contained noise related to changes of the STM tip that occurred during the measurement. A new STM head has recently been installed on the CreaTec that has better mechanical and electrical isolation. In principle, this should allow for measurements of the Cu(111) surface state with resolution on par with the best measurements performed on the Ag(111) surface state. These improved grid measurements should reveal the electron-phonon coupling kink near the Fermi energy, similar to the kink observed in Ag(111) [132]. Furthermore, they should have sufficient resolution and signal-to-noise that they should be able to observe the secondary

features observed in constant-height dI/dV maps. This is a necessary experiment because it would demonstrate whether these features are dependent on acquisition mode. When attempting these measurements the stabilization bias should be set in Region I, below the band onset of -420 meV, to avoid set-point artifacts masking the signal of interest.

High set-point current measurements of Ag(111)

The secondary dispersing feature observed in constant-height dI/dV maps of the Cu(111) surface has not been studied in the context of other (111) surface states. A return to the Ag(111) surface state to make constant-height measurements at set-point currents at or above 1 nA could provide useful information on the ubiquity of this feature in the (111)-terminated noble metals. The acoustic surface plasmon predicted by Sessi [113] should appear in Cu(111), Ag(111), and Au(111). The set-point current range in measurements of Ag(111) presented here was from 100 pA to 540 pA. Even in the event that the same feature seen in Cu(111) is not observed, an examination of FT-STs features observed at different set-point currents could reveal the presence of the second and third terms in the differential tunnelling conductance [80]:

$$\frac{dI_t}{dV_b} = e\rho_s(eV_b)\rho_t(0)T(z, eV_b, V_b) - \frac{\sqrt{2m}ez(V_b)}{2\hbar\sqrt{\phi}}I_s - \frac{2\sqrt{2m}}{\hbar} \frac{\partial z(V_b)}{\partial V_b} \sqrt{\phi}I_s. \quad (8.1)$$

The second and third terms in this expression are dependent upon the set-point current. These terms should exhibit increased signal at higher current, and may already have been observed in the highest current constant-height dI/dV measurements of Cu(111) presented here.

Development of T-matrix theory of Cu(111) for comparison

The numerous features in the FT-STs signal derived from constant-height dI/dV maps of Cu(111), which should be independent of effects of modulation of the tunnelling transmission probability, suggest the need for a rigorous theory of the Cu(111) surface state. The framework already developed to describe intra-band surface state scattering in Ag(111) could serve as a starting point. To adapt the same model for Cu(111) modifications would be required to the band onset, effective mass, and electron-phonon coupling according to experimentally determined values for the Cu(111) surface. Such a model provides a complete description of the intra-band scattering but does not include other processes, such as coupling to plasmons, electron-electron interactions, or spin-orbit coupling. These physical processes require different treatment, but could be developed within the context of the existing model.

Real-space simulation of multiple scattering impurities

The set-point model does a good qualitative job of predicting the observed set-point artifacts in grid and map measurements of Ag(111) and Cu(111). It does not, however, provide a quantitative comparison. This is expected, as the T-matrix theory considers only a single scattering impurity, while the experimental data measures many scattering impurities of different types. An attempt to simulate multiple scattering centres in real-space is explored in Appendix B. Simulating each experimental data set in this way may allow for a more precise fit of the entire experimental FT-STS line shape. This would be useful for two reasons: it would potentially allow a way to quantitatively characterize the effect of systematic uncertainties on the FT-STS scattering intensity and it would allow for extraction of physical quantities of interest, such as lifetime and scattering phase, from the entire FT-STS line shape and not just the peak position. Results gleaned from attempting a quantitative fit to the line shape could then be applied to the study of 2DEG QPI in semiconductors [82], while a thorough characterization of systematic uncertainties could be applied broadly to QPI studies of complex, strongly correlated materials.

8.3 Proposed Experiments with Magnetic Dipole-Dipole Sensing

The dipole-dipole iron sensing technique complements the atomic manipulation strengths of STM coupled with the high-energy resolution of ESR. At present, the detection range (4 nm) of the Fe sensor is mainly limited by the spectral line width of the ESR signal, which could be improved by lowering the magnitude of the applied microwave bias. With the fully characterized Fe sensing technique a number of exciting experiments are possible, a few of which are suggested below.

Dipole Sensing of Long-Lived Atomic Moments

Iron and cobalt both derive their magnetism from the orbital character of their d electrons. Magnetic species with f orbital character have larger magnetic moments and longer magnetic relaxation times, making them more suitable for single-atom magnetic information storage. Holmium atoms on magnesium oxide are a prime candidate in this regard [264] and during the writing of this thesis the Fe dipole sensing technique was used to remotely read out the magnetic states of two holmium atoms which had their magnetic states written by the STM tip [232]. These experiments could be scaled up to include arrays of Ho atoms, as was done for clusters of 5-12 atoms by Loth [137] and Khajetoorians [265] to examine the interface between single atom-magnetism and collective magnetic dynamics of magnetic structures.

Measuring molecular magnetism

The nano-GPS scheme presented here provides a new route to atomic-scale structural imaging of nanostructures that can be assembled or placed on the surface, such as magnetic molecules. An excellent candidate for the first experiments of molecular magnets with this technique is terbium (III) phthalocyanine (TbPc_2) as it has already demonstrated interesting magnetic behaviour when deposited on MgO [266]. The terbium atom has an electronic spin state of $J = 6$ with an unpaired electron delocalized over the phthalocyanine ligands. Dipole sensing the magnetic field from this unpaired electron could illuminate aspects of the internal magnetic structure not available to other techniques.

Probing nuclear spins

ESR-STM could allow for the measurement of nuclear spin via the hyperfine interaction between the electrons and the nuclei. The most common isotope of iron is ^{56}Fe , which has nuclear spin-0. As a result, ^{56}Fe does not have a nuclear spin with a non-zero magnetic moment and so it is not a suitable candidate for exploring hyperfine coupling with ESR-STM. However, ^{57}Fe has an additional neutron and a nuclear spin of $1/2$. By depositing isotopically pure ^{57}Fe on the MgO surface and performing ESR-STM frequency sweeps it may be possible to read out the nuclear spin state via the ESR signal. This is potentially very interesting as an architecture for engineering a qubit, as the nuclear spin should have a long relaxation time and quantum phase coherence in comparison to the electronic spin.

Developing a pulsed ESR-STM technique

The results reported in Part III relied on continuous wave ESR-STM, a technique which is not capable of phase coherent measurement of the electron spin. This limits continuous wave ESR-STM's usefulness for use in quantum computing. Pulsed ESR-STM, in which microwave bias pulses are delivered in short bursts on resonance, should allow quantum manipulation of the electron spin, if the technique can be realized. A potential method for doing so, involving oscillating the tip in phase with microwave pulse delivery and DC probe read-out is presented in Appendix C.

8.4 Leaving Flatland

This thesis has characterized two tools for exploring Flatland: FT-STs and dipole sensing ESR-STM. FT-STs is a heavily-used, important experimental method for probing complicated materials. It was demonstrated that set-point related artifacts that affect this measurement mode are not as well understood as needed even in the simplest of physical systems that exhibit QPI. Dipole sensing ESR-STM is an emerging experimental method that shows great potential but so far has only been performed by a single experimental group. By carefully

documenting the dipole sensing procedure and fully characterizing the Fe atom sensor this work will allow others to reproduce and test these results, applying them to other systems and probing new nanoscale magnetic phenomena.

This thesis concludes by reminding the reader that of the possible nanoscale Flatlands that can be explored, this work explores only two. The detailed physics of uncountably many more remains to be explored using as many experimental, theoretical, and computational techniques as scientists have the will to invent.

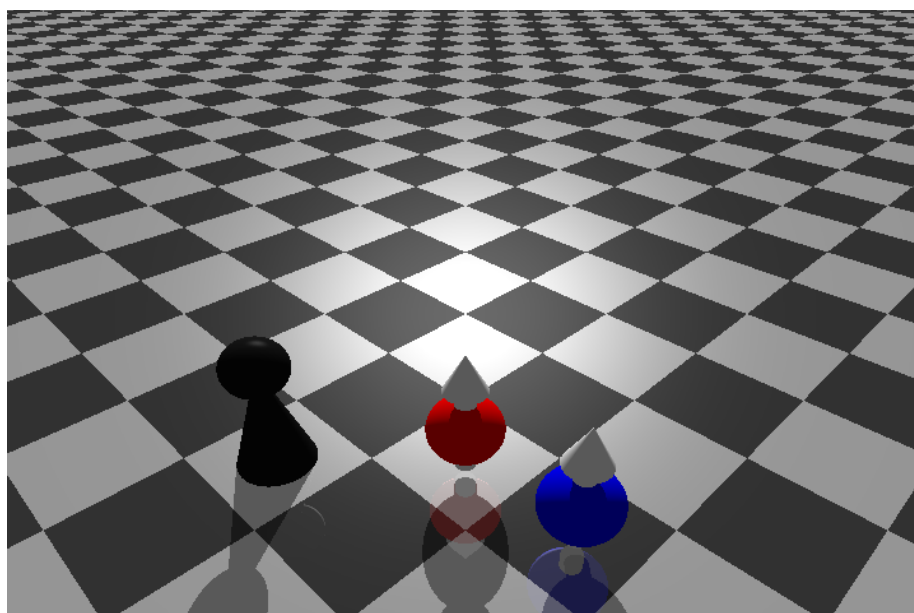


Figure 8.1: **Artistic depiction of nanoscale Flatland as a chessboard with electronic pieces.**

Bibliography

- [1] H. Fabing and R. Marr, editors. *Fischerisms*. Springfield, Ill., Baltimore, Md., 1944.
- [2] E. A. Abbott. *Flatland: A romance of many dimensions*. Seeley & Co, London, UK, 1884.
- [3] Into the Void. Flatland & the 4th Dimension - Carl Sagan. Accessed: 2017-06-12.
- [4] J. E. Moore. The birth of topological insulators. *Nature*, 464(7286):194–198, mar 2010.
- [5] M. Z. Hasan and C. L. Kane. Colloquium: Topological insulators. *Rev. Mod. Phys.*, 82:3045–3067, Nov 2010.
- [6] N. W. Ashcroft and D. Mermin. *Solid State Physics*. Holt Rinehart & Winston, 2002.
- [7] G. Baym and C. Pethick. *Landau Fermi-Liquid Theory: Concepts and Applications*. John Wiley & Sons, 2008.
- [8] S. D. Kevan and R. H. Gaylord. High-resolution photoemission study of the electronic structure of the noble-metal (111) surfaces. *Phys. Rev. B*, 36:5809–5818, Oct 1987.
- [9] J. Alicea. New directions in the pursuit of Majorana fermions in solid state systems. *Reports on Progress in Physics*, 75(7):076501, 2012.
- [10] K. S. Novoselov, A. K. Geim, S. V. Morozov, D. Jiang, Y. Zhang, S. V. Dubonos, I. V. Grigorieva, and A. A. Firsov. Electric field effect in atomically thin carbon films. *Science*, 306:666–669, 2004.
- [11] K. S. Novoselov, D. Jiang, T. Booth, V.V. Khotkevich, S. M. Morozov, and A. K. Geim. Two-dimensional atomic crystals. *Proc. Natl Acad. Sci. USA*, 102:10451–10453, 2005.
- [12] R. Paniago, R. Matzdorf, G. Meister, and A. Goldmann. Temperature dependence of Shockley-type surface energy bands on Cu(111), Ag(111) and Au(111). *Surface Science*, 336(1-2):113–122, 1995.
- [13] N. Nakagawa, H. Y. Hwang, and D. A. Muller. Why some interfaces cannot be sharp. *Nature Materials*, 5:204–209, 2006.

-
- [14] D. Fournier, G. Levy, Y. Pennec, J. L. McChesney, A. Bostwick, E. Rotenberg, R. Liang, W. N. Hardy, D. A. Bonn, I. S. Elfimov, and A. Damascelli. Loss of nodal quasiparticle integrity in underdoped $\text{YBa}_2\text{Cu}_3\text{O}_{6+x}$. *Nature Physics*, 6:905–911, 2010.
- [15] J. D. F. Mottorshead. *Angle Resolved Photoemission Spectroscopy Studies of $\text{Tl}_2\text{Ba}_2\text{CuO}_{6+\delta}$ and $\text{YBa}_2\text{Cu}_3\text{O}_{7-\delta}$: Analysis of recent results and the construction of a new system*. PhD thesis, University of British Columbia, Vancouver, BC, 2012.
- [16] T. Kinoshita and D. R. Yennie. High precision test of quantum electrodynamics - an overview. In T. Kinoshita, editor, *Quantum Electrodynamics*, pages 1–11. World Scientific Publishing Co. Pt. Ltd., Singapore, 1990.
- [17] Public Domain Pictures. DNA-Biology. Accessed: 2017-06-12.
- [18] Wikimedia Foundation. File:Third folio.JPG. Accessed: 2017-06-12.
- [19] S. Nadj-Perge, I. K. Drozdov, J. Li, H. Chen, S. Jeon, J. Seo, A. H. MacDonald, B. A. Bernevig, and A. Yazdani. Observation of Majorana fermions in ferromagnetic atomic chains on a superconductor. *Science*, 346(6209):602–7, 2014.
- [20] Y. Wang, D. Wong, A. V. Shytov, V. W. Brar, S. Choi, Q. Wu, H.-Z. Tsai, W. Regan, A. Zettl, R. K. Kawakami, S. G. Louie, L. S. Levitov, and M. F. Crommie. Observing Atomic Collapse Resonances in Artificial Nuclei on Graphene. *Science*, 340(6133):734–737, 2013.
- [21] K. A. Cochran, A. Schiffrin, T. S. Roussy, M. Capsoni, and S. A. Burke. Pronounced polarization-induced energy level shifts at boundaries of organic semiconductor nanostructures. *Nature communications*, 6:8312, 2015.
- [22] J. M. LeBeau, S. D. Findlay, L. J. Allen, and S. Stemmer. Quantitative Atomic Resolution Scanning Transmission Electron Microscopy. *Phys. Rev. Lett.*, 100:206101, May 2008.
- [23] S. J. Pennycook and P. D. Nellist, editors. *Scanning Transmission Electron Microscopy*. Springer, New York, 2011.
- [24] G. Binnig, C. F. Quate, and C. Gerber. Atomic Force Microscope. *Phys. Rev. Lett.*, 56:930–933, Mar 1986.
- [25] S. Morita, R. Wiesendanger, and E. Meyer. *Noncontact Atomic Force Microscopy*. Nanoscience and Technology. Springer, 2002.
- [26] G. Binnig, H. Rohrer, C. Gerber, and E. Weibel. Surface Studies by Scanning Tunneling Microscopy. *Phys. Rev. Lett.*, 49:57–61, Jul 1982.

-
- [27] R. Wiesendanger. *Scanning Probe Microscopy and Spectroscopy: Methods and Applications*. Scanning Probe Microscopy and Spectroscopy: Methods and Applications. Cambridge University Press, 1994.
- [28] Wikimedia Foundation. Chessboard and chess pieces. Accessed: 2017-06-15.
- [29] E. Merzbacher. The Early History of Quantum Tunnelling. *Physics Today*, pages 44–49, 2002.
- [30] A. B. Balantekin and N. Takigawa. Quantum tunneling in nuclear fusion. *Rev. Mod. Phys.*, 70:77–100, Jan 1998.
- [31] G. Gamow. Zer Quantentheorie des Atomkernes. *Z. Phys.*, 51(3):204–212, 1928.
- [32] R. W. Gurney and E. U. Condon. Wave Mechanics and Radioactive Disintegration. *Nature*, 122:439, September 1928.
- [33] R. W. Gurney and E. U. Condon. Quantum Mechanics and Radioactive Disintegration. *Phys. Rev.*, 33:127–140, Feb 1929.
- [34] B. Bleaney. Microwave spectroscopy in oxford: The first decade part I: Microwave gas spectroscopy. *Contemporary Physics*, 25(4):315–329, 1984.
- [35] F. Hund. Zur Deutung der Molekelspektren. I. *Z. Phys.*, 40(10):742–764, 1927.
- [36] F. Hund. Zur Deutung der Molekelspektren. III. *Z. Phys.*, 43(11):805–826, 1927.
- [37] L. Nordheim. Zur Theorie der thermischen Emission und der Reflexion von Elektronen an Metallen. *Z. Phys.*, 46(11):833–855, 1928.
- [38] R. H. Fowler and L. Nordheim. Electronic Emission in Intense Electric Fields. *Proc. R. Soc. London, Ser. A*, 119:173–181, 1928.
- [39] J. R. Oppenheimer. Three Notes on the Quantum Theory of Aperiodic Effects. *Phys. Rev.*, 31:66–81, Jan 1928.
- [40] J. R. Oppenheimer. On the Quantum Theory of the Autoelectric Field Currents. *Proceedings of the National Academy of Sciences*, 14(5):363–365, 1928.
- [41] C. Zener. A Theory of the Electrical Breakdown of Solid Dielectrics. *Proceedings of the Royal Society of London A: Mathematical, Physical and Engineering Sciences*, 145(855):523–529, 1934.
- [42] E. W. Müller. Elektronenmikroskopische Beobachtungen von Feldkathoden. *Z. Phys.*, 106(9):541–550, Sep 1937.

-
- [43] E. W. Müller. Weitere Beobachtungen mit dem Feldelektronenmikroskop. *Z. Phys.*, 108(9):668–680, September 1938.
- [44] J. Bardeen. Tunnelling from a Many-Particle Point of View. *Phys. Rev. Lett.*, 6:57–59, Jan 1961.
- [45] J. G. Simmons. Generalized Formula for the Electric Tunnel Effect between Similar Electrodes Separated by a Thin Insulating Film. *Journal of Applied Physics*, 34(6):1793–1803, 1963.
- [46] I. Giaever. Electron Tunneling Between Two Superconductors. *Phys. Rev. Lett.*, 5:464–466, Nov 1960.
- [47] B. D. Josephson. Possible new effects in superconductive tunnelling. *Physics Letters*, 1(7):251 – 253, 1962.
- [48] R. Young, J. Ward, and F. Scire. The Topografiner: An Instrument for Measuring Surface Microtopography. *Review of Scientific Instruments*, 43(7):999–1011, 1972.
- [49] G. Binnig and H. Rohrer. Scanning tunneling microscopy. *Helvetica Physica Acta*, 55:726–735, 1982.
- [50] G. Binnig, H. Rohrer, C. Gerber, and E. Weibel. 7 x 7 Reconstruction on Si(111) Resolved in Real Space. *Phys. Rev. Lett.*, 50:120–123, Jan 1983.
- [51] J. V. Barth, H. Brune, G. Ertl, and R. J. Behm. Scanning tunneling microscopy observations on the reconstructed Au(111) surface: Atomic structure, long-range superstructure, rotational domains, and surface defects. *Phys. Rev. B*, 42:9307–9318, Nov 1990.
- [52] W. D. Wise, M. C. Boyer, K. Chatterjee, T. Kondo, T. Takeuchi, H. Ikuta, Y. Wang, and Hudson E. W. Charge-density-wave origin of cuprate checkerboard visualized by scanning tunnelling microscopy. *Nat. Phys.*, 4:696–699, 2008.
- [53] B. Schuler, S. Fatayer, F. Mohn, N. Moll, N. Pavlicek, G. Meyer, D. Pena, and L. Gross. Reversible Bergman cyclization by atomic manipulation. *Nature Chemistry*, 8:220–224, 2016.
- [54] M. F. Crommie, C. P. Lutz, and D. M. Eigler. Confinement of Electrons to Quantum Corrals on a Metal Surface. *Science*, 262(5131):218–220, 1993.
- [55] E. J. Heller, M. F. Crommie, C. P. Lutz, and D. M. Eigler. Scattering and absorption of surface electron waves in quantum corrals. *Nature*, 369:464–466, 1994.
- [56] H. C. Manoharan, C. P. Lutz, and D. M. Eigler. Quantum mirages formed by coherent projection of electronic structure. *Nature*, 403:512–513, 2000.

-
- [57] F. E. Kalff, M. P. Rebergen, E. Fahrenfort, J. Girovsky, R. Toskovic, J. L. Lado, J. Fernandez-Rossier, and A. F. Otte. A kilobyte rewritable atomic memory. *Nature Nanotechnology*, 11:926–929, 2016.
- [58] IBM. A Boy and His Atom: The World’s Smallest Movie. Accessed: 2017-06-12.
- [59] J. Repp, G. Meyer, S. M. Stojković, A. Gourdon, and C. Joachim. Molecules on Insulating Films: Scanning-Tunneling Microscopy Imaging of Individual Molecular Orbitals. *Phys. Rev. Lett.*, 94:026803, Jan 2005.
- [60] J. Li, W.-D. Schneider, R. Berndt, O. Bryant, and S. Crampin. Surface-State Lifetime Measured by Scanning Tunneling Spectroscopy. *Physical Review Letters*, 81(20):4464–4467, 1998.
- [61] A. Damascelli. Probing the Electronic Structure of Complex Systems by ARPES. *Physica Scripta*, 2004(T109):61, 2004.
- [62] R. Ohmann, L. K. Ono, H.-S. Kim, H. Lin, M. V. Lee, Y. Li, N.-G. Park, and Y. Qi. Real-Space Imaging of the Atomic Structure of Organic-Inorganic Perovskite. *Journal of the American Chemical Society*, 137(51):16049–16054, 2015. PMID: 26639900.
- [63] Ø. Fischer, M. Kugler, I. Maggio-Aprile, C. Berthod, and C. Renner. Scanning tunneling spectroscopy of high-temperature superconductors. *Rev. Mod. Phys.*, 79:353–419, Mar 2007.
- [64] M. Bode. Spin-polarized scanning tunnelling microscopy. *Reports on Progress in Physics*, 66(4):523, 2003.
- [65] J. Tersoff and D. R. Hamann. Theory and Application for the Scanning Tunneling Microscope. *Phys. Rev. Lett.*, 50:1998–2001, Jun 1983.
- [66] J. Tersoff and D. R. Hamann. Theory of the scanning tunneling microscope. *Phys. Rev. B*, 31:805–813, Jan 1985.
- [67] T. E. Feuchtwang, P. H. Cutler, and N. M. Miskovsky. A theory of vacuum tunneling microscopy. *Physics Letters A*, 99(4):167 – 171, 1983.
- [68] J. G. Simmons. Generalized Formula for the Electric Tunnel Effect between Similar Electrodes Separated by a Thin Insulating Film. *Journal of Applied Physics*, 34(6):1793–1803, 1963.
- [69] V. A. Ukraintsev. Data evaluation technique for electron-tunneling spectroscopy. *Physical Review B*, 53(16):11176–11185, 1996.
- [70] C. J. Chen. Origin of atomic resolution on metal surfaces in scanning tunneling microscopy. *Phys. Rev. Lett.*, 65:448–451, Jul 1990.
- [71] C. J. Chen. Tunneling matrix elements in three-dimensional space: The derivative rule and the sum rule. *Phys. Rev. B*, 42:8841–8857, Nov 1990.

-
- [72] C. J. Chen. *Introduction to Scanning Tunnelling Microscopy*. Oxford series in optical and imaging sciences. Oxford University Press, USA, 1993.
- [73] J. A. Appelbaum and W. F. Brinkman. Theory of Many-Body Effects in Tunneling. *Phys. Rev.*, 186:464–470, Oct 1969.
- [74] T. E. Feuchtwang. Tunneling theory without the transfer-Hamiltonian formalism. I. *Phys. Rev. B*, 10:4121–4134, Nov 1974.
- [75] T. E. Feuchtwang. Tunneling theory without the transfer-Hamiltonian formalism. II. Resonant and inelastic tunneling across a junction of finite width. *Phys. Rev. B*, 10:4135–4150, Nov 1974.
- [76] T. E. Feuchtwang. Theory of tunneling without transfer Hamiltonian: Relation between continuum and discrete formalisms, and equivalence with elementary theory for noninteracting systems. *Phys. Rev. B*, 12:3979–3983, Nov 1975.
- [77] T. E. Feuchtwang. Tunneling theory without the transfer-Hamiltonian formalism. IV. The abrupt (zero-width) three-dimensional junction. *Phys. Rev. B*, 13:517–530, Jan 1976.
- [78] T. E. Feuchtwang. Tunneling theory without the transfer Hamiltonian formalism. V. A theory of inelastic-electron-tunneling spectroscopy. *Phys. Rev. B*, 20:430–445, Jul 1979.
- [79] M. Ziegler, N. Néel, A. Sperl, J. Kröger, and R. Berndt. Local density of states from constant-current tunneling spectra. *Physical Review B*, 80(12):1–6, 2009.
- [80] C. Hellenthal, R. Heimbuch, K. Sotthewes, E. S. Kooij, and H. J. W. Zandvliet. Determining the local density of states in the constant current STM mode. *Physical Review B*, 88(3):1–6, 2013.
- [81] J. Li, W.-D. Schneider, and R. Berndt. Local density of states from spectroscopic scanning-tunneling-microscope images: Ag(111). *Physical Review B*, 56(12):7656–7659, 1997.
- [82] C. Wittneven, R. Dombrowski, M. Morgenstern, and R. Wiesendanger. Scattering States of Ionized Dopants Probed by Low Temperature Scanning Tunneling Spectroscopy. *Phys. Rev. Lett.*, 81:5616–5619, Dec 1998.
- [83] A. Selloni, P. Carnevali, E. Tosatti, and C. D. Chen. Voltage-dependent scanning-tunneling microscopy of a crystal surface: Graphite. *Phys. Rev. B*, 31:2602–2605, Feb 1985.
- [84] R. M. Feenstra, J. A. Stroscio, and A. P. Fein. Tunneling spectroscopy of the Si(111)2×1 surface. *Surface Science*, 181(1):295 – 306, 1987.

-
- [85] P. T. Sprunger, L. Petersen, E. W. Plummer, E. Lægsgaard, and F. Besenbacher. Giant Friedel Oscillations on the Beryllium (0001) Surface. *Science*, 275(5307):1764–1767, 1997.
- [86] S. Baumann, W. Paul, T. Choi, C. P. Lutz, A. Ardavan, and A. J. Heinrich. Electron paramagnetic resonance of individual atoms on a surface. *Science*, 350(6259):417–420, 2015.
- [87] J. E. Hoffman, E. W. Hudson, K. M. Lang, V. Madhavan, H. Eisaki, S. Uchida, and J. C. Davis. A Four Unit Cell Periodic Pattern of Quasi-Particle States Surrounding Vortex Cores in $\text{Bi}_2\text{Sr}_2\text{CaCu}_2\text{O}_{8+\delta}$. *Science*, 295(5554):466–469, 2002.
- [88] J. E. Hoffman, E. McElroy, D.-H. Lee, K. M. Lang, H. Eisaki, S. Uchida, and J. C. Davis. Imaging Quasiparticle Interference in $\text{Bi}_2\text{Sr}_2\text{CaCu}_2\text{O}_{8+d}$. *Science*, 297(5584):1148–1151, 2002.
- [89] K. McElroy, R. W. Simmonds, J. E. Hoffman, D.-H. Lee, J. Orenstein, H. Eisaki, S. Uchida, and J. C. Davis. Relating atomic-scale electronic phenomena to wave-like quasiparticle states in superconducting $\text{Bi}_2\text{Sr}_2\text{CaCu}_2\text{O}_{8+\delta}$. *Nature*, 422(6932):592–596, 2003.
- [90] T. Hanaguri, Y. Kohsaka, J. C. Davis, C. Lupien, I. Yamada, M. Azuma, M. Takano, K. Ohishi, M. Ono, and H. Takagi. Quasiparticle interference and superconducting gap in $\text{Ca}_{2-x}\text{Na}_x\text{CuO}_2\text{Cl}_2$. *Nature Physics*, 3(12):865–871, 2007.
- [91] T. Hanaguri, Y. Kohsaka, M. Ono, M. Maltseva, P. Coleman, I. Yamada, M. Azuma, M. Takano, K. Ohishi, and H. Takagi. Coherence Factors in a High-Tc Cuprate Probed by Quasi-Particle Scattering Off Vortices. *Science*, 323(April):923–927, 2009.
- [92] K. Fujita, M. H. Hamidian, S. D. Edkins, C. K. Kim, Y. Kohsaka, M. Azuma, M. Takano, H. Takagi, H. Eisaki, S.-I. Uchida, A. Allais, M. J. Lawler, E.-A. Kim, S. Sachdev, and J. C. S. Davis. Direct phase-sensitive identification of a d-form factor density wave in underdoped cuprates. *Proceedings of the National Academy of Sciences*, pages 1–7, 2014.
- [93] Y. He, Y. Yin, M. Zech, A. Soumyanarayanan, M. M. Yee, T. Williams, M. C. Boyer, K. Chatterjee, W. D. Wise, I. Zeljkovic, T. Kondo, T. Takeuchi, H. Ikuta, P. Mistark, R. S. Markiewicz, A. Bansil, S. Sachdev, E. W. Hudson, and J. E. Hoffman. Fermi surface and pseudogap evolution in a cuprate superconductor. *Science*, 344(May):608–11, 2014.
- [94] T.-M. Chuang, M. P. Allan, J. Lee, Y. Xie, N. Ni, S. L. Bud’ko, G. S. Boebinger, P. C. Canfield, and J. C. Davis. Nematic electronic structure in the “parent” state of the iron-based superconductor $\text{Ca}(\text{Fe}_{1-x}\text{Co}_x)_2\text{As}_2$. *Science*, 327(5962):181–184, 2010.

-
- [95] T. Hanaguri, S. Niitaka, K. Kuroki, and H. Takagi. Unconventional s-wave superconductivity in Fe(Se,Te). *Science*, 328(2010):474–476, 2010.
- [96] M. P. Allan, A. W. Rost, A. P. Mackenzie, Y. Xie, J. C. Davis, K. Kihou, C. H. Lee, A. Iyo, H. Eisaki, and T.-M. Chuang. Anisotropic energy gaps of iron-based superconductivity from intraband quasiparticle interference in LiFeAs. *Science*, 336(6081):563–7, 2012.
- [97] S. Chi, S. Johnston, G. Levy, S. Grothe, R. Szedlak, B. Ludbrook, R. Liang, P. Dosanjh, S. A. Burke, A. Damascelli, D. A. Bonn, W. N. Hardy, and Y. Pennec. Sign inversion in the superconducting order parameter of LiFeAs inferred from Bogoliubov quasiparticle interference. *Physical Review B*, 89(10):1–10, 2014.
- [98] D. Huang, C. L. Song, T. A. Webb, S. Fang, C. Z. Chang, J. S. Moodera, E. Kaxiras, and J. E. Hoffman. Revealing the Empty-State Electronic Structure of Single-Unit-Cell FeSe/SrTiO₃. *Physical Review Letters*, 115(1):1–5, 2015.
- [99] P. Aynajian, E. H. da Silva Neto, A. Gyenis, R. E. Baumbach, J. D. Thompson, Z. Fisk, E. D. Bauer, and A. Yazdani. Visualizing heavy fermions emerging in a quantum critical Kondo lattice. *Nature*, 486(7402):201–6, 2012.
- [100] M. P. Allan, F. Massee, D. K. Morr, J. Van Dyke, A. W. Rost, A. P. Mackenzie, C. Petrovic, and J. C. Davis. Imaging Cooper pairing of heavy fermions in CeCoIn₅. *Nature Physics*, 9(8):14, 2013.
- [101] B. B. Zhou, S. Misra, E. H. da Silva Neto, P. Aynajian, R. E. Baumbach, J. D. Thompson, E. D. Bauer, and A. Yazdani. Visualizing nodal heavy fermion superconductivity in CeCoIn₅. *Nature Physics*, 9(8):474–479, 2013.
- [102] P. Roushan, J. Seo, C. V. Parker, Y. S. Hor, D. Hsieh, D. Qian, A. Richardella, M. Z. Hasan, R. J. Cava, and A. Yazdani. Topological surface states protected from backscattering by chiral spin texture. *Nature*, 460(7259):1106–1109, 2009.
- [103] H. Beidenkopf, P. Roushan, J. Seo, L. Gorman, I. Drozdov, Y. S. Hor, R. J. Cava, and A. Yazdani. Spatial fluctuations of helical Dirac fermions on the surface of topological insulators. *Nature Physics*, 7(12):939–943, 2011.
- [104] Y. Okada, C. Dhital, W. Zhou, E. D. Huemiller, H. Lin, S. Basak, A. Bansil, Y. B. Huang, H. Ding, Z. Wang, S. D. Wilson, and V. Madhavan. Direct observation of broken time-reversal symmetry on the surface of a magnetically doped topological insulator. *Physical Review Letters*, 106(20):1–4, 2011.

-
- [105] T. Zhang, N. Levy, J. Ha, Y. Kuk, and J. A. Stroscio. Scanning tunneling microscopy of gate tunable topological insulator Bi_2Se_3 thin films. *Physical Review B*, 87(11):1–6, 2013.
- [106] A. Eich, M. Michiardi, G. Bihlmayer, X. G. Zhu, J. L. Mi, B. B. Iversen, R. Wiesendanger, P. Hofmann, A. A. Khajetoorians, and J. Wiebe. Intra- and interband electron scattering in a hybrid topological insulator: Bismuth bilayer on Bi_2Se_3 . *Physical Review B*, 90(15):1–10, 2014.
- [107] P. Sessi, F. Reis, T. Bathon, K. A. Kokh, O. E. Tereshchenko, and M. Bode. Signatures of Dirac fermion-mediated magnetic order. *Nature communications*, 5(May):5349, 2014.
- [108] I. Zeljkovic, Y. Okada, C.-Y. Huang, R. Sankar, D. Walkup, W. Zhou, M. Serbyn, F. Chou, W.-F. Tsai, H. Lin, A. Bansil, L. Fu, M. Z. Hasan, and V. Madhavan. Mapping the unconventional orbital texture in topological crystalline insulators. *Nature Physics*, 10(8):572–577, 2014.
- [109] Y. Kohsaka, M. Kanou, H. Takagi, T. Hanaguri, and T. Sasagawa. Imaging ambipolar two-dimensional carriers induced by the spontaneous electric polarization of a polar semiconductor BiTeI . *Physical Review B*, 91(24):1–10, 2015.
- [110] G. M. Rutter, J. N. Crain, N. P. Guisinger, T. Li, P. N. First, and J. A. Stroscio. Scattering and interference in epitaxial graphene. *Science*, 317(5835):219–222, 2007.
- [111] P. Mallet, I. Brihuega, S. Bose, M. M. Ugeda, J. M. Gómez-Rodríguez, K. Kern, and J. Y. Veuillen. Role of pseudospin in quasiparticle interferences in epitaxial graphene probed by high-resolution scanning tunneling microscopy. *Physical Review B*, 86(4):1–14, 2012.
- [112] P. Leicht, J. Tesch, S. Bouvron, F. Blumenschein, P. Erler, L. Gragnaniello, and M. Fonin. Rashba splitting of graphene-covered $\text{Au}(111)$ revealed by quasiparticle interference mapping. *Physical Review B*, 90(24):1–5, 2014.
- [113] P. Sessi, V. M. Silkin, I. A. Nechaev, T. Bathon, L. El-Kareh, E. V. Chulkov, P. M. Echenique, and M. Bode. Direct observation of many-body charge density oscillations in a two-dimensional electron gas. *Nature communications*, 6:8691, 2015.
- [114] A. Peres. *Quantum Theory: Concepts and Methods*. Springer Netherlands, Netherlands, 1995.
- [115] S. H. Pan, E. W. Hudson, and J. C. Davis. ^3He refrigerator based very low temperature scanning tunneling microscope. *Review of Scientific Instruments*, 70(2):1459–1463, 1999.

-
- [116] J. Wiebe, A. Wachowiak, F. Meier, D. Haude, T. Foster, M. Morgenstern, and R. Wiesendanger. A 300 mK ultra-high vacuum scanning tunneling microscope for spin-resolved spectroscopy at high energy resolution. *Review of Scientific Instruments*, 75(11):4871–4879, 2004.
- [117] Y. J. Song, A. F. Otte, V. Shvarts, Z. Zhao, Y. Kuk, S. R. Blankenship, A. Band, F. M. Hess, and J. A. Stroscio. Invited Review Article: A 10 mK scanning probe microscopy facility. *Review of Scientific Instruments*, 81(12):121101, 2010.
- [118] K. Iwaya, R. Shimizu, T. Hashizume, and T. Hitosugi. Systematic analyses of vibration noise of a vibration isolation system for high-resolution scanning tunneling microscopes. *Review of Scientific Instruments*, 82(8):083702, 2011.
- [119] S. Misra, B. B. Zhou, I. K. Drozdov, J. Seo, L. Urban, A. Gyenis, S. C. J. Kingsley, H. Jones, and A. Yazdani. Design and performance of an ultra-high vacuum scanning tunneling microscope operating at dilution refrigerator temperatures and high magnetic fields. *Review of Scientific Instruments*, 84(10):103903, 2013.
- [120] M. Assig, M. Etzkorn, A. Enders, W. Stiepany, C. R. Ast, and K. Kern. A 10 mK scanning tunneling microscope operating in ultra high vacuum and high magnetic fields. *Review of Scientific Instruments*, 84(3):033903, 2013.
- [121] U. R. Singh, M. Enayat, S. C. White, and P. Wahl. Construction and performance of a dilution-refrigerator based spectroscopic-imaging scanning tunneling microscope. *Review of Scientific Instruments*, 84(1):013708, 2013.
- [122] B. Voigtländer, P. Coenen, V. Cherepanov, P. Borgens, T. Duden, and F. S. Tautz. Low vibration laboratory with a single-stage vibration isolation for microscopy applications. *Review of Scientific Instruments*, 88(2):023703, 2017.
- [123] B. MacLeod. An ultra-low-vibration facility for housing a dilution temperature scanning tunneling microscope. Master’s thesis, University of British Columbia, Vancouver, BC, 2015.
- [124] B. P. MacLeod, J. E. Hoffman, S. A. Burke, and D. A. Bonn. Acoustic buffeting by infrasound in a low vibration facility. *Review of Scientific Instruments*, 87(9):093901, 2016.
- [125] S. Zöphel. *The building of a low temperature scanning tunneling microscope and structural investigations on vicinal copper surfaces*. PhD thesis, Feie Universität Berlin, 2000.

-
- [126] A. Schiffrin. *Self-assembly of amino acids on noble metal surfaces: morphological, chemical and electronic control of matter at the nanoscale*. PhD thesis, University of British Columbia, Vancouver, BC, 2008.
- [127] S. Chi. *Scanning Tunneling Microscopy Study of Superconducting Pairing Symmetry: Application to LiFeAs*. PhD thesis, University of British Columbia, Vancouver, BC, 2014.
- [128] S. Grothe. *Many-body phenomena from a local perspective*. PhD thesis, University of British Columbia, Vancouver, BC, 2015.
- [129] K. Besocke. An easily operable scanning tunneling microscope. *Surface Science*, 181(1):145 – 153, 1987.
- [130] R. R. Schulz and C. Rossel. Beetle-like scanning tunneling microscope for ultrahigh vacuum and low-temperature applications. *Review of Scientific Instruments*, 65(6):1918–1922, 1994.
- [131] J. Frohn, J. F. Wolf, K. Besocke, and M. Teske. Coarse tip distance adjustment and positioner for a scanning tunneling microscope. *Review of Scientific Instruments*, 60(6):1200–1201, 1989.
- [132] S. Grothe, S. Johnston, S. Chi, P. Dosanjh, S. A. Burke, and Y. Peneec. Quantifying many-body effects by high-resolution fourier transform scanning tunneling spectroscopy. *Physical Review Letters*, 111(24):1–5, 2013.
- [133] G. P. Collins. STM Rounds up Electron Waves at the QM Corral. *Physics Today*, 46(11):17, 1993.
- [134] C. Toumey. 35 atoms that changed the nanoworld. *Nature Nanotechnology*, 5:239–241, 2010.
- [135] A. J. Heinrich. Atomic spins on surfaces. *Physics Today*, 68(3):42–47, 2015.
- [136] D. M. Eigler and E. K. Schweizer. Positioning single atoms with a scanning tunnelling microscope. *Nature*, 344:524–526, 1990.
- [137] S. Loth, S. Baumann, C. P. Lutz, D. M. Eigler, and A. J. Heinrich. Bistability in Atomic-Scale Antiferromagnets. *Science*, 335(6065):196–199, 2012.
- [138] A. J. Heinrich, J. A. Gupta, C. P. Lutz, and D. M. Eigler. Single-Atom Spin-Flip Spectroscopy. *Science*, 306(5695):466–469, 2004.
- [139] C. F. Hirjibehedin, C. P. Lutz, and A. J. Heinrich. Spin Coupling in Engineered Atomic Structures. *Science*, 312(5776):1021–1024, 2006.

-
- [140] C. F. Hirjibehedin, C.-Y. Lin, A. F. Otte, M. Ternes, C. P. Lutz, B. A. Jones, and A. J. Heinrich. Large Magnetic Anisotropy of a Single Atomic Spin Embedded in a Surface Molecular Network. *Science*, 317(5842):1199–1203, 2007.
- [141] A. F. Otte, M. Ternes, K. von Bergmann, S. Loth, H. Brune, C. P. Lutz, C. F. Hirjibehedin, and A. J. Heinrich. The role of magnetic anisotropy in the Kondo effect. *Nature Physics*, 4:847–850, 2008.
- [142] A. F. Otte, M. Ternes, S. Loth, C. P. Lutz, C. F. Hirjibehedin, and A. J. Heinrich. Spin Excitations of a Kondo-Screened Atom Coupled to a Second Magnetic Atom. *Phys. Rev. Lett.*, 103:107203, Sep 2009.
- [143] S. Loth, M. Etzkorn, C. P. Lutz, D. M. Eigler, and A. J. Heinrich. Measurement of Fast Electron Spin Relaxation Times with Atomic Resolution. *Science*, 329(5999):1628–1630, 2010.
- [144] S. Loth, C. P. Lutz, and A. J. Heinrich. Spin-polarized spin excitation spectroscopy. *New Journal of Physics*, 12(12):125021, 2010.
- [145] I. G. Rau, S. Baumann, S. Rusponi, F. Donati, S. Stepanow, L. Gragnaniello, J. Dreiser, C. Piamonteze, F. Nolting, S. Gangopadhyay, O. R. Albertini, R. M. Macfarlane, C. P. Lutz, B. A. Jones, P. Gambardella, A. J. Heinrich, and H. Brune. Reaching the magnetic anisotropy limit of a 3d metal atom. *Science*, 344(6187):988–992, 2014.
- [146] A. J. Heinrich, C. P. Lutz, J. A. Gupta, and D. M. Eigler. Molecule Cascades. *Science*, 2002.
- [147] S. Grothe, S. Chi, P. Dosanjh, R. Liang, W. N. Hardy, S. A. Burke, D. A. Bonn, and Y. Pennec. Bound states of defects in superconducting LiFeAs studied by scanning tunneling spectroscopy. *Phys. Rev. B*, 86:174503, Nov 2012.
- [148] S. Chi, S. Grothe, R. Liang, P. Dosanjh, W. N. Hardy, S. A. Burke, D. A. Bonn, and Y. Pennec. Scanning Tunneling Spectroscopy of Superconducting LiFeAs Single Crystals: Evidence for Two Nodeless Energy Gaps and Coupling to a Bosonic Mode. *Phys. Rev. Lett.*, 109:087002, Aug 2012.
- [149] C. Straßer, B. M. Ludbrook, G. Levy, A. J. Macdonald, S. A. Burke, T. O. Wehling, K. Kern, A. Damascelli, and C. R. Ast. Long-versus Short-Range Scattering in Doped Epitaxial Graphene. *Nano letters*, 15(5):2825–2829, 2015.
- [150] D. E. Shasha and C. A. Lazere. *Out of their Minds: The Lives and Discoveries of 15 Great Computer Scientists*. Springer-Verlag, New York, 1998.
- [151] É. Daniel. How the Friedel oscillations entered the physics of metallic alloys. *Comptes Rendus Physique*, 17(34):291 – 293, 2016.

-
- [152] J. Friedel. Metallic alloys. *Il Nuovo Cimento (1955-1965)*, 7(2):287–311, 1958.
- [153] J. E. Hoffman. Spectroscopic scanning tunneling microscopy insights into Fe-based superconductors. *Reports on Progress in Physics*, 74(12):124513, 2011.
- [154] M. F. Crommie, C. P. Lutz, and D. M. Eigler. Imaging standing waves in a two-dimensional electron gas. *Nature*, 363:524, 1993.
- [155] Y. Hasegawa and P. Avouris. Direct observation of standing wave formation at surface steps using scanning tunneling spectroscopy. *Physical Review Letters*, 71(7):1071–1074, 1993.
- [156] C. Bena. Friedel oscillations: Decoding the hidden physics. *Comptes Rendus Physique*, 17(34):302 – 321, 2016.
- [157] J. Villain, M. Lavagna, and P. Bruno. Jacques Friedel and the physics of metals and alloys. *Comptes Rendus Physique*, 17(3):276 – 290, 2016.
- [158] P. Debye and E. Hückel. Zur theorie der elektrolyte. i. gefrierpunktserniedrigung und verwandte erscheinungen. *Phys. Z.*, 24(9):185–206, 1923.
- [159] L. H. Thomas. The calculation of atomic fields. *Mathematical Proceedings of the Cambridge Philosophical Society*, 23(5):542–548, 1927.
- [160] E. Fermi. Un metodo statistico per la determinazione di alcune priorietà dellatomo. *Rend. Accad. Naz. Lincei*, 6:602–607, 1927.
- [161] M. P. Marder. *Condensed Matter Physics*. John Wiley & Sons, Inc., Hoboken, New Jersey, 2010.
- [162] P. Hohenberg and W. Kohn. Inhomogeneous Electron Gas. *Phys. Rev.*, 136:B864–B871, Nov 1964.
- [163] J. Friedel. Electronic Structure of Primary Solid Solutions in Metals. *Advances in Physics*, 3(12):446–507, 1954.
- [164] G. F. Giuliani and G. E. Simion. Friedel oscillations in a two dimensional Fermi liquid. *Solid State Communications*, 127(12):789 – 791, 2003.
- [165] R. Paniago, R. Matzdorf, G. Meister, and A. Goldmann. Temperature dependence of Shockley-type surface energy bands on Cu(111), Ag(111) and Au(111). *Surface Science*, 336(1-2):113 – 122, 1995.
- [166] L. Bürgi, L. Petersen, H. Brune, and K. Kern. Noble metal surface states: Deviations from parabolic dispersion. *Surface Science*, 447(1):157–161, 2000.

-
- [167] F. Reinert, G. Nicolay, S. Schmidt, D. Ehm, and S. Hüfner. Direct measurements of the L-gap surface states on the (111) face of noble metals by photoelectron spectroscopy. *Physical Review B*, 63(11):1–7, 2001.
- [168] G. D. Mahan. *Many-particle physics*. Kluwer Academic/Plenum Publishers, New York, 3rd edition, 2000.
- [169] L. Capriotti, D. J. Scalapino, and R. D. Sedgewick. Wave-vector power spectrum of the local tunneling density of states: Ripples in a d-wave sea. *Phys. Rev. B*, 68:014508, Jul 2003.
- [170] J. Callaway. Theory of Scattering in Solids. *Journal of Mathematical Physics*, 5(6):783–798, 1964.
- [171] J. Callaway. t Matrix and Phase Shifts in Solid-State Scattering Theory*. *Physical Review*, 154(2):515–521, 1967.
- [172] P. Hofmann, B. Briner, M. Doering, H.-P. Rust, E. Plummer, and A. Bradshaw. Anisotropic Two-Dimensional Friedel Oscillations. *Physical Review Letters*, 79(2):265–268, 1997.
- [173] D. Fujita, K. Amemiya, T. Yakabe, H. Nejoh, T. Sato, and M. Iwatsuki. Observation of two-dimensional Fermi contour of a reconstructed Au(111) surface using Fourier transform scanning tunneling microscopy. *Surface Science*, 423:160–168, 1999.
- [174] D. Fujita. Reply to ‘Comment on “Observation of two-dimensional Fermi contour of a reconstructed Au(111) surface using Fourier transform scanning tunneling microscopy” by D. Fujita, K. Amemiya, T. Yakabe, H. Nejoh, T. Sato, M. Iwatsuki’ [Surf. Sci. 423 (1999) 160]. *Surface Science*, 443(1-2):157–158, 1999.
- [175] L. Petersen, P. Sprunger, P. Hofmann, E. Lægsgaard, B. Briner, M. Doering, H.-P. Rust, A. Bradshaw, F. Besenbacher, and E. Plummer. Direct imaging of the two-dimensional Fermi contour: Fourier-transform STM. *Physical Review B*, 57(12):R6858–R6861, 1998.
- [176] L. Petersen, L. Bürgi, H. Brune, F. Besenbacher, and K. Kern. Comment on “Observation of two-dimensional Fermi contour of a reconstructed Au(111) surface using Fourier transform scanning tunneling microscopy” by D. Fujita, K. Amemiya, T. Yakabe, H. Nejoh, T. Sato, M. Iwatsuki [Surf. Sci. 423 (1999) 160]. *Surface Science*, 443(1-2):154–156, 1999.
- [177] L. Petersen, P. Hofmann, E. W. Plummer, and F. Besenbacher. Fourier Transform-STM: Determining the surface Fermi contour. *Journal of Electron Spectroscopy and Related Phenomena*, 109(1):97–115, 2000.
- [178] L. Petersen, B. Schaefer, E. Lægsgaard, I. Stensgaard, and F. Besenbacher. Imaging the surface Fermi contour on Cu(110) with scanning tunneling microscopy. *Surface Science*, 457(3):319–325, 2000.

-
- [179] M. P. Allan, K. Lee, A. W. Rost, M. H. Fischer, F. Masee, K. Kihou, C.-H. Lee, A. Iyo, H. Eisaki, T.-M. Chuang, J. C. Davis, and E.-A. Kim. Identifying the 'fingerprint' of antiferromagnetic spin fluctuations in iron pnictide superconductors. *Nature Physics*, 11(2):177–182, 2014.
- [180] L. Petersen, P. Laitenberger, E. Lægsgaard, and F. Besenbacher. Screening waves from steps and defects on Cu(111) and Au(111) imaged with STM: Contribution from bulk electrons. *Physical Review B*, 58(11):7361–7366, 1998.
- [181] K. Schouteden, P. Lievens, and C. Van Haesendonck. Fourier-transform scanning tunneling microscopy investigation of the energy versus wave vector dispersion of electrons at the Au(111) surface. *Physical Review B*, 79(19):1–7, 2009.
- [182] W. Shockley. On the Surface States Associated with a Periodic Potential. *Phys. Rev.*, 56:317–323, Aug 1939.
- [183] R. Paniago, R. Matzdorf, G. Meister, and A. Goldmann. High-resolution photoemission study of the surface states near gG on Cu(111) and Ag(111). *Surface Science*, 331-333:1233–1237, 1995.
- [184] D. C. Hodgins. What we see depends mainly on what we look for (john lubbock, british anthropologist, 1834-1913). *Addiction*, 103(7):1118–1119, 2008.
- [185] A. J. Macdonald, Y.-S. Tremblay-Johnston, S. Grothe, S. Chi, P. Dosanjh, S. Johnston, and S. A. Burke. Dispersing artifacts in FT-STs: a comparison of set point effects across acquisition modes. *Nanotechnology*, 27(41):1–7, 2016.
- [186] W. M. Haynes. *Crystal Structure Parameters of the Elements*. CRC Press/Taylor & Francis, Boca Raton, FL., 97th edition (internet version 2017) edition, 2017.
- [187] L. Bürgi, O. Jeandupeux, A. Hirstein, H. Brune, and K. Kern. Confinement of Surface State Electrons in Fabry-Pérot Resonators. *Physical Review Letters*, 81(24):5370–5373, 1998.
- [188] L. Bürgi. *Scanning tunneling microscopy as local probe of electron density, dynamics, and transport at metal surfaces*. PhD thesis, Swiss Federal Institute of Technology, Lausanne, Switzerland, 1999.
- [189] L. Bürgi, H. Brune, O. Jeandupeux, and K. Kern. Quantum coherence and lifetimes of surface-state electrons. *Journal of Electron Spectroscopy and Related Phenomena*, 109(1):33–49, 2000.
- [190] L. Bürgi, L. Petersen, H. Brune, and K. Kern. Noble metal surface states: deviations from parabolic dispersion. *Surface Science*, 447:L157L161, 2000.

-
- [191] J. Kliewer, R. Berndt, E. V. Chulkov, V. M. Silkin, and P. M. Echenique. Dimensionality Effects in the Lifetime of Surface States. *Science*, 288(5470):1399–1402, 2000.
- [192] A. Eiguren, B. Hellsing, F. Reinert, G. Nicolay, E. V. Chulkov, E. V. Chulkov, V. M. Silkin, S. Hafner, P. M. Echenique, and P. M. Echenique. Role of bulk and surface phonons in the decay of metal surface states. *Physical Review Letters*, 88(6):66805/1–66805/4, 2002.
- [193] L. Bürgi, N. Knorr, H. Brune, M. A. Schneider, and K. Kern. Two-dimensional electron gas at noble-metal surfaces. *Applied Physics A Materials Science & Processing*, 75:141–145, 2002.
- [194] L. Vitali, P. Wahl, M. A. Schneider, K. Kern, V. M. Silkin, E. V. Chulkov, and P. M. Echenique. Inter- and intraband inelastic scattering of hot surface state electrons at the Ag(111) surface. *Surface Science*, 523(12):L47 – L52, 2003.
- [195] G. Nicolay, F. Reinert, S. Hafner, and P. Blaha. Spin-orbit splitting of the L-gap surface state on Au(111) and Ag(111). *Physical Review B*, 65(3):334071–334074, 2002.
- [196] M. Steinbrecher, H. Harutyunyan, C. R. Ast, and D. Wegner. Rashba-type spin splitting from interband scattering in quasiparticle interference maps. *Physical Review B*, 87(24):1–5, 2013.
- [197] B. Koslowski, C. Dietrich, A. Tschetschetkin, and P. Ziemann. Evaluation of scanning tunneling spectroscopy data: Approaching a quantitative determination of the electronic density of states. *Physical Review B*, 75(3):1–8, 2007.
- [198] G. Hörmandinger. Imaging of the Cu(111) surface state in scanning tunneling microscopy. *Physical Review B*, 49(19):897–906, 1994.
- [199] A. Pronschinske, D. J. Mardit, and D. B. Dougherty. Modeling the constant-current distance-voltage mode of scanning tunneling spectroscopy. *Physical Review B*, 84(20):1–8, 2011.
- [200] G. Hormandinger. Comment on "Direct observation of standing wave formation at surface steps using scanning tunneling spectroscopy". *Physical Review Letters*, 73(6):910, 1994.
- [201] N. Sperling, editor. *Selections from the Journal of Irreproducible Results*. Andrews McNeel Publishing, LLC, Kansas City, Missouri, 2008.
- [202] P. O. Gartland and B. J. Slagsvold. Transitions conserving parallel momentum in photoemission from the (111) face of copper. *Phys. Rev. B*, 12:4047–4058, Nov 1975.

-
- [203] A. Tamai, W. Meevasana, P. D. C. King, C. W. Nicholson, A. de la Torre, E. Rozbicki, and F. Baumberger. Spin-orbit splitting of the Shockley surface state on Cu(111). *Phys. Rev. B*, 87:075113, Feb 2013.
- [204] J. Klijn, L. Sacharow, C. Meyer, S. Blügel, M. Morgenstern, and R. Wiesendanger. STM measurements on the InAs(110) surface directly compared with surface electronic structure calculations. *Phys. Rev. B*, 68:205327, Nov 2003.
- [205] K. Sagisaka and D. Fujita. Standing waves on Si(100) and Ge(100) surfaces observed by scanning tunneling microscopy. *Phys. Rev. B*, 72:235327, Dec 2005.
- [206] F. Mohn, L. Gross, and G. Meyer. Measuring the short-range force field above a single molecule with atomic resolution. *Applied Physics Letters*, 99(5), 2011.
- [207] A. Abragam and B. Bleaney. *Electron Paramagnetic Resonance of Transition Ions*. Oxford University Press, Oxford, 2012.
- [208] B. Bleaney. Paramagnetic Resonance in the Solid State. *The Journal of Physical Chemistry*, 57(5):508–517, 1953.
- [209] G. Jeschke and Y. Polyhach. Distance measurements on spin-labelled biomacromolecules by pulsed electron paramagnetic resonance. *Phys. Chem. Chem. Phys.*, 9:1895–1910, 2007.
- [210] M. A. Nielsen and I. L. Chuang. *Quantum computation and quantum information*. Cambridge University Press, Cambridge, UK, 2000.
- [211] D. Rugar, R. Budakian, H. J. Mamin, and B. W. Chi. Single spin detection by magnetic resonance force microscopy. *Nature*, 430:329–332, 2004.
- [212] A. R. Stegner, C. Boehme, H. Huebl, M. Stutzmann, K. Lips, and M. S. Brandt. Electrical detection of coherent ^3P spin quantum states. *Nature Physics*, 2:835–838, 2006.
- [213] F. H. L. Koppens, C. Buizert, K. J. Tielrooij, I. T. Vink, K. C. Nowack, T. Meunier, L. P. Kouwenhoven, and L. M. K. Vandersypen. Driven coherent oscillations of a single electron spin in a quantum dot. *Nature*, 442:766–771, 2006.
- [214] J. J. Pla, K. Y. Tan, J. P. Dehollain, W. H. Lim, J. J. L. Morton, D. N. Jamieson, A. S. Dzurak, and A. Morello. A single-atom electron spin qubit in silicon. *Nature*, 489:541–545, 2012.
- [215] J. T. Muhonen, J. P. Dehollain, A. Laucht, F. E. Hudson, R. Kalra, T. Sekiguchi, K. M. Itoh, D. N. Jamieson, J. C. McCallum, A. S. Dzurak, and A. Morello. Storing quantum information for 30 seconds in a nanoelectronic device. *Nature Nanotechnology*, 9:986–991, 2014.

-
- [216] S. Thiele, F. Balestro, R. Ballou, S. Klyatskaya, M. Ruben, and W. Wernsdorfer. Electrically driven nuclear spin resonance in single-molecule magnets. *Science*, 344(6188):1135–1138, 2014.
- [217] M. Assig, M. Etzkorn, A. Enders, W. Stiepany, C. R. Ast, and K. Kern. A 10 mK scanning tunneling microscope operating in ultra high vacuum and high magnetic fields. *Review of Scientific Instruments*, 84(3):033903, 2013.
- [218] S. Misra, B. B. Zhou, I. K. Drozdov, J. Seo, L. Urban, A. Gyenis, S. C. J. Kingsley, H. Jones, and A. Yazdani. Design and performance of an ultra-high vacuum scanning tunneling microscope operating at dilution refrigerator temperatures and high magnetic fields. *Review of Scientific Instruments*, 84(10):103903, 2013.
- [219] A. Roychowdhury, M. A. Gubrud, R. Dana, J. R. Anderson, C. J. Lobb, F. C. Wellstood, and M. Dreyer. a 30 mk, 13.5 t scanning tunneling microscope with two independent tips. *Review of Scientific Instruments*, 85(4):043706, 2014.
- [220] A. M. J. den Haan, G. H. C. J. Wijts, F. Galli, O. Usenko, G. J. C. van Baarle, D. J. van der Zalm, and T. H. Oosterkamp. Atomic resolution scanning tunneling microscopy in a cryogen free dilution refrigerator at 15 mK. *Review of Scientific Instruments*, 85(3):035112, 2014.
- [221] C. R. Ast, B. Jäck, J. Senkpiel, M. Eltschka, M. Etzkorn, J. Ankerhold, and K. Kern. Sensing the quantum limit in scanning tunnelling spectroscopy. *Nature Communications*, 7:13009, 2016.
- [222] E. Roduner, P. W. Percival, P. Han, and D. M. Bartels. Isotope and temperature effects on the hyperfine interaction of atomic hydrogen in liquid water and in ice. *The Journal of Chemical Physics*, 102(15):5989–5997, 1995.
- [223] C. Kittel. *Introduction to Solid State Physics*. John Wiley & Sons, New York, 5th edition, 1976.
- [224] Y. Manassen, R. J. Hamers, J. E. Demuth, and A. J. Castellano Jr. Direct observation of the precession of individual paramagnetic spins on oxidized silicon surfaces. *Phys. Rev. Lett.*, 62:2531–2534, May 1989.
- [225] Y. Manassen, I. Mukhopadhyay, and N. R. Rao. Electron-spin-resonance STM on iron atoms in silicon. *Phys. Rev. B*, 61:16223–16228, Jun 2000.
- [226] C. Durkan and M. E. Welland. Electronic spin detection in molecules using scanning-tunneling- microscopy-assisted electron-spin resonance. *Applied Physics Letters*, 80(3):458–460, 2002.
- [227] A. V. Balatsky, M. Nishijima, and Y. Manassen. Electron spin resonance-scanning tunneling microscopy. *Advances in Physics*, 61(2):117–152, 2012.

-
- [228] P. Berggren and J. Fransson. Electron Paramagnetic Resonance of Single Magnetic Moment on a Surface. *Scientific Reports*, 6:25584, 2016.
- [229] S. Müllegger, S. Tebi, A. K. Das, W. Schöffberger, F. Faschinger, and R. Koch. Radio Frequency Scanning Tunneling Spectroscopy for Single-Molecule Spin Resonance. *Phys. Rev. Lett.*, 113:133001, Sep 2014.
- [230] W. Paul, S. Baumann, C. P. Lutz, and A. J. Heinrich. Generation of constant-amplitude radio-frequency sweeps at a tunnel junction for spin resonance STM. *Review of Scientific Instruments*, 87(7):074703, 2016.
- [231] T. Choi, W. Paul, S. Rolf-Pissarczyk, A. J. Macdonald, F. D. Natterer, K. Yang, P. Willke, C. P. Lutz, and A. J. Heinrich. Atomic-scale sensing of the magnetic dipolar field from single atoms. *Nature Nanotechnology*, 12:420–424, 2017.
- [232] F. D. Natterer, K. Yang, W. Paul, P. Willke, T. Choi, T. Greber, A. J. Heinrich, and C. P. Lutz. Reading and writing single-atom magnets. *Nature*, 543:226–228, 2017.
- [233] W. Paul, K. Yang, S. Baumann, N. Romming, T. Choi, C. P. Lutz, and A. J. Heinrich. Control of the millisecond spin lifetime of an electrically probed atom. *Nature Physics*, 13:403–407, 2017.
- [234] D. Wortmann, S. Heinze, P. Kurz, G. Bihlmayer, and S. Blügel. Resolving Complex Atomic-Scale Spin Structures by Spin-Polarized Scanning Tunneling Microscopy. *Phys. Rev. Lett.*, 86:4132–4135, Apr 2001.
- [235] R. Wiesendanger. Spin mapping at the nanoscale and atomic scale. *Rev. Mod. Phys.*, 81:1495–1550, Nov 2009.
- [236] S. Loth, K. von Bergmann, M. Ternes, A. F. Otte, C. P. Lutz, and A. J. Heinrich. Controlling the state of quantum spins with electric currents. *Nature Physics*, 6:340–344, 2010.
- [237] A. A. Khajetoorians, J. Wiebe, B. Chilian, and R. Wiesendanger. Realizing All-Spin-Based Logic Operations Atom by Atom. *Science*, 332(6033):1062–1064, 2011.
- [238] S. Heinze, K. von Bergmann, M. Menzel, J. Brede, A. Kubetzka, R. Wiesendanger, G. Bihlmayer, and S. Blügel. Spontaneous atomic-scale magnetic skyrmion lattice in two dimensions. *Nature Physics*, 7:713–718, 2011.
- [239] S. Baumann, F. Donati, S. Stepanow, S. Rusponi, W. Paul, S. Gangopadhyay, I. G. Rau, G. E. Pacchioni, L. Gragnaniello, M. Pivetta, J. Dreiser, C. Piamonteze, C. P. Lutz, R. M. Macfarlane, B. A. Jones, P. Gambardella, A. J. Heinrich, and H. Brune. Origin of Perpendicular Magnetic Anisotropy and Large Orbital Moment in Fe Atoms on MgO. *Phys. Rev. Lett.*, 115:237202, Dec 2015.

-
- [240] S. Baumann. *Investigation of the unusual magnetic properties of Fe and Co on MgO with high spatial, energy and temporal resolution*. PhD thesis, Universität Basel, Basel, Switzerland, 2015.
- [241] A. Ferrón, F. Delgado, and J. Fernández-Rossier. Derivation of the spin Hamiltonians for Fe in MgO. *New Journal of Physics*, 17(3):033020, 2015.
- [242] J. Lambe and R. C. Jaklevic. Molecular Vibration Spectra by Inelastic Electron Tunneling. *Phys. Rev.*, 165:821–832, Jan 1968.
- [243] R. P. Feynman. There’s Plenty of Room at the Bottom. *Engineering and Science*, 23:22–36, 1960.
- [244] K. C. Nowack, F. H. L. Koppens, Y. V. Nazarov, and L. M. K. Vandersypen. Coherent Control of a Single Electron Spin with Electric Fields. *Science*, 318(5855):1430–1433, 2007.
- [245] J. J. Pla, Kuan Y. Tan, J. P. Dehollain, W. H. Lim, J. J. L. Morton, F. A. Zwanenburg, D. N. Jamieson, A. S. Dzurak, and A. Morello. High-fidelity readout and control of a nuclear spin qubit in silicon. *Nature*, 496:334–338, 2013.
- [246] S. Kotler, N. Akerman, N. Nir, Y. Glickman, and R. Ozeri. Measurement of the magnetic interaction between two bound electrons of two separate ions. *Nature*, 510:376–380, 2014.
- [247] M. S. Grinolds, S. Hong, P. Maletinsky, L. Luan, M. D. Lukin, R. L. Walsworth, and A. Yacoby. Nanoscale magnetic imaging of a single electron spin under ambient conditions. *Nature Physics*, 9:215–219, 2013.
- [248] H. J. Mamin, M. Kim, M. H. Sherwood, C. T. Rettner, K. Ohno, D. D. Awschalom, and D. Rugar. Nanoscale Nuclear Magnetic Resonance with a Nitrogen-Vacancy Spin Sensor. *Science*, 339(6119):557–560, 2013.
- [249] T. Staudacher, F. Shi, S. Pezzagna, J. Meijer, J. Du, C. A. Meriles, F. Reinhard, and J. Wrachtrup. Nuclear Magnetic Resonance Spectroscopy on a (5-Nanometer)³ Sample Volume. *Science*, 339(6119):561–563, 2013.
- [250] D. M. Toyli, C. D. Weis, G. D. Fuchs, T. Schenkel, and D. D. Awschalom. Chip-Scale Nanofabrication of Single Spins and Spin Arrays in Diamond. *Nano Letters*, 10(8):3168–3172, 2010.
- [251] M. Fuechsle, J. A. Miwa, S. Mahapatra, H. Ryu, S. Lee, O. Warschkow, L. Hollenberg, G. Klimeck, and M. Y. Simmons. A single-atom transistor. *Nature Nanotechnology*, 7(4):242–246, 2012.
- [252] A. A. Khajetoorians, B. Chilian, J. Wiebe, S. Schuwalow, F. Lechermann, and R. Wiesendanger. Detecting excitation and magnetization of individual dopants in a semiconductor. *Nature*, 467:1084–1087, 2010.

-
- [253] A. A. Khajetoorians, J. Wiebe, B. Chilian, S. Lounis, and S. Blugel. Atom-by-atom engineering and magnetometry of tailored nanomagnets. *Nature Physics*, 8:497–503, 2012.
- [254] B. W. Heinrich, L. Braun, J. I. Pascual, and K. J. Franke. Protection of excited spin states by a superconducting energy gap. *Nature Physics*, 9(12):765–768, 2013.
- [255] P. Jacobson, T. Herden, M. Muenks, G. Laskin, O. Brovko, V. Stepanyuk, M. Ternes, and K. Kern. Quantum engineering of spin and anisotropy in magnetic molecular junctions. *Nature Communications*, 6:8536, 2015.
- [256] L. Zhou, J. Wiebe, S. Lounis, E. Vedmedenko, F. Meier, S. Blugel, P. H. Dederichs, and R. Wiesendanger. Strength and directionality of surface Ruderman-Kittel-Kasuya-Yosida interaction mapped on the atomic scale. *Nature Physics*, 6:187–191, 2010.
- [257] X. Chen, Y.-S. Fu, S.-H. Ji, T. Zhang, P. Cheng, X.-C. Ma, X.-L. Zou, W.-H. Duan, J.-F. Jia, and Q.-K. Xue. Probing Superexchange Interaction in Molecular Magnets by Spin-Flip Spectroscopy and Microscopy. *Phys. Rev. Lett.*, 101:197208, Nov 2008.
- [258] B. C. den Hertog and M. J. P. Gingras. Dipolar Interactions and Origin of Spin Ice in Ising Pyrochlore Magnets. *Phys. Rev. Lett.*, 84:3430–3433, Apr 2000.
- [259] C. Castelnovo, R. Moessner, and S. L. Sondhi. Magnetic monopoles in spin ice. *Nature*, 451:42–45, 2008.
- [260] S. Baumann, I. G. Rau, S. Loth, C. P. Lutz, and A. J. Heinrich. Measuring the Three-Dimensional Structure of Ultrathin Insulating Films at the Atomic Scale. *ACS Nano*, 8(2):1739–1744, 2014.
- [261] S. V., S. Altieri, A. di Bona, P. Luches, C. Giovanardi, and T.S. Moia. Thickness-dependent strain in epitaxial MgO layers on Ag(001). *Surface Science*, 507510:311 – 317, 2002.
- [262] P. Luches, S. D’Addato, S. Valeri, E. Groppo, C. Prestipino, C. Lamberti, and F. Boscherini. X-ray absorption study at the Mg and O *K* edges of ultrathin MgO epilayers on Ag(001). *Phys. Rev. B*, 69:045412, Jan 2004.
- [263] S. Yan, L. Malavolti, J. A. J. Burgess, A. Droghetti, A. Rubio, and S. Loth. Nonlocally sensing the magnetic states of nanoscale antiferromagnets with an atomic spin sensor. *Science Advances*, 3(5), 2017.
- [264] F. Donati, S. Rusponi, S. Stepanow, C. Wäckerlin, A. Singha, L. Persichetti, R. Baltic, K. Diller, F. Patthey, E. Fernandes, J. Dreiser, Ž. Šljivančanin, K. Kummer, C. Nistor, P. Gambardella, and H. Brune. Magnetic remanence in single atoms. *Science*, 352(6283):318–321, 2016.

-
- [265] A. A. Khajetoorians, B. Baxevanis, C. Hübner, T. Schlenk, S. Krause, T. O. Wehling, S. Lounis, A. Lichtenstein, D. Pfannkuche, J. Wiebe, and R. Wiesendanger. Current-Driven Spin Dynamics of Artificially Constructed Quantum Magnets. *Science*, 339(6115):55–59, 2013.
- [266] C. Wäckerlin, F. Donati, A. Singha, R. Baltic, S. Rusponi, K. Diller, F. Patthey, M. Pivetta, Y. Lan, S. Klyatskaya, M. Ruben, H. Brune, and J. Dreiser. Giant Hysteresis of Single-Molecule Magnets Adsorbed on a Nonmagnetic Insulator. *Advanced Materials*, 28(26):5195–5199, 2016.
- [267] N. Pertaya, K.-F. Braun, and K.-H. Rieder. On the stability of Besocke-type scanners. *Review of Scientific Instruments*, 75(8):2608–2612, 2004.

Appendix A

Upgrades and Operation for the UBC CreaTec LT-STM

Progress is made by trial and failure; the failures are generally a hundred times more numerous than the successes; yet they are usually left unchronicled.

William Ramsay

A.1 A Brief History of the CreaTec LT-STM

The CreaTec LT-STM in the LAIR has a fifteen-year operating history that includes a number of major upgrades and part replacements. The purpose of this appendix is to provide details of the operational status of this STM as of 2017. A short timeline of the instrument is shown below in Table A.1.

Table A.1: History of the CreaTec highlighting major upgrades.

Year	Event
2003	CreaTec purchased by Professor Johannes Barth.
2010-2011	This cryostat is replaced and a thermal braid is added.
2013	The CreaTec STM is moved into c-pod, part of the LAIR.
2014	The tunnelling current line is replaced.
2015	Addition of a Nanonis controller with high voltage amplifier.
2016-2017	The STM head is upgraded to an AFM-STM model.

A.2 Components of the CreaTec

The Createc is composed of a large number of electrical, mechanical, and cryogenic systems that work together to create and maintain a low-temperature, UHV environment at the STM tip-sample junction. These systems and their individual components are described in detail in this section, with many of them shown in Figure A.1.

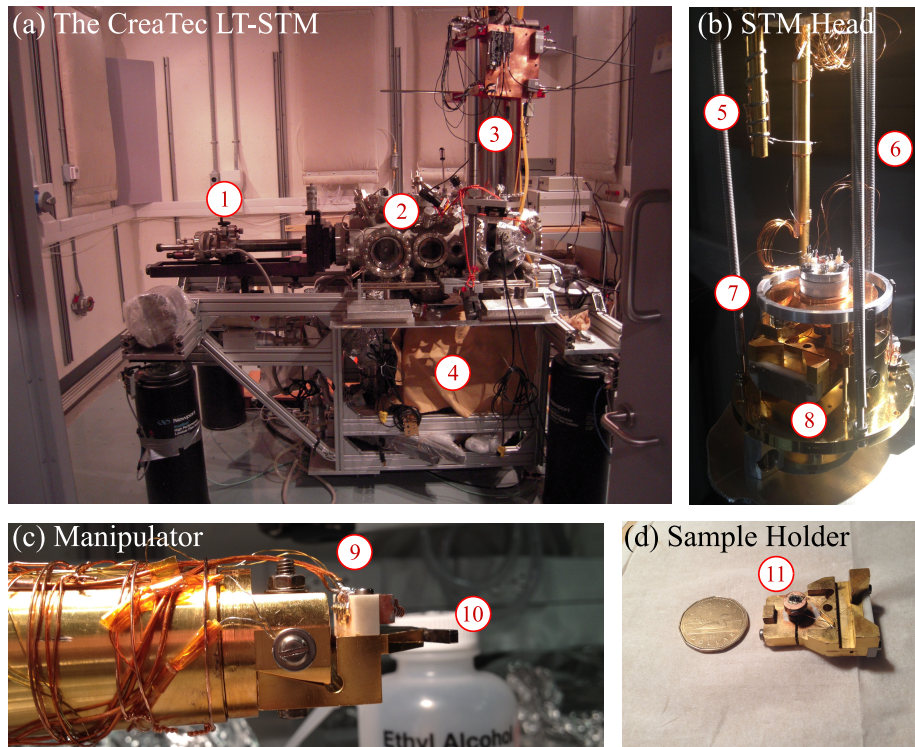


Figure A.1: **The CreaTec LT-STM in c-pod.** (a) The vacuum chamber consists of (1) the manipulator arm, (2) the preparation chamber, (3) the cryostat, and (4) the pumping system. (b) The STM/AFM head being installed outside of vacuum. The visible components are (5) tunnelling current cold finger, (6) damping springs, (7) walking disc, and (8) a sample holder mounted in the measurement position. (c) The manipulator is used to move samples within the vacuum space. It consists of (9) sample bias and annealing contacts and (10) sample clamping mechanism. (d) The sample holder (11) with a graphite sample mounted, coin shown for scale.

The Manipulator Arm: The manipulator arm allows transfer and control of samples inside the UHV environment of the preparation and STM chamber. The manipulator is capable of motion in x, y, and z directions as well as 360 degrees of rotation. It is mounted on a rotary feedthrough that allows it to be differentially pumped and it has a cooling line through which liquid helium or liquid nitrogen can be circulated to pre-cool a sample holder to as low as 20 K before transfer inside the STM cryogenic shields.

The Preparation Chamber: The preparation chamber houses samples in ultra-high vacuum, between 10^{-10} – 10^{-9} mbar and allows for sample preparation and characterization of samples before they are inserted into the STM chamber. The preparation chamber is equipped with state-of-the-art surface science technique tools for in-situ sample preparation and characterization, such as a low-energy electron diffraction (LEED) setup¹, a quadrupole mass spectrometer², electron beam tip heating tool³, and argon ion sputtering gun⁴. The preparation chamber is also connected to a load lock that can be used to transfer in samples from ambient conditions without breaking vacuum and contains a sample garage theoretically capable of holding six samples in-situ.

The STM Chamber: The STM chamber houses the STM head, including the electrical wiring used for measurement and control, within a 77 K nitrogen heat shield and 4.2 K helium heat shield. The nominal pressure in the chamber outside of the heat shields is $3 - 5 \times 10^{-10}$ mbar during measurement, and pressure inside the 4.2 K cold space where the sample is measured is less than 10^{-12} mbar due to cryogenic pumping by the heat shields.

The Cryostat: The cryostat is a two-layer system of heat shields and cryogenic reservoirs mounted on the top of the STM chamber. The outer reservoir consists of 13.3 L shroud filled with liquid nitrogen while the inner reservoir is filled with 4.3 L of liquid helium and coupled directly to the STM head [125]. The maximum time that cryogenic liquids last before boiling off, known as the hold time, is approximately 72 hours, making this the longest time possible for a single measurement.

Pumping System: The pumping system keeps the STM chamber, preparation chamber, and manipulator arm under ultra-high vacuum. The system consists of a series of interconnected turbo molecular vacuum pumps⁵, a roughing pump⁶, a titanium sublimation pump⁷, and ion pumps mounted on the bottom of each chamber. The pressure is monitored at each pumping stage by a set of vacuum gauges⁸ and a mass spectrometer in the preparation chamber⁹.

The STM head: The STM head is a beetle-style STM head [129, 131]. A beetle design uses a walking plate sitting atop three piezo tubes to achieve lateral

¹Specs ErLEED 100/150

²SRS RGA300

³Ferrovac GmbH.

⁴Specs IQE 11/35

⁵Varian TV 301 Navigator Turbo Pump and TMU 071 P Turbo Pump

⁶TriScroll Dry Vacuum Pump

⁷Varian Model 929-0022

⁸IK 270 Compact Cold Cathode Gauges

⁹SRS RGA300

and vertical motion on the order of millimetres. Coarse positioning of the STM tip, which hangs off of a piezo tube mounted in the centre of the walking plate, is possible with a maximum radial lateral range of 3 mm and a vertical range of 0.9 mm. The coarse controls can be used to position the tip within micrometres of the sample surface. Fine motion of the tip, on the scale of Angstroms to hundreds of nanometres, is generally performed using the main piezo tube upon which the tip is mounted, but can also be split between the outer piezo tubes and the main piezo tube. The beetle-style head offers relatively large lateral motion at the potential expense of reduced mechanical stability [267]. Work has been done to find the optimum configuration for minimal mechanical noise on the LAIR CreaTec. The set-up and voltage profiles used to move a beetle-style STM head are shown in Figure A.3. The current incarnation of the CreaTec has a head capable of performing STM/AFM measurements, though this upgrade was only completed at the beginning of 2017 and AFM measurements are not featured in this thesis.

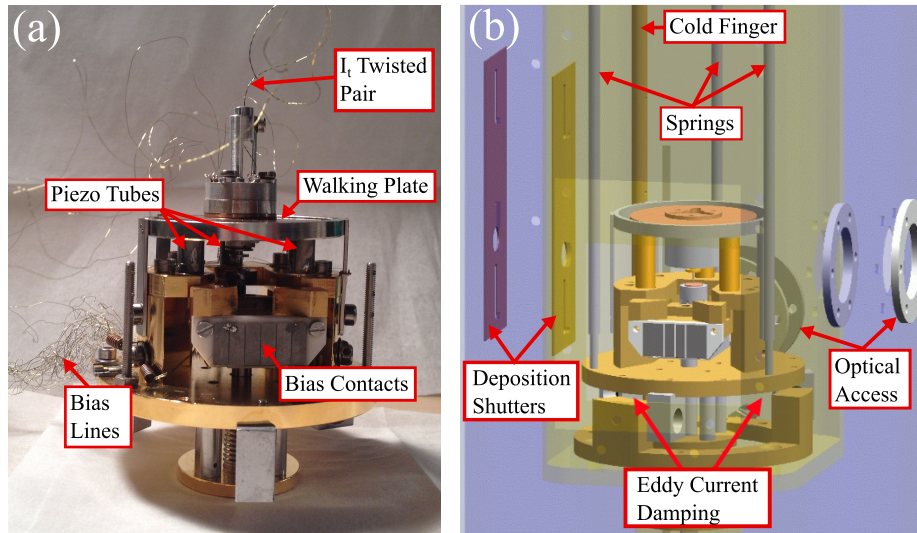


Figure A.2: **The CreaTec STM head.** (a) The upgraded UBC STM head used for the bulk of the measurements in Part II. The wiring is designed to be slack to avoid coupling vibration into the tip-sample junction and is extremely fine in order to prevent heat leaks from room temperature to the STM head. (B) A model of the original CreaTec head when mounted inside the heat shields.

The Sample Holder: The sample holder is a copper piece which mechanically holds the sample atop an electrically isolated heating stage. Bias and annealing contacts are run from the sample to electrical contacts on the back of the sample holder. The height profile of the sample holder can be manually ad-

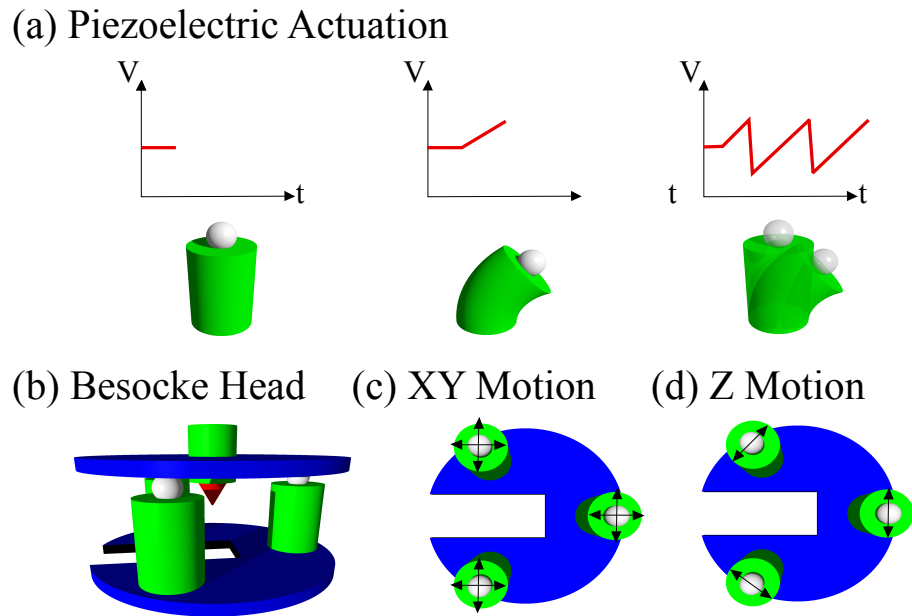


Figure A.3: **Operation of a beetle/Besocke style STM head.** (a) The voltage profile applied to the quadrants of a piezo tube to make it move. The voltage is slowly ramped from a constant value up to a maximum before being quickly inverted. This produces a sawtooth waveform that moves the walking plate. (b) A basic model of a beetle-style STM head such as the one used in the CreaTec STM. (c) Forces generated from the piezo tubes on the walking plate for X and Y motion. (d) Torque on the walking plate from the piezo tubes in Z motion. When all three piezo tubes produce clockwise forces a net torque is produced that moves the walking plate and STM tip towards the sample. Counterclockwise forces produce a net torque that moves the walking plate and STM tip away from the sample.

justed and additional contacts can be applied to measure temperature or apply a back gate voltage.

The Isolation Pod (c-pod): The frame housing the CreaTec sits atop pneumatic isolation legs¹⁰ on a 22 tonne concrete block that is positioned on a set of even larger set of pneumatic isolators. This setup ensures a very high degree of passive damping of ambient seismic and acoustic noise [123]. The baseline noise spectrum of c-pod is shown in Figure 2.2.

Electronic Measurement: For measurement of the tunnel current the CreaTec is paired with either a FEMTO DLPCA-200 or FEMTO LCA-4K-1G amplifier. Both offer roughly $4 - 5 \text{ fA}/\sqrt{\text{Hz}}$ of electrical noise. The DLPCA-200 offers manually adjustable gain with 1.2 kHz bandwidth at 10^9 V/A gain while the LCA-4K-1G offers 1.1 kHz bandwidth at 10^9 V/A gain, making it preferred for fast measurement acquisition. The baseline noise spectrum of both amplifiers, expressed as amplitude spectral density, is shown in Figure 2.2.

Data Acquisition: Data acquisition is performed by a Nanonis SPM RC5 Control System¹¹. The Nanonis is responsible for applying the direct current bias between tip and sample and generating the high voltage sawtooth waveforms sent to the piezoelectric tubes in order to move the tip over the sample, as shown in Figure A.3. The Nanonis is also used to measure the tunnelling current signal from the FEMTO amplifiers and contains an internal lock-in amplifier that can be used to add AC excitations to the bias line and measure derived quantities. It has an 18-bit analog-to-digital converter, and measures signals differentially with a $\pm 10 \text{ V}$ range. Electrical grounding of all STM lines is done through the Nanonis ground in order to prevent the formation of ground loops, which can pose a significant measurement problem if left unaddressed. Ideal tunnelling noise spectra, both in and out of tunnelling, are shown in Figure 2.2.

¹⁰Newport

¹¹This controller runs National Instruments LabVIEW Real-Time OS and routes signals through a National Instruments Field Programmable Gate Array (FPGA)

Appendix B

Real Space Simulation of Multiple Scatterers

Science is not built on success.
It's built on failure. It's built on
frustration. Sometimes it's built
on catastrophe.

Summer Redstone

B.1 Using Bessel Functions to Simulate QPI Data

The T-matrix scattering calculations combined with set point theory does a very good job qualitatively reproducing the measurement mode dependent feature seen in the experimental data. It does not, however, produce quantitative agreement away from the surface state peak in the line cuts. To obtain further information one must take into account both the presence of multiple scattering centres within a single experimental image and also the different phase of each scattering centre. One of the reasons the T-matrix theory fails to reproduce the full QPI line shape is that it takes as its starting point only a single scattering centre, while the experimental data features many scattering sites.

To verify that the differences between the theoretical and experimental FT-STS radially projected data could be accounted for by the presence of multiple scatterers a real space model was developed. This model does not have the ability to simulate many-body effects, such as electron-phonon coupling [132], but in sacrificing this it is able simulate many scattering centres.

Following the real-space fitting of QPI signals undertaken by Crommie *et al.* [154] the scattering off of both step edges and point defects (CO molecules) can be performed using Bessel functions

$$\rho_{step}(E, x) = (1 - J_0(2k_0x))L_0 \quad (\text{B.1})$$

$$\rho_{CO}(E, r) \propto \frac{1}{k_0r} [\cos^2(k_0r - \frac{\pi}{4} + \delta) - \cos^2(kr - \frac{\pi}{4})] \quad (\text{B.2})$$

where δ is the phase shift discussed in Chapter 4 and $L_0 = m^*/\pi\hbar^2$ is an approximate form for the density of states of the surface state in the absence of scattering.

Figure B.1 shows a comparison at the Fermi level between an experimental grid and the Bessel function model. Unlike the T-matrix theory the real space simulation does a much better job of replicating the features of the FT-STs radial projection away from the surface state peak. This result establishes the general shape of a QPI line cut on Ag(111) independent of the surface state and set point effects is determined by the spatial position of the scattering centres and the image analysis used to correct for step edges and z drift.

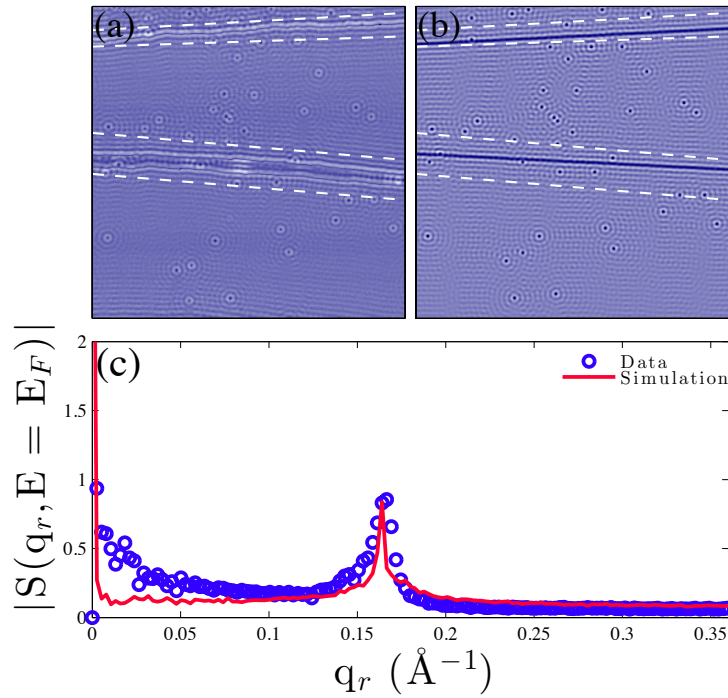


Figure B.1: **Spectroscopic grid simulated in real-space by Bessel functions.** (a) Experimental measurement of the differential tunnelling conductance at E_F from a spectroscopic grid with measurement conditions: $V_s = -100$ mV, $I_s = 100$ pA, $V_b = (-100, 120)$ mV, 239×239 nm² with 380×380 pixels. (b) Simulation of the experimental data using Equation B.2 and identifying the pixels corresponding to the centre of each CO. (c) FT-STs scattering intensity of both experiment and simulation projected onto the q_r axis. The simulation results deviate from the experiment at low- q_r , possibly indicating the need to add a degree of noise to the simulation data.

Appendix C

A Scheme for Pulsed ESR-STM

Upward, not Northward.

Edwin A. Abbott - 1884 [2]

C.1 Development of a Pulsed ESR-STM Technique

The ESR-STM results presented in Part III were achieved using the continuous wave (CW) mode of ESR-STM described in Chapter 6. This technique has proven extremely fruitful in achieving spin resonance, providing a new STM acquisition mode with unprecedented energy resolution, and developing a new form of magnetometry. By sweeping the microwave frequency over a single atom the resonance frequency can be measured via the SP-STM tip as the tunnelling magnetoresistance changes.

One weakness of CW ESR-STM is its inability to coherently manipulate the quantum spin of an atom in a way that would allow for applications in either quantum computing or spintronics. This shortcoming stems from the ratio between the energy relaxation time (T_1), the quantum phase coherence time (T_2), and the Rabi flop time (T_{Rabi}). The energy relaxation time quantifies the time it takes for the resonant spin to return to the thermally distributed equilibrium population. This can be characterized by pump-probe spectroscopy for Fe and is found to be $T_1 \approx 100 \mu\text{s}$ [86]. The quantum phase coherence time describes the amount of time that a resonant spin maintains its phase, a crucial time scale as it sets the decoherence time of spin-based qubits [210]. For ESR-STM on Fe the T_2 can be deduced by fitting the ESR resonance peak width as a function of microwave drive amplitude, which gives a $T_2 = 100 \text{ ns}$ [86]. The Rabi flop time is the time it takes to coherently reverse the magnetic state, and it depends on the strength of the driving field. For CW ESR-STM this time is $T_{Rabi} = 1.2 \pm 0.1 \mu\text{s}$ [86].

In CW ESR-STM the T_1 time is three orders of magnitude larger than the T_2 time. From results in traditional ESR [207], this implies that when on resonance the spin is performing a random walk consisting of many periods of coherent evolution (each one lasting roughly one T_2 period) over the course of a single

T_1 period. Though this is useful for observing resonance, it does not allow for coherent control of the spin because the spin loses its phase orientation on too short a timescale compared to the manipulation time, which is characterized by T_{Rabi} . The three order of magnitude difference between T_{Rabi} and T_2 means that the spin cannot be coherently driven hard enough to reverse the magnetization before the phase is lost. One potential route to avoid this difficulty is a pulsed ESR-STM set-up.

C.1.1 Introduction to Pulsed ESR

In pulsed ESR, a microwave pulse is used to coherently manipulate spin centres using either a single pulse or series of pulses on resonance. The difference between continuous wave resonance and pulsed resonance is illustrated in Figure C.1. In Figure C.1 (a)(i) the familiar microwave chopping scheme is shown for CW-ESR. To understand how this affects the resonant spin the concept of the Bloch sphere is introduced in (a) (ii). The Bloch sphere is a useful theoretical concept that visually represents an arbitrary superposition state of a spin or qubit [210]. When on resonance the spin wave function is a coherent superposition of two spin eigenstates

$$|\psi\rangle = \alpha |0\rangle + \beta |1\rangle. \quad (\text{C.1})$$

It is a requirement of quantum mechanics that $|\alpha|^2 + |\beta|^2 = 1$ to ensure that probabilities sum to one. The conservation of probability allows the superposition state prefactors to be rewritten in terms of spherical coordinates

$$|\psi\rangle = e^{i\phi} (\cos(\theta/2) |0\rangle + \sin(\theta/2) |1\rangle). \quad (\text{C.2})$$

This expression illustrates that the superposition state of the resonant spin can be represented by a vector of unit length that lives on the unit sphere. This sphere has the $|0\rangle$ state aligned with $+z$ axis and the $|1\rangle$ state aligned with $-z$ axis.

The Bloch sphere representation of a spin in CW ESR-STM is shown in Figure C.1 (a)(ii). The red arrow evolves coherently, with set phase, for the duration of one T_2 period, before losing that phase and evolving coherently with a new phase. This is a visual representation of the random walk described in the previous section. The optimal case for CW ESR-STM consists of the superposition state being located in the $x - y$ plane of the Bloch sphere, corresponding to an evenly weighted coherent state and leading to the increase in tunnelling current on resonance observed in the experiment.

Pulsed ESR, in contrast, is shown in Figure C.1 (b). In this measurement mode a microwave pulse is delivered at the resonant frequency that causes that spin to precess. The spin is detected using a DC electrical probe which collapses it's state to either $|0\rangle$ or $|1\rangle$. It is then hit with another resonant RF pulse

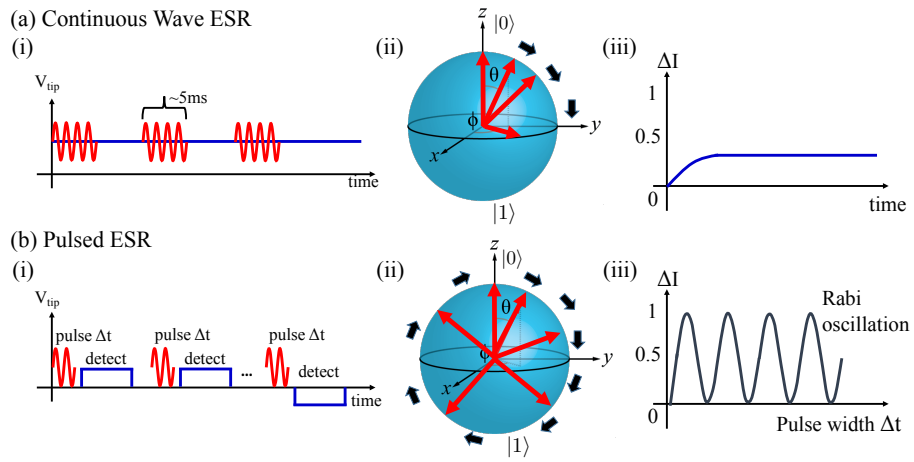


Figure C.1: **Continuous wave versus pulsed ESR-STM** (a) Continuous wave ESR-STM uses (i) a chopped microwave frequency sweep to (ii) randomly walk the spin state along the Bloch sphere, resulting in (iii) an increase in the tunnel current. (b) Pulsed ESR-STM uses a (i) series of resonant pulses to (ii) coherently manipulate the spin state around the Bloch sphere, resulting in (iii) observation of Rabi oscillations in the tunnelling current signal.

that restarts the coherent evolution. Instead of a continuous increase in the tunnelling current signal on resonance the observed signal instead corresponds to a Rabi oscillation, as the coherent superposition moves from a completely $|0\rangle$ state to a $|1\rangle$ state and back (called a Rabi flop) [210].

Pulsed ESR-STM experiments did not show signatures of the expected Rabi oscillations. Instead only a small change in tunnelling magnetoresistance was observed. The lack of Rabi oscillations can be attributed to the small T_2 time, in particular when compared to the time needed for the microwave pulse to perform a full coherent rotation of the spin state (the Rabi rate Ω). This poses a technical problem, as the Rabi flop rate can only be increased by increasing the magnitude of the driving pulse V_μ , and this cannot be increased significantly without exceeding the 14 meV excitation threshold to state $|2\rangle$. Thus, the only way to achieve fully coherent control is via increasing the T_2 time, which necessitates better isolation of the spin from its environment.

One method of increasing the T_2 time is by engineering the spin environment. This has been used to successfully optimize the T_1 time [230], resulting in a long and tunable lifetime of the excited spin. One potential method is to examine Fe atoms on thicker MgO thin films, such as three or four monolayer films, as thicker films should have a smaller scattering rate from conduction electrons. Thicker films have the disadvantage that it increases the tunnelling junction resistance, meaning that the tip must move closer to the Fe atom in order to achieve the same tunnelling current. This potentially causes a large relaxation rate due to scattering of the spin state by tunnelling electrons.

Interaction with the tunnelling electrons is the limiting factor that determines T_2 , as the limit imposed by substrate electron scattering is greater than 100 ns [230]. This leads to a proposal for a pulsed ESR scheme that works in conjunction with oscillations of the tip. This method, as detailed in the next section, has the potential to increase the quantum phase coherence time enough to observe a Rabi oscillation.

C.1.2 A Scheme for Tip-Oscillating Pulsed (TOP) ESR-STM

The number of tunnelling current electrons passing through the Fe atom depends exponentially on the tip-sample vacuum gap, as discussed in Chapter 2. Withdrawing the tip on the order of a nanometre therefore causes a drop in the number of tunnelling electrons probing the Fe electronic spin, and reduces the probability of a tunnelling electron spin scattering from the Fe spin and causing a loss of phase coherence. At a tunnelling current of 1 pA, roughly 10 million tunnelling electrons cross the tunnel barrier every second. If the tip is retracted by 5 Angstroms than the tunnelling current falls by roughly e^{-5} to roughly 1 fA and the number of tunnelling electrons that can perturb the spin state of the atom falls by three orders of magnitude. Unfortunately, the tunnelling electrons are needed to read out the spin state, and withdrawing the tip causes a loss of the read-out signal. By oscillating the STM tip in phase with the microwave pulsed sequence a compromise can be made between minimizing the interaction

of the spin via tunnelling electrons and allowing high enough tunnelling currents to ensure read-out of the spin state.

The set-up for this measurement scheme, dubbed Tip-Oscillating Pulsed (TOP) ESR-STM, is shown in Figure C.2. The tip height is modulated at a frequency from 10–25 kHz by applying an AC voltage to the piezomotor holding the tip. The ESR microwave pulse that sets the spin into resonance is delivered when the tip is at the maximum distance away from the Fe atom. This sets the Fe atom spin into resonance when the tunnelling current is at a minimum, making it the least likely that tunnelling electrons scatter the spin and cause loss of phase. At the point of closest tip–atom approach a DC electrical bias probe is applied to the tip which causes a large tunnelling current to read-out the spin state. This likely causes loss of phase coherence but only after a period of phase evolution free of tunnelling electron induced phase loss. The Fe spin state is then reset to a known initial configuration using a DC pump voltage. The entire sequence is repeated many times and demodulated by the lock-in amplifier at 95 Hz. Every half-period of the lock-in amplifier frequency the microwave trigger is turned off, in order to measure the change in tunnelling current caused by the microwave excitation, as in CW ERS-STM. The lock-in amplifier measures the tunnelling current at the chopping frequency, detecting the spin state of the Fe atom. In addition to limiting the possibility of tunnelling electron phase decoherence this method also has the advantage that the microwave power that can be delivered is much higher, as the DC bias is 0 meV when the microwave pulse is applied and the tunnelling electrons are exponentially suppressed as the tip moves away from the sample surface.

C.1.3 Benchmarking the TOP ESR-STM Technique

In order to successfully measure a Rabi oscillation and achieve coherent control over the Fe spin state the TOP ESR-STM technique had to be optimized for the 1K-STM. This involved the following series of steps:

- Calibration of the applied AC piezomotor voltage used to oscillate the tip against the physical amplitude of tip oscillations observed.
- Characterization of the magnitude of the tip oscillations as a function of tip shaking frequency.
- Testing whether the tip can still image in topography mode while the tip is oscillating.
- Tuning experimental parameters and phases to optimize the T_2 period.

TOP ESR-STM begins by using continuous wave ESR-STM to find the resonance frequency of the Fe atom located under the STM tip. This Fe atom is characterized using pump-probe spectroscopy to ensure a T_1 time on the order of 100 μ s. The T_1 time can be optimized by careful control of the tip–sample gap and tunnelling current set-point [233]. Before attempting any tip oscillations

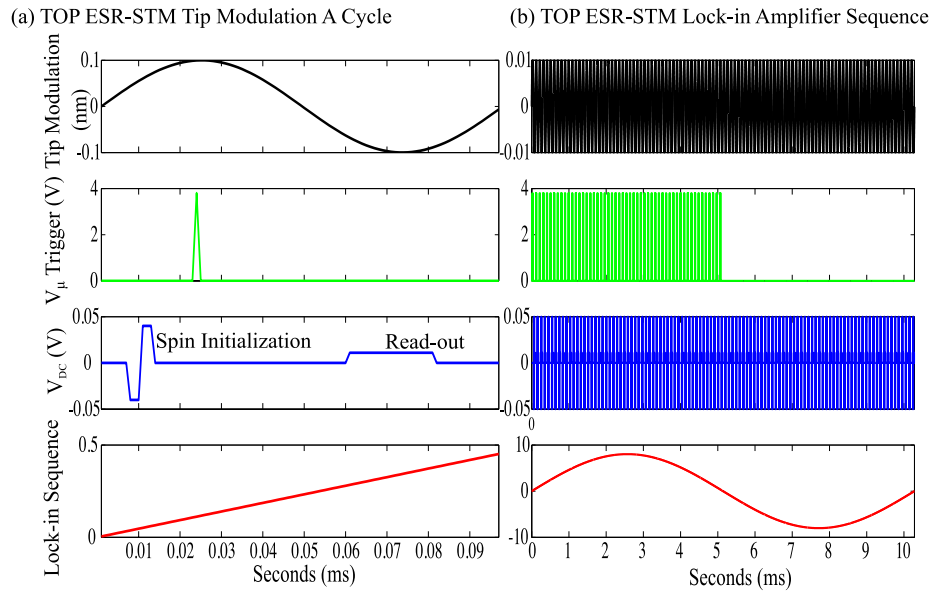


Figure C.2: **Tip Oscillating Scheme** (a) A single set of TOP ESR-STM signals over one period of the tip oscillation. The V_{μ} pulse is triggered at the maximum tip sample separation and V_{DC} is used for initialization of the spin and read-out using a positive polarity DC bias pump. (b) Many tip shaking cycles occur during one cycle of the lock-in measurement. The lock-in measurement compares the average tunnelling current during sequences with and without the spin-manipulation microwave pulses.

on top of the target Fe $I_t(z)$ spectroscopy is used to characterize the relation between the tip height and tunnelling current. $I_t(z)$ spectroscopy is similar in methodology to the STS point spectroscopy introduced in Chapter 2. Instead of sweeping the bias voltage the tip height is adjusted via a linear voltage ramp applied to the z piezo motor. As shown in Chapter 2, $I_t(z) \propto e^{-\kappa z}$, which means that a linear ramp of z while measuring the tunnelling current allows for extraction of κ and a conversion from height in \AA to pA. The change in height must be measured with respect to a reference as the absolute size of the tip-sample gap is not known. In TOP ESR-STM that reference is chosen to be the height at which the set-point condition is met by the feedback, typically at values of $I_t = 1$ pA and $V_s = 5$ mV. Measured $I_t(z)$ spectroscopy over an Fe atom is shown in Figure C.3 (a) on a semi-log plot. An accompanying linear fit allows for extraction of κ , which is equal to 1.704 \AA^{-1} .

Tip oscillation at a single frequency can be characterized in a similar way to $I_t(z)$ spectroscopy, except in this case the feedback remains engaged. By delivering an AC voltage to the tip piezo motor and ramping the magnitude of this voltage while recording the tunnelling current a relation between I_t and the excitation voltage can be established. The excitation voltage applied can be converted into an effective change in height of the tip using the κ factor extracted from conventional $I_t(z)$ spectroscopy. An example of the measured tunnelling current as a function of the excitation (converted to \AA) is shown in Figure C.3 (b) at a frequency of $f_z = 17241$ Hz. The DC tunnelling current increases as a function of increased excitation amplitude because the tunnelling current is sampling smaller tunnelling gaps, which correspond to higher tunnelling currents at a fixed bias.

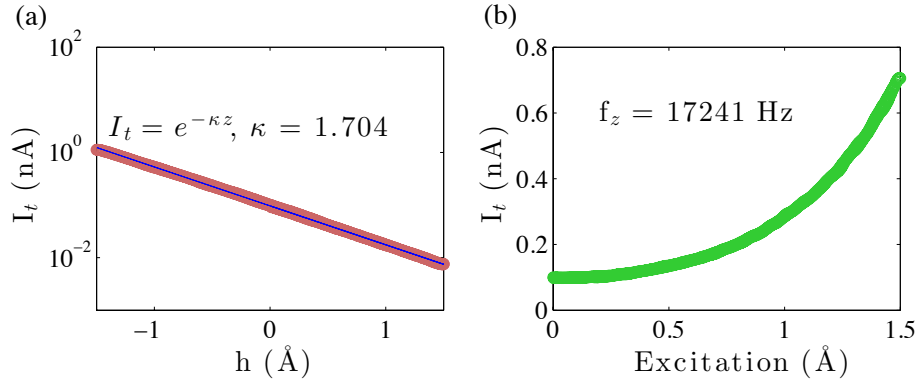


Figure C.3: **Characterization of the tip modulation amplitude.** (a) $I_t(z)$ spectroscopy can be used to fit for the κ factor at a particular point, giving a relation between the tunnelling current and the relative tip-sample gap. (b) The tunnelling current is measured as a function of tip modulation amplitude.

In order to successfully perform the TOP ESR-STM technique the oscillation magnitude of the tip must be stable. This is not trivial, as unlike atomic force microscopy instruments, STMs are not optimized for stable mechanical oscillation of the tip-sample junction at kHz frequencies. To find a stable set of frequencies that demonstrates a flat response as a function of constant AC voltage applied to the tip piezo the frequency (f_z) was swept while the tunnelling current was recorded. Figure C.4 illustrates the response of the feedback loop under constant-current feedback as a function of modulation frequency delivered to the z piezo motor at constant power. The degree of modulation demonstrates a non-monotonic response due to frequency-dependent mechanical resonances being excited in the STM head. The frequency sweep characterization allows for identification of an area with a relatively flat response, centred at 17241 Hz. The relation between the applied shaking voltage and the change in tip height is deduced by the previously measured tunnelling current spectroscopy curve at this frequency shown in Figure C.3.

A major milestone in establishing the feasibility of the TOP ESR-STM mode is the ability to image individual Fe atoms on the MgO surface while oscillating the tip at kHz frequencies. The inset of Figure C.4 shows STM topography of an Fe atom while the tip is being modulated at 17241 Hz with a 2 Å peak-to-peak amplitude. This demonstrates a proof of concept for one of the largest technical hurdles to the TOP ESR-STM method, and marks the first time topography has been measured with the 1-K STM using this technique.

C.2 Conclusion

A scheme for performing successful pulsed ESR-STM was introduced. TOP ESR-STM should be able to measure Rabi oscillations of an Fe spin by delivering a kHz AC voltage to the tip piezomotor and synchronizing the tip motion with microwave excitation and pump-probe readout of the spin state. A milestone was achieved in benchmarking this new technique by demonstrating that it is possible to perform stable STM topography measurements over single Fe atoms while oscillating the tip at over 17 kHz. Additional work to ensure phase synchronization between the microwave pulse sequences, DC pump-probe signals, and tip oscillation is needed to ensure the best possible chance of measuring a coherent Rabi oscillation of the Fe spin.

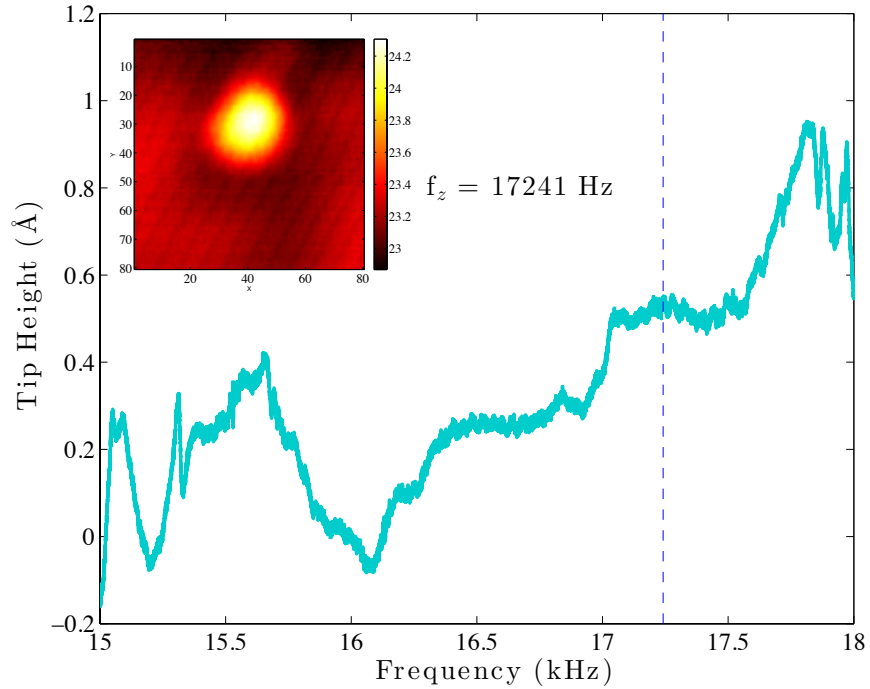


Figure C.4: **Tip response as a function of modulation frequency.** A relatively stable area, away from mechanical resonances, is found at 17241 Hz and so this frequency is chosen for TOP ESR-STM. The inset is a STM topograph of an Fe atom taken while the STM tip is being modulated with a peak-to-peak height of 2 Å. Imaging conditions are $I_s = 25 \text{ pA}$, $V_b = 100 \text{ mV}$, and $30 \times 30 \text{ Å}$.